Fluid-Dispersed 2D Material Composites for Integrated Optoelectronic and Photonic Devices

Submitted by Benjamin Thomas Hogan to the University of Exeter
as a thesis for the degree of
Doctor of Philosophy in Physics/Engineering (CDT)
In August 2019

I certify that all material in this thesis which is not my own work has been identified and that no material has previously been submitted and approved for the award of a degree by this or any other University.

Signature: …………………………………………………………..

Abstract.

In this thesis, fluid dispersed two-dimensional (2D) material composites with the potential for integration with optoelectronic and photonic devices are looked at. By considering the existing literature, three key areas that require further development are identified. Firstly, new materials with improved properties (faster switching, facile reconfigurability, *etc.*) are required to enable the development of new devices with improved performance over the state-of-the-art. Fluid dispersed 2D material composites are then synthesised by two routes: dispersing 2D materials in a nematic liquid crystal host, and using 2D materials dispersed in an organic solvent as the mesogens of a liquid crystal phase. By dispersing 2D materials such as graphene, graphene oxide, and transition metal dichalcogenides in a nematic liquid crystal, one can take advantage of the orientational reconfigurability of the liquid crystal to controllably reorient the dispersed 2D materials. The properties of the fluid composites are also investigated – namely the switching time, threshold voltage, critical temperature and dichroism properties. Switching times, threshold voltages, and critical temperatures were found to compare favourably to the pure liquid crystal independent of the dispersed 2D material. Dichroism measurements were inconclusive, but demonstrate possible suppression or enhancement of the dichroism of the pure liquid crystal under the correct 2D material doping conditions. Liquid crystals based on tungsten disulfide dispersed in organic solvents by a scalable liquid phase exfoliation method were also synthesised. The particle sizes were analysed by scanning electron microscopy, atomic force microscopy, optical microscopy, Raman spectroscopy, and dynamic light scattering. Dynamic light scattering results are particularly promising as this technique has not previously been successfully applied to the determination of sizes of high aspect ratio particles. The linear and circular dichroic properties of the tungsten disulfide liquid crystals were also considered. Particularly interesting is the emergence under applied magnetic field of circular dichroism, suggesting a helical alignment of the dispersed 2D material particles. Secondly, a new characterisation technique to analyse particle positions using Raman spectroscopy was developed. Microfluidic structures were designed to maximise the Raman signal intensity for the different Raman bands of 2D materials by numerically analysing the expected Raman intensity *via* a scattering matrix method. The enhancement was experimentally verified. It is then shown that integrated 2D material particles can be dynamically controlled through the application of electric field, or by the use of a laser. How the Raman signal varies as a function of the particle position within the microfluidic cavity is considered. It is demonstrated that this variation can be used, by combining numerical analysis with experimental data, to track particles first in one dimension and then in two dimensions. A discussion of how three-dimensional tracking would be achieved is also presented. Consideration of how the particle alignment angle could further affect the Raman signal is included. The effect of having arrays of multiple particles, rather than a single particle, is also considered. The laser focus position is shown to affect only the intensities of the Raman signal, rather than the ratios between the intensities of the different peaks. Further analysis shows how the shape and size of the particle can affect the Raman signal intensity. A technique is presented to extract the concentration of fluid dispersed particles from Raman spectra, by considering only the Raman bands of the fluid. Finally, the possible applications of 2D material fluid composites are looked at, focusing on optoelectronic and photonic devices. Highly uniform thin films are produced from tungsten disulfide liquid crystalline dispersions. These films are then transferred to a variety of substrates. The terahertz regime performance of the tungsten disulfide thin films shows great promise for their future use in terahertz generation and detection applications. Unstable Q-switched lasing operation can also be observed for thin films transferred to silver mirrors and used to form a laser cavity. Methods for how the thin films can be integrated with photonic structures such as waveguides and microring resonators are discussed. Analysis is presented for how the integration of graphene or transition metal dichalcogenides on top of the photonic structures can affect their resonance and absorption properties, depending on the film area and thickness. The future prospects for the application of these materials are also outlined.

Acknowledgements.

I would like to give thanks to my supervisors, Prof. Anna Baldycheva and Prof. Monica Craciun, for their ideas, discussion and input throughout this PhD. Without them, the project would never have existed, let alone been successful. Further thanks are due to all the researchers from the Baldycheva research group. In particular, Dr. Evgeniya Kovalska and Joaquin Faneca have provided great assistance with some of the research in this thesis. As for others, thanks to all the research interns and Master's students who have worked with me over the last four years – there are too many of you to name, but your assistance has been invaluable. Thanks also to my collaborators away from Exeter, whose time, equipment, and expertise have been invaluable.

It should be mentioned that this PhD would not have been possible without the financial backing of the EPSRC Centre for Doctoral Training in Metamaterials. But it was not just finance that was provided, I've also been lucky enough to participate in their fantastic training programme, and enjoyed many further benefits beyond those typical for a PhD. Specific thanks go to the administrators of the CDT whose time and effort in aiding our success as students is so often underappreciated.

Finally, thanks to the friends and family who have supported me during my time here. To Ben Ash and Toby Octon – you made starting a PhD so much easier. I'm sorry if I distracted you both too much with our (occasionally research-relevant) conversations over the years. To my parents, my grandparents, and perhaps even my brothers, for always being there. And especially to my mum, for listening so often to my complaints on the phone. To all the others not mentioned here, I'm sorry for not including you, but I wanted to keep this short.

And finally finally, to Iveta Steblevska. I met you as a result of doing this PhD, and even if nothing else came of it, you would have made the last four years of work worthwhile. Thank you.

Contents.

List of Publications and Presentations.

Publications.

1. Galaburda M, Kovalska I, **Hogan BT**, Baldycheva A, Nikolenko A, Dovbeshko GI, Oranska OI, Bogatyrov VM. (*Under Review*) Mechanochemical synthesis of carbon-stabilized Cu/C, Co/C and Ni/C nanocomposites with prolonged resistance to oxidation, *Scientific Reports*.
2. Faneca J, **Hogan BT**, Diez IR, Gardes FY, Baldycheva A. (*Under Review*) Tuning silicon-rich nitride microring resonances with graphene capacitors for high-performance computing applications, *Optics Express*.
3. **Hogan BT**, Kovalska I, Zhukova MO, Yildirim M, Craciun MF, Baldycheva A. (*2019*) 2D WS_2 Liquid Crystals: Tunable Functionality Enabling Diverse Applications, *Nanoscale*, DOI:10.1039/C8NR07205A.
4. Osipov VY, Treussart F, Abbasi Zargaleh S, Takai K, Shakhov FM, **Hogan BT**, Baldycheva A. (*2019*) Photoluminescence from NV^- Centres in 5nm Detonation Nanodiamonds: Reliable Identification and Large Sensitivity to Magnetic Field, *Nanoscale Research Letters*, DOI:10.1186/s11671-019-3111-y.
5. Zhukova MO, **Hogan BT**, Grachev YV, Kovalska I, Walsh K, Craciun MF, Baldycheva A, Tcypkin AN. (2019) Transmission Properties of $FeCl_3$-Intercalated Graphene and WS_2 Thin Films for Terahertz Time-Domain Spectroscopy Applications, *Nanoscale Research Letters*, DOI:10.1186/s11671-019-3062-3
6. Kovalska I, Lesongeur P, **Hogan BT**, Baldycheva A. (2019) Multi-layer graphene as a selective detector for future lung cancer biosensing platforms, *Nanoscale*, DOI:10.1039/C8NR08405J.
7. Ushakova EV, Cherevkov SA, Volgina DOA, Zakharov VV, Komissarenko FE, Shcherbakov AA, **Hogan BT**, Baldycheva A, Fedorov AV, Nabiev IR. (2018) From colloidal CdSe quantum dots to microscale optically anisotropic supercrystals through bottom-up self-assembly, *Journal of Materials Chemistry C*, DOI:10.1039/C8TC04780D.
8. Faneca J, **Hogan BT**, Torres Alonso E, Craciun M, Baldycheva A. (2018) 2D materials integrated in Si3N4 photonics platform, *Proceedings of SPIE*, volume 10537, pages 105370A-105370A, DOI:10.1117/12.2290410.
9. **Hogan BT**, Kovalska E, Craciun MF, Baldycheva A. (2017) 2D Material Liquid Crystals for Optoelectronics and Photonics, *Journal of Materials Chemistry C*, DOI:10.1039/C7TC02549A.

10. **Hogan BT**, Dyakov SA, Brennan LJ, Younesy S, Perova TS, Gun'ko YK, Craciun MF, Baldycheva A. (2017) Dynamic in-situ sensing of fluid-dispersed 2D materials integrated on microfluidic Si chip, *Scientific Reports*, volume 7, pages 42120-42120, DOI:10.1038/srep42120.
11. **Hogan BT**, Kovalska I, Craciun MF, Baldycheva A. (2018) Probing Raman scattering for particle tracking: A novel spectroscopic analysis method, *Wiley Microscopy and Analysis.*

Presentations.

*(Oral presentations **in bold**)*

1. MMC 2019, Manchester, UK, 1-4/7/2019**,** Abstract title: Microscopy and Microspectroscopy of 2D Material Liquid Crystal Nanocomposites: From Fundamental Properties to Application in Devices.
2. **INVITED**: Photonic and Optoelectronic Materials 2019, London, UK, 9-12/4/2019, Abstract title: **In-situ Monitoring of Nanoparticle Self-Assembly Processes.**
3. SNAIA 2018, Paris, France, 10-13/12/2018, Abstract titles: Modified 2D materials' optical properties for terahertz time-domain spectroscopy applications; **2D Material Liquid Crystal Nanocomposites for Optoelectronic and Photonic Devices**; Raman Spectroscopy as a Tool for Characterisation of Liquid Phase Devices.
4. **INVITED:** Photonex Europe 2018, Coventry, UK, 10-11/10/2018, Abstract title: **2D Material Liquid Crystal Nanocomposites for Photonic Applications.**
5. OSA Frontiers in Optics / Laser Science 2018, Washington DC, USA, 17-20/9/2018, Abstract titles: Raman Spectroscopy as a Tool for Characterisation of Liquid Phase Devices; 2D Material Liquid Crystal Nanocomposites for Optoelectronic and Photonic Devices.
6. RMS Photonic & Optoelectronic Materials, Exeter, UK, 9-10/4/2018, Abstract title: Microscopy and Microspectroscopy of 2D Material Liquid Crystal Nanocomposites for Optoelectronic and Photonic Devices.
7. MRE 2018, London, UK, 12-13/3/2018, Abstract title: Chiral 2D Material Liquid Crystal Nanocomposites for Optoelectronic and Photonic Devices.
8. MRS Fall Meeting 2017, Boston, USA, 26/11 - 1/12/2017, Abstract titles: **Label Free *In-Situ* Three-Dimensional Monitoring of Nanoparticle Self-Assembly Processes**; **Novel 2D Material Liquid Crystalline Composites as a Platform for Optoelectronic Devices.**
9. RAMS 2017, Exeter, UK, 11-12/9/2017, Abstract title: Novel 2D Material Liquid Crystalline Composites as a Platform for Optoelectronic Devices.

10. MMC 2017, Manchester, UK, 3-6/7/2017, Abstract title: *In-situ* Control and Characterisation of Meta-Structured Liquid Crystalline Nanocomposites as a Platform for Optoelectronic Devices.
11. PIERS 2017, St Petersburg, Russia, 22-25/5/2017, Abstract title: ***In-situ* optical characterisation of the spatial dynamics of liquid crystalline nanocomposites**.
12. Joint Conference of the German & British Liquid Crystal Societies, Würzburg, Germany, 3-5/4/2017, Abstract title: **Control and Characterisation of Meta-Structured Liquid Crystalline Nanocomposites as a Platform for Optoelectronic Devices.**
13. META'16, Malaga, Spain, 25-28/7/2016, Abstract title: **Characterisation and Dynamic Control of Graphene-Liquid Crystal Composite Microfluidic Systems.**
14. MSI 2016, Dublin, Ireland, 8-10/6/2016, Abstract title: **Enhanced Raman scattering of liquid crystal – graphene oxide nano-composites: an opto-fluidic approach.**
15. EMRS Spring Meeting 2016, Lille, France, 2-5/5/2016, Abstract title: **Enhanced Raman scattering of liquid crystal nano-composites: an opto-fluidic approach.**

List of Figures.

List of Tables.

Abbreviations.

Notation	Definition
2D	Two-Dimensional
3D	Three-Dimensional
ADC	Analogue-Digital Converter
AFM	Atomic Force Microscope
BOX	Buffer Oxide
BPD	Balanced Photodetector
BS	Beam Splitter
CARS	Coherent Anti-Stokes Raman Spectroscopy
CD	Circular Dichroism
CHF	Chloroform
CMOS	Complementary Metal-Oxide-Semiconductor
DLS	Dynamic Light Scattering
DOS	Density of States
EOC	Electro-Optical Crystal
FIR	Far Infrared
FTIR	Fourier Transform Infrared Spectroscopy
GO	Graphene Oxide
h-BN	Hexagonal Boron Nitride
IPA	Isopropanol
LC	Liquid Crystal
LCD	Liquid Crystal Display
LD	Linear Dichroism
MEMS	Micro Electro-Mechanical Systems
OC	Optical Chopper
PDMS	Polydimethylsiloxane
PET	Polyethylene Terephthalate
PM	Parabolic Mirror
PTFE	Polytetrafluoroethylene
Q	Quality Factor
RF	Radiofrequency
RGO	Reduced Graphene Oxide
SEM	Scanning Electron Microscope
SMM	Scattering Matrix Method
SOI	Silicon-On-Insulator
THF	Tetrahydrofuran
TMDC	Transition Metal Dichalcogenide
UV	Ultraviolet

1. Introduction.

Two-dimensional (2D) nanocomposite materials with dynamically tunable functional properties have recently emerged as a novel, highly promising class of optoelectronic materials, opening up new routes not only for the emerging field of photonic metamaterials but also to chip-scale multifunctional complementary metal-oxide-semiconductor (CMOS) photonics metadevices[1–4]. However, CMOS compatible integration of 2D nanoparticles into electronic-photonic circuits is still a huge challenge. Dispersions of 2D materials in a host fluid open up new pathways to overcome this barrier[5].

The recent development of nanocomposites consisting of fluid-dispersed, atomically thin, two-dimensional materials has sparked a great level of interest as a promising *in-situ* tailored meta-material device platform for the next generation of multi-functional (opto)-electronic systems with a wide range of important applications, such as renewable energy, optical communications, bio-chemical sensing, and security and defence technologies[1,6–9]. Dynamically controlled three-dimensional self-assembly of suspended 2D liquid-exfoliated nanoflakes not only provides a breakthrough route for technological realisation of 2D material based 3D device architectures[10–12], but

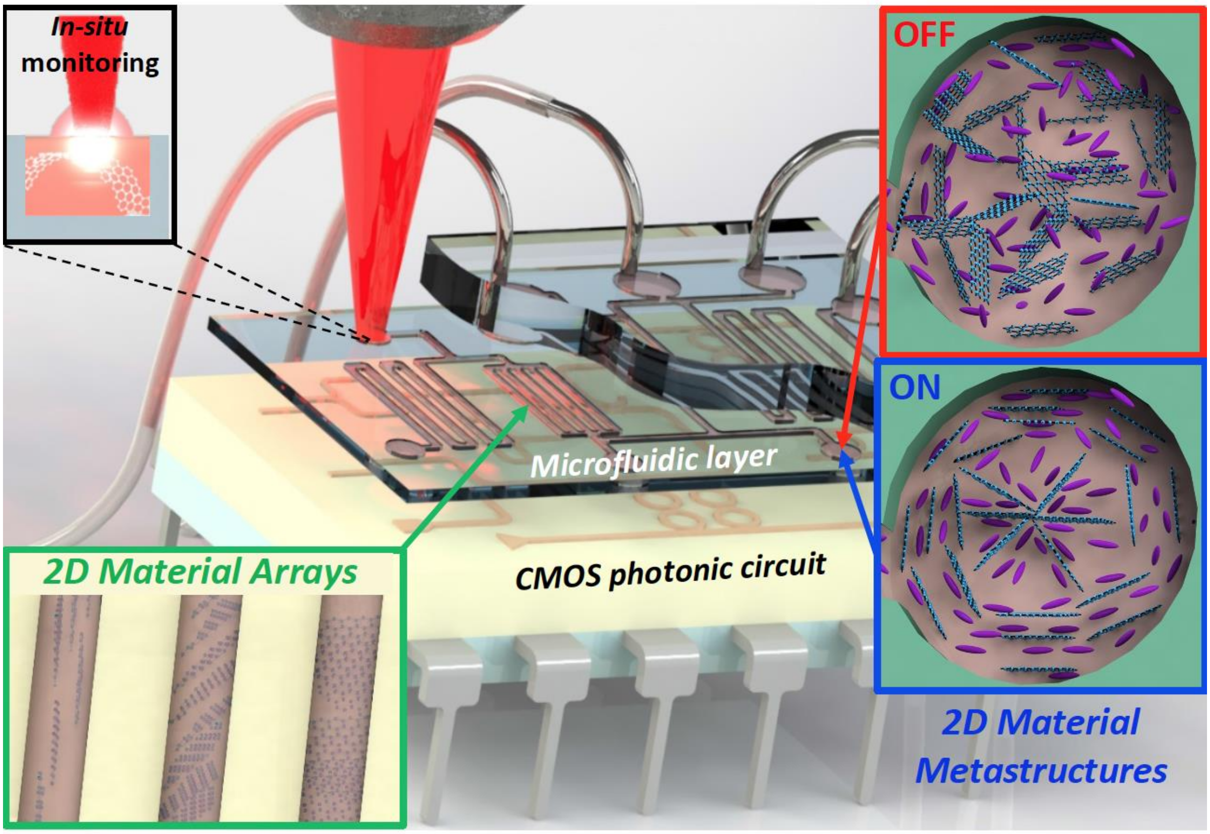

***Figure 1**: A possible device based on a CMOS photonic circuit coupled to a microfluidic layer integrating dynamically reconfigurable 2D material metastructures, with in-situ micro-spectroscopy detection and monitoring.*

also their fluidic nature allows CMOS-compatible back-end integration on chip using microfluidic technology[13]. This opens up almost limitless possibilities in the fabrication of compact and low-power systems for the realisation of commercially viable, miniaturised, multi-functional light-management devices, for example light sources[14], tuneable optical filters[15] and nanoantenna phased arrays[16]. An example of a possible device is shown in Fig. 1, in which dynamically reconfigurable 2D material fluid metastructures are integrated into a microfluidic system and coupled with a CMOS photonic circuit. The combination of conventional CMOS photonic technology with novel microfluidic structures would lead to great advances in device functionality, leading to significant enhancement of the viability of CMOS photonics replacing conventional electronics in everyday applications. Due to recent advances in CMOS photonics, the practicable application of any 2D material fluid composites, in particular those dispersed in liquid crystals (LCs), in microfluidic electronic-photonic devices is technologically viable. 2D material fluid composites also open up other possibilities, for instance the development of highly uniform thin films which can then be transferred to substrates for device integration.

In this thesis, the different scientific paradigms relevant to the synthesis, characterisation, and application of 2D material fluid composites (Section 2) are outlined. Then, the current and prospective applications of 2D material fluid composites in relation to the existing literature, and the key scientific challenges that remain to be explored (Section 3) are discussed. Section 3 is largely drawn from the review article “2D material liquid crystals for optics and photonics”, published in the Journal of Materials Chemistry C[17] and primarily authored by the author of this thesis. It is shown that 2D material liquid crystal composites can be synthesised by two routes. In Section 4.1, nematic liquid crystals doped with dispersed 2D materials are considered. The synthesis of the materials is described, and their key properties in relation to applications in optoelectronic and photonic devices are analysed. In Section 4.2, the first ever synthesis of dispersions of tungsten disulfide in organic solvents showing a liquid crystal phase is described. Consideration is given to the particle sizes present in the liquid crystal phase, in particular discussing the use of dynamic light scattering to extract information on the aspect ratios of 2D materials. Analysis of the optical properties of the tungsten disulfide liquid crystals, including the unexpected circular dichroism is presented. Section 4.2 is built upon results in the Nanoscale article “2D WS_2 liquid crystals: tuneable functionality enabling diverse applications”[18], primarily authored by the author of this thesis, and wherein all experimental work described in this section was undertaken by the author.

In Section 5, a new characterisation technique is developed, based on Raman spectroscopy, in order to ascertain information about the positions and alignment of 2D material particles dispersed in fluids. In Section 5.1, microfluidic structures to enhance the Raman signal from the 2D materials are designed, and experimentally confirm the enhancement. It is also shown that integrated 2D material fluid composites can be dynamically controlled using either applied electric fields, or by laser excitation. In Section 5.2, it is demonstrated that the enhanced Raman signal is utilised to enable the tracking of particle positions in one and two dimensions respectively, and a discussion of how the technique would be further applied to three-dimensional particle tracking is included. Sections 5.1 and 5.2 are based on the Scientific Reports article "Dynamic in-situ sensing of fluid-dispersed 2D materials integrated on microfluidic Si chip"[5], for which the author of this thesis was the first author and undertook the majority of simulation and experimental work. In Section 5.3, analysis of how other geometric properties of the particle, or experimental considerations, can influence the Raman signal intensity is given. Specifically, consideration is given to how particle rotation and angle, the presence of arrays of multiple particles, the focus of the laser, or changing the material under investigation can modify (or otherwise not) the Raman spectrum of the sample. In Section 5.4, it is shown that the shape of the particle strongly influences the Raman signal, demonstrating potential for shape analysis *via* Raman spectroscopy. In Section 5.5, a method to extract the concentration of dispersed particles from the Raman spectra by only looking at the Raman bands of the host fluid is presented.

In Section 6, the first applications of the developed 2D material fluid composites are considered. In Section 6.1, the production of thin films of tungsten disulfide using the liquid crystal phase dispersions is described. The developed thin films show remarkable uniformity when compared to those produced from non-liquid crystalline dispersions. In Section 6.2, the terahertz transmission properties of the developed thin films are investigated, and are found to show strong potential for future applications in terahertz generation and detection. Sections 6.1 and 6.2 amalgamate work published in the Nanoscale article "2D WS_2 liquid crystals: tuneable functionality enabling diverse applications"[18] and the Nanoscale Research Letters article "Transmission Properties of $FeCl_3$-Intercalated Graphene and WS_2 Thin Films for Terahertz Time-Domain Spectroscopy Applications"[19]. The author of this thesis prepared all thin films in section 6.1, and assisted with the experimental measurements and analysis of terahertz transmission properties in section 6.2. In Section 6.3, consideration is given to potential laser cavity applications of the thin films. It is shown that unstable Q-switched lasing can be achieved using the tungsten disulfide thin films as saturable absorbers coated on the mirrors forming the laser cavity. In Section 6.4, a study of the prospective integration of 2D materials with photonic structures such as waveguides and microring resonators is presented. The route to integration of the thin films, and the expected properties obtained for the photonic structures after integration are discussed. It is shown that the integration of the 2D materials can modify the effective refractive index of the photonic structures, and that the resonance of the structures can therefore be tuned. Section 6.4 is based on the Proceedings of SPIE article "2D materials integrated in Si_3N_4 photonics platform"[20], where the author of this thesis contributed to the modelling, simulation and data analysis. In Section 7, the future prospects for the development and application of 2D material fluid composites in relation to optoelectronic and photonic devices are outlined. Where not specifically mentioned previously in this introduction, all results in this thesis are as yet unpublished and predominantly the work of the author of this thesis.

2. Background and Context.

The development of future optical and photonic technologies will demand a significant increase in the ease of component integration and energy efficiency, far greater than that achievable using conventional optical components and silicon photonics. Such a level of integration can be achieved by embedding the data-processing and flow control functionalities at the material level. Devices where this is achieved are termed ‘metadevices’[21]. Photonic metadevices show great potential for replacing conventional electronics in a wide range of applications- from telecommunications to computing- with the prospect of becoming a ubiquitous technological paradigm in the years to come[21]. The development of facilely reconfigurable photonic and optoelectronic materials is a key goal for the development of multi-functional photonic metadevices. To enhance potential device functionality, it is also desirable to find materials or technologies that allow dynamic tuning of their properties across broad ranges rather than the simple on/ off states achievable with conventional photonic systems. Ideally, these materials should combine this tunability (that is, the ability to controllably change the materials’ properties) with rapid (on the order of ns) switching times and complete reversibility of the switching processes.

One possibility for achieving reconfigurable photonic materials is the use of so-called phase change materials, where the reconfigurability is achieved by switching from one phase to another under some applied external stimulus which modifies the temperature of the material[21,22]. This technology initially found applications in optical disks (CDs, DVDs), where the fast write time for changing the state, relatively high potential data density and ability to be rewriteable were significant advantages[23]. Typically, the thermal excitation is achieved using a laser pulse, but can also be provided electrostatically or by any other method by which heat can be transferred to the sample[23]. The phase change can be either a liquid-solid change or a solid-solid change, whereby the molecular structure is reconfigured from an amorphous state to an ordered crystalline state and is a reversible process. Different phase change materials have been developed for which the temperature required to change the phase as desired can span a large range of possible values[21,22]. On changing the phase of the material, the refractive index for the material is altered. On-Off tunability of the refractive index gives rise to potential applications as a reconfigurable photonic material. However the binary nature of the tunability (one phase considered as an ‘off’ state and the other as an ‘on’ state) limits the achievable possibilities. Additionally, when reconfiguration is induced by light (the most common case) the minimum domain size at which domains of different phases can be achieved is limited by the minimum spot size achievable by the focussing of the light onto the material.

Another option that has been considered is microelectromechanical systems (MEMS), where reconfigurability is achieved by the physical displacement of components of the system under an applied stimulus.[21,24] MEMS are typically made up of components of micron sizes[2]. The large surface area to volume ratio means that surface effects dominate the interactions of MEMS components[2]. MEMS components can be constructed using a range of materials including metals, polymers and ceramics but the most common material used is silicon[2] due to its ubiquitous use in integrated circuits and advantageous physical properties (facile deposition and patterning, high thermal and mechanical stability). MEMS components are typically manufactured by standard lithographic techniques. MEMS components have been developed which act as thermal actuators, piezoelectric actuators and resonistors[21]. However, MEMS technology is limited by the lithographic processes required as well as material limitations at small size scales where a device's mechanical properties are less stable and devices themselves less durable[2]. MEMS devices have been fabricated for the tuning of transmission lines of a material[21]. They have also been used for the switching of terahertz metamaterials using micro-actuators to control separations of microstructures[25,26]. Using flexible substrates when manufacturing devices can allow for indirect reconfiguration of structures by manipulation of the substrate[27].

To develop a reconfigurable photonic material capable of non-binary switching, with fast response time and a fine degree of spatial control, one can look to combine a number of existing technological paradigms to develop a novel approach towards developing optoelectronic materials. The critical paradigms to this approach are as follows: silicon photonics, 2D materials, liquid crystals, microfluidics, and metamaterials concepts.

2.1 Silicon photonics.

Silicon photonics is a category of photonic systems using silicon as the optical medium[28,29]. The silicon can be patterned with a micron or sub-micron pattern to define the photonic components. Typically, silicon photonics are engineered to operate at the 1.55 μm wavelength used in most fiber optic telecommunications[29] which corresponds to a band of very low absorbance for silicon. Silicon photonic devices are typically manufactured on silicon on insulator (SOI) where the silicon device layer is supported on a silicon dioxide (SiO_2) insulating layer[30]. The main advantage of silicon photonics is that as silicon is already used as the substrate in most integrated electronic circuits, it is easy to create hybridised devices combining traditional electronic components with novel optical components making use of silicon photonics to enhance device functionality.

Silicon is transparent to electromagnetic radiation with wavelengths above 1.1 μm and has a very high refractive index (around 3.5) in this range[30]. This high refractive index allows for tight optical confinement in silicon components with dimensions of only a few hundred nanometres[31]. This means that single mode waveguides with subwavelength dimensions can be designed. The insulating silicon dioxide layer has a much lower refractive index (around 1.44 in the same range[30]) meaning that total internal reflection can be achieved for a very broad angular range at the interface between the silicon waveguide structures and the silica layer. The silica layer is also used to optically isolate the silicon device layer from the bulk silicon of the wafer on which the devices are fabricated. There are strong dielectric boundary effects resulting from the confinement of the light within a silicon waveguide. These effects greatly affect the optical dispersion relation such that by careful design of the waveguide geometry the dispersion can be tailored to give properties as desired.

For applications in the visible range, silicon is no longer a useful material due to its strong absorbance of light at visible wavelengths. Silicon nitride (Si_3N_4) however shows far less absorbance in this range while retaining similar properties and interactions to those seen for silicon in the infrared. Therefore, for visible range photonics silicon nitride can present a suitable candidate material for the fabrication of waveguiding structures. Liquid crystals have also been shown to present a suitable candidate for fabricating waveguide structures and can be easily integrated with conventional silicon photonics[32]. Silicon photonics provides a basis for defining waveguiding structures and nanoscale control of light, but suffers from a lack of tunability and dynamic response.

2.2 Two-dimensional materials.

Since the advent of graphene in 2004[33], when a monolayer of the material was first isolated and characterised, there has been an explosion in the investigation of a wide range of atomically thin (two-dimensional) materials. Two-dimensional materials are intrinsically nanomaterials, as by definition one of the dimensions must be on the order of nanometres. In addition to graphene (exfoliated from graphite), materials that can be reduced to monolayer size have been shown to include: graphene oxide (from graphite oxide); transition metal dichalcogenides (TMDCs) including MoS_2, WSe_2 and $MoTe_2$; hexagonal boron nitride (*h*-BN) amongst others. The possibilities for applications of these materials are almost limitless, owing to the diverse properties that they show. The monolayer nature of the materials means that they absorb very little incident light. The varied properties of 2D materials provide a basis for multifunctional light management devices across a wide range of applications. Their 2D geometry allows for the possible assembly of complex 3D structures while also providing possibilities for low power consumption and minimal signal losses in device applications. In this thesis, various terminology is used to describe the materials. Particles refers to a piece of material of any arbitrary shape and size (including thickness), unless additional descriptions are given. Flakes and platelets refer to pieces of material where one dimension is significantly smaller than the other two. Agglomerates refers to the grouping of multiple individual particles. In this section, the synthesis routes enabling the production of 2D materials are detailed, and further discussion of the key characteristics of the 2D materials pertinent to this thesis is presented.

Synthesis methods for 2D materials.

There are several methods by which 2D materials can be exfoliated, each with their own advantages and disadvantages. Firstly, a mechanical cleavage method can be used (the so-called 'sticky-tape' method) where layers are separated by adhering one layer to a sticky surface and mechanically peeling it away from the bulk[33]. This method produces very pure materials with few defects induced and can also give relatively large areas of material coverage. However, this method has poor scalability and production of large quantities of 2D material is extremely time intensive. Alternatively, a vapour deposition method can be used where a 2D material is grown directly on a substrate from vapourised precursor molecules at very high temperatures[34–37]. This method can produce large areas of 2D material and can be scaled to produce large quantities. However, there are numerous sources for the introduction of defects in the material including substrate induced defects and impurities in the vapours used amongst others. The material must be transferred from the substrate after deposition which can be problematic.

Liquid phase exfoliation is a method where a bulk material is dispersed in a solvent and then layers are broken apart[6,38–40]. In most cases, the layers are broken apart using ultrasonication where high frequency sound waves are transmitted through the solution[6,38–44]. The sound waves induce the formation of bubbles and cavities between layers which break the layers apart as they expand. However, they also cause strains in the material which cause intralayer cleavage of the particles, reducing the lateral sizes of the products obtained after exfoliation[38,45]. The solvent used for liquid phase exfoliation using ultrasonication should be chosen so that it's Hansen parameters closely match those of the material to be exfoliated to maximise the yield of the exfoliation[40]. The Hansen parameters, or Hansen solubility parameters, of a material give an indication of whether or not it can be stably dispersed in a solution. A given unit (molecule, nanosheet etc.) of a material has three predominant energetic interactions with a solvent: non-polar dispersive forces E_D, polar cohesive energy E_P, and hydrogen bonding E_H. Summing these interactions gives a total cohesive energy E:

$$\mathrm{E} = E_D + E_P + E_H \,. \tag{1}$$

The individual energy values should be scaled to the volume V of the unit. The square root of the scaled energy value is a Hansen solubility parameter δ. The three Hansen solubility parameters have the form:

$$\delta = \sqrt{E/\mathrm{V}} \,. \tag{2}$$

The summation of the squares of the three individual Hansen solubility parameters gives the Hildebrand solubility parameter δ^2:

$$\delta^2 = \delta_D{}^2 + \delta_P{}^2 + \delta_H{}^2 . \tag{3}$$

This can be used to express a Flory-Huggins parameter[46] for the interaction between a solvent (terms denoted S) and a unit of a material (terms denoted M):

$$\chi \approx \frac{V_0}{k_B T}\left[\left(\delta_{D,S} - \delta_{D,M}\right)^2 + \left(\delta_{P,S} - \delta_{P,M}\right)^2 + \left(\delta_{H,S} - \delta_{H,M}\right)^2\right] ; \tag{4}$$

where V_0 is the solvent molecular volume and k_B is the Boltzmann constant. The Flory-Huggins parameter is directly related to the enthalpy of mixing. As such, a value of the parameter closer to zero indicates that the material will disperse more readily (with greater energetic favourability) in the solvent. It is clear that to minimise the Flory-Huggins parameter, the individual Hansen solubility parameters for the solvent and the material should be matched as closely as possible. Hence for a material to be dispersed in a solvent effectively, the three contributing Hansen parameters should be considered.

The use of intercalating surfactants to weaken the interlayer forces before exfoliation can greatly increase the yield of the exfoliation[6,39], but the subsequent removal of the surfactant is liable to damage the quality of the exfoliated product. It has also been reported that the parameters of the sonication process itself impact significantly on the dispersion of carbon nanotubes[47] (although has not been reported for 2D material exfoliation). Hence it is suggested that parameters of the solvent such as vapour pressure, viscosity, surface tension and density are important considerations for the sonication process. However, it should be noted that there is a difference between dispersing (as done for the nanotubes) and exfoliating (as desired for 2D materials), and that there is no evidence to suggest that consideration of the sonication parameters of the solvent are more important to

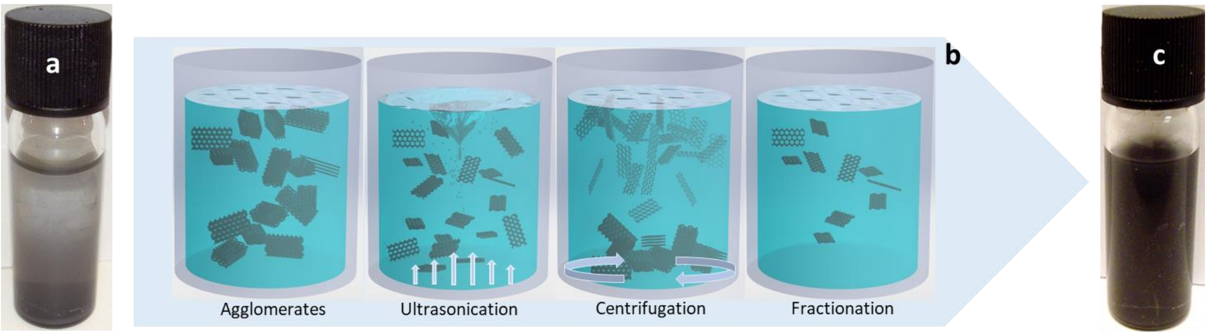

Figure 2.1: a) *A dispersion of a bulk 2D material in an organic solvent showing the low solubility of large, unexfoliated particles.* ***b)*** *Schematic of the liquid phase exfoliation of bulk layered materials to low- or two-dimensional particles. Beginning from agglomerates dispersed in the solvent (bulk material), ultrasonication is used to exfoliate down to smaller flake sizes. Centrifugation then aggregates the largest particles, with the smallest remaining suspended in the solution. Fractionation then allows the selection of aliquots containing* ***c)*** *the resultant homogeneous distributions of similarly sized particles.*

successful exfoliation than the minimisation of the Flory-Huggins parameter. In any case, many of the mentioned properties of the solvent are in themselves related to the terms in the calculation of the Flory-Huggins parameter. Other than ultrasonication, other methods have been developed for liquid phase exfoliation, including strong acid induced oxidation reactions causing cleavage[48] and freezing of water intercalated layered structures where expansion of water as it freezes causes interlayer cleavage[49]. Following exfoliation, particles of specific sizes can be isolated by centrifugation of the dispersion[50,51], solvent induced selective sedimentation[52] or by pH-assisted selective sedimentation[53] amongst others. The general process for the liquid exfoliation of 2D materials is outlined in Fig. 2.1. Materials of interest for optoelectronics and photonics that can be reduced to few-layer or monolayer by means of liquid phase exfoliation encompass a broad range; from graphene and its derivatives to transition metal dichalcogenides, metal oxides and hexagonal boron nitride amongst many others.

Graphene.

Graphene can be exfoliated from bulk graphite owing to the weak van der Waals interactions between layers in graphite[54]. Graphene is an allotrope of carbon consisting of a two-dimensional hexagonal lattice with a single carbon atom at each vertex. The carbon atoms in graphene are sp^2 hybridised in-plane with these sp^2 electrons forming three carbon- carbon bonds. The final p orbital is unhybridised and directed out of the plane. For a graphene sheet these out of plane p orbitals form the delocalised π and π* bands which are responsible for graphene's exceptional electronic properties. Pristine graphene is a zero-gap semiconductor, where the conduction and valence bands meet at the six Dirac points in momentum space[55]. Graphene displays exceedingly high electron mobility at room temperature, with values greater than 15,000 $cm^2V^{-1}s^{-1}$ reported[56]. Although there is an intrinsic limit of 200,000 $cm^2V^{-1}s^{-1}$ at room temperature due to phonon scattering[46], this still represents orders of magnitude improvement over typical metallic conductors. Monolayer graphene absorbs approximately 2*%* of light across the visible spectrum, although it strongest absorbance is at red wavelengths[56]. The band gap in graphene can be tuned by either chemical doping or by an applied voltage.

Graphene oxide.

Graphene oxide (GO) is the 2D material produced by the exfoliation of graphite oxide[57]. Graphite oxide is produced by treating bulk graphite with strong oxidising agents (mostly strong acids) in a process known as the modified Hummers' method[54,58]. Maximum oxidation of the graphite results in a carbon to oxygen ratio between 2.1 and 2.9. Graphite oxide retains the layered structure of graphite but the interlayer spacing is increased and no longer regular for bulk graphite oxide. The oxidation of graphite introduces three types of oxygen containing functional groups to the structure: epoxy bridges (oxygen bridging between two carbons on the surface of a graphitic sheet), hydroxyl groups (on either the surface or the edges) and carboxyl groups (on the edges of the graphitic sheets)[59]. Graphene oxide can be exfoliated from bulk graphite oxide analogously to graphene from graphite[54,57]. However, the intercalation of the graphitic carbon sheets by oxygenated functional groups results in graphene oxide being more readily exfoliatable. This means that graphene oxide can be exfoliated to few layers and even monolayer in large quantities without the use of additional surfactant molecules[42,44]. Graphene oxide possesses nonlinear optical properties of significant interest for applications in ultrafast photonics and optoelectronics. While other 2D materials also possess non-linear properties, the relatively facile production of graphene oxide, and greater magnitude of non-linear effects make graphene oxide a prime candidate for nonlinear applications. The saturable absorption can be used for pulse compression, mode locking and Q-switching of laser systems[60]. The large observed Kerr effect introduces possibilities in all-optical switching and signal regeneration and hence optical communications devices[61]. The nonlinear optical properties of graphene oxide can be tuned by controlling the carbon to oxygen ratio of the material[62], this tuning has been achieved using laser irradiance to reduce the material. The addition of metallic nanoparticles has been shown to greatly enhance the nonlinear response of graphene oxide in solution[63].

Molybdenum disulfide.

Bulk molybdenum disulfide (MoS_2) consists of layers of molybdenum atoms bound to six sulfide ligands in a trigonal prismatic coordination sphere[64,65]. The layers are held together by weak van der Waals interactions between the layers of sulfur atoms and therefore present an ideal candidate for reduction to few-layer or monolayer materials. Cleavage to monolayer is typically achieved using mechanical exfoliation methods but few-layer material can be readily attained using liquid-phase exfoliation methods[66]. Molybdenum disulfide is mostly unreactive and shows long term stability in air. Molybdenum disulfide is insoluble in water. MoS_2 is an indirect bandgap semiconductor with a band gap of 1.23 eV in its bulk form[67] but the monolayer form has a direct bandgap of 1.8 eV [68] so can be used in switchable transistors and photodetection devices[64]. MoS_2 can emit light opening applications in *in-situ* light generation devices[64].

Tungsten disulfide.

In its bulk crystalline form, tungsten disulfide (WS_2) consists of dark grey hexagonal crystals built up of layered sheets held together by van der Waals forces. Within each individual sheet (Fig. 2.2), the tungsten has a trigonal prismatic co-ordination geometry, while the sulfur has a pyramidal co-ordination, such that each sulfur bridges between three tungsten centres, whilst each tungsten is bonded to six sulfurs. Dating back 60 years, the bulk crystalline form found applications as a catalyst for numerous reactions[69,70]. More recently, significant interest was generated from the discovery that WS_2 can form nanotube structures analogous to carbon nanotubes, representing the first inorganic nanotubes to be discovered[71]. However, with the current explosion in the investigation of 2D materials, it is the van der Waals layered nature of WS_2 that generates the greatest interest[9,72]. The weak nature of the interlayer bonding makes it a prime candidate for exfoliation to few- or single-layered flakes of high aspect ratio. Whereas bulk WS_2 is an indirect bandgap semiconductor, with a bandgap of around 1 *eV*, monolayers possess a direct bandgap of 1.8 *eV*. This direct bandgap presents a significant advantage for applications over graphene which has no bandgap.

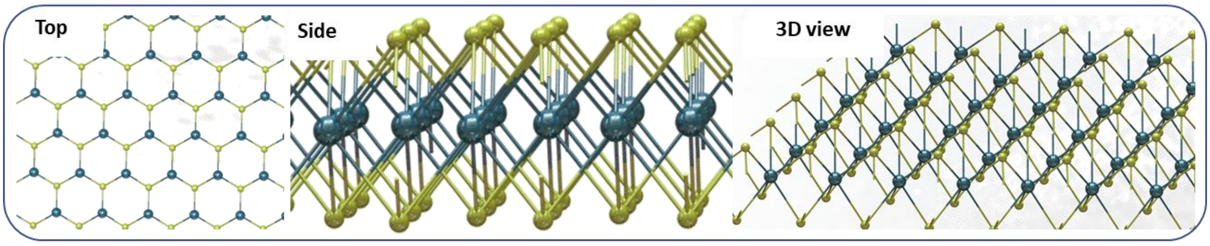

Figure 2.2: *Top, side and 3D views of the bonding structure of tungsten disulfide. Tungsten atoms are represented in blue and sulfur in yellow.*

Other transition metal dichalcogenides.

Tungsten diselenide (WSe_2) adopts a hexagonal crystal structure similar to that of molybdenum disulphide, with each tungsten atom covalently bonded to six selenium ligands within a trigonal prismatic co-ordination sphere[65,73]. The material is layered with the separate layers held together with only van der Waals forces. Tungsten diselenide is a very stable semiconducting material[65,73]. Pure tungsten diselenide has a band gap of around 1.35 *eV* at room temperature[73]. Monolayers of WSe_2 are transparent photovoltaics with light emitting diode properties[65,73]. The doping of the materials can be tuned from p-type to n-type under an applied external field, allowing tuning of the band gap of the material *in-situ*[65,73]. Molybdenum ditelluride ($MoTe_2$) has a similar structure and bonding scheme to molybdenum disulfide[65]. It is a semiconductor with a band gap of 1.1 *eV* for a monolayer compared to 0.9 *eV* in the bulk[74]. $MoTe_2$ has been shown to fluoresce[74]. $MoTe_2$ is unstable in air and will gradually oxidise to form molybdenum dioxide. A wide variety of other TMDC materials have also been synthesised and present a broad range of exploitable properties while retaining the layered bulk structure that enables exfoliation to few-layer.

Hexagonal boron nitride.

Hexagonal boron nitride (*h*-BN) is the most stable crystalline form of boron nitride. It has a hexagonal lattice and a layered structure similar to graphite and hence it is often referred to as graphitic boron nitride. The boron and nitrogen atoms contained within each layer are held together by strong covalent bonds whereas the separate layers are held together by van der Waals forces only. This makes it an ideal candidate for reduction to monolayer[65]. Compared to graphene, *h*-BN has reduced delocalisation of the sp^3 electrons resulting in a large band gap and a lack of colour. Importantly, it also shows considerably reduced conductivity. Under an applied voltage, *h*-BN is an emitter of UV light and therefore shows potential for applications in *in-situ* light generation devices[75]. Exfoliation of bulk *h*-BN is typically undertaken mechanically resulting in mostly few-layer *h*-BN but some monolayer domains are typically obtained also[46,76]. Monolayer *h*-BN has been shown to be a good proton conductor with a high proton transport rate[77].

2.3 Microfluidics.

Microfluidics is a technological area concerned with the manipulation of low volumes of liquids by either movement, mixing or separation[78,79]. There are two main categories of microfluidic system; passive microfluidics, where the fluid is manipulated by capillary forces or by some external actuation (such as centrifuging the microfluidic system), and active microfluidics where the fluid is manipulated through the use of active components such as pumps or valves. Microfluidic structures can be manufactured on a wide range of substrates, from silicon-on-insulator (Fig. 2.3) through to flexible polymers such as polydimethylsiloxane (PDMS) using conventional lithographic techniques[79,80].

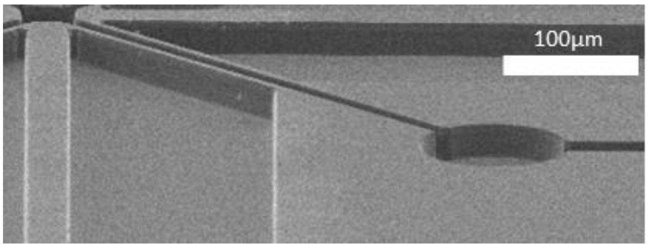

Figure 2.3*: Microfluidic structures etched on a silicon-on-insulator wafer.*

In microfluidic systems, the surface tension and fluidic resistance dominate the physical processes the fluid undergoes[78,79]. This can result in the appearance of interesting properties in microfluidic systems that are not observed in 'macrofluidic' counterparts. In particular, fluids in microfluidic channels are often defined by a very low Reynolds number such that laminar flow is observed rather than turbulent flow. This presents challenges to the mixing of liquids in microfluidic systems where the mixing is therefore diffusion controlled[79,80]. However, despite this challenge, microfluidic systems present a method for a fine degree of *in-situ* control over liquid samples[81]. Microfluidics technology allows the integration and control of liquid materials into defined structures on a range of substrates.

2.4 Metamaterials concepts.

Metamaterials are materials that are specifically engineered to have a property not found in nature[21]. They are typically constructed from assemblies of multiple elements arranged in repeating patterns with scales less than the wavelengths with which they are designed to interact. Control of the precise shape, geometry, size and orientation of the individual elements and the overall ensemble allows the manipulation of electromagnetic waves, for example, by absorption, enhancement or redirection. Photonic metamaterials have typical feature sizes on the order of nanometres and are optimised to interact with light covering the terahertz, infrared and visible regions of the electromagnetic spectrum. Metamaterial absorbers have been developed where the imaginary component of the permittivity is manipulated by careful design of the feature sizes and array dimensions of a metamaterial lattice to facilitate the maximal absorption of incident electromagnetic radiation[82]. A photonic crystal is a periodic structure where the period is on the order of the photonic wavelength[83]. Photonic crystals can be fabricated in one, two or three dimensions. Tuning the photonic crystal lattice parameters can allow for control of the wavelength of propagating electromagnetic waves. A photonic crystal has an associated photonic band structure which determines whether photons of a particular wavelength can propagate through the structure. Propagating wavelengths are known as modes. Groups of allowed modes form bands, disallowed bands of wavelengths are known as bandgaps. The use of photonic crystal structures allows low-loss waveguiding of the allowed modes. Metamaterials concepts present opportunities for the development of novel nanostructures for the modulation of light in photonic circuits.

2.5 Liquid crystals.

The liquid crystal phase is a phase of matter that exists for a variety of molecules and materials, depending on their geometric and chemical properties, with characteristics intermediate to those of a conventional crystalline solid and a liquid[84,85]. Liquid crystals (LCs) have found use in a variety of applications through the years (Fig. 2.4). The liquid crystal phase was initially described by Austrian botanist Friedrich Reinitzer in 1888 when looking at the properties of cholesterol derivatives[86,87], although some credit also goes to Julius Planer, who reported similar observations 27 years prior[88,89]. This new and distinct state of matter was then identified as the "*liquid crystal phase*" by Otto Lehmann in 1890 and in 1904 the first commercially available LCs were produced by Merck-AG[90]. Over the following 18 years, scientists established the existence of three distinct liquid crystalline phases

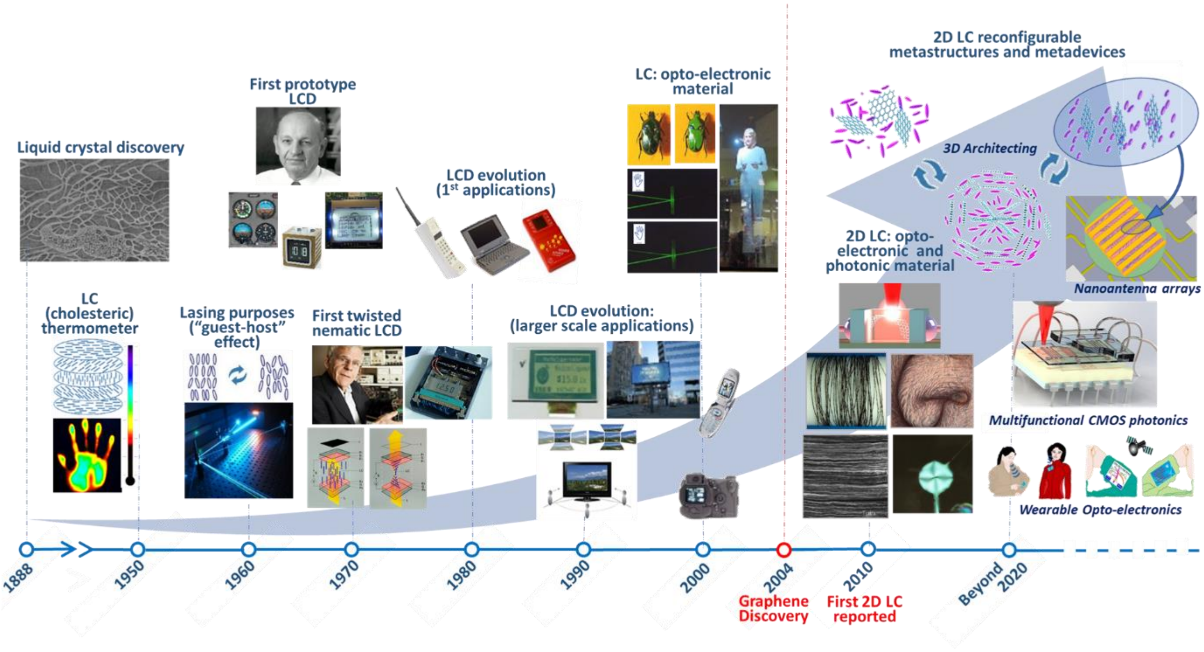

Figure 2.4: *Timeline of the history of liquid crystal phase applications, from their discovery to the present day. (Images reproduced with permission from: Mitov, ChemPhysChem, 2014[227], (© 2014 Wiley-VCH); Xu & Gao, Nature Communications, 2011[98] (©2011 Nature Publishing Group); He et al, Nanoscale, 2014[11] (©2014 The Royal Society of Chemistry); Jalili et al, ACS Nano, 2013[10] (©2013 American Chemical Society)).*

(nematic, smectic and cholesteric)[90] but, with no applications of note forthcoming, the study of LCs was halted. For the next 30 years, the scientific community ignored LC materials, considering them as an interesting curiosity. However, following a renaissance in liquid crystal science in the 1950s, the previously scientific curiosity has become a ubiquitous part of the modern technology landscape.

During the 1950s, the invention of the first cholesteric LC temperature indicators, as well as advances in analytical metrology, cancer diagnostics and non-destructive material testing methods drove a new era in liquid crystal science. By 1962, liquid crystals were already finding applications in state-of-the-art laser devices utilising the switchable orientation of the LC molecules, despite the relative youth of laser science. However, the most important technological innovation came in 1965 with the development of the first LC displays (LCDs) by George H. Heilmeier[91–93], although the usability and application of LCDs was limited initially. Subsequently, twisted nematic LCDs developing initially (1969 - 1971) from the work of Martin Schadt, advanced the field further and began to be incorporated in devices[91–93]. Significant breakthroughs in the evolution of liquid crystal technologies occurred in the 1980-1990s and continue to have a profound impact on day-to-day life: the miniaturisation of display technologies facilitated the development of portable PCs, mobile telephones and countless other innovations[91–93]. From the 1990s onwards, much larger LCDs have appeared while advances in the technology have allowed the production of high resolution small-scale displays. Since the start of the new millennium, LCs and recently discovered 2D material LCs have come into demand as optoelectronic and photonic materials[5,94–97]. They have, as such, been studied from natural sources such as can be found in beetles, as well as in polarisation-selective waveguiding and in holography. The discovery of graphene in 2004 opened up new avenues for LC science and, since 2010, the emergence of LCs combined with 2D materials has opened applications in developing 2D material fibers[98], reflective displays[11], deposition of uniform layered structures[10], and as a platform for novel optofluidic devices[5]. The future of the field promises to revolutionise fields from CMOS photonics, to metastructures and metadevices and wearable technologies.

Liquid crystals flow like a liquid but have an ordered arrangement of their molecules as is typical of a solid. Liquid crystals are in general birefringent materials such that the optical response of the material is different for different molecular orientations relative to the incident light. When viewed under polarised light, a liquid crystal will appear to have a distinct patterned texture, which exists where domains of different molecular orientation are formed with different optical properties as a result.

To describe the anisotropic structure of a liquid crystal, a unitless vector called the director can be introduced to represent the average direction of preferred orientation of the molecules at any given point[85]. Each domain of the liquid crystal phase will have a separate director and this different ordering of the molecules determines the different optical response of separate domains. The properties of a liquid crystal phase are also determined by the how closely aligned individual molecules are to the local director. An orientational order parameter S can be used to quantify this alignment, given by;

$$S = \langle \frac{3cos^2\theta - 1}{2} \rangle \; ; \tag{5}$$

where θ is the angle between the molecular alignment axis and the local director for an individual molecule $S = 1$ defines a perfectly aligned homogeneous phase whereas $S = 0$ suggests a completely random isotropic phase. The possibility of the existence of a liquid crystal phase stems principally from the geometric structure of the molecules in the material as well as the chemical functional groups present in the molecule. However, there is more than one type of possible liquid crystal phase. Liquid crystals can be divided into three broad categories: thermotropic, lyotropic and metallotropic . These categories are defined by the conditions required for the liquid crystal phase to exist. Within each of these categories, different liquid crystal phases (defined by the pattern of the ordering of the molecules) can exist. Liquid crystal phases can be distinguished by their unique Schlieren textures- the patterns of domains of homogeneous orientation- visible by microscopy using crossed polarisers.

The ordinary and extraordinary refractive indices of a liquid crystal can be calculated by utilising a three-coefficient Cauchy model;

$$n_{o,e} = A_{o,e} + \frac{B_{o,e}}{\lambda^2} + \frac{C_{o,e}}{\lambda^4} \; ; \qquad (6)$$

where n is the refractive index, λ is the wavelength and A, B and C are suitable fitting parameters. The subscripts o and e represent the ordinary and extraordinary indices respectively. For example, for commercially available LC MLC 6608, A_o, B_o and C_o should be set to 1.4609, 5×10^{-3} μm^2 and 0 μm^4 respectively to give good agreement with experimental measurements of the ordinary refractive index in the visible region[99]. For liquid crystals with a low birefringence, it is sufficient to simplify to a two coefficient Cauchy model by setting C to zero.

Thermotropic liquid crystals.

Thermotropic liquid crystals are the most common and exhibit a liquid crystal phase within a certain range of temperatures[84,85]. Thermotropic liquid crystals are normally organic molecules. A large number of different organic molecules have been observed to exhibit one or more thermotropic liquid crystalline phases despite possessing different compositions and functional groups. However, all these different molecules adhere to general requirements for liquid crystallinity. The molecules should be relatively thin (either flat or bowl-like). Secondly, the molecule should have a length of at least 1.3 *nm* which typically indicates the inclusion of a long alkyl chain within the molecule[84,85]. In general, long, rigid anisotropic molecules are preferred candidates for exhibiting liquid crystalline behaviour[84].

There are three general classes of molecule that fulfil the requirements and exhibit thermotropic liquid crystalline phases[84]: discotics- flat molecules with a core of adjacent aromatic rings forming a disc-like structure, bowlics- similar to discotics but the aromatic rings are bent to give a bowl-like structure, and rod-shaped molecules with elongated geometries. Rod-like molecules are of particular interest as they possess significant shape anisotropy, allowing preferential alignment along one particular spatial axis. Discotics and bowlics align due to columnar stacking of the molecules aided by the delocalised electrons in their aromatic cores.

As the temperature is varied for a thermotropic liquid crystal, one or more disparate phases will exist[84,85]. One of the most common thermotropic phases is the nematic phase. The nematic phase is typically observed for rod-like molecules. In this phase there is no positional order of the molecules (i.e. there is no common vector defining the separation of neighbouring molecules) but the long axes of the molecules are roughly coaxial giving long range directional order of the molecules within the phase[13,84,85]. This leaves the molecules free to flow as in a liquid but they can easily be aligned by an external applied field. Smectic phases are typically found at lower temperatures than the nematic phases and are also typical of rod-like molecules[13]. In smectic phases, molecules retain the long-range directional ordering of nematic liquid crystals but combine it with one dimensional positional ordering of the molecules. This means that smectic phases can be considered as layered, and within a layer the material is liquid-like. The smectic phase can be subdivided into several phases characterised by different types and degrees of positional ordering. In particular, the A phase where the molecules are oriented along the normal to a given positionally ordered layer, and the C phase where the molecules are tilted away from it. Chiral smectic phases can also be observed where there is a handedness of the spatial variation of the liquid crystal director between separate layers[13,84]. This phase is also known as the cholesteric phase or smectic C* phase. For a chiral phase to be observed, the individual liquid crystal molecules themselves must also be chiral. The chiral phase is described by a pitch p which is the distance over which the molecules undergo a complete 360˚ twist. The pitch of a chiral liquid crystal phase can typically be tuned by either varying the temperature or by introducing other molecules into the liquid crystal mixture[100]. A discotic phase is observed for disk-like molecules where the molecules are packed into stacks which can then have additional ordering, for example into rectangular or hexagonal arrays[84]. Bowlic phases are observed for bowl-shaped liquid crystalline molecules which are stacked similarly to discotics[84].

Lyotropic liquid crystals.

In lyotropic liquid crystals, the active liquid crystal molecules (mesogens) are dispersed in a host solvent (typically water but other organic solvents can be used depending on the molecule)[13,84,85]. Lyotropic liquid crystals exhibit a liquid crystal phase within a certain range of temperatures but also require a concentration of the active mesogens that falls within a certain range. The active molecules in lyotropic liquid crystals are normally organic in nature although some inorganic minerals can exhibit a lyotropic phase also[101]. In the lyotropic phase, the fluidity of the material is induced by the solvent molecules rather than being intrinsic to the mesogens themselves. Compounds that exhibit lyotropic liquid crystallinity are known as amphiphilic molecules. Amphiphilic molecules comprise immiscible solvophilic and solvophobic parts separated at opposing ‘ends’ or facets of the molecule. As one end has a preferential interaction with the host solvent, ordering of the amphiphilic molecules typically occurs to maximise the hydrophilic ‘head’ interaction with the host solvent while minimising that for the hydrophobic ‘tail’. The structures formed by the molecules is dependent on the relative volumes of the ‘head’ and ‘tail’ as well as the concentration of the molecules within the solvent.

At very low concentrations, there will be no ordering of the amphiphilic molecules dispersed in the solvent[13,84,85]. As the concentration is increased, there will be a critical concentration at which micelles are spontaneously formed- however, the micelles do not order themselves, so this still does not represent a liquid crystal phase. At higher concentrations, the micelles must order themselves as the inter-micelle interactions become energetically important above a critical micelle concentration within the solvent. Typically, a hexagonal columnar phase is formed where long cylindrical rods of amphiphilic molecules arrange themselves into a hexagonal lattice structure, but other structures are possible depending on the molecule. As the concentration increases further, a lamellar phase will form, with layers of the liquid crystalline molecules separated by thin layers of solvent. In lyotropic liquid crystals, it is objects formed by the aggregations of amphiphiles that can then be ordered in the same ways as observed for molecules in thermotropic liquid crystals (into nematic, smectic, *etc*. phases). Lyotropic liquid crystals possess significant tunability as the structural properties are highly sensitive to changes in concentration. For example, within in the hexagonal columnar phase, the lattice parameters can be varied by varying the solvent volume in the mixture.

Metallotropic liquid crystals.

Metallotropic liquid crystals are always composed of a mixture of organic and inorganic molecules[84,85]. The liquid crystal phase is observed only when the material is within a specific temperature range, concentration range and ratio of organic to inorganic molecules[84,85]. Metallotropic liquid crystal systems are rare, and in general offer no advantage over other liquid crystals, particularly due to the more specific requirements for observation of a liquid crystal phase. Hence, little work has been done with regards to such liquid crystals and almost no applications are currently existent.

Controlling the properties of liquid crystals.

Liquid crystals are of particular interest due to their ability to align the director along an external field[102,103]. Permanent electric dipoles can exist in the individual liquid crystal molecules when one end of the liquid crystal molecule has a positive charge while the other end has a negative charge. When an external electric field is then applied to the liquid crystal, the molecular dipoles orient along the direction of the field as the electric field exerts a force on the dipoles. Some liquid crystal molecules, however, do not have a permanent dipole but can still be influenced by an electric field[85]. The rod-like structure of many liquid crystal molecules means that they are highly polarisable and as such an applied electric field can induce a dipole by rearranging the electron density within the molecule. In fact, the shape anisotropy of many liquid crystal mesogens (including those that form lyotropic phases) means that they are highly polarisable. The polarizability of a liquid crystal molecule can also be enhanced by the presence of benzene-like rings within the molecular structure which hold highly polarisable delocalised electron density. While not as strong as permanent dipoles, orientation of the induced dipoles with the external field still occurs. The effects of magnetic fields on liquid crystal molecules are analogous to electric fields with the molecules aligning with or against the magnetic field.

In the absence of an applied external field, the director of a liquid crystal is free to point in any direction, hence the patterns seen when looked at under polarised light. It is possible, however, to force the director to take up a specific orientation by introducing an alignment agent to the system[104]. For example, when a thin polymer coating (usually a polyimide such as Nylon-6 but many other molecules have been used to the same effect) is spread on a substrate and rubbed in a single direction with a fine velvet cloth, it is observed that liquid crystal molecules in contact with that surface align with the rubbing direction[13,84,85]. Rubbing the polymer with the cloth gives a directional alignment to the polymer due to the electrostatic interaction between the cloth and the individual polymer chains. The polymer then interacts through van der Waals forces, hydrogen bonding and other effects to induce alignment of the liquid crystal molecules next to it[13]. These aligned molecules then impart their preferred alignment to neighbouring molecules which must adopt the same alignment as this holds the lowest energy when the material is in the liquid crystal phase. Similarly, patterning the substrate can impart an aligning force to the liquid crystal due to increased surface interactions[13,14]. Liquid crystalline materials present a technological platform for the dynamic tunability of the optical properties of a system while also being usable as a waveguiding medium in combination with silicon photonics.

2.6 Liquid crystals from 2D materials.

It has been shown that, by dispersing nanoparticles or molecules in a liquid crystal host, the ordering of the liquid crystal mesogens can impart ordering to the dispersed particles[100,105,106]. The nanoparticles have been shown theoretically[107] and experimentally[5,108–112] to align with the disclinations of the liquid crystal due to the energetic favourability of such an alignment. More recently, the impartment of ordering from a liquid crystal host has also been shown with dispersed 2D material particles[5,113]. Additionally, dispersions of graphene oxide in water have been shown to have a lyotropic liquid crystal phase within a specific range of concentrations of dispersed graphene oxide particles (Fig. 2.5), where the dispersed discotic graphene oxide particles are either stacked in the columnar manner typical of discotic liquid crystals or exhibit ordering analogous to a nematic phase[114–116]. The liquid crystal phase of the graphene oxide dispersions arises due to the competition between the long-range electrostatic repulsion between particles, originating from ionised functional groups at the edges of the particles, and the weak attractive interactions originating from the unoxidised graphitic domains on the surface[117,118]. The liquid crystallinity is therefore dependent on the particle size; more precisely to the ratio of the surface area to the circumference (and number of layers) as

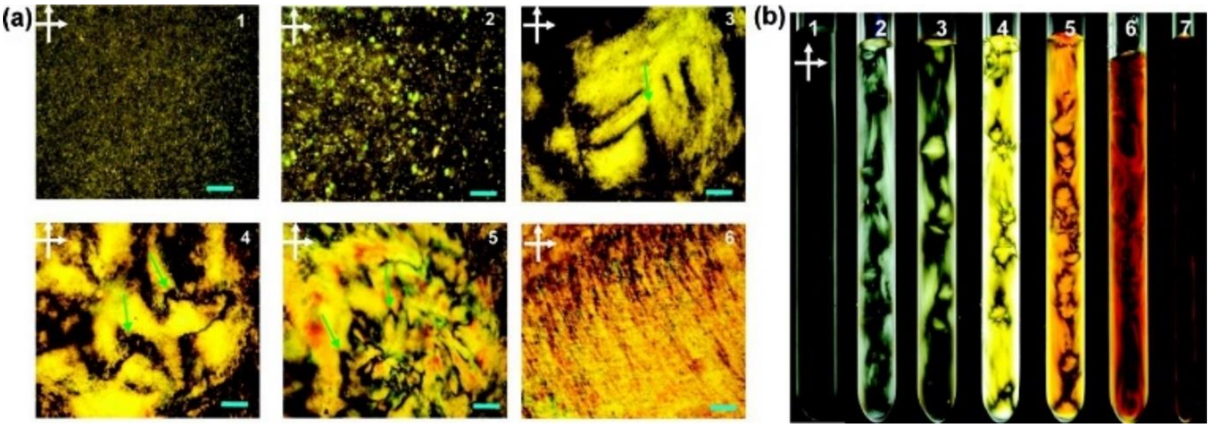

Figure 2.5:* *a) *Polarised light microscopic images between crossed polarisers of GO aqueous dispersions in planar cells with increasing maximum mass fractions from 1 to 6. Green arrows indicate disclinations of the liquid crystal phase, and the scale bars represent distances of 200 µm.* ***b)*** *Macroscopic images between crossed polarisers of GO aqueous dispersions in test tubes with increasing maximum mass fractions from 1 to 7. Reproduced with permission from Xu & Gao, ACS Nano, 2011[114]. (©2011, American Chemical Society).*

this determines the balance of the attractive and repulsive forces[118]. Most dispersions of liquid phase exfoliated graphene oxide will consist of particles of differing sizes and therefore the polydispersity of the particles becomes an important factor[119]. Additionally, this balance is affected by the degree of oxidation- the carbon to oxygen ratio of the material[118]. The stability of the liquid crystal phase can also be strongly affected by the ionic content of the solvent as this determines the degree of ionisation of the oxygen containing functional groups on graphene oxide[118,120]. The pH of the solvent also affects the critical concentration for the onset of liquid crystalline behaviour[121]. By tuning these separate parameters, it is possible to observe either a nematic phase or a columnar phase of the graphene oxide dispersion (Fig. 2.6). The different liquid crystalline phases can be observed using photoluminescence measurements as there is a strong polarisation dependence of the photoluminescence for ordered mesophases in graphene oxide dispersions[122].

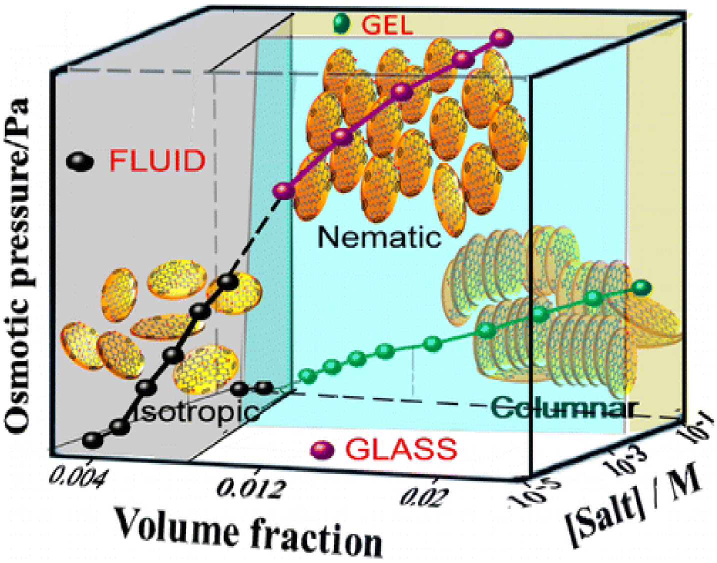

Figure 2.6*: Phase diagram of graphene oxide aqueous dispersions in terms of osmotic pressure, volume fraction of GO and salt concentration in the solution. Reproduced with permission from Konkena & Vasudevan, J. Phys. Chem. C, 2014[118]. (©2014, American Chemical Society).*

Similarly, this liquid crystal phase has been observed in a range of other organic solvents including acetone, dimethylformamide, ethanol, cyclohexylpyrrolidone and tetrahydrofuran[10,42] (Fig. 2.7). The

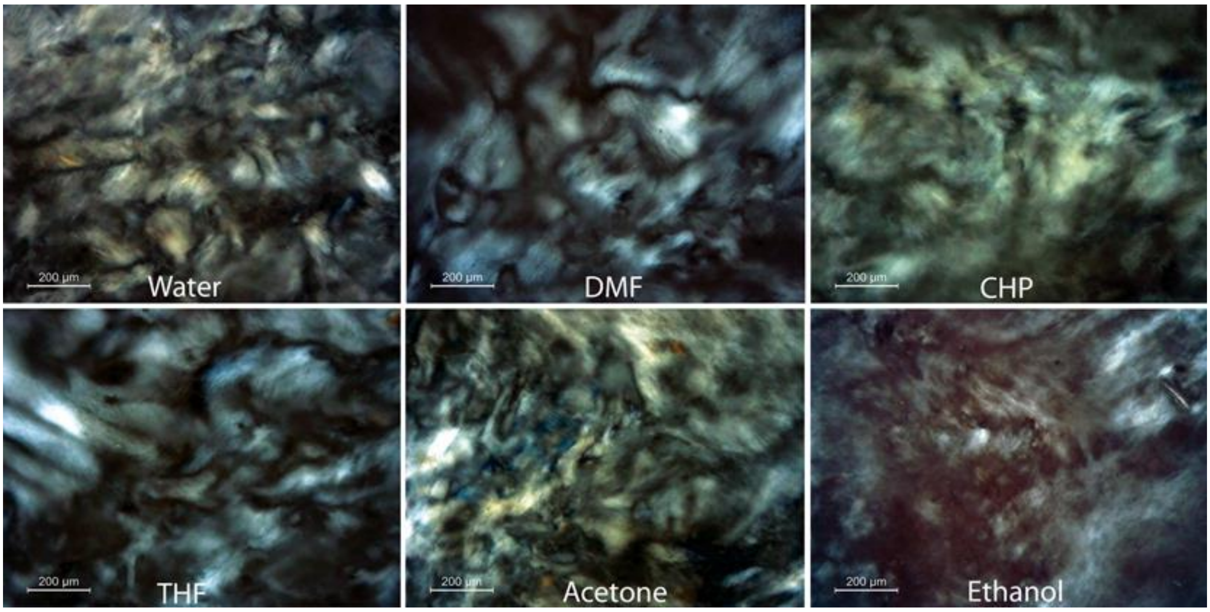

***Figure 2.7**: Schlieren textures observed in dispersions of graphene oxide in a range of organic solvents under microscopy using crossed polarisers. Reproduced with permission from Jalili et al, ACS Nano, 2013 [10]. (©2013 American Chemical Society).*

concentration of particles required to give rise to the liquid crystal phase is different for each solvent, but there is also some discrepancy between the threshold concentrations observed for the same solvent due to the effect of the size, shape and polydispersity of the graphene oxide particles in the solution[101]. A nematic liquid crystal phase has also been observed for graphene exfoliated and dispersed in chlorosulfuric acid[6]. A similar phase has been observed in other solvents for graphene and small graphitic particles although only with the addition of either stabilising surfactant[98,123,124] or polymer coatings[125]. Dispersions of graphene oxide in water have been reported to show an extrinsic chirality associated with a cholesteric liquid crystal phase[98]. This has been explained by a model wherein the electrostatic repulsion between the individual graphene oxide particles' edges causes a helical twist to form to minimise the repulsive force. More recently a nematic liquid crystal phase has been observed for dispersions of molybdenum disulfide at high concentration in water[66] suggesting the possibility of liquid crystalline phases existing for a far greater range of dispersions of 2D materials[124].

2.7 Experimental techniques.

Within the work undertaken here, there are five main experimental methods and techniques that recur repeatedly. Here, an overview of those techniques is provided, including what information can be gained from them. The techniques that will be discussed are: Raman spectroscopy; scanning electron microscopy; atomic force microscopy; dynamic light scattering; and dichroism measurements.

Raman spectroscopy.

Raman spectroscopy is a technique typically used to characterise or identify the vibrational modes of a molecule. The Raman spectra of a molecule can act as a 'fingerprint' to identify the particular molecule involved. In a Raman spectroscopy system, a monochromatic laser beam interacts with the target molecule. The laser photons interact with molecular vibrations or phonons, causing energy to be either transferred to or from the photon. The spectrum reports the changes in energy of the photons. Raman spectroscopy has become a leading technique for the characterisation of 2D materials[126]. 2D materials' properties such as the number of layers, doping level, thermal conductivity and others can be extracted from the Raman spectrum.

When light interacts with matter, the oscillating electromagnetic field of the light causes perturbation of the charge distribution in the matter. This can lead to the exchange of energy and momentum leaving the matter in a modified state. Examples include electronic excitations and molecular vibrations or activation of rotational modes. When an incident photon interacts with a molecule, it can be scattered either elastically (with no change in energy), or inelastically (either gaining or losing energy). The majority of photons will be elastically (Rayleigh) scattered. Inelastic scattering of the photons is known as the Raman effect. In an inelastic scattering process, it is considered that the photon is absorbed by the molecule, thus exciting the molecule to a virtual state. A photon with different energy is then emitted by the molecule. As the photon has gained or lost energy, it follows that the molecule must have lost or gained energy in order that energy be conserved. Therefore, the interaction with the photon must have adjusted the final state of the molecule to a different energy level. The scattered photon has an angular frequency ω_{scat} given by:

$$\omega_{scat} = \omega_l \pm \omega_{vib}\ ; \tag{7}$$

where ω_l is the pump laser frequency and ω_{vib} is the frequency of the molecular vibration with which the photon has interacted. When the energy of the scattered photon is less than that of the incident photon (i.e. energy has been transferred to a vibration of the molecule), the process is called Stokes Raman scattering. Conversely, when the energy of the scattered photon is greater than that of the incident photon (i.e. energy has been transferred from a vibration of the molecule), the process is called anti-Stokes Raman scattering.

The change in energy of the photon is called the Raman shift. Raman shifts are typically reported in wavenumbers. The Raman shift $\Delta\omega$ can be related to the wavelengths of the incident λ_l and scattered λ_{scat} photons by the relationship:

$$\Delta\omega(cm^{-1}) = \left(\frac{1}{\lambda_l(nm)} - \frac{1}{\lambda_{scat}(nm)}\right) x \frac{10^7(nm)}{(cm)}. \tag{8}$$

The Raman effect is typically very weak, with typically only one in 10^8 photons of the incident radiation undergoing spontaneous Raman scattering. The transition from the virtual state to the final state, and corresponding emission of the scattered photon, can occur at any point in time and to any possible final state based on probability. Therefore, spontaneous Raman scattering is an inherently incoherent process. The total output Raman signal power is directly proportional to the input laser power, but is scattered in random directions. The output Raman signal power also depends on the quantum efficiency of the interaction between the input laser and the molecular vibration, which is in turn dependent on the laser wavelength. The scattered spectrum will exhibit peaks related all Raman active vibrational modes with relative intensities determined by the scattering cross-section of the mode.

Scanning electron microscopy.

A scanning electron microscope (SEM) is a type of electron microscope where images are produced by scanning across a surface with a tightly focused beam of electrons. The electrons in the beam interact with the atoms in the sample under view, and various different signals are produced that contain information about the topography and composition of the sample. The electron beam is raster scanned across the surface, and by combining the known position of the beam with the detected signal, and image of the sample can be formed.

In a typical SEM system, the electron beam is either thermally- or field-emitted from an electron gun. The beam is the focused to a spot with size on the order of a nanometre. When the electron beam interacts with the sample, the electrons lose energy due to scattering and absorption within a volume called the interaction volume. The interaction volume assumes a tear drop shape due to the scattering of the electrons within the sample. The interaction volume’s size is dependent on the energy of the beam electrons, and the sample characteristics (specifically the atomic composition and the density). The exchange of energy between the beam and the sample results in the reflection of beam electrons due to elastic scattering, the emission of secondary electrons by inelastic scattering, and the emission of electromagnetic radiation. Each of these emissions can be detected to form an image of the sample, and each gives different information about the sample.

The typical mode of operation for an SEM involves the detection of the secondary electrons emitted by the atoms that are excited by the beam. Secondary electrons are emitted only close to the surface, and therefore secondary electron imaging can produce very high-resolution images of the surface of a sample. The brightness of the SEM image at a given point is dependent on the number of secondary electrons reaching the detector. If the beam enters the sample perpendicular to the surface, then the interaction volume is uniformly distributed around the beam axis and a certain number of secondary electrons are emitted from the surface. As the angle of incidence of the beam on the surface increases, the interaction volume increases. This allows emission of a greater number of secondary electrons from the surface. Therefore, steep surfaces and edges tend to be brighter than flat surfaces, resulting in images with a three-dimensional appearance due to the brightness contrast. SEM images using secondary electrons are capable of achieving sub-nanometre resolution, with magnification up to 500,000x possible, greatly surpassing the ability of light microscopy. In SEM, the material under investigation is probed by an electron, hence the fundamental limit on the minimum feature size to be imaged is on the order of the wavelength of an electron.

Atomic force microscopy.

Atomic force microscopy (AFM) is a very high-resolution imaging technique capable of giving truly atomic scale resolution. A topographical image is obtained from the response of a mechanical probe to the surface of the sample. This is achieved by raster scanning the sample position with respect to the probe tip, and recording the height at which the probe must be held in order to maintain a constant tip-sample interaction. An AFM probe typically consists of an ultrasharp (atomic sharpness) tip mounted on a cantilever, hence the limit on the resolution of an AFM image is on the order of size of an atom. The deflection and motion of the cantilever are measured by shining a laser onto the back of the cantilever and monitoring the reflected light. AFM imaging can be operated in one of three possible modes:

1. Contact mode.
2. Tapping mode
3. Non-contact mode.

In contact mode, the tip is directly in contact with the surface of the sample at all times as it is scanned. The contours of the surface can then be measured either from the deflection of the cantilever, or by using the feedback signal required to maintain the same value of the cantilever deflection. Low stiffness cantilevers with a low spring constant are used, giving a large deflection (easy to measure) while having a low interaction force (less potential for damage of the sample). Close to the surface of the sample, attractive forces can cause the tip to snap to the sample surface, giving a negative deflection. To ensure a positive deflection, contact mode AFM is undertaken with the cantilever brought much closer to the surface such that the force on the tip is repulsive and there is a firm contact with the surface.

In tapping mode AFM, the cantilever is oscillated at its resonant frequency. The frequency and amplitude of the driving signal applied to the cantilever are kept constant, such that any change in the amplitude of the cantilever’s oscillation is due to the interaction between the tip and the surface. The interaction of the tip and the surface, when the tip is brought sufficiently close, due to Van der Waals forces and other electrostatic forces causes a change in the oscillation amplitude of the cantilever. This is fed back to the system and the height of the cantilever adjusted such the original amplitude is regained. Although peak forces acting on the sample surface can be greater in tapping mode operation than in contact mode, the damage to the surface is typically reduced due to both the short duration of the force and the fact that the force is applied predominantly vertically rather than laterally.

In non-contact mode AFM, the tip is never in contact with the sample surface. The cantilever is oscillated as in tapping mode. The amplitude in this case is modulated by long range forces acting within a few nanometres of the surface. The amplitude of the cantilever oscillation is maintained via a feedback loop again as in tapping mode.

Dynamic light scattering.

Dynamic light scattering is a technique that can be used to determine the size distribution of small particles dispersed in a fluid host. In a dynamic light scattering system, a monochromatic, polarised light source (typically a laser) is sent into a sample. The sample is some fluid, typically contained within a cuvette, containing dispersed particles of interest. The scattered laser light is then passed through a polariser and the speckle pattern image is recorded. The speckle pattern forms as a result of the constructive or destructive interference at different points. Speckle patterns are collected at short time intervals and autocorrelation techniques are then used to compare the intensities at different points as a function of time. From this data, the particle sizes causing the scattering can be established.

Assuming the particles dispersed in the liquid are small when compared to the wavelength, Rayleigh scattering will occur in which the light is scattered in all directions. As the particles are not fixed (they undergo Brownian motion within the fluid), the intensity of the overall scattering varies with time as the individual scatterers are moving relative to one another. The fluctuation of the intensity contains information on the time scale of the movement of the scatterers, and consequently on their sizes. That information is extracted from the autocorrelation of the time-variance of the recorded intensity pattern. Autocorrelation is the process of correlating a signal with a time-delayed copy of itself, as a function of the time-delay – i.e. a measure of the similarity or difference between observations over time. A second order autocorrelation value g^2 can be found between two points in two intensity patterns separated by a delay τ from the relationship:

$$g^2 = \frac{\langle I(t)I(t+\tau)\rangle}{\langle I(t)\rangle^2}; \tag{9}$$

where $\langle x \rangle$ denotes the expectation value of x. For short time delays, the correlation is expected to be high as there is little time for the scatterers to move. The Siegert equation relates the second order autocorrelation value with the first order value g^1:

$$g^1 = \sqrt{\frac{g^2 - 1}{\beta}} \; ; \tag{10}$$

where β is a correction coefficient that takes into account the specifics of the laser setup. As the time delay increases, an exponential decay of the correlation is expected. This exponential decay is directly related to the motion of the particles, and more specifically to their diffusion coefficient. The decay can then be fitted by numerical methods by making assumptions about the particle size distributions. In most cases, the samples are polydisperse (that is, they contain particles with a range of sizes). Whereas for a monodisperse sample the first order autocorrelation can be treated trivially as a single exponential decay, for polydisperse samples a more complex consideration is required. The first order autocorrelation is the sum of the exponential decays related to each of the individual scatterer sizes in the solution. Hence, for as system containing n scatterers:

$$g^1 = \sum_{i=1}^{n} G_i \Gamma_i \exp(-\Gamma_i \tau) = \int G(\Gamma)\exp(-\Gamma\tau)\mathrm{d}\Gamma \; ; \tag{11}$$

where Γ is the decay rate due to a given scatterer, and $G(\Gamma)$ is a value related to the proportional scattering from that scatterer. $G(\Gamma)$ therefore contains information on the distribution of sizes. To access that information, a cumulant method is typically used. One then has the equation:

$$g^1 = \exp\left(-\bar{\Gamma}\left(\tau - \frac{\mu_2}{2!}\tau^2 + \frac{\mu_3}{3!}\tau^3 - \dots\right)\right) \; ; \tag{12}$$

where $\bar{\Gamma}$ is the average decay rate across all scatterers, ${}^{\mu_2}/_{\bar{\Gamma}^2}$ is the second order polydispersity index, and ${}^{\mu_3}/_{\bar{\Gamma}^3}$ is the third order polydispersity index. The z-averaged diffusion coefficient D_z for a particular point with wave vector q can then be found from the relationship:

$$\bar{\Gamma} = q^2 D_z \, , \tag{13}$$

with:

$$\mathrm{q} = \frac{4\pi n_0}{\lambda}\sin\left(\frac{\theta}{2}\right) \; ; \tag{14}$$

where n_0 is the refractive index of the material, λ is the laser wavelength, and θ is the angle at which the detector is placed relative to the sample cell. D_z can then be used to calculate the particle size (hydrodynamic radius) *via* the Stokes-Einstein equation:

$$D_z = \frac{k_B T}{6\pi\eta r} \; ; \tag{15}$$

where k_B is the Boltzmann constant, T is the absolute temperature, η is the viscosity of the fluid, and r is the desired hydrodynamic radius.

This technique is only truly applicable to spherical particles. For aspherical particles, rotational motion must also be accounted for. The complexity of such systems means that dynamic light scattering is rarely applied except for either spherical or approximately spherical particles.

Dichroism measurements.

A dichroic material is one for which light in different polarisation states experiences a different absorption coefficient, causing the different polarisations to be attenuated differently. The dichroism is a function of wavelength, and can be either associated with specific absorptions within the material, or can be broader, relating to the structure of the material itself. There are two main kinds of dichroism of interest: linear dichroism and circular dichroism.

Linear dichroism (LD) is the difference in the absorption for two orthogonal polarisations of light - that is, for light polarised parallel and perpendicular respectively to a defined orientation axis. Linear dichroism uses linearly polarised light. Linear polarisation means that the light has been polarised in a single direction such that the electric and magnetic field vectors of the wave oscillate in a single plane perpendicular to the direction of propagation (Fig. 2.8). To find the linear dichroism of a material, the different absorptions for the light parallel to the orientation axis and perpendicular to the orientation axis are measured. The difference between these two absorptions is the linear dichroism of the material:

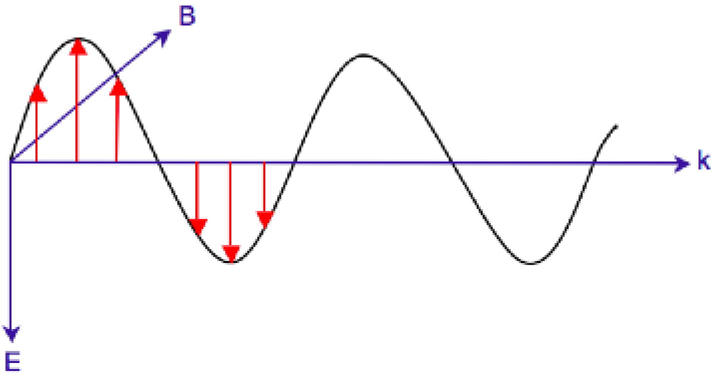

***Figure 2.8**: Oscillation of the electric field for linearly polarised light propagating in the direction of k.*

$$\mathrm{LD} = A_{\parallel} - \mathrm{A}_{\perp}; \qquad (16)$$

where $A_{\perp}$is the absorption of the light polarised perpendicular to the orientation axis, and $A_{\parallel}$ is the absorption of the light polarised parallel to the orientation axis. In linear dichroism measurements, the incident light is typically cycled through a range of wavelengths to give the linear dichroism spectrum of the material.

Circular dichroism (CD) is the difference in the absorption for left- and right-circularly polarised light for a material. Circular dichroism is exhibited by the absorption of optically active chiral materials. A chiral material is one for which the mirror image cannot be superimposed on the original. Optically active materials are those for which the polarisation orientation of linearly polarised light is rotated as it passes through the material.

While linearly polarised light has an electric field vector that oscillates in a single fixed plane, circularly polarised light has an electric field vector which rotates around the propagation direction (Fig. 2.9). For light travelling towards a fixed observer, the electric field vector can be seen as rotating either clockwise or anti-clockwise. If the rotation is clockwise, the polarisation is denoted as right-circularly polarised. If the rotation is counter-clockwise, the polarisation is denoted as left-circularly polarised. In a circular dichroism experiment, left and right circularly polarised light of a given wavelength are alternately transmitted through a sample, and the intensity of the transmitted light recorded. From this, the absorptions of the two different polarisations can be established. Measuring across a range of wavelengths yields the CD spectrum of the material. At a given wavelength, the circular dichroism can be expressed directly as the difference in absorbances for left and right circularly polarised light:

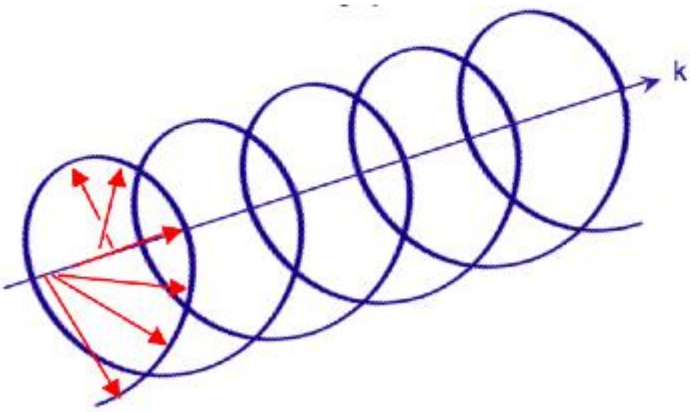

***Figure 2.9**: Oscillation of the electric field for right-circularly polarised light propagating in the direction of k.*

$$\Delta A = A_L - A_R; \tag{17}$$

where A_L and A_R are the absorbances for left and right circularly polarised light respectively. Circular dichroism is often reported in units of ellipticity θ, where:

$$\theta = 32.98 \,.\, \Delta A. \tag{18}$$

3. Prospects and Challenges for 2D Material Liquid Crystals' Application.

In this chapter, the current state-of-the-art applications of 2D material liquid crystals will be described and discussed. The potential for future applications will also be considered. A perspective will then be given on the further work that is necessary to increase the scope for applications of these materials.

3.1 Current and Prospective Applications.

Films, fibers, membranes and inks.

Behabtu *et al.*[6], demonstrated that graphite spontaneously exfoliates into single-layer graphene in chlorosulfonic acid, and spontaneously forms liquid-crystalline phases at high concentrations. Transparent, conducting films were produced from the liquid crystalline dispersions. The self-assembling nature of liquid crystalline materials has led to the use of graphene oxide dispersions for the formation of well-ordered layers and stacks of 2D materials. Jalili *et al.*[10] showed that self-assembly of graphene oxide sheets is possible in a wide range of organic solvents. The prepared dispersions were employed to achieve self-assembled layer-by-layer multifunctional 3D hybrid architectures comprising carbon nanotubes and GO with promising mechanical properties (Fig.

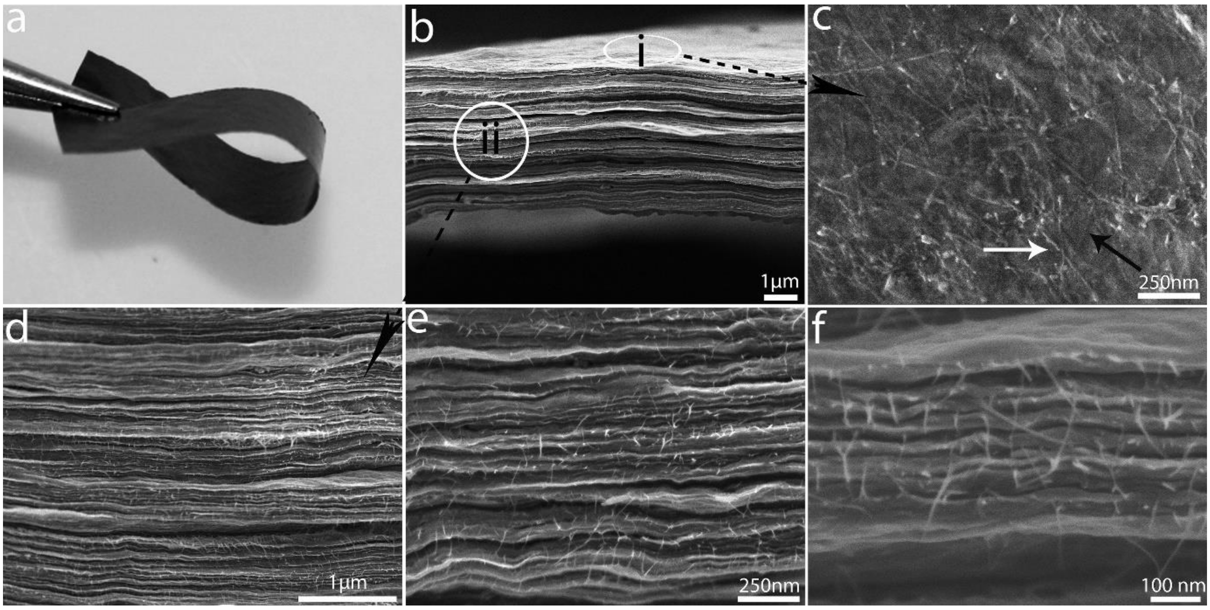

***Figure 3.1**: **a)** Photograph of a flexible free-standing paper of LC GO made by a cast drying method. **b)** SEM image of the cross section of as-cast dried LC GO paper. **c)** SEM image of the surface of the layer-by-layer composite, marked as region (i) in **(b)**. **(d–f)** Cross section of composite paper at different magnifications. Reproduced with permission from Jalili et al, ACS Nano, 2013[10]. (©2013 American Chemical Society).*

3.1). More recently, the same group has showed that similar self-assembly can be achieved using liquid crystalline dispersions of molybdenum disulfide[66]. Layers of these materials have been combined with other materials for a variety of diverse applications such as photovoltaics[127] and improving the mechanical properties of composite materials[128], the more homogeneous layers produced from the liquid crystalline dispersions are of significant interest to applications of these natures. The use of liquid crystalline dispersions of graphene oxide to produce uniform layers has been used as a precursor to forming similarly uniform structures of graphene through the reduction of the graphene oxide[98,129]. Akbari *et al.* demonstrated that the discotic nematic phase of GO can be shear aligned to form highly ordered, continuous films of multi-layered GO on a supporting membrane. The highly ordered graphene sheets in the plane of the membrane make organised channels and give greater permeability. The nanoporous membranes may find application in a variety of filtering applications[130]. Fu *et al.* demonstrated the use of graphene oxide liquid crystals can be applied as composite inks for the formation of electrodes in 3D printing applications[131] due to the intrinsic self-assembly that means they retain ordering of the GO platelets on drying of the solvent.

The development of fibers formed from graphene, GO or reduced GO is a widely-reviewed, maturing area for investigation, with many proposed applications such as in conducting wires, energy storage and conversion devices, actuators, field emitters, catalysis and optoelectronic and photonic devices[132–135]. One of the most promising developments in this field, and of particular interest here, has been the use of the liquid crystal phase to improve the homogeneity and ordering of the fibers produced; numerous examples exist where fibers comprised of 2D materials have also been produced by the wet-spinning of liquid crystalline solutions[66,98,114,129,136]. Xu and Gao[98] developed a method by which aqueous graphene oxide liquid crystals were continuously spun into metres of macroscopic graphene oxide fibers; subsequent chemical reduction gave the first macroscopic neat graphene fibers with high conductivity and good mechanical performance (Fig. 3.2). Jalili *et al.* demonstrated a method

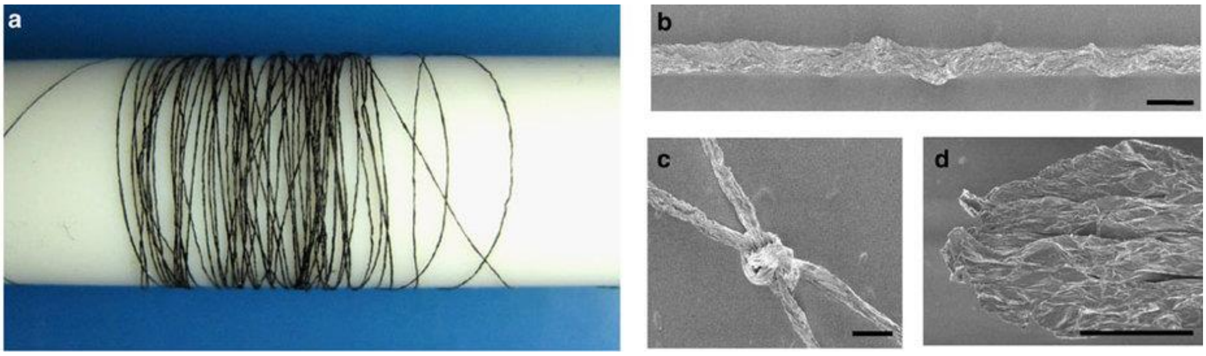

***Figure 3.2**: **a)** Four-metre-long wound GO fiber. SEM images of the fiber **(b)**, and a typical tighten knot **(c)**. **d)** The morphology of the GO fiber after tensile tests. All scale bars 50 µm. Reproduced with permission from Xu & Gao, Nature Communications, 2011[98]. (©2011 Nature Publishing Group).*

for one-step continuous spinning of graphene fibers where the need for post-treatment processes is eliminated by the use of basic coagulation baths for reduction of GO during the spinning process[129], as well as the applicability of wet-spinning to the formation of fibers of other 2D materials[66].

Optoelectronics.

Liquid crystalline nanocomposites incorporating 2D material particles show great promise for optoelectronic applications due to their field induced tunability and enhanced functionality stemming from the plethora of properties displayed by the range of exfoliatable materials. For example, dispersions of liquid crystalline graphene oxide have been shown to undergo electro-optical switching with low threshold voltage requirements[137]. Kim *et al.* show that GO LCs possess an extremely large Kerr coefficient, making them attractive for low power consumption optoelectronic devices[137]. By stabilising a suspension of reduced GO using surfactants, they demonstrated increased time stability and drastically improved electro-optic properties with an induced birefringence twice as large at the same field strength as that with an unreduced GO suspension.

Zhu *et al.*[138] have shown that the preparation of poly(*N*-isopropylacrylamide) /GO nanocomposite hydrogels with macroscopically oriented LC structures, after polymerisation, can be readily achieved under assistance from a flow-field- induced by vacuum degassing. Nanocomposites prepared with a GO concentration of 5.0 $mg.mL^{-1}$ exhibit macroscopically aligned LC structures, which endow the gels with anisotropic optical properties. Furthermore, they showed that the oriented LC structures are not damaged during switching of the hydrogels, and hence their behaviour undergoes reversible changes. Additionally, they showed that the oriented LC structures in the hydrogels can be permanently maintained after drying the nanocomposite samples. The liquid crystalline properties of such nanocomposites facilitate their applicability to switching in optoelectronic devices.

Kim *et al.*[139] have demonstrated significant improvement of the electro-optic performance of a polymer-stabilised liquid crystalline blue phase using a reduced graphene oxide (RGO) enriched polymer network. The conductivity of the nanocomposite system is increased by the inclusion of the RGO. Furthermore, reductions in the operational voltage (~32%), response time (~51%) and hysteresis (~53%) compared to those of a conventional polymer-stabilised blue phase LC signify great potential for the use of 2D materials in enhancing novel electro-optic device applications of conventional LC systems.

Recently, it has been proposed that by tuning the liquid crystal director by means of an applied field, one could induce the formation of metastructures formed of the dispersed 2D material particles as they are repositioned. In particular, it has been shown that nanocomposites of nematic phase liquid crystals with dispersed graphene oxide particles can be integrated with CMOS photonics devices as a back-end process as part of microfluidic systems and that the integrated nanocomposites can be readily controlled by use of either an electric field or laser light to reposition and rearrange the dispersed particles[5].

Displays.

2D material liquid crystals can be used in back-illuminated liquid crystal display applications as they exhibit electro-optic switching. The large Kerr coefficient of graphene oxide liquid crystals observed by Shen *et al*[140], for example, facilitates this application. However, the slow switching times reported by Kim & Kim (>1 *s*)[141] must be considered, although Ahmad *et al.*[142] report that this can be improved by approximately an order of magnitude by careful selection of the size of graphene oxide mesogens.

More promisingly, 2D material liquid crystals have also been proposed for application in liquid crystal displays- particularly in so-called ‘e-ink’ displays-without requiring the polarising optics typically necessary for these applications[11,121]. He *et al.*[11] demonstrated a process by which graphene oxide liquid crystals can be used for reflective displays without the need for polarizing optics (Fig. 3.3). By using flow-induced mechanical alignment, they prepared graphene oxide in different orientational

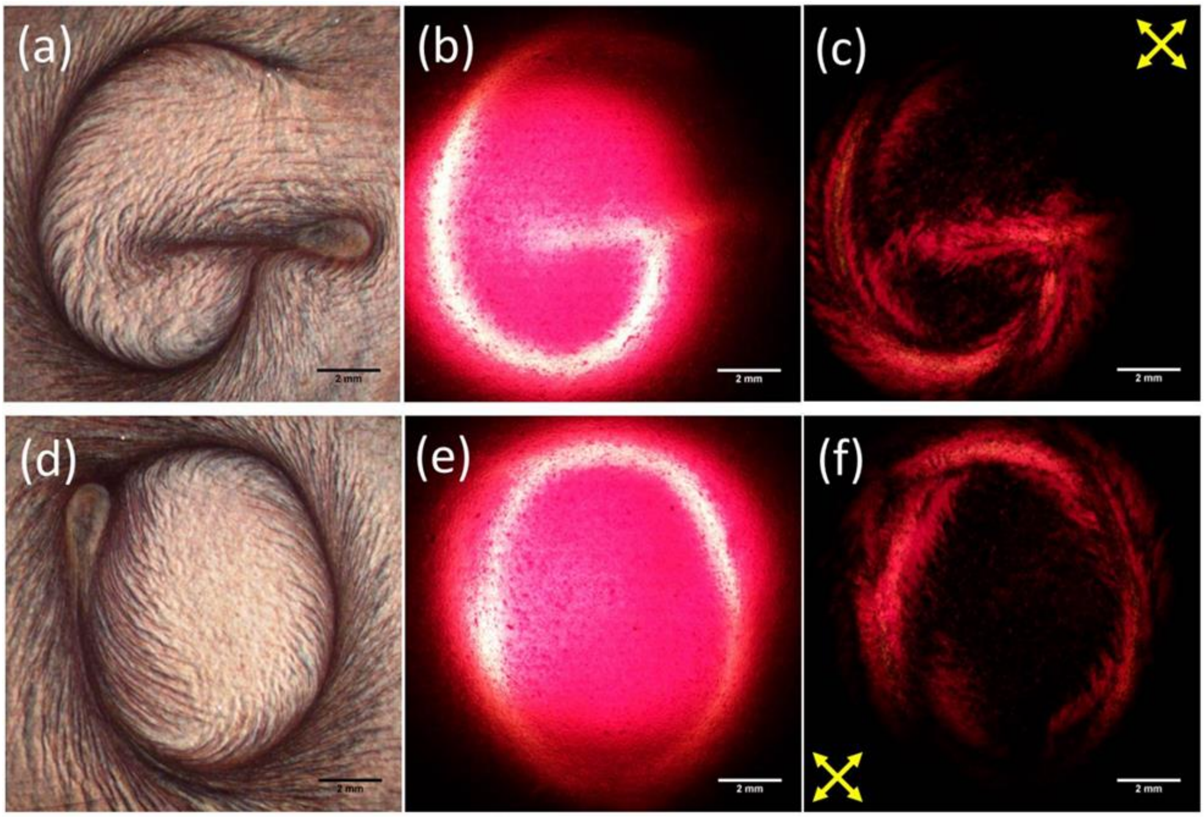

Figure 3.3: *Images of a defined structure in a liquid crystalline e-ink of graphene oxide dispersed in water in* ***(a,d)*** *reflection with unpolarised light,* ***(b,e)*** *transmission with unpolarised light and* ***(c,f)*** *transmission between crossed polarisers. Reproduced from He et al, Nanoscale, 2014*[11] *with permission from The Royal Society of Chemistry ©2014.*

orders and demonstrated that the ordered graphene oxide liquid crystals can be used as a rewritable display medium. The surface of the graphene oxide liquid crystal can be switched from a bright, reflective state to a dark, transmissive state using, for example, a wire to manually draw patterns on the surface. They explain that the contrast between the two states arises due to the anisotropic response of the flakes due to the inherent high aspect ratio of the 2D material.

Quality control.

Inducing the onset of a liquid crystal phase in a dispersion of graphene oxide has been used for size selection of the graphene oxide particles[143]. Lee *et al.* introduced a method for facile size selection of large-size graphene oxide particles by exploiting liquid crystallinity. They show that in a biphasic graphene oxide dispersion where both isotropic and liquid crystalline phases are in equilibrium, large-size GO flakes (>20 μm) are spontaneously concentrated within the liquid crystalline phase. Selectivity of large flake sizes without the need of filtering presents several advantages for photonics and optoelectronics applications; primarily larger flakes allow for greater uniformity of device characteristics over wider areas and can help to increase the uniformity of depositions.

Outlook.

2D materials encompass a fascinating range of diverse properties with a myriad of possible applications in optoelectronics and photonics. The development of liquid crystalline nanocomposite materials incorporating 2D materials represents a significant advance in the opportunities for integration and exploitation of 2D materials within these fields. However, there remain a large number of questions that demand further investigation before 2D material liquid crystals can find wider application. Primarily, there remain many candidate 2D materials for which a liquid crystal phase is theoretically possible but not yet shown; the discovery of further 2D material liquid crystals would broaden the range of utilisable properties available. Similarly to that observed for graphene oxide, observation of this liquid crystallinity should require a combination of careful solvent selection, tuning of the 2D material particle sizes and control of the concentration of the particles. Additionally, the use of surfactant molecules may be necessary to stabilise the liquid crystalline phase of the dispersions by maximising the aligning forces acting on the dispersed particles. However, this raises the additional question of the exploration- both theoretical and experimental- of the conditions required for the existence of the liquid crystal phase, an area in which little work has thus far been explored for the specific systems of interest here. A significant part of such work remains to be done in the comparison of the different synthetic routes towards the LC phase, and how the synthesis can affect the observed properties.

Additionally, dispersion of 2D materials in conventional liquid crystal host fluids presents superb new possibilities in optofluidic systems; from light generation to dynamic sensing applications. This is owing to the dramatic improvements that can be observed in the operational parameters of the nanocomposite systems in comparison to the conventional LC systems currently used in optoelectronics and photonics. Such nanocomposites can not only improve properties such as switching times and threshold voltages, but can also add further functionality, for example by metastructuring of nanoparticle dispersions. For these nanocomposite systems, the most important advances to be made are in the fundamental understanding of the basis for improvements in their intrinsic properties; and in the exploration of predicting metastructuring as well as experimental observation. Overall, the existence of liquid crystal phase 2D material dispersions presents fantastic opportunities in the exploration of novel optoelectronic and photonic systems, allowing new highly scalable production processes for thin film integration and novel fiber systems amongst numerous other applications.

3.2 Challenges.

There are several challenges to be addressed in the application of fluid-dispersed 2D materials within the field of optoelectronic and photonic devices. Firstly, the on-chip integration of such materials has as yet never been demonstrated. Secondly, the controlled assembly of functional microstructures remains to be shown both off- and on-chip. Finally, the breadth of available materials and properties requires increasing to facilitate a greater range of potential device functionalities. This work aims to address the practicable and repeatable demonstration of the synthesis, integration and dynamic microstructure architecting using CMOS compatible back-end techniques.

Development of novel materials.

There are two main possibilities for developing novel photonic materials where dynamic reconfigurability is delivered through the exploitation of liquid crystalline properties and 2D materials. Firstly, 2D material particles can be dispersed in a conventional liquid crystal host. Alternatively, 2D materials dispersed in specific solvents have been shown to display liquid crystalline phases within certain ranges of 2D material concentration[98,123]. Liquid phase exfoliated 2D materials are of significant interest for the production of 2D material liquid crystal composites as the exfoliating solvent can be used as the fluid host for spontaneous liquid crystal phase self-assembly[6,11,140,144–146,66,98,114–116,119,120,129], or to allow combination with conventional liquid crystals[5]. Specifically, liquid crystallinity has been shown for graphene oxide flakes dispersed in water as well as a range of organic solvents[10,114,121]. However, despite the potential for other 2D materials to show similar lyotropic liquid crystallinity there have been no demonstrations of such behaviour recorded until recently, where a liquid crystal phase has been shown for MoS_2[66]. However, there remain a large number of candidates for which a liquid crystal phase is possible but not yet shown. Similarly, to graphene oxide, observation of this liquid crystallinity should require a combination of careful solvent selection, tuning of the 2D material particle sizes and control of the concentration of the particles. Additionally, the use of a surfactant molecule may be necessary to stabilise the liquid crystalline phase of the dispersions by maximising the aligning forces acting on the dispersed particles.

Development of new characterisation methods.

A significant challenge on the path to the first realisation of on-chip controlled assembly of 2D flakes into functional microstructures is the lack of a reliable and sensitive method for the *in-situ* characterisation of the 2D flakes. Such a method would be required to provide information not only about the success or otherwise of the integration of the composites into the device structure, but --most importantly could enable determination of parameters such as spatial alignment and size of incorporated nanomaterials dynamically during the photonic device operation. There are several existing characterisation methods which could be applied to overcome this challenge; including, Raman spectroscopy[8,14] and coherent anti-Stokes Raman spectroscopy (CARS)[147], as well as Fourier Transform Infrared Spectroscopy (FTIR)[148]. However, none of these techniques are suitable for investigation of fluid nanocomposites with relatively low concentrations of nanoparticles dispersed, since the significantly greater scattering volume of the host fluid always increases the intensity of the vibrational signal for the bands of that host compared to those of the integrated particles. Therefore, monitoring of the signal from considerably weaker bands associated with dispersed nanoparticles is extremely difficult and often impossible. Furthermore, laser-induced heating of liquids can cause their evaporation or even burning at high powers or after long exposure times, limiting the options for increasing signal-to-noise ratio. Most importantly, none of the existing characterisation methods can be used for *in-situ* characterisation of fluid dispersed nanoparticles integrated into CMOS photonics chip, due to either weak signals, strong absorption, or interaction with other parts of the chip. As such, a new *in-situ* method for the dynamic monitoring of self-assembly of fluid-dispersed nanoparticles on-chip.

In-situ assembly of functional microstructures.

The assembly of functional microstructures on-chip requires careful tuning of both the material properties and overall device structure to generate the required effect. The tuning of the self-assembly of liquid crystalline materials can be achieved through a number of methods; specifically-electric field[103], magnetic field[85] and temperature gradients[13]. Fine control of 2D particle positions can be achieved through optical trapping[149]. Although electric field, magnetic field and temperature tunability of liquid crystal alignment have been shown multiple times[150–152], there has been little investigation of the effect of dispersing 2D material particles within the liquid crystal. The impact of graphene incorporation on the ordering of nematic crystal 5CB has been determined[153], but, as the interaction depends on the interactions between the functional groups of the liquid crystal with those of the 2D material, there is nothing to suggest that the observed effects in this system would occur similarly for other liquid crystal molecules and/ or 2D materials. To understand the degree of control of microstructure formation, the initial state of the material without applied stimuli must be fully characterised. To achieve controllability of the microstructure formation by fluid dispersed 2D materials, the response of new nanocomposite liquid crystalline materials under various applied stimuli must first be investigated. Threshold field strengths for reorientation of novel liquid crystalline materials must be established, along with the resultant alignment of the dispersed 2D material particles. The optical properties of assembled microstructures can be numerically determined using a scattering matrix method[154–156].

4. Preparation of 2D Material Liquid Crystals.

As discussed in Section 3.2, there are two main possibilities for developing novel photonic materials where dynamic reconfigurability is delivered through the exploitation of liquid crystalline properties and 2D materials. Firstly, 2D material particles can be dispersed in a conventional liquid crystal host. Secondly, 2D materials dispersed in a solvent host can be induced to form a liquid crystal phase by controlling the particle aspect ratio and concentration. In this chapter, the synthesis and characterisation of 2D material liquid crystals formed by each of these methods is detailed.

4.1 Nematic liquid crystals doped with 2D materials.

Synthesis of graphene oxide – liquid crystal nanocomposites.

Graphene oxide (GO) was prepared from bulk graphite *via* the Hummers method[58]. 1 *g* of graphite, 0.5 *g* of sodium nitrate and 23 *mL* of sulfuric acid (H_2SO_4) were added to a 500 *mL* round bottomed flask contained within an ice bath and stirred at 4 *°C* for 15 minutes. 3 *g* of potassium permanganate ($KMnO_4$) was added slowly with vigorous stirring (all initial materials supplied by Sigma Aldrich). Once all the $KMnO_4$ was added, the ice bath was removed and the suspension was heated to 35 *°C* for 30 minutes. This produced a murky brownish-grey solution. Following this, 46 *mL* of water was added and the suspension was set to stir for 15 minutes. The solution was then treated with 1.4 *mL* of hydrogen peroxide (H_2O_2). The product was washed through centrifugation up to 10 times with a 10 % aqueous solution of hydrochloric acid (HCl) followed by copious amounts of deionised water. The resulting GO was suspended in H_2O and filtered under vacuum onto an omniporous 200 *nm* membrane, washed with 1 *L* of H_2O and then dried at 80 *°C* for several days. Once dried, the GO was dispersed in tetrahydrofuran (THF) through ultrasonication, exfoliating the material down to a few layers[42]. The dispersions were then centrifuged, allowing for extraction of the lowest mass GO flakes from the top layer of the suspension. An aliquot from this layer was mixed with the chosen liquid crystal (E7, MLC 6608, or 5CB) and the mixture underwent further ultrasonication to ensure thorough mixing of the two components. The resulting dispersion was dried in a Schlenk flask, under vacuum, allowing for complete evaporation of the residual solvent, resulting in a nanocomposite of GO nanoplatelets uniformly (as observed by eye and under optical microscopy) dispersed in the liquid crystal. The concentration of GO in the final nanocomposites was approximately 0.01 $g.ml^{-1}$. This was determined by drying and determining the mass of GO in an equivalent aliquot. Dispersed flakes had average sizes of around 1 μm^2 (observed by optical microscopy and SEM) and were typically found to be between 1 and 5 layers thick (as determined by AFM). The number density of graphene oxide particles was calculated to be approximately 10^{12} *particles/ mL* by taking the average sizes to determine the volume, multiplying by the density of graphene oxide to give the average mass per particle, and finally dividing the concentration by the average mass per particle. Graphene nanocomposites were produced by a similar method starting from bulk graphite powder.

Synthesis of molybdenum disulfide – liquid crystal nanocomposites.

Liquid crystalline nanocomposite materials consisting of molybdenum disulfide flakes dispersed in a nematic liquid crystal (E7, MLC 6608, or 5CB) were synthesised via the following procedure. MoS_2 was exfoliated to few-layer thicknesses from the bulk solid by use of a liquid phase exfoliation method, wherein ultrasonication of MoS_2 dispersed in a suitably chosen organic solvent induces cleavage of the interlayer van der Waals bonding. The solvent chosen for exfoliation of MoS_2 was chloroform. Resulting dispersions of few-layer MoS_2 were then centrifuged to remove any residual bulk, or otherwise large, MoS_2 particles. The centrifuged dispersions were then mixed with a commercial nematic liquid crystal formulation (E7, MLC 6608, or 5CB) and then ultrasonicated to ensure homogeneous mixing. The organic solvent was then removed from the mixture under vacuum using a Schlenk line to leave homogeneously dispersed MoS_2 particles suspended in the liquid crystal host.

Synthesis of graphene – liquid crystal nanocomposites.

Liquid crystalline nanocomposite materials consisting of graphene flakes dispersed in a nematic liquid crystal (E7, MLC 6608, or 5CB) were synthesised via a procedure largely similar to that previously described for molybdenum disulfide. Graphene was exfoliated to few-layer thicknesses from the bulk (graphite) solid by use of a liquid phase exfoliation method, wherein ultrasonication of graphite flakes dispersed in a suitably chosen organic solvent induces cleavage of the interlayer van der Waals bonding. The solvent chosen for exfoliation of graphene was water. Resulting dispersions of graphene were then centrifuged to remove any residual bulk, or otherwise large, particles. No surfactant was used as the removal of surfactant would have been challenging while also combining with the liquid crystal. However, this meant that the yield of fully exfoliated graphene particles was low. The yield was estimated by comparing the initial mass of graphite with the mass contained in an aliquot from the top fraction after centrifugation. As the nematic liquid crystals used are hydrophobic, it was necessary then to add isopropanol to the dispersions to allow it to mix with the liquid crystal. The final dispersion was mixed in a solution containing 60:40 isopropanol to water. The centrifuged dispersions were then mixed with a commercial nematic liquid crystal formulation (E7, MLC 6608, or 5CB) and ultrasonicated to ensure homogeneous mixing. The organic solvent was then removed from the mixture under vacuum using a Schlenk line to leave homogeneously dispersed (as observed by eye and under optical microscopy) graphene particles suspended in the liquid crystal host.

Switching time measurements.

To analyse the performance of the nematic liquid crystals with dispersed 2D materials, the first consideration was how the switching time of the liquid crystal was affected. To do so, liquid crystal cells were used. Faster switching times are desirable as they allow faster device operation frequencies. One of the major limitations of liquid crystals currently is that the switching speeds are relatively slow compared to other methods of modulation; hence, it would be desirable to decrease the time taken to switch the liquid crystal. The liquid crystal cells consisted of two glass substrates coated with indium tin oxide and a polyimide alignment layer. The two substrates were separated by 10 µm using silica spacers (balls of silica of a defined diameter of 10 µm) dispersed in epoxy. The indium tin oxide is used as an electrode to apply an electric field across the cell. The polyimide alignment layer ensures that the liquid crystals within the cell preferentially align in the same direction under ambient conditions.

The liquid crystals with dispersed 2D materials were infiltrated into the liquid crystal cells via small openings in the spacer layer. Once the gap between the two glass substrates was completely filled, the openings were sealed using epoxy resin. Wires were attached to the indium tin oxide electrodes to allow the application of electric fields to the cells. To test the switching time, six cells were produced. These contained:

1. Nematic liquid crystal E7 only;
2. E7 with dispersed graphene particles at a concentration of around 128 mg.mL^{-1};
3. E7 with dispersed graphene oxide particles at a concentration of around 62 mg.mL^{-1};
4. E7 with dispersed MoS_2 particles at a concentration of around 5 mg.mL^{-1}, denoted MoS_2 low concentration (LC).
5. E7 with dispersed MoS_2 particles at a concentration of around 50 mg.mL^{-1}, denoted MoS_2 medium concentration (MC).
6. E7 with dispersed MoS_2 particles at a concentration of around 250 mg.mL^{-1}, denoted MoS_2 high concentration (HC).

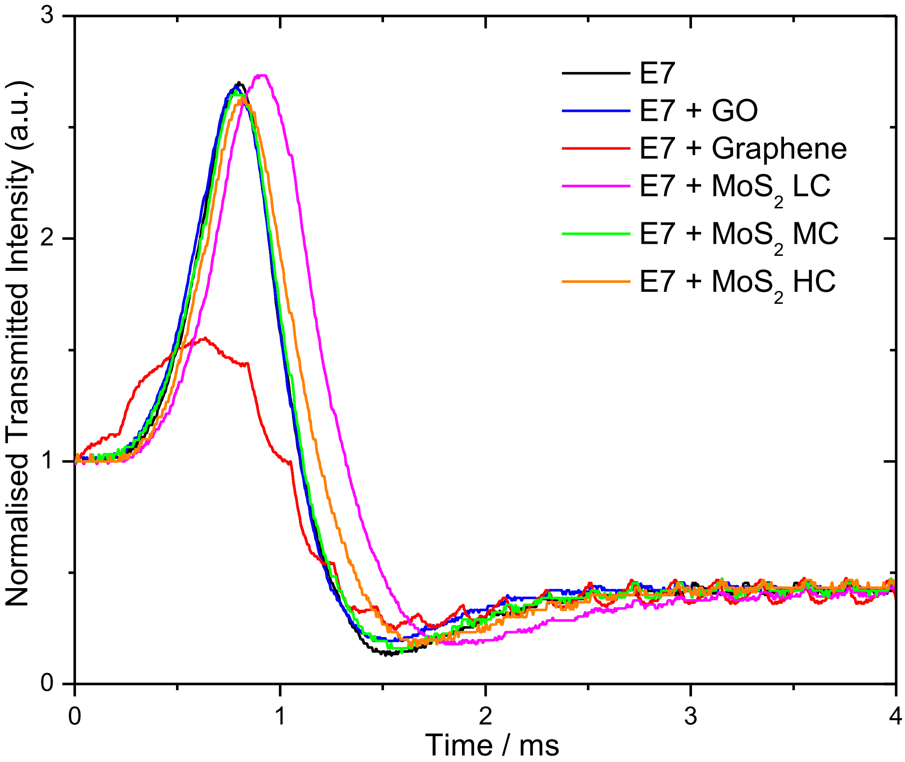

***Figure 4.1**: 'On' switching times for the liquid crystal cells containing: liquid crystal E7 (black); E7 with dispersed graphene oxide (blue); E7 with dispersed graphene (red); E7 with dispersed molybdenum disulfide at a low concentration (magenta); E7 with dispersed molybdenum disulfide at a medium concentration (green); and E7 with dispersed molybdenum disulfide at a high concentration (orange). Switching times are found from the change in the normalised transmitted intensity as a function of time, under the application of a voltage to the liquid crystal cell.*

Particle concentrations were established by by drying and determining the mass of the 2D material in an equivalent aliquot to that dispersed in the liquid crystal. The transmission through these cells of a broadband white light source was then monitored as an electric field was applied. Initially, for all samples, an AC electric field with a peak amplitude of 5V and a frequency of 1 kHz was applied. The 'on' time after which the transmission reached 90% of the steady state value after the applied field was turned on (Fig. 4.1) was analysed. The temperature of the liquid crystal cell was maintained at 30±0.05°C throughout for all samples. All data are normalised such that the transmission is 1 at t=0.

The 'off' time after which the transmission returned to its initial state after removal of the electric field (Fig. 4.2) was also analysed.

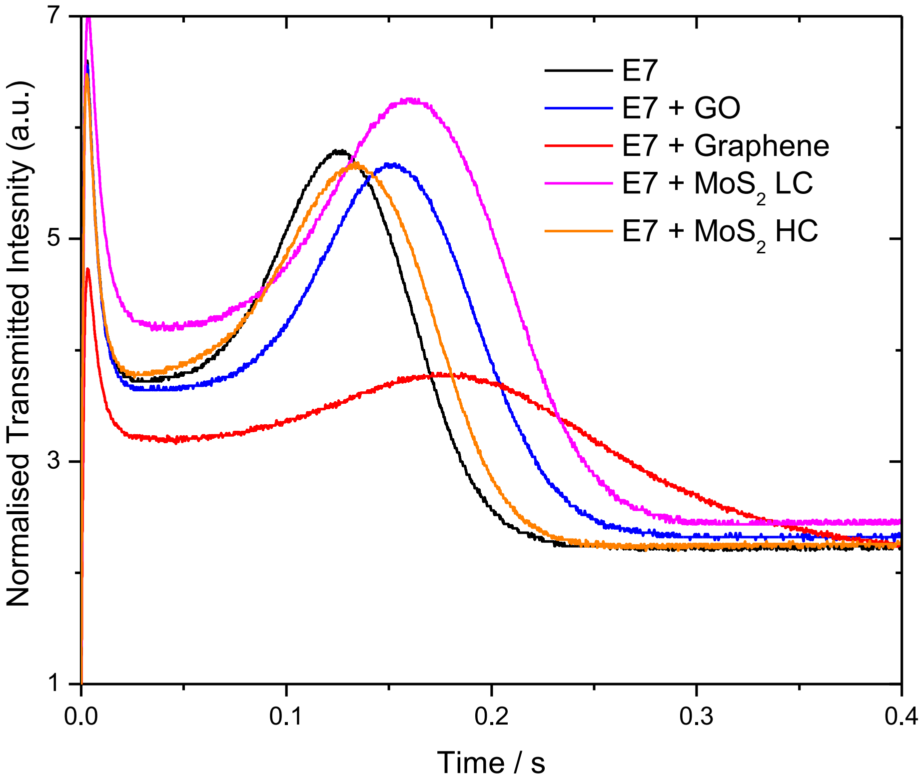

***Figure 4.2**: 'Off' switching times for the liquid crystal cells containing: liquid crystal E7 (black); E7 with dispersed graphene oxide (blue); E7 with dispersed graphene (red); E7 with dispersed molybdenum disulfide at a low concentration (magenta); and E7 with dispersed molybdenum disulfide at a high concentration (orange). Switching times are found from the change in the normalised transmitted intensity as a function of time, after the removal of a voltage applied to the liquid crystal cell.*

For all samples, the 'on' time when compared to the liquid crystal with no 2D material dispersed was slower. While the 'off' time was found to be more or less unchanged, although in the case of the off time the uncertain ties are significantly greater. The recorded switching times are given in Table 4.1.

***Table 4.1:** Summary of the measured 'on' and 'off' switching times for liquid crystal samples containing different dispersed 2D materials, and switching at different applied electric field frequencies.*

Sample	Frequency / kHz	Off time / s	On time / ms
E7	1	0.4 ± 0.2	1.24 ± 0.01
E7 + Graphene	1	0.6 ± 0.2	1.29 ± 0.01
E7 + GO	1	0.4 ± 0.2	1.23 ± 0.01
E7 + MoS$_2$ LC	1	0.4 ± 0.2	1.51 ± 0.01
E7 + MoS$_2$ MC	1	0.4 ± 0.2	1.27 ± 0.01
E7 + MoS$_2$ HC	1	0.4 ± 0.2	1.37 ± 0.01
E7	5.1	0.4 ± 0.2	0.31 ± 0.01
E7 + Graphene	5.1	0.6 ± 0.2	0.86 ± 0.01
E7 + Graphene	0.6	0.6 ± 0.2	1.81 ± 0.05

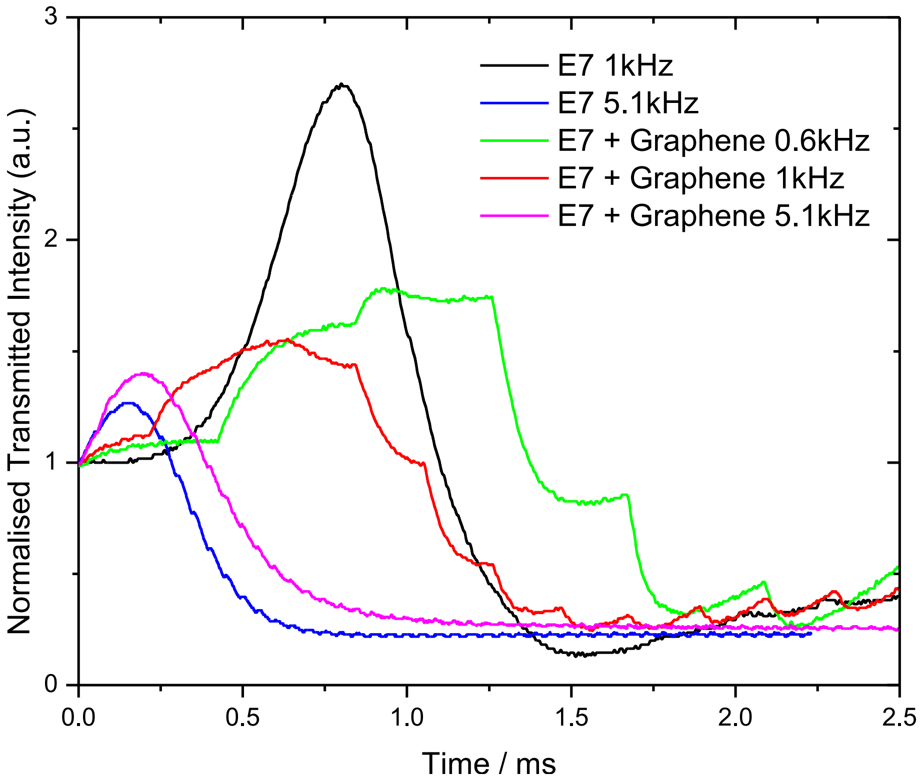

Figure 4.3*: Frequency dependence of the 'on' switching times for the liquid crystal cells: containing liquid crystal E7 switched at 1kHz (black); containing liquid crystal E7 switched at 5.1kHz (blue); containing liquid crystal E7 with dispersed graphene switched at 0.6kHz (green); containing liquid crystal E7 with dispersed graphene switched at 1kHz (red); and containing liquid crystal E7 with dispersed graphene switched at 5.1kHz (magenta). Switching times are found from the change in the normalised transmitted intensity as a function of time, under the application of a voltage to the liquid crystal cell.*

One should also note the significantly different form of the 'on' response curve for the sample containing E7 with dispersed graphene particles. The conductive nature of graphene, as compared to the semiconductor or insulator nature of the other 2D materials used, causes the formation of 'hotspots' of switching activity within the liquid crystal due to the stronger electric field in the vicinity of the graphene particles. This can be observed when monitoring the cell under cross-polarised optical microscopy during the switching, where switching is observed to initiate first in the areas around the particles. This leads to localised switching at a faster rate than the switching of the cell as a whole, and hence to the perturbations observed in the switching curve. It is notable that these perturbations only appear in the 'on' curve – evidencing that they relate purely to the material's response to the electric field. By increasing or decreasing the electric field frequency, one can observe either amplification (when decreasing the frequency) or suppression (when increasing) of this effect (Fig. 4.3). It is particularly of note that when decreasing the frequency, there is a significant increase in the 'on' time for the switching. There is no effect on the off times for the switching (Fig. 4.4). The switching times recorded are also given in Table 4.1.

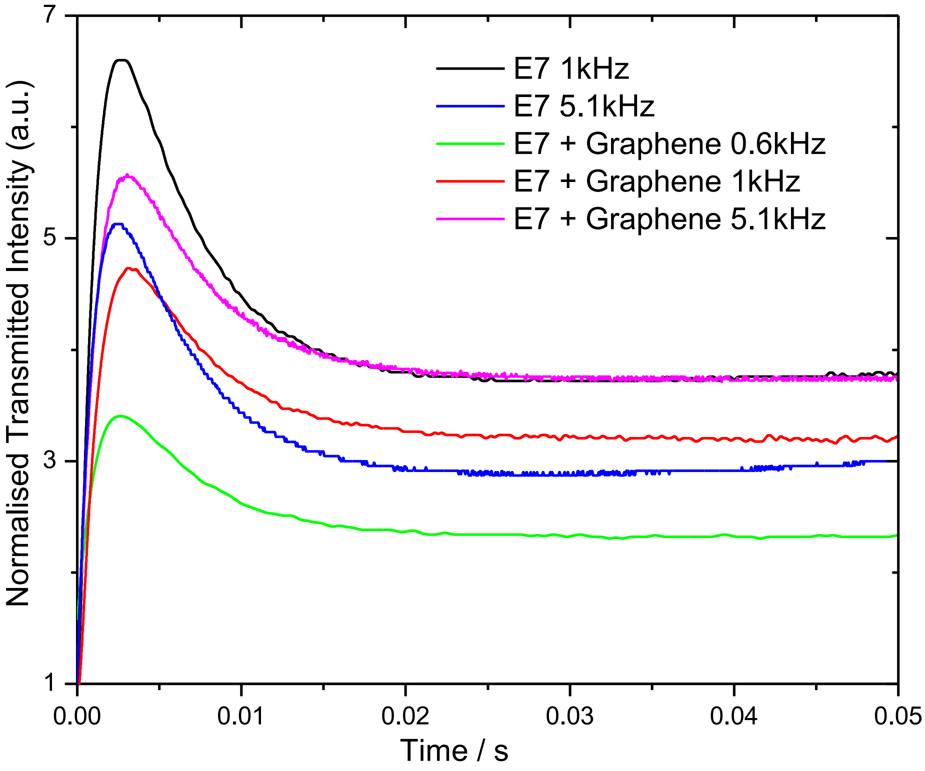

***Figure 4.4**: Frequency dependence of the 'off' switching times for the liquid crystal cells: containing liquid crystal E7 switched at 1kHz (black); containing liquid crystal E7 switched at 5.1kHz (blue); containing liquid crystal E7 with dispersed graphene switched at 0.6kHz (green); containing liquid crystal E7 with dispersed graphene switched at 1kHz (red); and containing liquid crystal E7 with dispersed graphene switched at 5.1kHz (magenta). Switching times are found from the change in the normalised transmitted intensity as a function of time, after the removal of a voltage applied to the liquid crystal cell.*

One can therefore conclude that the addition of 2D materials to the liquid crystal has a negative impact on the switching time of devices. Furthermore, when using conductive 2D materials, the operating frequency of devices should be higher to mitigate effects of localised electric field responses.

Threshold voltage measurements.

Furthermore, analysis of the threshold voltage at which the switching of the liquid crystal is initiated was undertaken. Typically, lower values of the threshold voltage are desirable in order to minimise the energy requirements for switching a device. Again let us consider the transmission through the liquid crystal cell of a broadband white light source. The intensity of the transmitted light as a function of the applied voltage (Fig. 4.5) was measured. The electric field was again applied with a frequency of 1 kHz. The temperature of the liquid crystal cell was maintained at 30.00±0.05°C throughout for all samples. All data are normalised such that the transmission is 1 when no voltage is applied. The extracted threshold voltages, and other parameters, are summarised in Table 4.2.

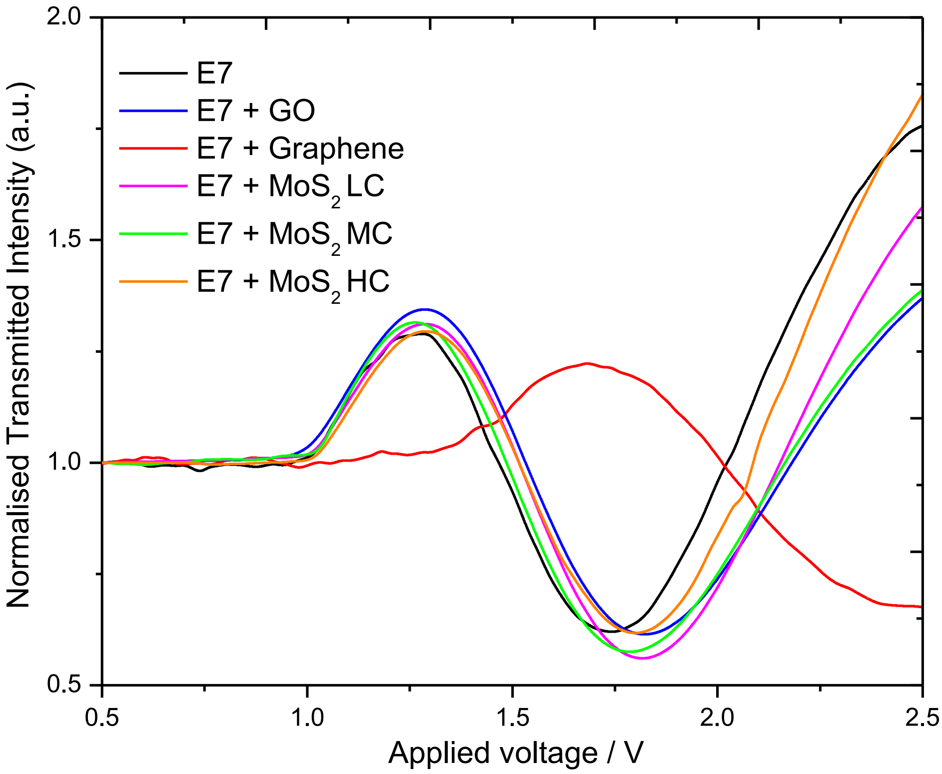

***Figure 4.5**: Normalised transmitted intensity dependence on the applied voltage for the liquid crystal cells containing: liquid crystal E7 (black); E7 with dispersed graphene oxide (blue); E7 with dispersed graphene (red); E7 with dispersed molybdenum disulfide at a low concentration (magenta); E7 with dispersed molybdenum disulfide at a medium concentration (green); and E7 with dispersed molybdenum disulfide at a high concentration (orange). Threshold voltages are established from the point at which a change in the transmitted intensity is recorded.*

***Table 4.2:** Summary of the recorded threshold voltages for switching, and the voltages required to obtain the first maxima and minima in the normalised transmitted intensity.*

Sample	**Threshold voltage / V**	**Voltage at first transmitted intensity maximum / V**	**Voltage at first transmitted intensity minimum / V**
E7	1.02 ± 0.02	1.28 ± 0.02	1.74 ± 0.02
E7 + MoS_2 LC	1.02 ± 0.02	1.3 ± 0.02	1.82 ± 0.02
E7 + MoS_2 MC	1.02 ± 0.02	1.28 ± 0.02	1.78 ± 0.02
E7 + MoS_2 HC	1 ± 0.02	1.3 ± 0.02	1.8 ± 0.02
E7 + Graphene	1.36 ± 0.05	1.68 ± 0.02	2.5 ± 0.02
E7 + GO	0.96 ± 0.02	1.3 ± 0.02	1.82 ± 0.02

There is little effect on the threshold voltage at which switching begins for the samples containing either graphene oxide or MoS_1. However, when looking at the value for the sample containing graphene, one sees a marked shift to higher voltage (an increase of 33%). When one looks at the positions of the maxima one can see little difference for any of the samples, again with the exception of that containing graphene. However, when looking at the voltage at which the minimum value of the transmitted intensity is obtained (i.e. the point at which the cell can be considered fully switched) one can see a slight shift to higher voltage for all samples relative to the pure liquid crystal. By the point of the minimum, the increase in the voltage required for the graphene sample relative to the pure liquid crystal is 43%. The large difference for the sample with graphene can again be related to the conductivity of the dispersed nanoparticles. Essentially, the conductive graphene particles can be considered to 'short-circuit' the capacitive structure of the liquid crystal cell.

In terms of threshold voltages, much like with switching times, one can again conclude that the addition of 2D materials to the liquid crystal has a negative impact on the performance.

Critical temperature measurements.

The critical temperature at which the liquid crystal changes from the nematic phase to an isotropic phase was also analysed. In general, a higher critical temperature is desirable as it extends the operational window of devices. Again, let us consider the transmission through the liquid crystal cell of a broadband white light source. The intensity of the transmitted light as a function of the liquid crystal cell temperature was measured. In this case, no electric field was applied. The transmitted intensity was measured as the temperature was first increased until the transition occurred and the

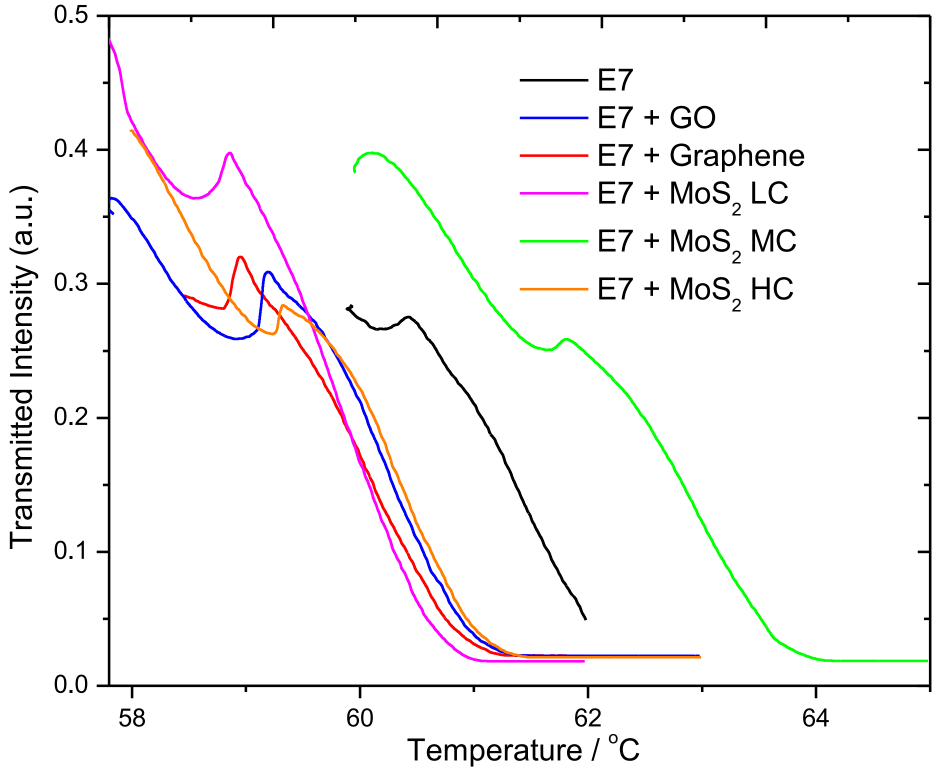

Figure 4.6*: Transmitted intensity dependence on the (increasing) temperature of the liquid crystal cells containing: liquid crystal E7 (black); E7 with dispersed graphene oxide (blue); E7 with dispersed graphene (red); E7 with dispersed molybdenum disulfide at a low concentration (magenta); E7 with dispersed molybdenum disulfide at a medium concentration (green); and E7 with dispersed molybdenum disulfide at a high concentration (orange). Transition temperatures can be extracted from the curves.*

transmission subsequently reached a steady state value, and then again as the temperature was decreased back through the transition to an approximately steady value. Observing the curves as the temperature was increased, a kink in the curve – corresponding to the transition – is seen. As the temperature is increased (Fig. 4.6), one can see a decrease in the transmitted intensity down to a minimum. One then observes an increase to a maximum, before a further decrease until an equilibrium is reached. One can then extract the values of the minimum corresponding to the point at which the transition begins, the maximum during the transition, and the end point at which a steady state transmission is obtained (Table 4.3). The temperature at which the first minimum is found is that of the onset of the phase transition. The final equilibrium value represents the end of the phase transition.

Table 4.3: *Summary of the transition temperatures and ranges, and the temperatures at which other features of interest occur, in the transmitted intensity of light through liquid crystal cells containing E7 with dispersed 2D materials as the temperature is increased.*

Sample	**Temperature increasing**				
	First transmitted intensity minimum / °C	**Transmitted intensity maximum / °C**	**Transmitted intensity at equilibrium / °C**	**First minimum to maximum / °C**	**Transition range / °C**
E7	60.16 ± 0.05	60.4 ± 0.05	62.3 ± 0.3	0.24 ± 0.05	2.14 ± 0.35
E7 + MoS_2 LC	58.54 ± 0.05	58.87 ± 0.05	61.09 ± 0.05	0.33 ± 0.05	2.55 ± 0.05
E7 + MoS_2 MC	61.65 ± 0.05	61.81 ± 0.05	64.08 ± 0.05	0.16 ± 0.05	2.43 ± 0.05
E7 + MoS_2 HC	59.24 ± 0.05	59.33 ± 0.05	61.46 ± 0.05	0.09 ± 0.05	2.22 ± 0.05
E7 + Graphene	58.81 ± 0.05	58.96 ± 0.05	61.3 ± 0.05	0.15 ± 0.05	2.49 ± 0.05
E7 + GO	58.93 ± 0.05	59.21 ± 0.05	61.38 ± 0.05	0.28 ± 0.05	2.45 ± 0.05

Observing the curves as the temperature was decreased (Fig. 4.7), one can extract values for the temperature at the onset of the transition, at the point of maximum transmission during the transition, and at the end of the transition (Table 4.4).

Comparing the values, one can observe that in general the samples containing the dispersed 2D materials perform worse than the pure liquid crystal, showing lower critical temperatures. The

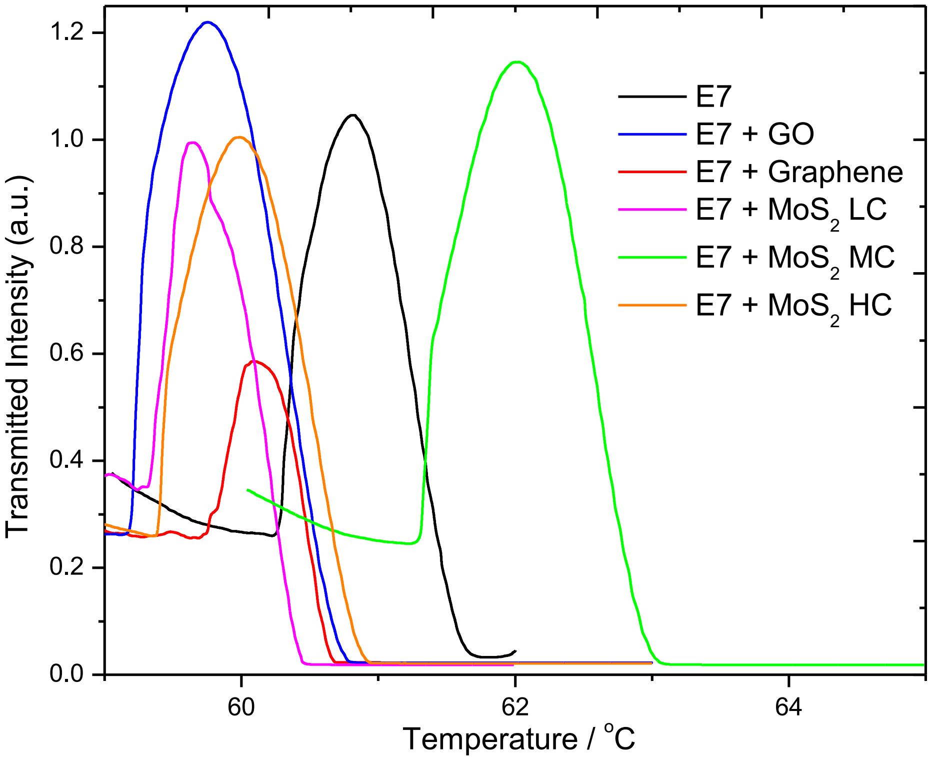

Figure 4.7: *Transmitted intensity dependence on the (decreasing) temperature of the liquid crystal cells containing: liquid crystal E7 (black); E7 with dispersed graphene oxide (blue); E7 with dispersed graphene (red); E7 with dispersed molybdenum disulfide at a low concentration (magenta); E7 with dispersed molybdenum disulfide at a medium concentration (green); and E7 with dispersed molybdenum disulfide at a high concentration (orange). Transition temperatures can be extracted from the curves.*

Table 4.4: *Summary of the transition temperatures and ranges, and the temperatures at which other features of interest occur, in the transmitted intensity of light through liquid crystal cells containing E7 with dispersed 2D materials as the temperature is decreased.*

Sample	Temperature decreasing					
	Transition onset / °C	**Transition end / °C**	**Maximum transmitted intensity / °C**	**Transition range / °C**	**Onset to maximum transmitted intensity / °C**	**Maximum intensity to transition end / °C**
E7	61.67 ± 0.05	60.23 ± 0.05	60.81 ± 0.05	1.44 ± 0.05	0.86 ± 0.05	0.58 ± 0.05
E7 + MoS_2 LC	60.48 ± 0.05	59.31 ± 0.05	59.66 ± 0.05	1.17 ± 0.05	0.82 ± 0.05	0.35 ± 0.05
E7 + MoS_2 MC	63.09 ± 0.05	61.28 ± 0.05	62.03 ± 0.05	1.81 ± 0.05	1.06 ± 0.05	0.75 ± 0.05
E7 + MoS_2 HC	60.95 ± 0.05	59.37 ± 0.05	59.99 ± 0.05	1.58 ± 0.05	0.96 ± 0.05	0.62 ± 0.05
E7 + Graphene	60.69 ± 0.05	59.68 ± 0.05	60.12 ± 0.05	1.01 ± 0.05	0.57 ± 0.05	0.44 ± 0.05
E7 + GO	60.8 ± 0.05	59.14 ± 0.05	59.77 ± 0.05	1.66 ± 0.05	1.03 ± 0.05	0.63 ± 0.05

exception is the sample containing a medium concentration of MoS_2 which showed higher critical temperature. Further work is required to understand precisely what causes that higher critical temperature for that particular sample. For the samples showing lower critical temperature, the difference can be justified as the nanoparticles perturb the liquid crystal structure and act as nucleation points for the phase transition.

Dichroism measurements.

Initial measurements of the circular dichroism of liquid crystals containing dispersed 2D materials showed some potentially interesting results. CD spectra were measured using a JASCO 815 dichroism spectrometer. Two samples were measured, the first containing MoS_2 dispersed in liquid crystal E7, and the second containing GO dispersed in liquid crystal MLC 6608. The CD spectra for the two composites were compared to those for the pure liquid crystal. MLC 6608 shows broad band circular dichroism throughout the visible range, however the sample containing dispersed GO showed no circular dichroism (Fig. 4.8a), suggesting that the dispersed particles quench the optical activity of the liquid crystal. E7 presents a more complex, but less intense, CD spectrum. However, the addition of the MoS_2 particles in this case lead to a strong enhancement of the circular dichroism signal (Fig. 4.8a). One suggestion here was that the increased CD intensity may be due to LD 'leaking' into the CD spectrum. However, an analysis of the LD showed that it was in fact less intense for the sample containing the nanoparticles as opposed to that for the pure liquid crystal (Fig. 4.8b).

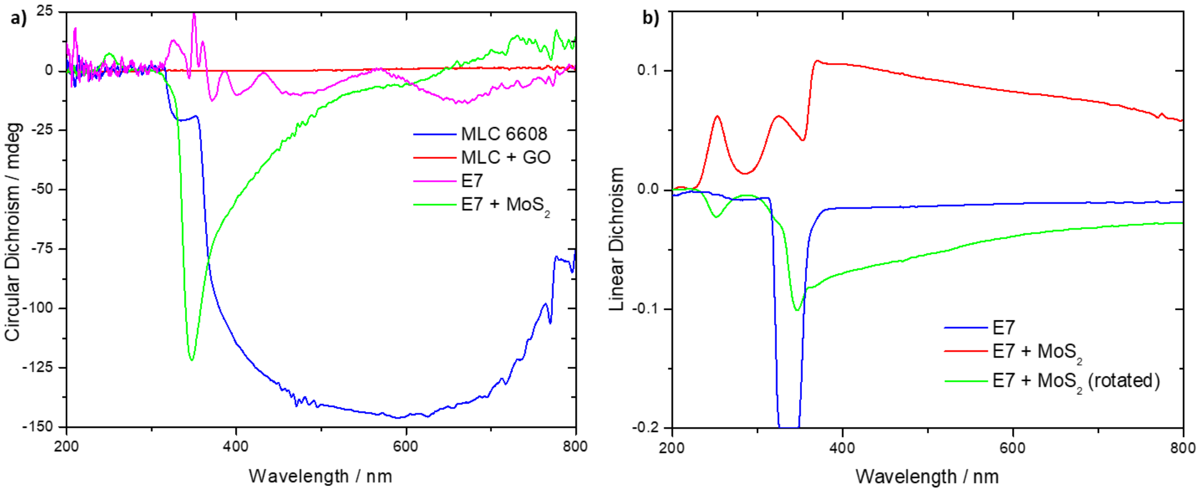

***Figure 4.8**: **a)** The circular dichroism spectra for: liquid crystal MLC 6608 (blue); liquid crystal MLC 6608 with dispersed graphene oxide particles (red); liquid crystal E7 (magenta); and E7 with dispersed MoS_2 particles. **b)** The linear dichroism spectra for: liquid crystal E7 (blue); E7 with dispersed MoS_2 particles (red); and the same sample of E7 with dispersed MoS_2 particles, but with the cuvette rotated through 90° to account for any change in the liquid crystal alignment (green).*

Further measurements were carried out using a different system where the linear and circular dichroism could be recorded simultaneously. In this case, a wider range of samples were used. The possible effect of nanoparticle concentration was also considered here.

First to be considered were WS_2 nanoparticles dispersed in liquid crystal E7 at concentrations of approximately 0.01, 0.1, 1 and 10 mg.mL^{-1}. Both the circular (Fig. 4.9a) and linear dichroism (Fig. 4.9b) were measured. However, almost no difference was observed between the spectra with dispersed nanoparticles and the spectrum of the pure liquid crystal. One can ignore the disparity in the magnitude of both the CD and LD signals between samples – there are many experimental factors that could lead to this. The absolute intensities of the peaks do vary, but there is no clear dependence on the concentration, suggesting that the intensity is varying due to some experimental parameter (likely to be the thickness of the liquid crystal layer) rather than due to the optical properties of the material itself. Rather, the interest is found in the form of the spectra and the positions of any features in the spectra. Where differences are observed, there is no clear correlation with the changing concentration of the nanoparticles. The peak positions and magnitudes taken from the circular and

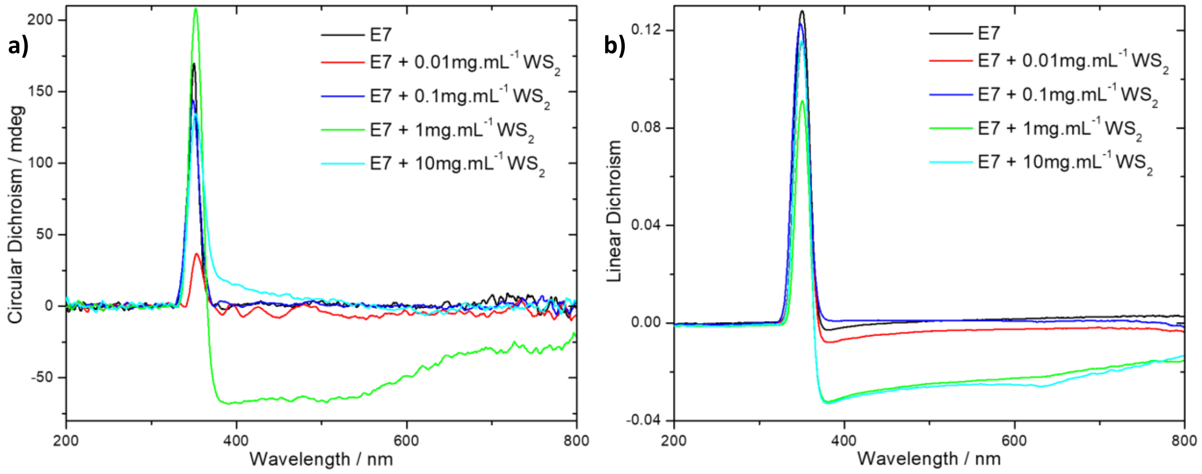

***Figure 4.9**: **a)** The circular dichroism spectra for liquid crystal E7 with tungsten disulfide particles dispersed at different concentrations. **b)** The linear dichroism spectra for liquid crystal E7 with tungsten disulfide particles dispersed at different concentrations.*

***Table 4.5:** Summary of the peak positions and magnitudes for the circular dichroism and linear dichroism spectra of the pure liquid crystal E7, and E7 with tungsten disulfide particles dispersed at different concentrations. In some cases repeat measurements are shown for the same concentration.*

Sample		Circular Dichroism		Linear Dichroism	
Material dispersed	**Concentration / mg.mL^{-1}**	**Peak position / nm**	**Peak magnitude / mdeg**	**Peak position / nm**	**Peak magnitude**
E7 only	N/A	349	240	336	0.0169
		350	150.6	348	0.0596
		350	171.2	350	0.1282
		350	211	350	0.1329
		347	197.4	347	0.131
		345	154.4	345	0.1243
		344	157.4	344	0.1235
Tungsten disulfide	0.01	353	37.02	350	0.1155
	0.1	349	144.3	348	0.1227
	1	352	208.8	350	0.0912
	10	352	135	350	0.1157

linear dichroism spectra, for the pure liquid crystal E7 and for E7 with WS_2 dispersed at different concentrations, are summarised in Table 4.5.

Next to be considered was MoS_2 dispersed in E7, the combination which had previously produced interesting results, at concentrations of 0.01, 0.05, 0.1, 0.5, 1, 5 and 10 mg.mL^{-1}. Again no difference in the shape of the spectra is observed for either the LD or CD (Fig. 4.10). The peak positions

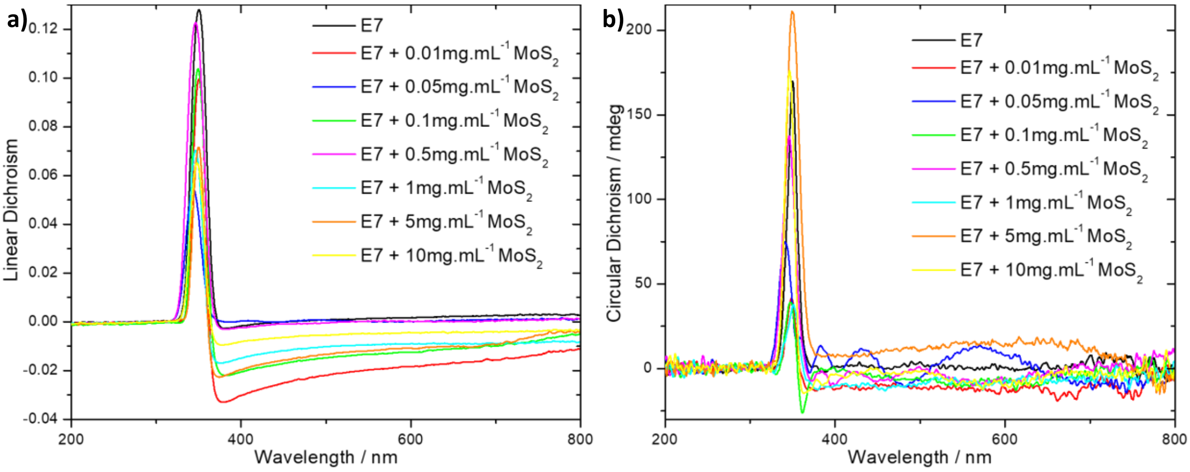

***Figure 4.10**: **a)** The linear dichroism spectra for liquid crystal E7 with molybdenum disulfide particles dispersed at different concentrations. **b)** The circular dichroism spectra for liquid crystal E7 with molybdenum disulfide particles dispersed at different concentrations.*

***Table 4.6:** Summary of the peak positions and magnitudes for the circular dichroism and linear dichroism spectra of E7 with molybdenum disulfide particles dispersed at different concentrations. In some cases repeat measurements are shown for the same concentration. Where two values are given for the peak, two peaks were observed in close proximity and of similar magnitude.*

Sample		Circular Dichroism		Linear Dichroism	
Material dispersed	**Concentration / mg.mL^{-1}**	**Peak position / nm**	**Peak magnitude / mdeg**	**Peak position / nm**	**Peak magnitude**
Molybdenum disulfide	0.01	343 / 357	44.65 / 24.38	352	0.0525
		345	204.8	352	0.0599
		349	41.76	350	0.0999
		347	26.96	350	0.0065
		345	36.65	352	0.0303
	0.05	348	140.6	349	0.1131
		342	68.02	346	0.0664
		341	75.15	343	0.0545
	0.1	342 / 355	23.23 / 52.71	349	0.1014
		347	103.3	348	0.0306
		347	39.3	349	0.1041
	0.5	348	110	352	0.0559
		346	80.77	345	0.065
		348	179.4	349	0.1301
		346	138.2	346	0.1229
	1	348	158.9	350	0.0933
		343	70.1	341	0.0054
		351	38.17	349	0.1135
		346	148.4	346	0.0705
	5	345	157.2	350	0.0719
		340	89.32	338	0.021
		349	211.3	361	0.0087
	10	351	114.6	351	0.1058
		349	93	349	0.0765
		347	176.6	350	0.1132
		343	122.5	348	0.0654
		342	109.6	347	0.0468

and magnitudes taken from the circular and linear dichroism spectra for E7 with MoS_2 dispersed at different concentrations are summarised in Table 4.6.

Finally, consideration was given to dispersions of GO in E7 at concentrations of 0.01, 0.05, 0.1, 0.5, 1, 5 and 10 mg.mL^{-1}. Again, no difference in the shape of the spectra is observed for either the LD or CD (Fig. 4.11). The peak positions and magnitudes taken from the circular and linear dichroism spectra for E7 with GO dispersed at different concentrations are summarised in Table 4.7.

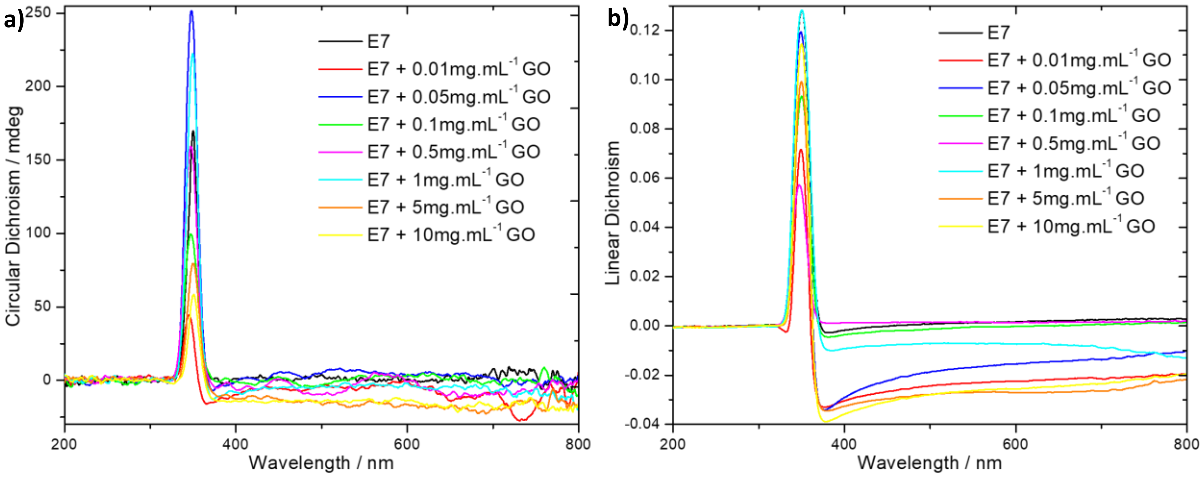

***Figure 4.11**: **a)** The circular dichroism spectra for liquid crystal E7 with graphene oxide particles dispersed at different concentrations. **b)** The linear dichroism spectra for liquid crystal E7 with graphene oxide particles dispersed at different concentrations.*

***Table 4.7:** Summary of the peak positions and magnitudes for the circular dichroism and linear dichroism spectra of E7 with graphene oxide particles dispersed at different concentrations. In some cases repeat measurements are shown for the same concentration.*

Sample		Circular Dichroism		Linear Dichroism	
Material dispersed	**Concentration / mg.mL^{-1}**	**Peak position / nm**	**Peak magnitude / mdeg**	**Peak position / nm**	**Peak magnitude**
Graphene oxide	0.01	350	150.6	348	0.0596
	0.05	372	13.84	350	0.0547
		348	252.3	349	0.1196
	0.1	347	99.75	350	0.0935
	0.5	364	160.4	352	0.0678
		347	159.5	347	0.0573
	1	349	22.7	350	0.1284
	5	350	79.62	350	0.0994
	10	351	58.63	350	114.7

It should be noted that there was a potentially key difference between the experimental setup for the initial measurements compared to the later measurements. In the initial measurements, a well-defined 100 µm path length cuvette (consisting of a glass cover plate held over an etched reservoir on a slide) was used to contain the LC, whereas in the later measurements the LC was simply placed on the surface of a slide. Therefore, in the later measurements the path length was likely to be much larger, and also to vary between samples. As the data gathered from each system is conflicting, further experiments are required to determine the true effect of the nanoparticle inclusion on the linear and circular dichroism of the liquid crystal.

Conclusions.

From the results gained, it is clear that the inclusion of 2D materials in a conventional nematic liquid crystal host either negatively or negligibly impacts the performance of the liquid crystal. Switching times are found to be slower, threshold voltages more or less unchanged, nematic-isotropic transition temperatures to be lower, and the linear and circular dichroism to be inconclusively impacted. This limits the potential applications of the materials. Particularly damaging is the slower switching time – modern technology increasingly demands faster operation of devices. Significant further work would be needed to mitigate the negative impacts of the inclusion of the 2D materials.

4.2 Tungsten disulfide liquid crystals.

The first observation of liquid crystalline dispersions of liquid phase-exfoliated tungsten disulfide flakes is reported in a range of organic solvents. The liquid crystals demonstrate significant birefringence as observed in the linear and circular dichroism measurements respectively. In particular, linear dichroism is observed throughout the visible range while broad-band circular dichroism can be observed in the range from 500 – 800 *nm*. Under an applied magnetic field of ±1.5T the circular dichroism can be switched ON/OFF, while the wavelength range for switching can be tuned from large to narrow range by the appropriate selection of the host solvent. In combination with the photoluminescence capabilities of WS_2, this opens a pathway to a wide variety of applications, such as deposition of highly uniform films over large areas for photovoltaic and terahertz devices.

Introduction.

Two-dimensional (2D) material-based liquid crystals with dynamically tunable properties are currently emerging as a promising- and desirable- class of novel functional materials, owing to the diverse properties that they can possess[9,17,101]. By producing liquid crystals based on 2D materials, structural reconfigurability with associated tailoring of properties has recently been achieved[5,6,25,66,123,157]. However, until now, such lyotropic (and typically nematic) liquid crystal phases[101] have been reported predominantly for graphene oxide dispersions[11,114,116,121,130,133,140] with some limited reports for carbon allotropes such as graphene[6,137,158] and carbon nanotubes[123] as well as for one transition metal dichalcogenide (TMDC), molybdenum disulfide[66]. The possibility of liquid crystalline states in dispersions of 2D materials owes to their intrinsic shape anisotropy. It has long been known (from theory described by Onsager in the 1940s) that both rigid and flexible anisotropic molecules or particles undergo an isotropic/liquid-crystalline transition as their concentration is raised[159], forming a lyotropic liquid crystal (LC). The main condition for this phase to be observed is that a significant anisotropy of the mesogens must exist; i.e. a large aspect ratio. This transition was initially observed with clay particles and variations on Onsager theory used to determine the phase diagram[117,160].

Comparing existing examples of liquid crystals based on two-dimensional materials to the breadth of such materials known, one can immediately see the limitations of the range of materials explored; while there are in excess of 1000 known exfoliatable two-dimensional materials[161], there are only liquid crystalline dispersions known for three of them[6,66,114]. Of significant intrigue are reports that such liquid crystalline phases can also show chirality[98,158] as reconfigurable chiral materials are in strong demand for photonics applications[162,163]. One of the most desirable methods for chiral material reconfiguration is magnetic tuning, due to the possibility for either *in-* or *ex-situ* switching with favourable power requirements[164,165].

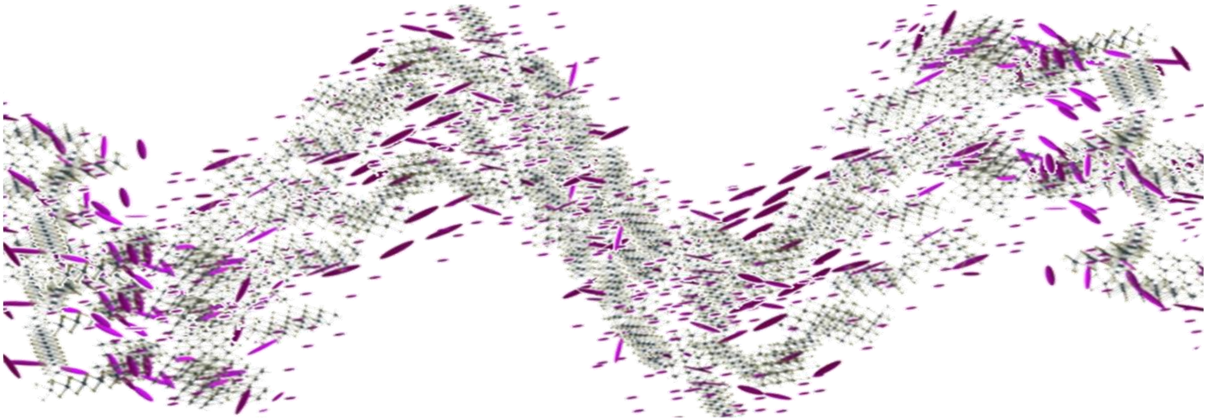

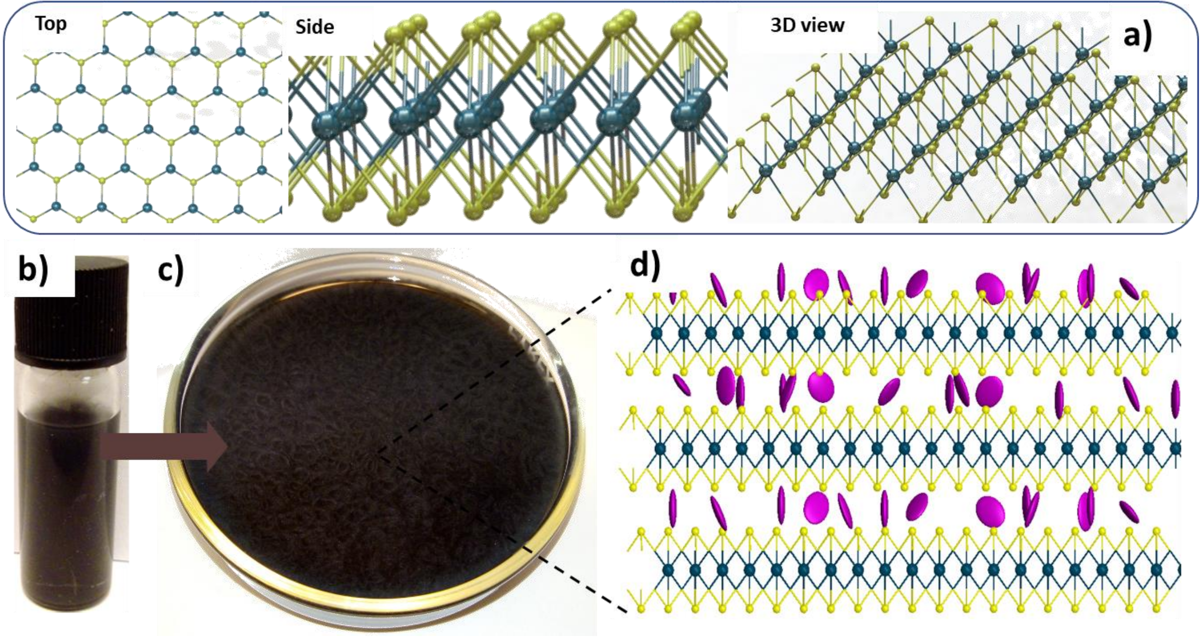

Figure 4.12: *Schematic representations of liquid crystalline dispersions of tungsten disulfide.* ***a)*** *Top, side and 3D views of the bonding structure of tungsten disulfide. Tungsten atoms are represented in blue and sulfur in yellow.* ***b-c)*** *Vial and Petri dish containing a tungsten disulfide dispersion in solvent.* ***d)*** *Liquid crystalline assembly of monolayers of tungsten disulfide, separated by intercalating solvent molecules (purple), retaining crystalline ordering between sheets.*

Of particular interest, tungsten disulfide (Fig 4.12a) is a TMD with significant potential for applications in a variety of areas. Its various exciting properties have led to widescale integration of WS_2 in heterostructures and junctions[7,166–169] amongst other applications such as field effect transistors[168], hydrogen evolution[170], saturable absorbers[171], supercapacitors[169] and battery anodes[172]. In particular, strong room temperature photoluminescence makes it an ideal candidate for applications in solar power[166,173], for instance, while second harmonic generation allows use in non-linear photonic devices[7].

Herein, a demonstration is presented- for the first time- of the possibility of a liquid crystalline phase of dispersions of WS_2 particles (Fig.4.12b-d) in a variety of solvents. Of particular interest is the emergence under applied magnetic field, or without applied field, of circular dichroism of dispersions in particular solvents. This observation is particularly unexpected due to the achiral nature of both WS_2 and the solvents used. As such it is demonstrated that a material with reconfigurable circular dichroism that can be readily integrated or applied within photonic and optoelectronic devices by a variety of different means.

Synthesis of liquid crystalline samples.

Starting from bulk WS_2 particles (Sigma-Aldrich 243639), with dimensions around five microns on average (maximum particle dimensions were observed to be on the order of 10-15 μm), dispersions were produced in a range of solvents (water, isopropanol, chloroform, tetrahydrofuran, methanol, acetone and ethanol), with a range of concentrations (from $0.1 mg.mL^{-1}$ to $5 mg.mL^{-1}$). To accurately compare the effect of different solvents, it was necessary to have homogeneous particle size distributions between samples. Hence, an initial 500 *mL* dispersion was prepared, with IPA as the solvent, at a concentration of 5 $mg.mL^{-1}$, in a sealed beaker.

To break down the material a process of ultrasonication in an ultrasonic bath (James Products 120W High Power 2790ml Ultrasonic Cleaner) filled with deionised water was used. Five, hour-long, periods, separated by 30 minutes each to prevent excessive heating of the solvent, were used to ensure sufficient exfoliation of the sample. The resultant dispersions were then put through a process of centrifugation for 10 minutes at 2000 *rpm* to residual bulk material and narrow the distribution of particle sizes present in the dispersion.

After centrifugation, the dispersion was fractioned, with only the supernatant extracted, to ensure only suitably sized particles remained. The resultant dispersion was then dried under vacuum

(~0.1 *atm*) in a Schlenk line to fully remove the solvent, before being re-dispersed in the required solvents for the final dispersions.

Redispersion involved transfer of a suitable mass of the exfoliated tungsten disulfide to give the desired concentration into small volumes (<5 *mL*) of IPA, chloroform and THF. After re-dispersion, the dispersions were again ultrasonicated (for a few minutes) to prevent any aggregated exfoliated particles remaining in the dispersions. As the concentration is changed significantly following the centrifugation step, it is necessary to re-establish the concentration following that step. The re-dispersion process allowed for accurate knowledge of the concentrations of the dispersions. Additionally, as all steps up until redispersion were the same for all samples, the size distribution of particles in the dispersion is as uniform as possible between samples. It is known from the extensive literature[76,174,175] on liquid phase exfoliation of 2D materials that both the solvent and concentration can have significant effects on the yield and size distribution obtained. Hence, the process used here offers the significant advantage of allowing direct comparability between dispersions, to the greatest degree achievable.

Samples dispersed in other solvents (e.g. water, ethanol etc.) were produced by the same methods, but using a different initial dispersion. Hence, direct comparability cannot be claimed. However, these samples did not display any indications of liquid crystallinity.

Analysis of WS_2 particle sizes was undertaken by five separate methods:

1) Optical microscopy
2) Raman spectroscopy
3) Dynamic light scattering (DLS)
4) Scanning electron microscopy (SEM)
5) Atomic force microscopy (AFM)

Synthesis of unexfoliated samples.

The unused fraction from the synthesis of the LC samples was used to produce the unexfoliated samples. This fraction was dried and redispersed using the same process as described for the exfoliated fraction that gave the better liquid crystallinity. These samples were used in order to analyse the effect of the particle aspect ratio on the dichroism results given later. While they are denoted as "unexfoliated", some exfoliation from the bulk had still occurred during ultrasonication. However, the degree of exfoliation was less than that for the liquid crystalline samples described before, hence the separation of the particles under centrifugation. They are labelled as unexfoliated whenever referred to later herein, in order to simplify and be consistent with nomenclature.

Synthesis of non-LC samples.

Non-LC samples were produced to compare the films producible using the LC state to those given without it in later work. The same tungsten disulfide powder was dispersed at a concentration of 5 $mg.mL^{-1}$ in IPA. This dispersion was then ultrasonicated for 2 minutes to ensure dispersion with minimal exfoliation. No optical anisotropy was observable in the dispersions. They are labelled as non-LC whenever referred to later herein, in order to simplify and be consistent with nomenclature.

Particle size analysis by optical microscopy.

Using optical microscopy, it was determined that 'unexfoliated' particles dispersed in chloroform had typical sizes of 1-10µm, with the mean size around 5µm x 5µm and that exfoliated particles had typical dimensions of around 500nm up to a few microns in length and width with mean size around 2µm x 2µm. This characterisation also revealed the presence of occasional much larger particles with bulk like characteristics, and some particles <500nm in length or width.

Particle size analysis by Raman spectroscopy.

One can extract the thickness of a tungsten disulfide particle by comparing the intensities of the E_{2g} and A_{1g} peaks and their corresponding shift frequencies[176–178]. This method involves taking the ratio of the intensities of the two peaks, and the separation of the two in terms of wavenumber. Both the relative peak intensities and the positions of the two peaks are known to vary as a function of the number of layers, due to the effect of interlayer forces. The most profound difference is observed when comparing bulk and monolayer material. As more layers are added, starting from monolayer, the positions and relative intensities converge on those of the bulk material. Hence, if one has a Raman spectrum for a tungsten disulfide particle, one can first extract the positions and intensities of the two peaks. From this, the difference in the peak positions can be calculated. The ratio of the peak intensities can also be calculated. These two values can then be compared to literature values which have been both calculated *ab-initio* and corroborated by experiment for different layer thicknesses[176–178]. The available data in the literature means that only numbers of layers from one to six can be differentiated accurately from bulk material. For unexfoliated particles dispersed in chloroform, thickness was determined to be predominantly bulk-like from Raman spectroscopy. Determination of any shape anisotropy was not possible with Raman spectroscopy for which accurate determination of thickness is limited beyond ~6 layers, so in essence it is determined that the particles are in excess of six layers, but no more accurate value can be obtained by this method.

Exfoliated particles dispersed in chloroform had typical thicknesses of 1-6 layers as observed in Raman measurements again by comparing the intensities of the E_{2g} and A_{1g} peaks and their corresponding shift frequencies[176–178]. However, characterisation also revealed the presence of occasional much larger particles with bulk like characteristics.

Particle size analysis by dynamic light scattering.

Dynamic light scattering (DLS) measurements were performed to analyse the particle sizes in the dispersion, in addition to microscopy and Raman spectroscopy of individual drop-cast flakes. For example, for the dispersion in chloroform (Fig. 4.13as), broad peaks of scattered intensity were observed at four different particle sizes: 3.98 *nm*; 93.9 *nm*; 320 *nm*; 1610 *nm*. However, quantitative analysis (Fig. 4.13b) of the numbers of particles possessing each size measured suggests that the particles are predominantly of around 3.98 nm, with some measuring around 94 nm. Conventionally, the number as given would be considered, however there is an expectation that there should certainly be larger particles. SEM and AFM data presented later suggest that there are indeed larger particles. SEM and AFM, as direct imaging and analysis methods, are known to be accurate and therefore the results from DLS should be considered in that light. If we look at the number of particles of each size determined by DLS, there is no corroboration by other methods – it can therefore be considered inaccurate. However, sizes found from measured intensity in the DLS were in agreement with those obtained by the other methods, and therefore warrant further inspection despite being a non-conventional method of size determination. In Fig. 4.13a, the first peak is indicative of flakes on the order of few-layer thickness being present in the dispersion. The last peak is in agreement with the

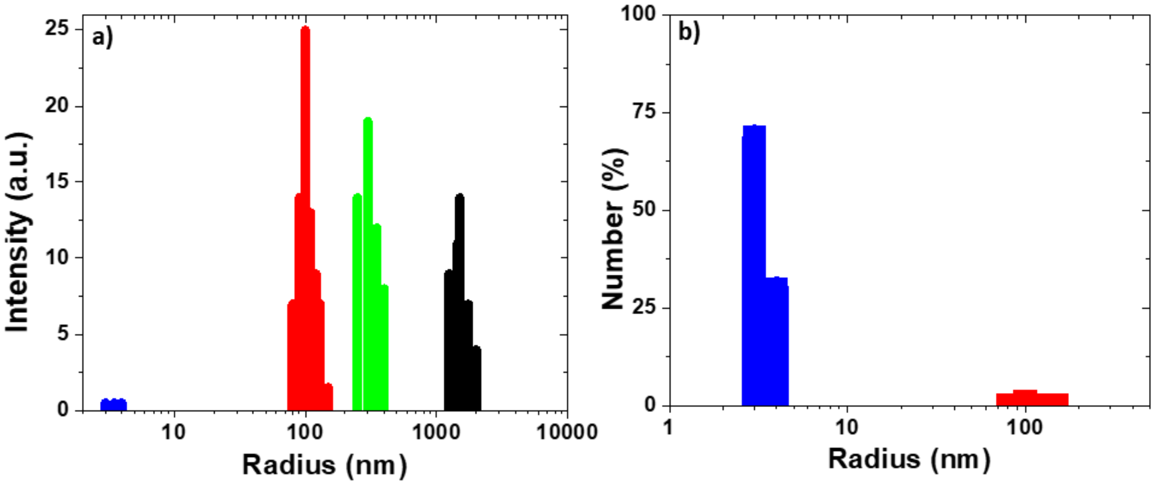

average flake lateral sizes being on the order of a micron. The other two peaks are consistent with the flakes <500 *nm* that were also observed.

With these results in mind, one can note from the literature[179] that DLS has been used previously to accurately establish the lateral particle sizes in solution and has been verified against other characterisation methods. The accurate determination thickness however has never been reported. However, it can be suggested that it should be possible to accurately obtain both the thickness and lateral sizes of the particles, provided that the orientation of the particles can be fixed. Typically, particles dispersed in a liquid will have random orientations and move and change orientation randomly due to Brownian motion. However, the key property of lyotropic liquid crystalline phases is that the orientation of the dispersed particles is not random, but generally aligned along a director. Domains will then exist with the dispersion with different directors. Of course, the different directors for different domains mean that when considering a large volume of the dispersion, there is no overall average director, but rather the orientation of the particles is still effectively random. However, it is also well-known that interfaces between liquid crystals and other materials can cause preferential alignment of the director due to anchoring of the mesogens at the surface; this being a key concept in their use in liquid crystal displays. In this case, if the tungsten disulfide particles in the LC state align at the interface with the cuvette used for DLS measurements, with a director either parallel or perpendicular to the interface, then the scattering cross-section for those particles is fixed, non-random, and suitably aligned relative to the incoming light. Hence it would be possible to obtain the thickness and lateral sizes of the particles. It is suggested that this alignment occurs during these measurements, allowing the accurate determination of the sizes that has been observed, as verified by other methods.

Particle size analysis by scanning electron microscopy.

SEM was also used. Particles were drop-cast onto a silicon-on-insulator substrate and then imaged (Fig. 4.14). From the images produced, the size of the particles present was analysed, with over 400 individual particles measured. A range of particle sizes from 508 *nm* up to 11.06 *µm* was observed. The mean lateral particle size was determined to be 2.61 *µm*, while the mode of the particle size distribution was determined as 1.63 *µm* and the median value was 2.34 *µm*. This is in close agreement with the 1610 *nm* peak seen in the DLS spectrum, particularly when considering that the peak value reported in the DLS spectrum would correspond to the modal value. It was also noticed that there were some significantly smaller particles (<500 *nm*), which are likely responsible for the DLS peaks at 93.9 *nm* and 320 *nm*. These particles were excluded from the size analysis. A histogram

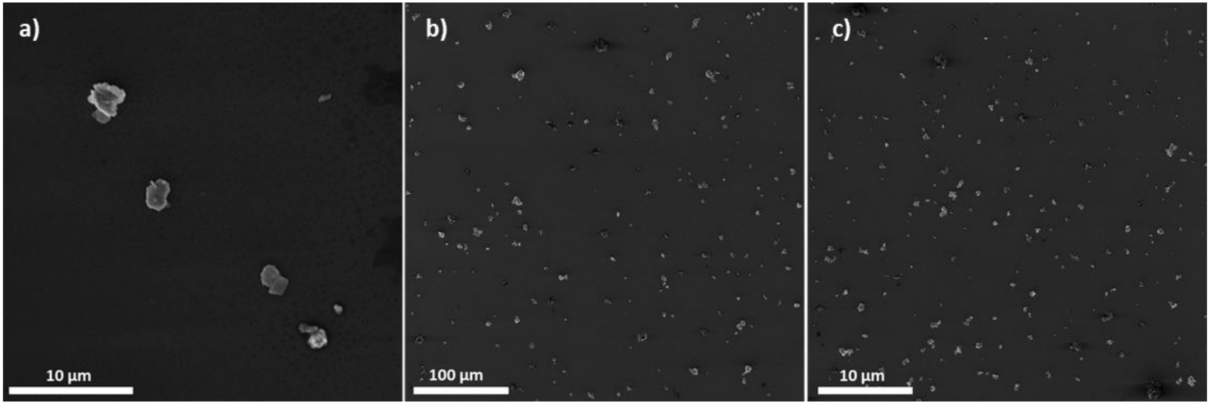

***Figure 4.14: a)** SEM image of a few drop cast WS_2 particles, representative of the mix of aggregation, defects and more pristine particles observed throughout the drop cast particles. **b,c)** SEM images of multiple WS_2 particles drop cast on silicon-on-insulator.*

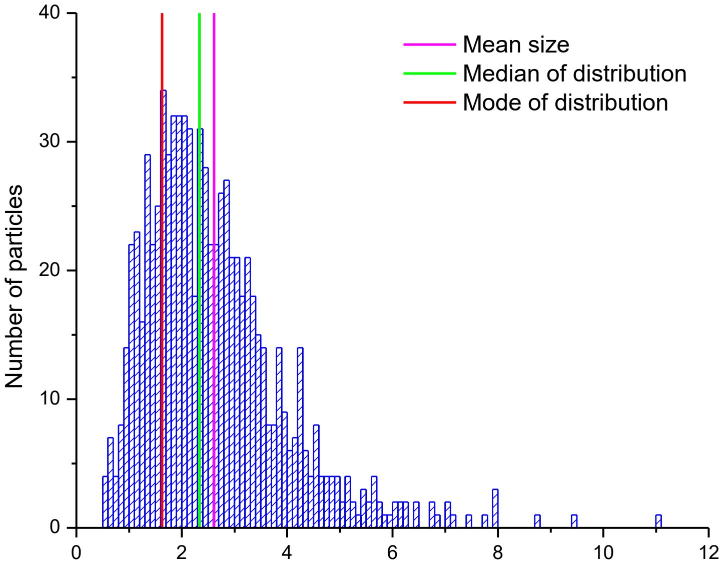

***Figure 4.15:** Histogram of the measured distribution of the lateral sizes of WS_2 particles as determined from SEM, with the arithmetic mean (purple), median (green) and mode(red) of the distribution shown.*

showing the distributions of particle sizes (with statistical averages marked also) is presented in Figure 4.15. Dispersions in other solvents showed very similar size distributions, as expected. It was also observed that there were significant differences in the shapes of the exfoliated particles produced.

Particle size analysis by atomic force microscopy.

AFM images were also produced for the drop-cast particles (Fig. 4.16). The step heights for each of these particles were measured. From analysis of the step heights for a large number of particles, an average thickness of around 4 *nm* was observed, again in close agreement with the peak in the DLS spectrum attributed to the particle thickness. For example, in the area shown in Fig. 4.16c-d, a subset of 20 particles were found. The step heights of these particles were: 5.830; 1.186; 2.875; 1.985; 4.030; 5.337; 2.744; 2.709; 1.893; 4.034; 2.354; 2.467; 4.611; 6.331; 4.961; 3.094; 4.721; 7.902; 6.34 and 4.161 *nm* respectively – giving an average height of 3.978 *nm* (corresponding to approximately 6.5 layers). A more thorough analysis of a greater number of particles (578) over a large area gave a similar figure, with an average thickness of 4.04 *nm* (6.63 layers). Again, this is in close agreement with the value obtained from DLS. A histogram showing the distributions of particle sizes (with statistical averages marked also) is presented in Figure 4.17. Dispersions in other solvents showed very similar size distributions, as expected. It was also observed that there were significant differences in the shapes of the exfoliated particles produced.

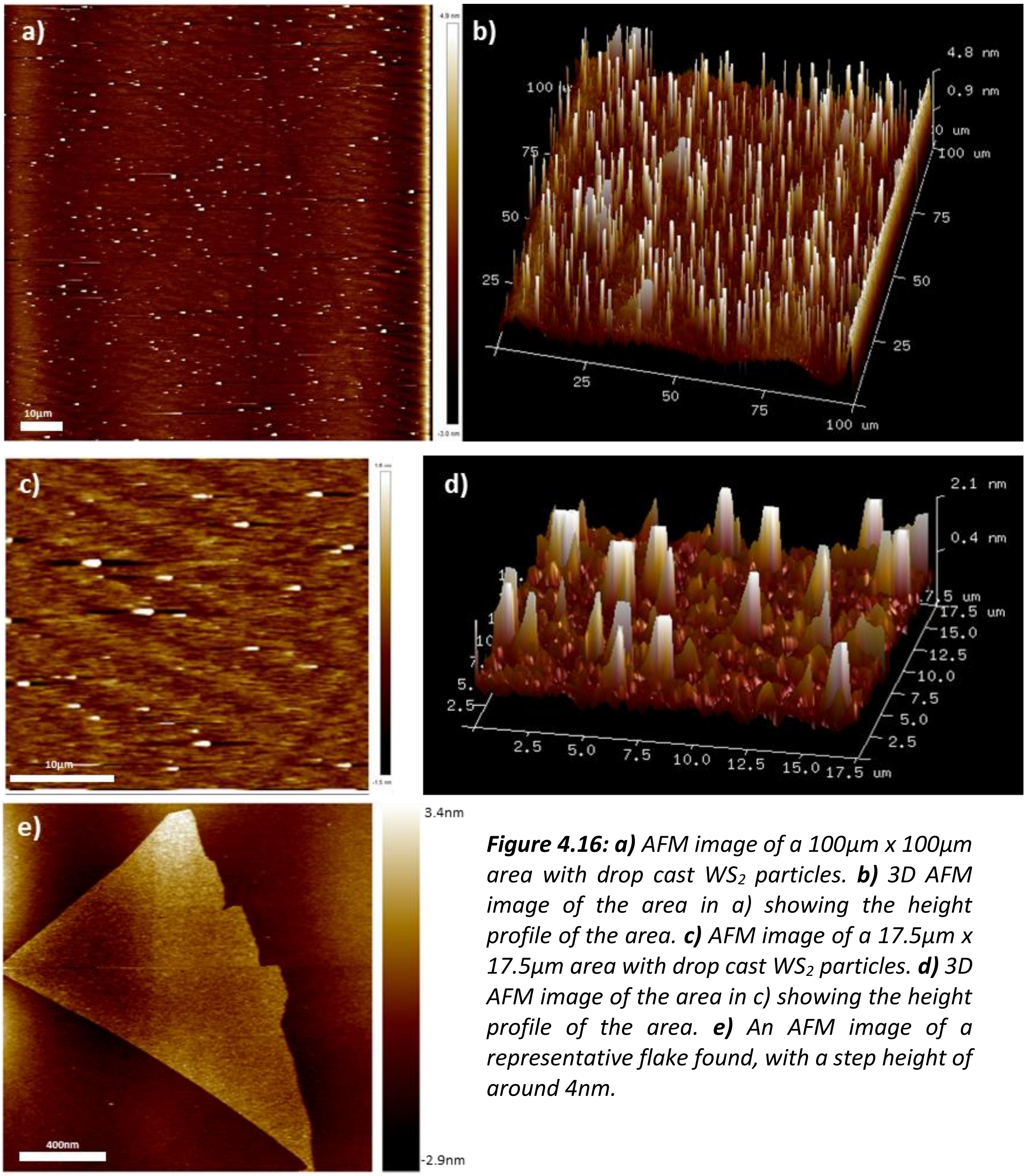

Figure 4.16: a) *AFM image of a 100µm x 100µm area with drop cast* WS_2 *particles.* ***b)*** *3D AFM image of the area in a) showing the height profile of the area.* ***c)*** *AFM image of a 17.5µm x 17.5µm area with drop cast* WS_2 *particles.* ***d)*** *3D AFM image of the area in c) showing the height profile of the area.* ***e)*** *An AFM image of a representative flake found, with a step height of around 4nm.*

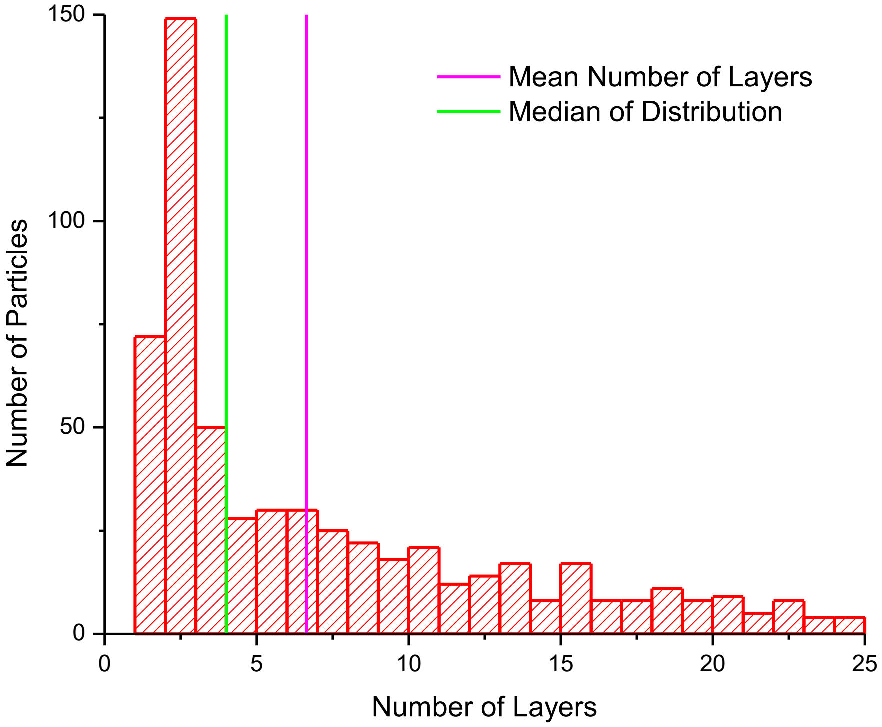

Figure 4.17: *Histogram of the measured distribution of the thickness of WS_2 particles as determined from AFM, with the arithmetic mean (purple) and median (green) of the distribution shown.*

Optical evidence of dichroism.

Schlieren-like textures can be observed in the liquid crystals without the need for polarising optics with bright and dark regions corresponding to changes in reflectance of the sample due to alignment of the particles relative to the incident light used for imaging- shown here for dispersions in isopropanol- (Fig. 4.18) across a range of concentrations, from 5mg.mL^{-1} to 0.1mg.mL^{-1}, with textures observed for all concentrations except the lowest. Similar textures are observed in other solvents. Such textures are equally observed in liquid crystals based on graphene oxide without requiring polarising optics[11]. Under cross-polarised optical microscopy, after suitable control of the concentration by solvent evaporation, some evidence of liquid crystallinity was observed (Figures 4.19 and 4.20).

Under illumination by linearly polarised light, microscopy images taken through an analyser with polarisation at 90° and 45° to that of the incident light are shown in Figure 4.19. Some texturing is observed when looking at the reflection from the liquid surfaces for a range of solvents. However, there are many challenges to imaging these liquids optically. When looking at reflection from the liquids, self-assembly or aggregation at the substrate interfaces is observed. Self-assembly is particularly prevalent for chloroform- and tetrahydrofuran-based dispersions. It is known that the

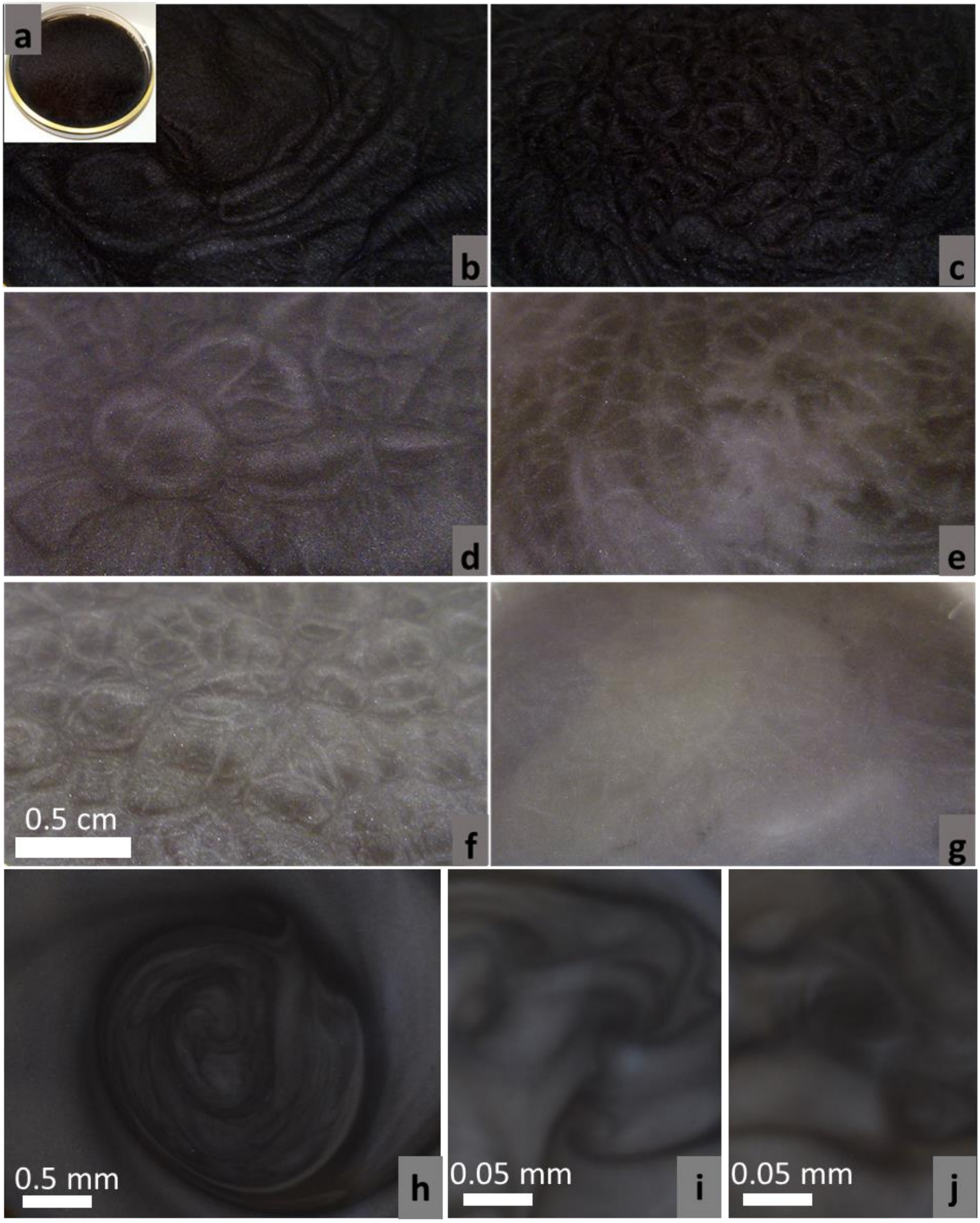

Figure 4.18: a-g) *Optical images of WS_2 dispersions in isopropanol with clear bright and dark states visible depending on flake orientation relative to the incident light;* ***a)*** *shows the texture across a large surface of the dispersion,* ***b-g)*** *give a closer look at the surface for concentrations of 5mg.mL^{-1}, 2.5 mg.mL^{-1}, 1 mg.mL^{-1}, 0.5 mg.mL^{-1}, 0.25 mg.mL^{-1}, and 0.1 mg.mL^{-1} respectively.* ***h-j)*** *Optical images (no polarisation) of tungsten disulfide dispersions in isopropanol at 5 mg.mL^{-1} with clear bright and dark states visible depending on flake orientation relative to the incident light.*

liquid crystallinity of dispersions of anisotropic rigid board-like particles can be suppressed by confined geometries such as those existing near interfaces[101]. When looking at the transmission, there is some texturing observable. However, to prevent the aggregation seen for small confined volumes, a greater

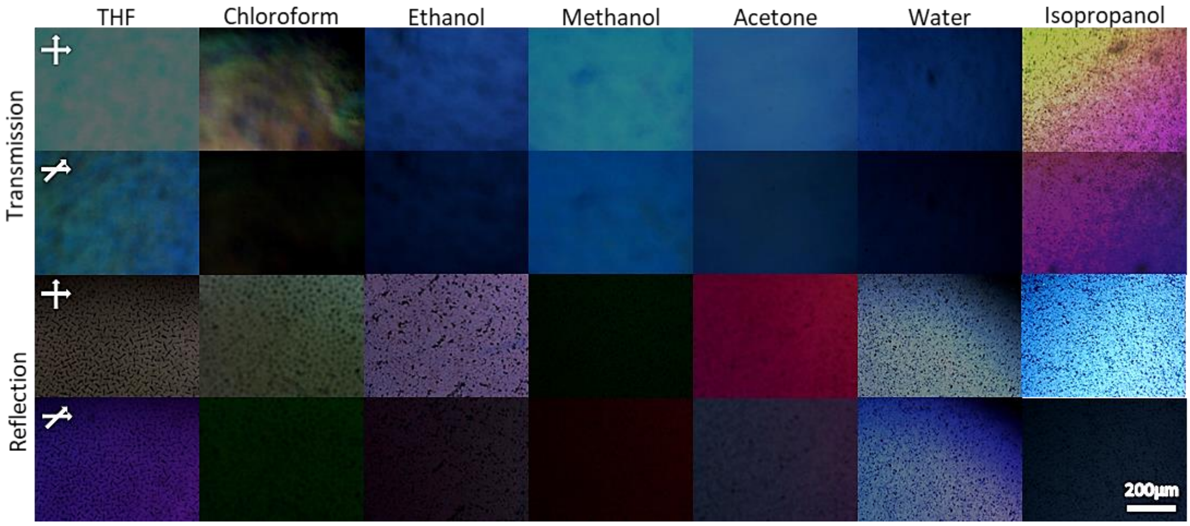

***Figure 4.19:** Optical microscopy images of the reflection and transmission from tungsten disulfide dispersions in different solvents, with crossed polarisers at 90° and 45°.*

volume of the dispersion was required. With a sufficient volume, there is a high level of absorption to be overcome. To overcome this further barrier, an intense light source was required, along with longer expo sure times for the images. As the dispersions are produced in organic solvents with low viscosity, there is significant Brownian motion. Hence, for longer image exposure times, there is blurring of the images due to this Brownian motion. Additionally, greater intensity of the light source can allow significant transmission of light through the crossed polarisers regardless of any change in polarisation as the light passes through the material, due to the imperfection of the polarisers' absorbance. As such, one can observe bright states for dispersions in solvents such as ethanol, methanol, acetone and water despite there being no evidence of liquid crystallinity for those dispersions. However, it is not necessary to use crossed polarisers to observe the textures of these liquid crystals. Figure 4.18 shows the bright and dark states that exist in the liquid crystal dependent on the flake orientation relative to the incident light. These bright and dark states are clearly visible without the need for polarising optics[11]. Figure 4.20 shows polarised optical microscopy images of a WS2 dispersion in IPA. In these images, by looking closely, one can observe the general directional ordering of the dispersed particles directly (shown as black arrows on the images).

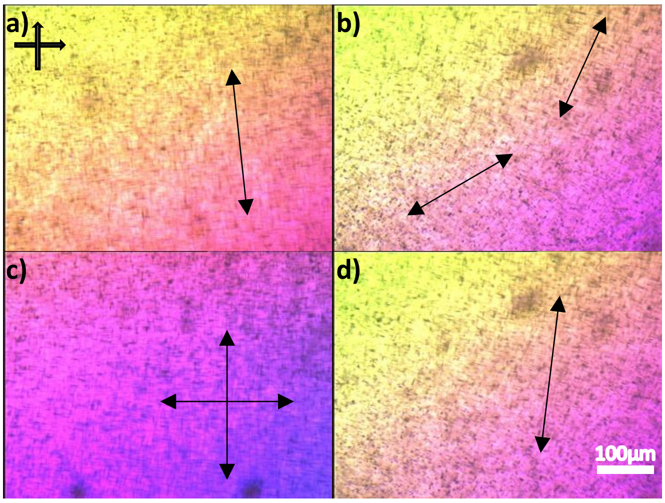

***Figure 4.20: a-d)** Polarised optical microscopy images of a dispersion of WS_2 in IPA at a concentration of 0.5 mg.mL^{-1}. The polariser and analyser were oriented orthogonally. The arrows indicate the observed directions of particle alignment in the images.*

In particular, samples in tetrahydrofuran (THF), isopropanol (IPA) and chloroform (CHF) demonstrated promising properties with the dispersions showing general alignment of the individual particles when observed under optical microscopy (Fig. 4.20), and birefringent textures as would be expected for a liquid crystal (Fig. 4.19), hence these samples were chosen for further investigation.

Linear dichroism.

The linear dichroism spectra of the dispersions in THF, IPA and chloroform were measured in the visible range (200-800 *nm*). For these measurements, a quartz cuvette with a path length of 2mm was filled with the dispersion and the transmission of light through it analysed. Bulk WS_2 has no dichroic response, however dichroism can be induced after exfoliation due to the shape anisotropy of the resultant board-like particles. The possibility of liquid crystalline states in dispersions of 2D materials owes to their intrinsic shape anisotropy. It has long been known (from theory described by Onsager in the 1940s) that both rigid and flexible anisotropic molecules or particles undergo an isotropic/liquid-crystalline transition as their concentration is raised[159], forming a lyotropic liquid crystal (LC). The main condition for this phase to be observed is that a significant anisotropy of the mesogens must exist; i.e. a large aspect ratio. This transition was initially observed with clay particles and variations on Onsager theory used to determine the phase diagram[117,160]. The transition concentration scales inversely with the aspect ratio (comparing the two large dimensions to the particle thickness); hence the requirement for a high aspect ratio, as the required concentration should be balanced against the solubility of the particles in the solvent used. As is observed in rigid rods[180,181] , the polydispersity of the dispersed molecules broadens the biphasic region in which both an isotropic phase and nematic phase can be observed. Hence it is desirable to have a low polydispersity of the dispersed particles. Additionally, pure solvents are wanted as the maximum isotropic concentration of the platelets and the ability to form liquid crystals is strongly influenced by impurities in the host solvent[182].

In an isotropic distribution of particles in the dispersion, no dichroism would be observed as the orientation of the particles would be random. However, where there is an ordering of the particles relative to one another, a dichroic response can be observed; such ordering is the principle property determining liquid crystallinity. The dichroism is a product of the different effective refractive indices produced by particles being aligned with their short axes either parallel or perpendicular to the polarisation of the incident light. The dichroism is induced by self-assembly in the solvent, therefore let us look at the composite effects of both the solvent and the dispersed particles. For reference, linear dichroism spectra for the pure solvents are presented in Figure 4.21a. As such, the absorbance of the cuvette and solvents below 225nm may mask any dichroism (see Figure 4.21b). However, from a material application viewpoint, the dichroism can therefore be considered negligible in this region in any case.

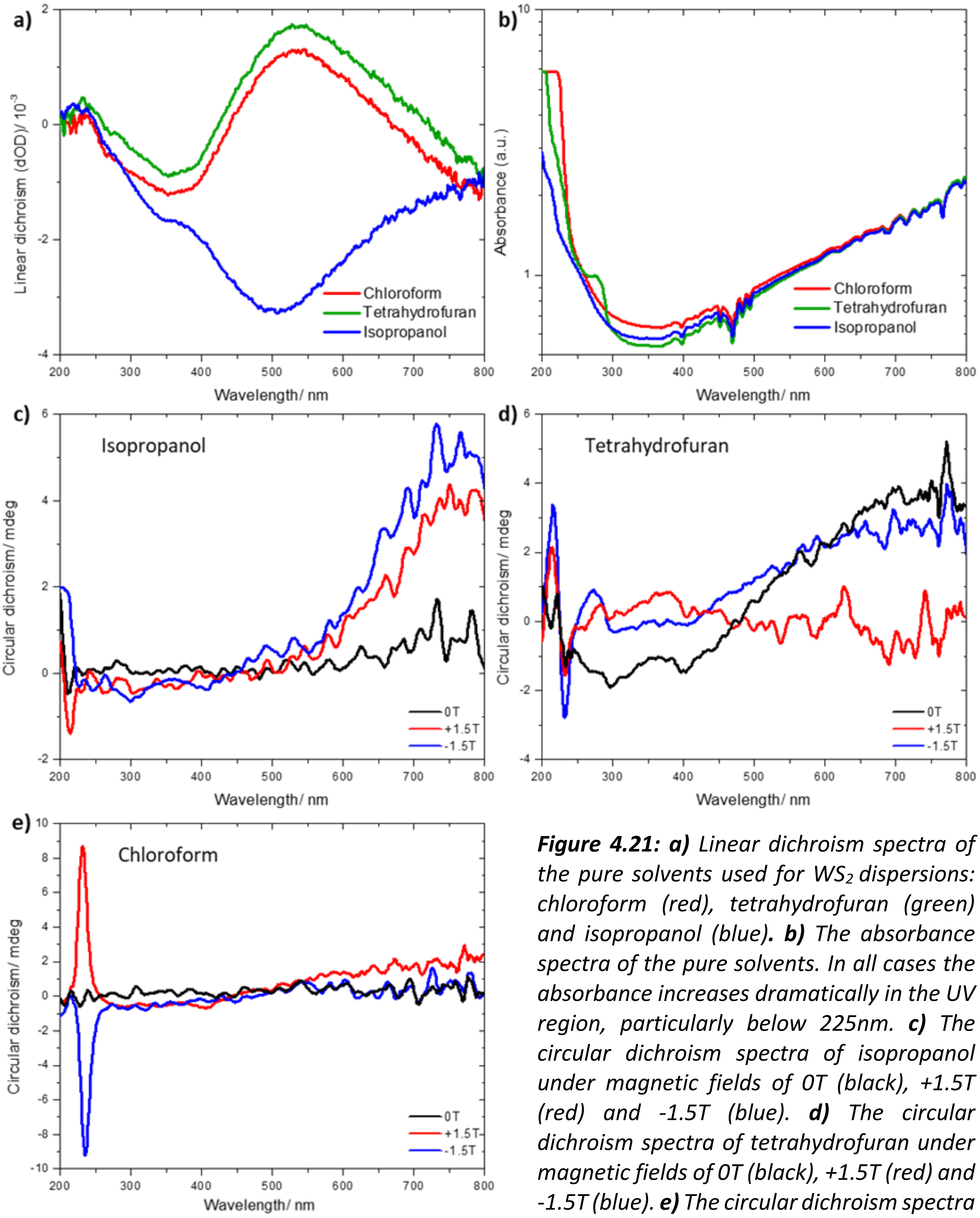

Figure 4.21: ***a)*** *Linear dichroism spectra of the pure solvents used for* WS_2 *dispersions: chloroform (red), tetrahydrofuran (green) and isopropanol (blue).* ***b)*** *The absorbance spectra of the pure solvents. In all cases the absorbance increases dramatically in the UV region, particularly below 225nm.* ***c)*** *The circular dichroism spectra of isopropanol under magnetic fields of 0T (black), +1.5T (red) and -1.5T (blue).* ***d)*** *The circular dichroism spectra of tetrahydrofuran under magnetic fields of 0T (black), +1.5T (red) and -1.5T (blue).* ***e)*** *The circular dichroism spectra of chloroform under magnetic fields of 0T (black), +1.5T (red) and -1.5T (blue), showing a strong peak at around 230nm under applied magnetic field.*

As seen in Figure 4.22a, linear dichroism can be observed across a broad range of wavelengths for dispersions in all three solvents. For these measurements, a concentration of 1 mg.mL^{-1} was used for THF and a concentration of 5 mg.mL^{-1} for IPA and chloroform. However, there is expected to be a significant concentration dependence of the liquid crystallinity. Hence, dispersions with a range of

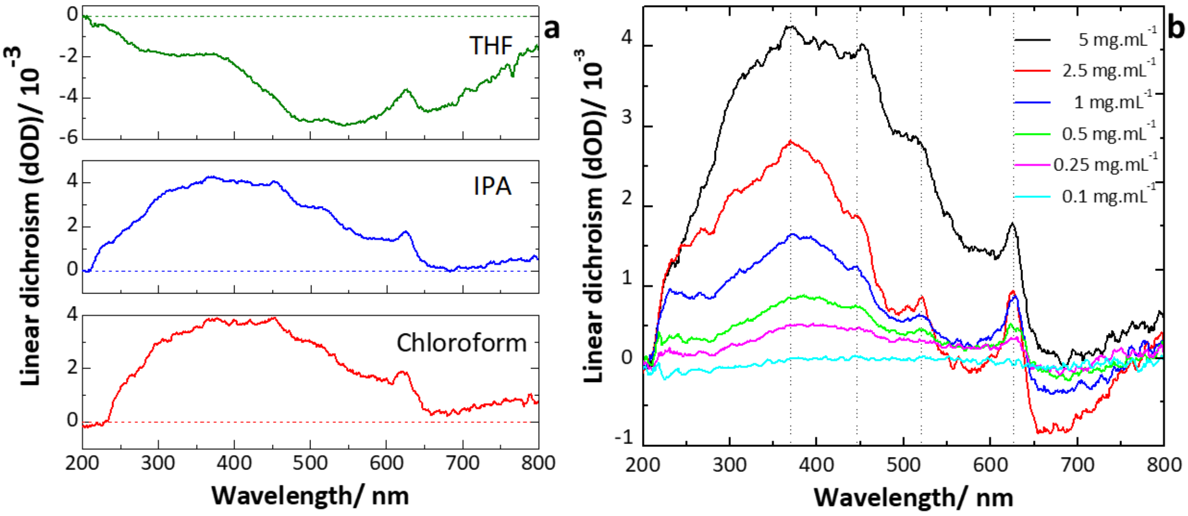

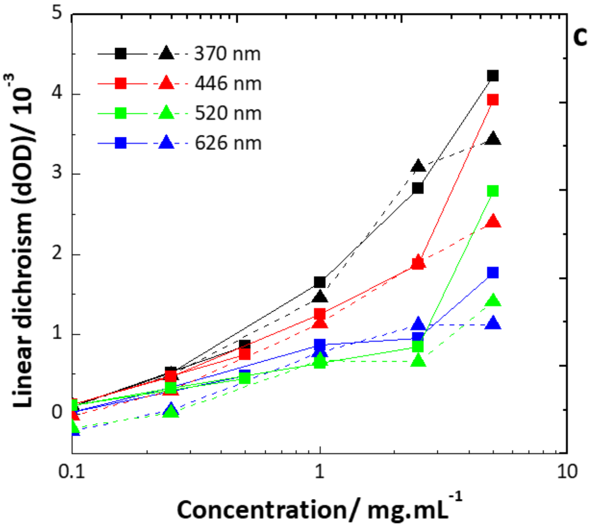

Figure 4.22: ***a)*** *Linear dichroism of* WS_2 *dispersions in THF (1mg.mL*$^{-1}$*), IPA (5 mg.mL*$^{-1}$*) and chloroform (5mg.mL*$^{-1}$*).* ***b)*** *Linear dichroism of dispersions of* WS_2 *in IPA at different concentrations: 5mg.mL*$^{-1}$ *(black); 2.5mg.mL*$^{-1}$ *(red); 1mg.mL*$^{-1}$ *(blue); 0.5mg.mL*$^{-1}$ *(green); 0.25mg.mL*$^{-1}$ *(magenta); 0.1 mg.mL*$^{-1}$ *(cyan).* ***c)*** *Linear dichroism of dispersions of* WS_2 *in IPA at specific wavelengths: 370 nm (black); 446 nm (red); 520 nm (green); 626 nm (blue). Solid lines (and squares) are for samples that had been exfoliated as described whereas dashed lines (and triangles) are for dispersions of much larger (unexfoliated) particles. Error bars are smaller than the symbol size.*

concentrations were measured, to establish where the onset occurs. Significant increases can be observed in the linear dichroism of dispersions in IPA (Fig. 4.22b) and chloroform (Fig. 4.23) as the concentration is increased from 0.1 mg.mL^{-1} to 5 mg.mL^{-1}. However, no clear transition concentration from isotropic to liquid crystalline is observed. This is likely due to the non-homogeneous distribution of particle sizes present in the dispersion, leading to a broad region of biphasic stability where liquid crystallinity occurs in localised isolation rather than throughout the entirety of the dispersion.

The effect of the particle size was investigated by comparing dispersions of exfoliated particles, with those of largely unexfoliated bulk material (see Subsection on Synthesis of unexfoliated samples) which still possessed some shape anisotropy. For lower concentrations, little difference is observed between the values of the linear dichroism recorded for the exfoliated and unexfoliated samples respectively (Fig. 4.22c, Figure 4.23b). For all concentrations below 5 *mg.mL*$^{-1}$, the recorded difference is less than the noise level in the measurements. However, as the concentration was increased to 5 *mg.mL*$^{-1}$, significant increases in the linear dichroism were observed for both the exfoliated and unexfoliated dispersions. At this concentration, the exfoliated dispersion showed much

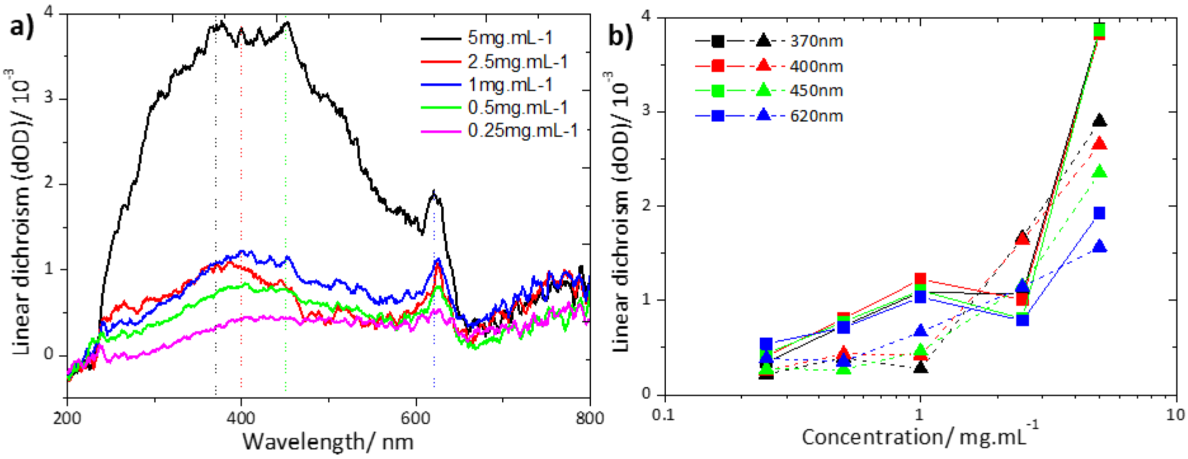

Figure 4.23: a) *Linear dichroism of dispersions of tungsten disulfide in chloroform at different concentrations.* ***b)*** *Linear dichroism of dispersions of tungsten disulfide in chloroform at specific wavelengths; solid lines (and squares) are for samples that had been exfoliated as described whereas dashed lines (and triangles) are for dispersions of much larger (unexfoliated) particles.*

stronger dichroism (up to two times greater) than the unexfoliated across the full wavelength range (Fig 4.22c). For all samples, nanoparticle precipitation partially occurred due to the containment in the confined geometry of the cuvette, as observed from sedimentation after measurements. With continued precipitation over time, a trend towards the pure solvent spectrum would be expected and hence for the spectra to tend towards zero after normalisation. This is not observed in the spectra recorded and the results were consistent over time, hence there is negligible effect of the precipitation on the dichroism results obtained. It is suggested that the least colloidally stable tungsten disulfide particles precipitate rapidly within the confined geometry of the cuvette but that the resultant dispersion is then stable with time.

Circular dichroism.

The circular dichroism of the samples was also analysed for the dispersions in THF, IPA and chloroform (spectra for the pure solvents are given in Figure 4.21c-e). As can be seen in Figure 4.24, circular dichroism was observed for all three solvents. Similar circular dichroism has previously been observed for liquid crystals of graphene oxide[17,98,143,183–185], where a twisted lamellar structure is proposed (Fig. 4.24d). In this structure, sheets of the 2D material form lamellar blocks of concentration dependent sizes. Separate blocks then arrange with a helical pitch between them, giving rise to a twisted ordering over long ranges; thus leading to circular dichroism. However, this mechanism is currently both disputed and unproven[101]. Here, the inherent noise in the measurements due to absorption and scattering makes any qualitative analysis difficult. Whereas molecular chirality is related directly to the electronic transitions as seen in the absorption spectra of the molecule, for supramolecular chiral assemblies the chirality is related to the helical pitch of the structures- hence

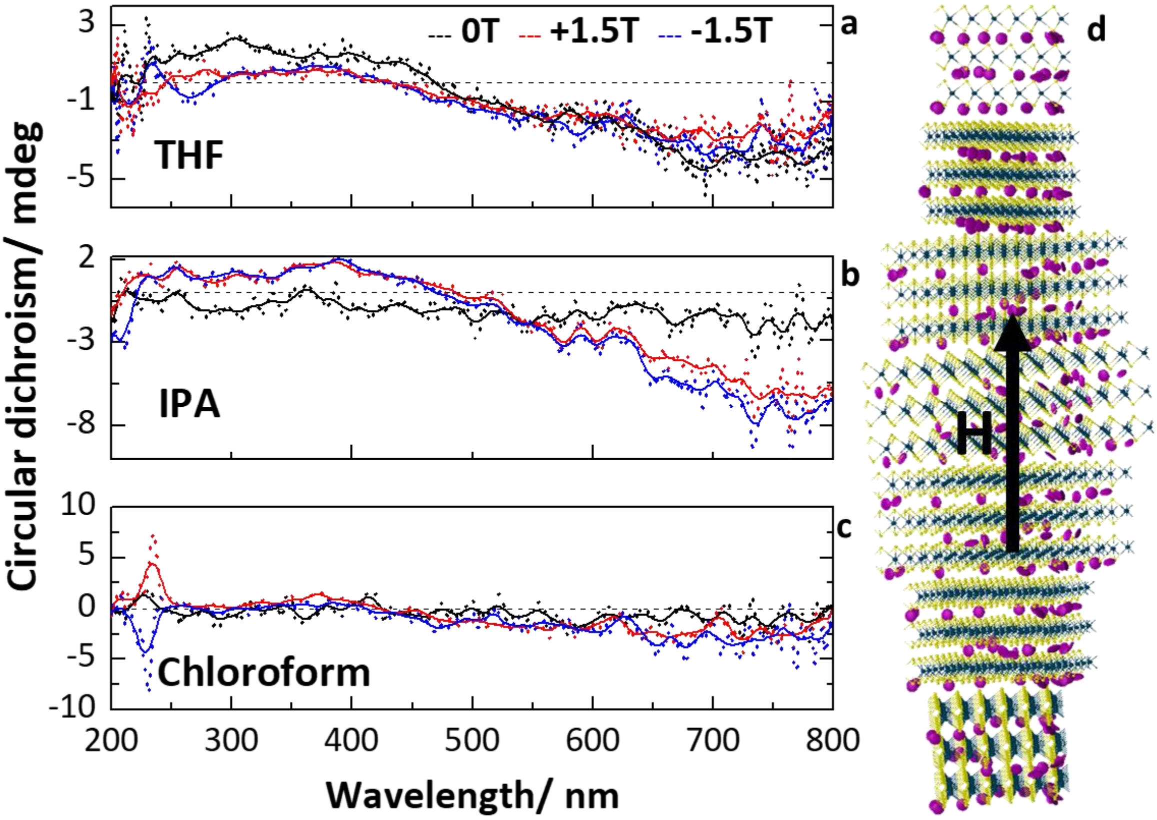

Figure 4.24: *Circular dichroism of dispersions of* WS_2 *in different solvents:* ***a)*** *THF,* ***b)*** *IPA and* ***c)*** *chloroform, under applied fields of 0T (black), +1.5T (red) and -1.5T (blue). Dashed lines are normalised data including noise, solid lines give an indication of the general trend of the circular dichroism accounting for the noise.* ***d)*** *A possible structure of the circular dichroic self-assembly of tungsten disulfide liquid crystalline dispersions under applied magnetic field.*

the chirality is unrelated to the absorption band of tungsten disulfide (measured in the liquid phase dispersion at 635nm). By applying a magnetic field to the dispersions during measurement, significant (up to 6x) enhancement of the circular dichroism is observed for IPA, with a clear broad band emerging for wavelengths >500nm. However, for the dispersion in THF, the application of the magnetic field is seen to have a negligible effect on the circular dichroism. The magnetic field was applied parallel to the incident light in the measurements (Faraday geometry), *i.e.* at normal incidence to the face of the cuvette. Under applied magnetic field, especially for dispersions in IPA, the circular dichroism can be enhanced due to an aligning force giving a preferred directional axis for the helicity (Fig. 4.24d). Enhancement of the circular dichroism by up to six times is observed in the dispersion in IPA in the region from 500-800 *nm* where the strongest circular dichroism is observed. The dispersion in THF however, shows negligible enhancement under magnetic field. The dispersion in chloroform also shows negligible enhancement in the region from 500-800 *nm*. Broad widths of the circular dichroic bands are expected due to the non-homogeneity of the particle sizes present in the dispersion.

Additionally, for the dispersion in chloroform under the applied magnetic field, a very strong peak in the circular dichroism is observed at around 230nm. This peak switches sign with the applied field. The peak can also be observed in the pure solvent, however, as results are normalised versus the pure solvent spectrum there is enhancement observed due to the presence of the dispersed nanoparticles. However, it is the properties of the composite liquid crystalline system that are of interest, hence it is justifiable that the composite system of tungsten disulfide dispersed in chloroform represents a magnetically reconfigurable chiral material.

Conclusions.

While different solvents can affect the rate, efficiency and quality of particles obtained by liquid phase exfoliation, due to the fact that controlling the concentration generally relies on drying and redispersion the solvent choice for obtaining a liquid crystalline state can be independent of that for exfoliation. The different properties achievable with different solvents show that there is no single definable 'best' solvent for use. Rather, the choice of solvent should be application driven. For example, to achieve reconfigurable circular dichroism at 750 nm, IPA would be the best choice, whereas at 230nm chloroform is preferable. The single condition is that WS_2 should be soluble enough to allow dispersion at the necessary concentrations, which is broadly true for all organic solvents. This work demonstrates that using only standard liquid phase exfoliation processes (ultrasonication, centrifugation and control of concentration) a liquid crystalline state of WS_2 particles can be achieved in a range of solvents.

The discovery that WS_2 LC dispersions can simultaneously demonstrate reconfigurability under applied magnetic field and circular dichroism, while also combining the intrinsic optical and electrical properties of the 2D WS_2 flakes is of significant interest, opening the way towards countless applications in opto-electronics and photonics such as switchable filtering devices. Future optimisation and tuning of the synthesis holds great potential for the generation of a new class of true reconfigurable '*wonder materials*', with applications encompassing: thin film and membrane depositions; display devices; inks; terahertz modulators; and others. The discovery of this novel reconfigurable phase could lead to a marked expansion in the uptake of WS_2 for device-based applications, due to the increased scope for scalable integration with reduced drawbacks such as time, cost and quality as well as the significant boost in the range of potential uses with the observation of reconfigurable circular dichroism.

5. Raman Spectroscopy Characterisation of 2DLCs.

It is demonstrated that the design of an optofluidic waveguide system can be optimised to enable simultaneous *in-situ* Raman spectroscopy monitoring of dispersed 2D flakes during the device operation. Moreover, the possibility of label-free 2D flake detection via selective enhancement of the Stokes Raman signal at specific wavelengths has been successfully demonstrated. An ultra-high signal sensitivity to the *xyz* alignment of 2D flakes within an optofluidic waveguide was discovered, which in turn enables precise *in-situ* alignment detection. It is demonstrated that particle positions can be established in one, two and three dimensions using a methodology that combines simulation and analysis with experimental results. It is shown that this methodology can be further extended to give other information on the dispersed particles. This technique is intended to form the basis of characterisation to allow the first practicable realisation of 3D photonic microstructure shaping based on 2D-fluid composites and CMOS photonics platform while also representing a useful technological tool for the control of liquid phase deposition of 2D materials.

The recent development of nanocomposites consisting of fluid-dispersed atomically thin two-dimensional (2D) materials has sparked a great level of interest as a highly promising *in-situ* tailored meta-material device platform for the next generation of multi-functional optoelectronic systems[1,6,187–189,7–9,113,123,130,140,186]. Dynamically controlled three-dimensional (3D) self-assembly of fluid-suspended 2D materials not only provides a new breakthrough route for technological applications of 2D material based 3D device architectures[11,12,190], but also their fluidic nature allows CMOS-compatible wafer-scale back-end integration on chip using microfluidic technology[4,13,191]. The practical realisation of dynamically reconfigurable 3D material fluid metastructures integrated into a microfluidic system and coupled with a CMOS photonic circuit (as illustrated in Fig. 1) opens up limitless possibilities in the fabrication of compact and low-power systems for commercially viable, miniaturised, multi-functional light-management devices such as light emitting sources[14], tuneable optical filters[15] and nanoantenna phased arrays[16]. For example, 1D photonic crystals of graphene which could act as optical filters have been theoretically explored[192] but as yet no method exists for the precise reconfigurable control of such structures. Additionally, self-assembly of fluid dispersed 2D materials represents a remarkable precursor state for liquid phase deposition of ordered lamellae, stacks and other structures in the solid phase[10,66,129]. Reconfigurability of the metastructures can be achieved by exploiting liquid crystal technology[12,140] with *in-situ* monitoring used to characterise the metastructure formation.

However, the primary challenge for the first realisation of on-chip controlled assembly of 2D flakes into functional metastructures is the lack of a reliable and sensitive method for *in-situ* characterisation. Such a method is pivotal to the confirmation of the integration of composites in the device and to enable determination of parameters, such as spatial alignment of incorporated 2D materials, dynamically during device operation. Conventional characterisation methods such as Raman spectroscopy[8,193,194], coherent anti-Stokes Raman spectroscopy (CARS)[195] and Fourier Transform Infrared Spectroscopy (FTIR)[148] are not suitable for studies of fluid nanocomposites with relatively low concentrations of nanoparticles dispersed. In this case, the significantly greater scattering volume of the host fluid compared to that of the dispersed nanoparticles always dominates the vibrational signal intensity, rendering the monitoring of the considerably weaker bands of dispersed nanoparticles impossible. Proposed and subsequently demonstrated herein is a novel approach for ultra-sensitive, label-free, *in-situ* detection and monitoring of integrated 2D-fluid composite materials on-chip. Specifically, an *in-situ* micro-Raman characterisation approach, whereby the Raman signal of 2D dispersed nanoparticles is selectively enhanced through the design of optofluidic waveguide geometry on silicon-on-insulator (SOI) platform. It has previously been shown that the Raman signal from micro-structured silicon cavities can be enhanced due to Fabry-Pérot type resonances[196–198]. Here, the structure is designed to simultaneously enhance different resonant modes relating to different parameters of the optofluidic waveguides, balancing the required enhancement of the signal from multiple vibrational bands with the desire for the greatest achievable intensity for the individual bands. The developed approach demonstrates ultra-high sensitivity to the *xyz* alignment of 2D nanoparticles within optofluidic waveguides. Hence, for the first time, these findings demonstrate the possibility of monitoring the dynamics of fluid-dispersed 2D nanoparticles on chip. This work paves the way for the practical realisation of dynamically reconfigurable photonic metastructures based on 2D-fluid composites integrated on CMOS photonics platform with a range of important applications, such as renewable energy, optical communications, bio-chemical sensing, and security and defence technologies[7,9,199].

5.1 Microfluidic structure design.

Typically, large-scale CMOS photonics builds on a SOI platform; a high index-contrast waveguide platform which prevents interference between the photonic integrated circuit components and the substrate. Therefore, let us consider use an SOI based Fabry-Pérot type optofluidic waveguide channel, with an open top cladding to allow *in-situ* micro-Raman detection and monitoring of the integrated 2D fluid nanocomposite system during device operation. To optimise the optofluidic waveguide design for facilitating strong confinement of light on chip and to significantly enhance the Raman back-scattered signal of the individual incorporated 2D nanoplatelets, one can model the variation in the intensity of the Raman bands of dispersed nanoparticles while varying parameters that can be experimentally controlled, such as: the waveguide width, *w*, and the buffer oxide (BOX) layer thickness, h_{BOX}.

Scattering matrix method analysis.

The backscattered Raman signal intensity is numerically determined for wavelengths corresponding to the Raman active bands using the scattering matrix method. The scattering matrix method (SMM) is a powerful tool for numerical determination of the near- and far-field light distribution for structures which can be split into layers uniform along at least one direction[200–203]. The main principle of this method is the decomposition of electric and magnetic fields into Fourier series in each layer and connecting the Fourier components of adjacent layers in accordance with the boundary conditions of Maxwell's equations.

The optofluidic waveguide design was optimised to significantly enhance the back-scattered Raman signal from incorporated 2D nanoplatelets. Raman scattering is a quantum mechanical process with a random spatial distribution of the photons involved, however the optical behaviour of the scattered light can be modelled using a classical electrodynamics approach. 2D flakes within nanocomposites are modelled as a system of chaotically-oriented oscillating electrical dipoles[156] within a microfluidic channel, with the dipole emission defining the Raman signal wavelength. To numerically determine the far-field intensity of the dipole emission the SMM was used.

To reach convergence, 801 Fourier harmonics were used. This value was determined by simulating a simplified channel with increasing numbers of Fourier harmonics used, until no change in the result was observed when further increasing the number of harmonics. The local components of the electromagnetic field were found, forming material matrices in each layer. By applying an iterative procedure, the total scattering matrix for the whole structure was calculated[155]. The back-scattered Raman intensity was calculated from the components of the scattering matrix.

All numerical analyses were made for normal angles of Raman laser incidence and signal collection. The electric field vector of the incident light is oriented parallel to the channel walls. The nematic LC host is a birefringent material, however, an advantage of the microfluidic infiltration into SOI cavities is the spontaneously induced planar alignment of the LC through interaction with the surfaces of the Si walls[204]. The LC will therefore have a director which is either parallel or perpendicular to the walls of the channel such that only either the extraordinary or ordinary refractive index is required. The refractive indices of the specific liquid crystals used were determined as described in the next sub-section.

The spot size of the Raman laser was effectively considered as equal to the microfluidic cavity width. As the microfluidic cavity width was changed in the simulations, the spot size was also considered to change. To account for this, all Raman intensities were normalised by accounting for the incident field strength in the channel. Since the incident and Raman-scattered wavelengths of the light are considerably greater than the thickness of 2D flakes in nanocomposites, the flake is considered to be a point dipole- an emitter of only Stokes or anti-Stokes photons within the system- and hence the refractive index of the flake material has no effect on the propagation of backscattered light in the cavity. For Fabry-Pérot effects in a layer to be observed experimentally, its thickness should be less than the coherence length of the Raman scattered light[156]. However, this condition is not fulfilled for the silicon substrate layer, hence it is modelled as a semi-infinite material by removing all

Fabry-Pérot resonances within the substrate layer. Very thick silicon walls were considered; the thickness of the silicon walls has been shown to have little effect on the intensities determined by numerical analysis.

Let us consider the specific case of the D and G bands of 2D carbon-based materials (Figs. 5.1 and 5.2) - such as graphene and graphene oxide (GO) - dispersed in a nematic liquid crystal (LC) host, however the proposed methodology can be utilised for any fluid-dispersed material. Maps were

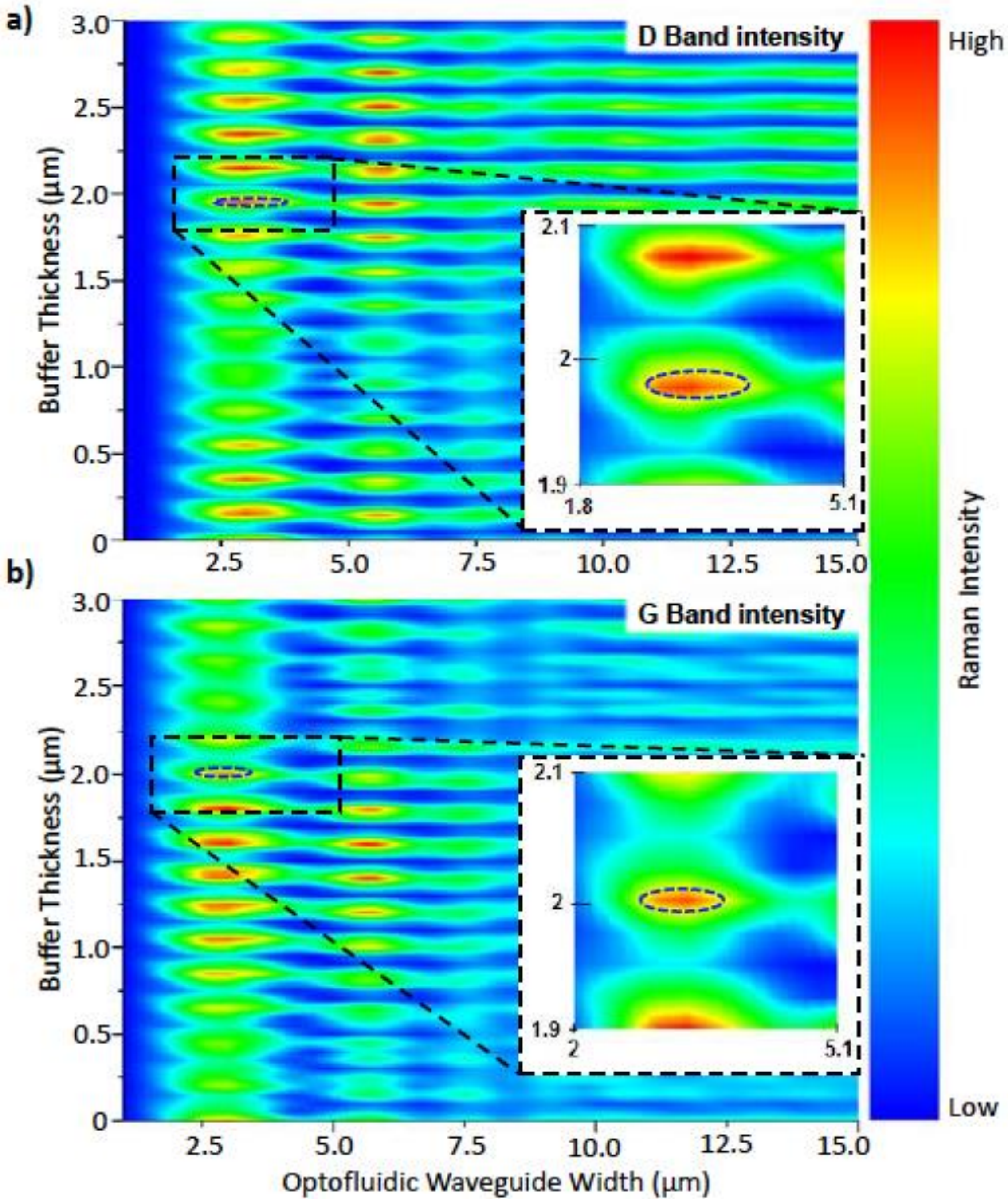

***Figure 5.1**: Maps of the Raman signal intensity at wavelengths corresponding to **a**) the D band and **b**) the G band of fluid-dispersed 2D carbon-based materials, under excitation by a 532nm Raman laser, as the optofluidic waveguide width and buffer oxide layer thicknesses are varied. High intensity areas of interest are highlighted.*

produced separately for the D and G bands of 2D carbon-based materials such as graphene or GO (Fig. 5.1). Strong variations in the Raman intensity are observed as various parameters of the optofluidic waveguide are varied. The complex variation of the Raman signal as a result of modifying the optofluidic waveguide parameters can be rationalised as the superposition of Fabry-Pérot resonance effects in different parts of the geometry. Enhancement of up to 100x can be observed between maximising and minimising combinations of the optofluidic waveguide parameters. One can then take the intensity maps for the two individual bands and overlay them so as to map the regions where the intensity is highest for the G and D bands simultaneously (Fig. 5.2).

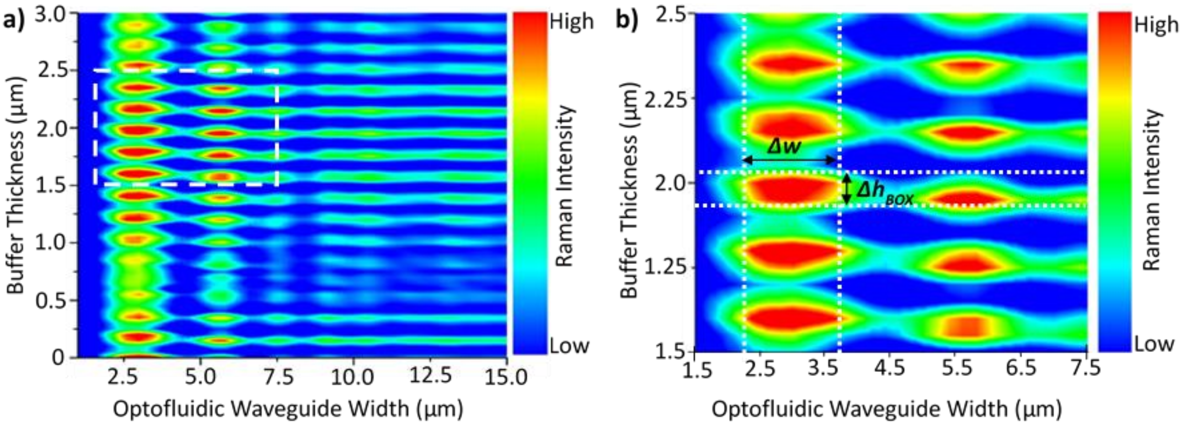

Figure 5.2. a) *Map showing regions where both the D and G bands of 2D carbon-based materials are determined numerically to be strongly enhanced in Raman spectroscopy measurements.* ***b)*** *Expanded view of the region of interest highlighted in a. The range of parameters for which strong enhancement is observed are shown with the white lines including fabrication deviation Δh_{BOX} and Δw.*

Calculation of LC refractive indices.

The ordinary and extraordinary refractive indices were calculated at all wavelengths subsequently utilised in the numerical analysis by utilising a three-coefficient Cauchy model, $n_{o,e} = A_{o,e} + \frac{B_{o,e}}{\lambda^2} + \frac{C_{o,e}}{\lambda^4}$; where n is the refractive index and A, B and C are suitable fitting parameters. The subscripts o and e represent the ordinary and extraordinary indices respectively. For example, for commercially available LC MLC 6608, A_o, B_o and C_o were set to 1.4609, 5x10^{-3} μm^2 and 0 μm^4 respectively to give good agreement with experimental measurements in the visible region[99]. As MLC 6608 has a low birefringence in the visible region, the two-coefficient Cauchy model is a sufficient approximation. For liquid crystal E7, A_o, B_o and C_o were set to 1.6933, 7.8x10^{-3} μm^2 and 2.8x10^{-3} μm^4 respectively. For liquid crystal 5CB, A_o, B_o and C_o were set to 1.5139, 5.2x10^{-3} μm^2 and 0.8x10^{-3} μm^4 respectively. The calculated values for liquid crystal E7 are presented in Figure 5.3.

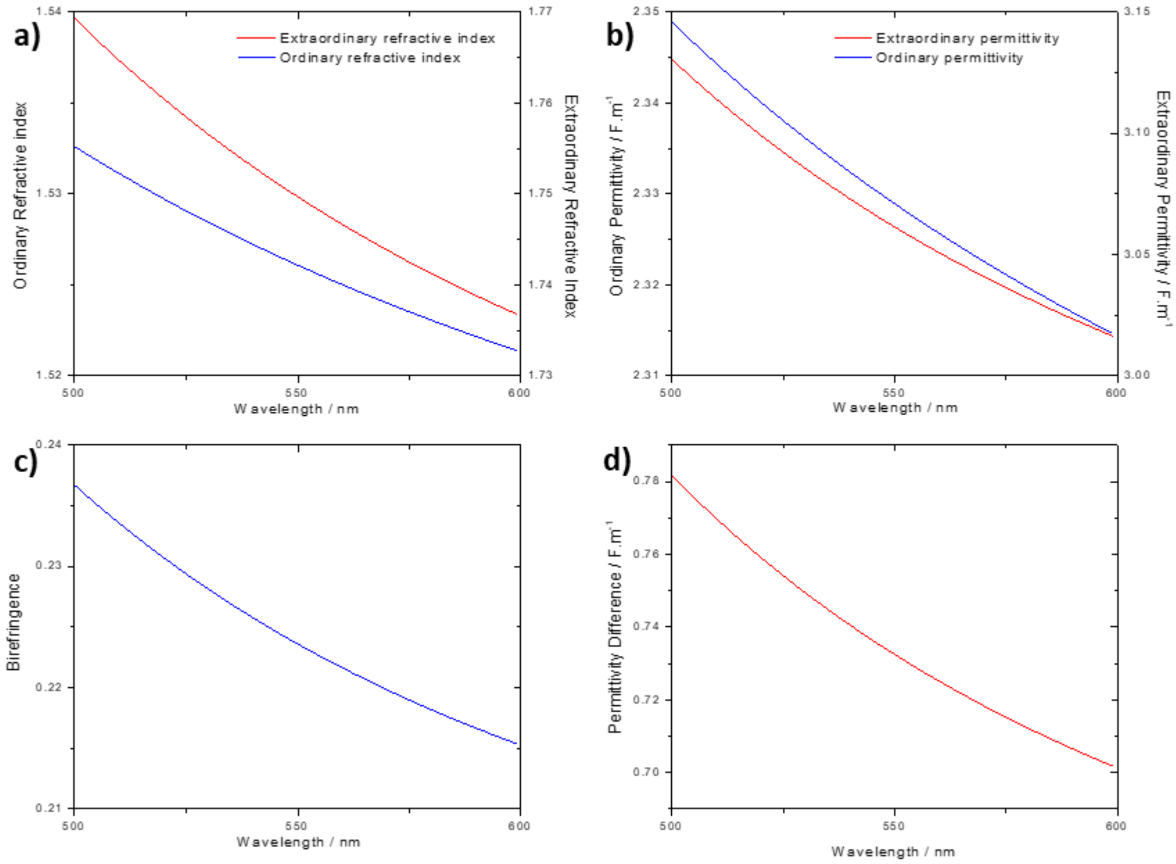

***Figure 5.3**: **a)** Calculated ordinary and extraordinary refractive indices of liquid crystal E7 and **b)** the corresponding ordinary and extraordinary permittivities. **c)** The calculated birefringence of liquid crystal E7 (the difference between the ordinary and extraordinary refractive indices). **d)** The calculated permittivity difference for between the ordinary and extraordinary case for liquid crystal E7.*

Experimental verification of numerical analysis.

In order to experimentally demonstrate the enhancement of the Raman intensity, 2D material- fluid nanocomposites- consisting of graphene and GO nanoplatelets dispersed in LCs- were prepared by a liquid phase exfoliation and dispersion method [See Section 4.1]. The optimal parameters for the microfluidic structures were determined from the calculated Raman signal intensity maps shown in Figures 5.1 and 5.2. Resonator devices consisting of optofluidic waveguide channels of different widths were fabricated on SOI wafer with a thick buffer oxide (h_{BOX}=2 *µm*) layer and with a silicon device layer of 15 µm. The prepared nanocomposites were integrated into

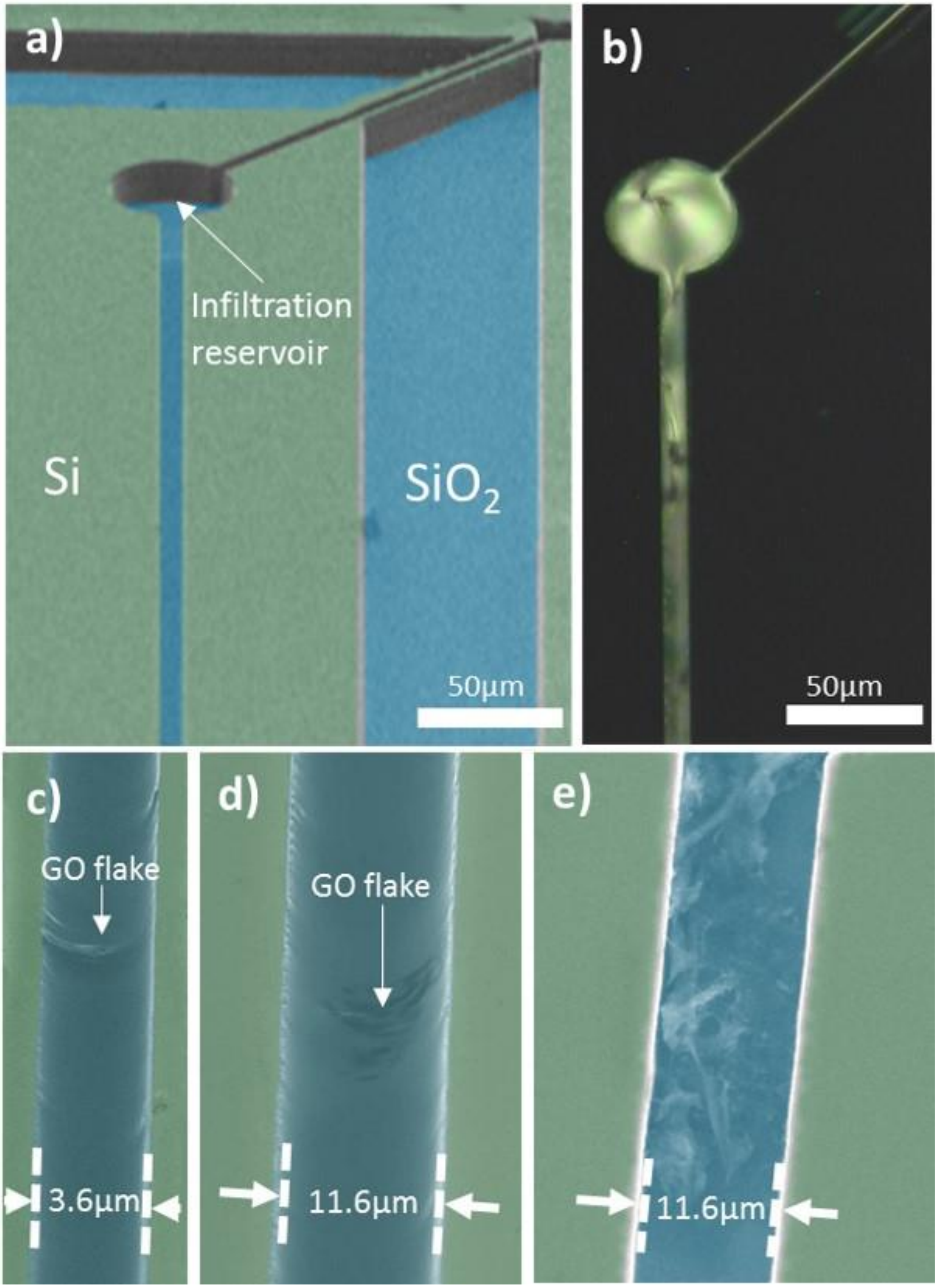

***Figure 5.4**: **a)** SEM image of the chip used for Raman measurements, before infiltration with the nanocomposite. **b)** Polarised microscopy image of the structure infiltrated with a composite of MLC 6608 and graphene oxide. Integration of the composite, including GO flakes, into all microfluidic structures on the chip can be seen. **c)** SEM of GO flakes infiltrated with a host LC into a 3.6 µm channel. **d)** SEM of GO flakes infiltrated with a host LC into an 11.6 µm channel. **e)** SEM of an 11.6 µm channel, with the LC removed, showing the integration of large numbers of GO flakes.*

optofluidic waveguide channels via infiltration reservoirs on the chip (Fig. 5.4). The selected microfluidic channels had widths in the ranges 3.7±0.2 *μm* (narrow channels, strong enhancement) and 10.5±1.5 *μm* (wide channels, weaker enhancement). Optical microscopy (Fig. 5.4b) and scanning electron microscopy (Fig. 5.4c-e) both confirmed the successful integration of the nanocomposite into all channels. Polarised light images were obtained using a Zeiss Axioscope 2 microscope with a Zeiss Axiocam MRc 5 camera, with x20 and x50 objectives used. Scanning electron microscopy (SEM) measurements were performed on a Hitachi S3200N system with a practical operational magnification between 20-60000x, accelerating voltages from 0.3 to 30 *kV*, vacuum chamber pressure <0.1 *mbar* and a maximum resolution of 3.5 *nm*.

Micro-Raman measurements were performed using a Renishaw 1000 system (with a 514.5 nm excitation wavelength from Ar^+ laser, a power of 5 *mW* and a spot size of approximately 3 *μm*) and

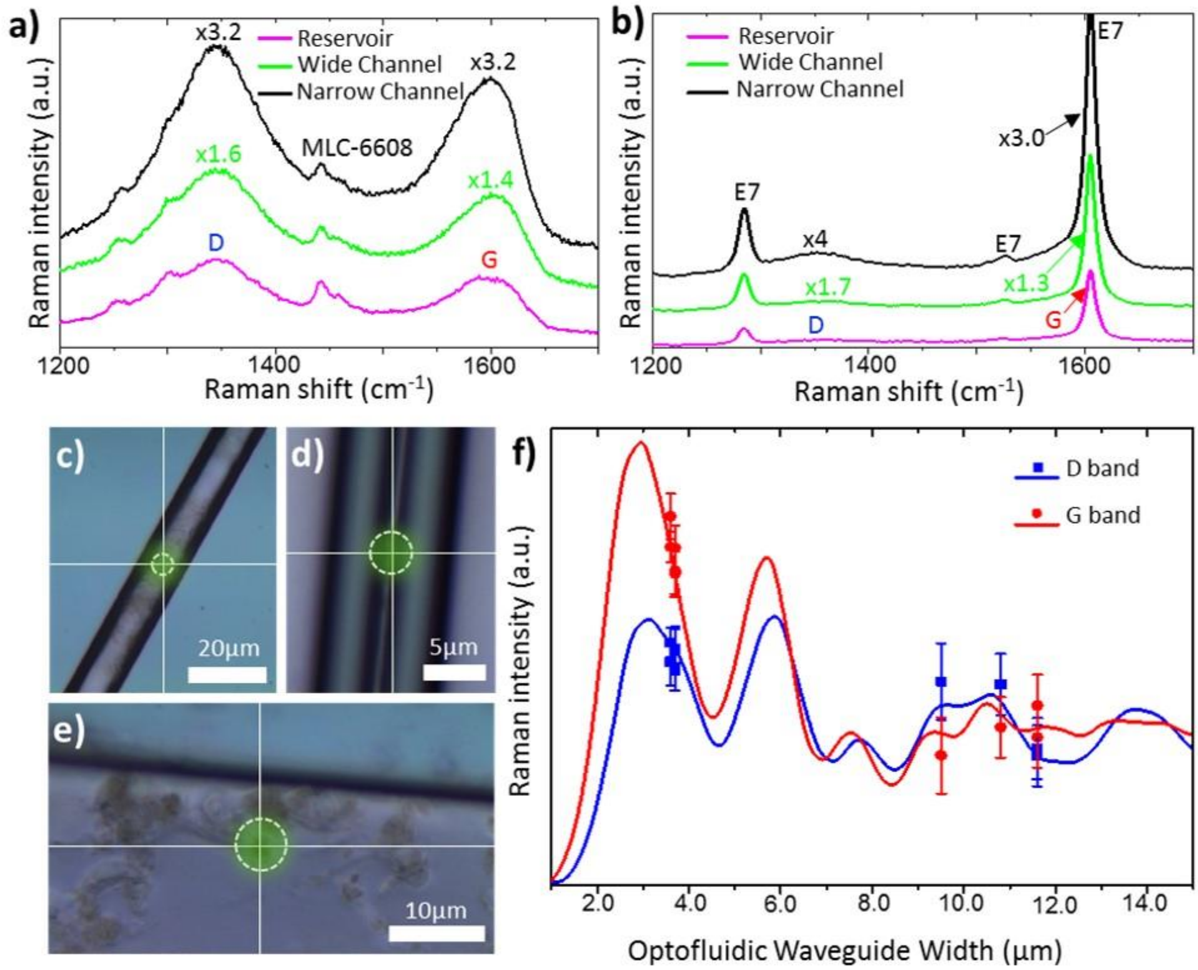

Figure 5.5. a-b) *Normalised Raman spectra showing the enhancement of the D and G bands for graphene oxide dispersed in* ***(a)*** *liquid crystal MLC 6608 and* ***(b)*** *liquid crystal E7. Spectra are shown for three microfluidic geometries: in* ***(c)*** *an infiltration reservoir of width 100μm (magenta), in* ***(d)*** *a microfluidic cavity of width 11.6μm (green) and in* ***(e)*** *a microfluidic cavity of width 3.6μm (black). Approximate laser spot sizes are shown in* ***(c-e)****.* ***f)*** *Comparison of numerically determined (solid lines) and experimentally measured (points) Raman intensities of the graphene oxide D (blue) and G (red) bands. All data is normalised to the case where the walls are separated by a distance great enough for Fabry-Pérot resonances to have no effect.*

on a Horiba Raman system (with an excitation wavelength of 532 *nm*, a power of 8.75 *mW* and a spot size of approximately 5 *µm* when focused through a x50 objective). Raman spectra are presented for the GO-LC nanocomposites- with MLC-6608 (Fig. 5.5a) and with E7 (Fig. 5.5b) as the fluid host- at three points *in-situ* on the chip; more specifically: in a wide channel (Fig. 5.5c), in a narrow channel (Fig. 5.5d) and in an infiltration reservoir (Fig. 5.5e).

The liquid crystal host materials used for the nanocomposites in experimental measurements have several characteristic bands in their Raman spectra (Fig. 5.6) which are then also present in the spectra of the nanocomposites. The spectra were recorded for droplets of the liquid crystal greater than 100 *µm* deep, on a SOI substrate. The spectrum for MLC 6608 has been scaled by a factor of four.

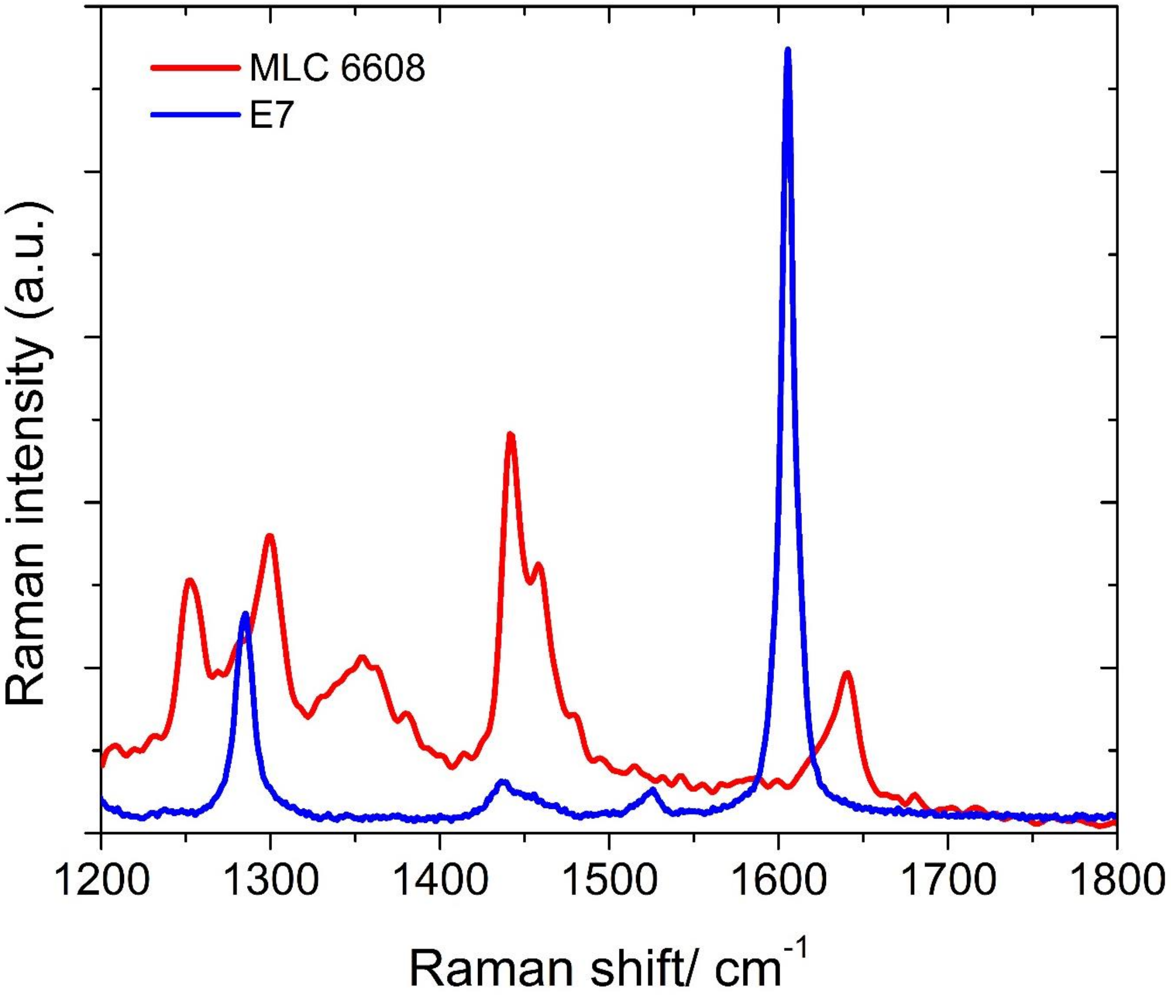

***Figure 5.6**: Raman spectra for droplets of the liquid crystal host fluids used in the synthesised nanocomposites on a SOI substrate: MLC 6608 (red) and E7 (blue). The spectrum for MLC 6608 has been scaled by a factor of four.*

E7 (Fig. 5.6 [blue line]) shows a strong Raman active vibrational band at around 1605 cm^{-1}, overlapping with the G band of graphene oxide. There is an additional strong band at around 1280 cm^{-1}, which partially overlaps with the D band of graphene oxide, as well as two very weak bands at around 1440

cm^{-1} and 1525 cm^{-1}. MLC 6608, however, only shows weak bands at around 1245 cm^{-1}, 1305 cm^{-1}, 1355 cm^{-1}, 1450 cm^{-1}, 1460 cm^{-1} and 1640 cm^{-1}.

Liquid crystal MLC-6608 exhibits weak Raman bands (Fig. 5.6 [red line]) that have no strong overlap with the D and G bands, allowing for clear determination of the GO bands in gathered spectra. Raman spectra were recorded for individual monolayer flakes of area 1.0±0.1 μm^2 in all cases. For GO dispersed in MLC-6608, the D band Raman intensities were observed in the approximate ratio 5:8:16 for an infiltration reservoir, 11.6 μm channel and 3.6 μm channel respectively. For the G band, intensities were observed in the ratio 5:7:16. E7, however, has a strong Raman active vibrational band at around 1605 cm^{-1}, overlapping with the G band. Nevertheless, utilising the proposed signal enhancing design, the observation of the G band as a broad shoulder on this band is feasible (Fig. 5.5b). In addition, similar results were obtained for nanocomposites with graphene instead of GO.

The close agreement, in Figure 5.5f, between the relative intensities of the D and G bands found experimentally for all nanocomposites (points) and those determined numerically (solid lines) verifies the method for predicting the Raman signal enhancement. For both the D and G bands, the numerically determined enhancement ratio was within the error of the experimental measurements; slight differences occur due to the flake not being positioned precisely at the centre of the channel. Therefore, this technique presents an effective tool for maximising the enhancement of the Raman signal.

Control of integrated nanocomposites.

The GO flakes dispersed in the LC can be manipulated by re-orienting the LC director (Video available online[5,205]). Applying an electric field across the channel results in a switching of the orientation of the LC molecules when a threshold voltage between the two walls is reached[12,140] (Videos available online[5,205]). This is observed as a change from a bright to a dark state in polarised optical microscopy. For the GO dispersion in LC E7, an off-chip threshold voltage of approximately 3.5 V was observed in a 50 μm wide channel (Fig. 5.7). As the voltage was increased further above the threshold voltage, bands of light and dark states appeared, with the light state bands centred around GO flakes positioned next to the channel walls. Smaller flakes in the centre of the channel are observed to move as the voltage is increased.

The Raman laser can also be used to induce repositioning and reorientation of the dispersed flakes[206]. Flakes can be induced to rise within the fluid host or to move towards (or away from) the walls of the channel controllably. Flake movement can be observed as strong changes in the interference pattern observed in the back-scattered light. In particular, flakes were shown to be drawn towards the laser spot and to circle the centre of the spot (Video available online[5,205]) when the laser intensity was suitably high. This allowed controllable repositioning of the flakes within the microfluidic channels.

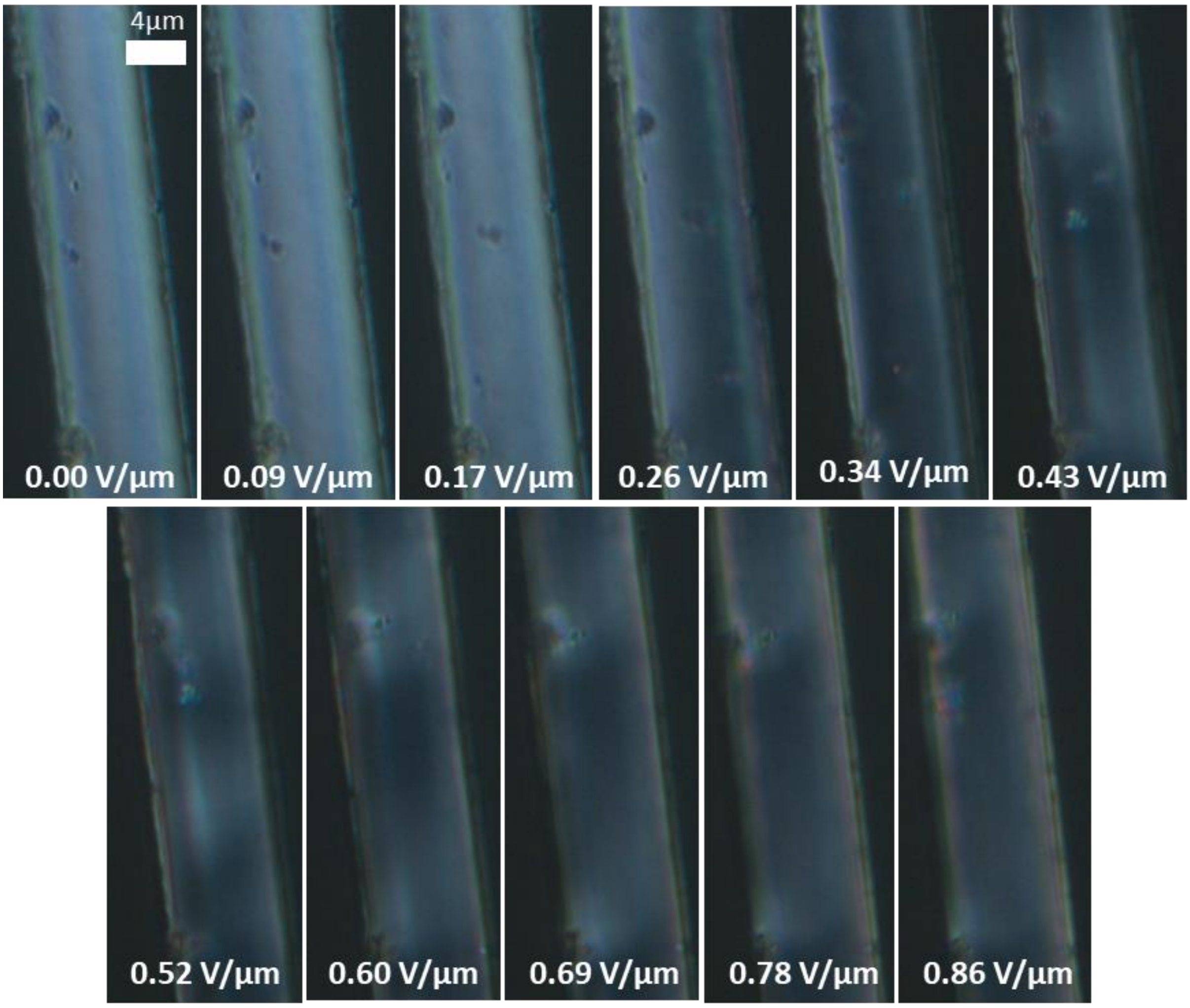

Figure 5.7*: Polarised optical microscopy images showing the change in orientation of liquid crystal E7, with GO flakes dispersed, as the applied field strength between the walls of an 11.6 μm wide channel is increased.*

5.2 Determination of nanoparticle positions.

In one dimension.

Understanding the dynamics of 2D nanoplatelet spatial alignment is essential for the realisation of three-dimensional metastructure formation. External stimuli, such as applied electric field and light coupling[12,140] [Videos available online[5,205]], induce dynamic re-ordering of suspended 2D nanoparticles. Here, a Raman laser was exploited to move a GO flake within a channel (Fig. 5.8a), while simultaneously being used to monitor the *xyz* alignment over time. The variation in the experimental Raman spectra for different flake positions within the channel is illustrated in Fig. 5.8b. Raman measurements were performed using a Renishaw 1000 system (with a 514.5 nm excitation wavelength from Ar$^+$ laser, a power of 5 *mW* and a spot size of approximately 3 *µm*) and on a Horiba

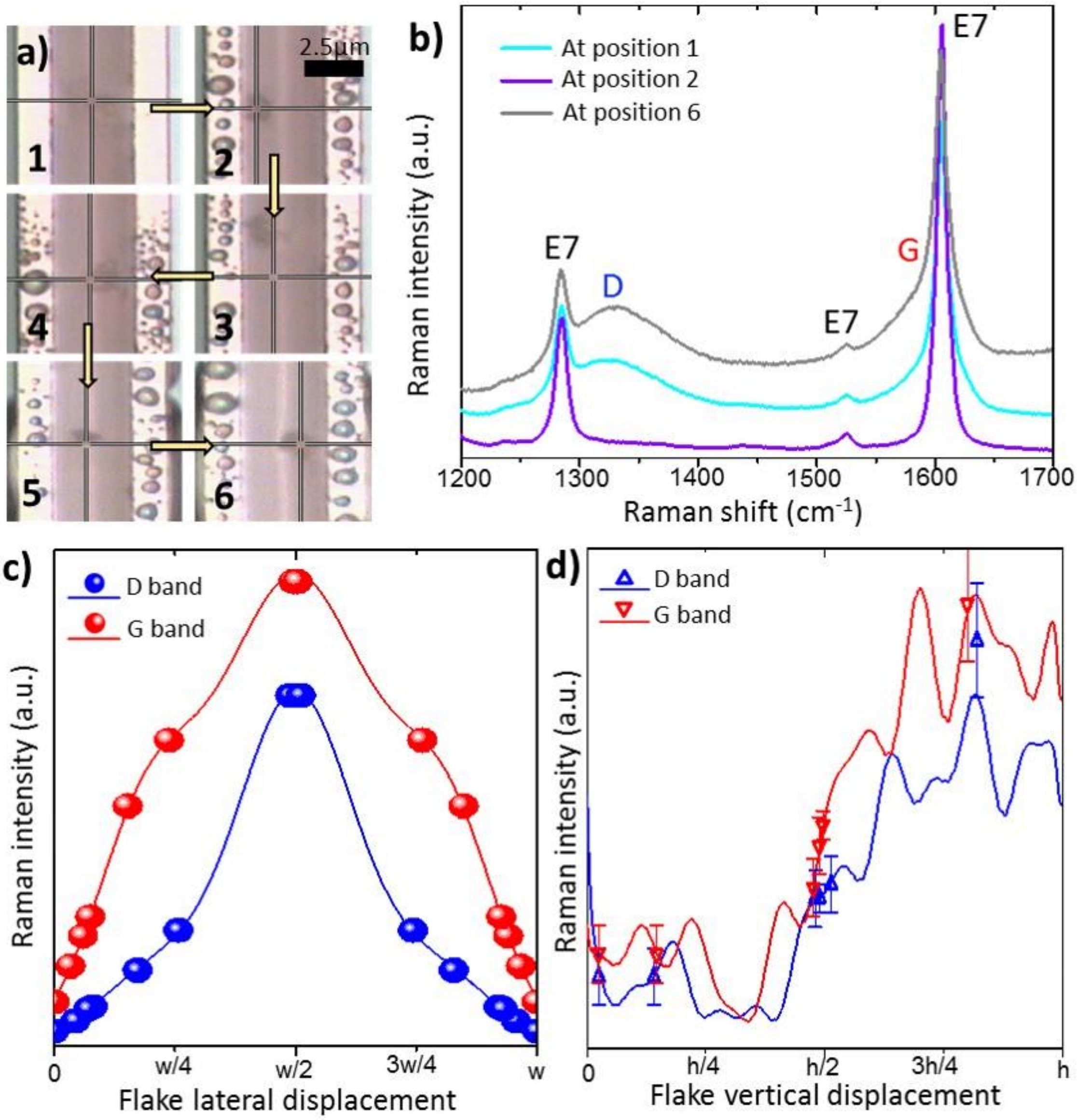

Figure 5.8. a) *GO flake movement induced by the Raman laser. Each image represents the change after 10 s exposure time in the order in which they were observed.* ***b)*** *Raman spectra of a GO flake dispersed in liquid crystal E7 within a narrow channel (approx. 3.6 µm) at positions 1 (cyan), 2 (violet) and 5 (grey) as seen in* ***(a)****.* ***c-d)*** *The variation of the Raman intensity of the GO D (blue) and G (red) bands for lateral (****c****) and vertical* ***(d)*** *displacements of a GO flake within the microfluidic channel. Solid lines give the numerically determined Raman intensities. Flake positions determined from normalised experimental spectra are shown as points. For lateral displacements, the error in the experimental measurement is given by the size of the symbols.*

Raman system (with an excitation wavelength of 532 *nm*, a power of 8.75 *mW* and a spot size of approximately 5 *μm* when focused through a x50 objective).

The effect of the flake position on the Raman signal intensity was modelled, using the SMM, by varying the position of the oscillating dipoles within the optofluidic waveguide channel both laterally and vertically. Vertical displacements were defined from the bottom surface of the channel and lateral displacements from a side wall. For vertical displacement variation, the flake was fixed at the lateral centre while for lateral displacement variation it was fixed at the vertical centre. The liquid crystal in this case was defined as commercially available E7. One can then choose parameters of the optofluidic waveguide that demonstrate strong enhancement of both the D and G bands. The ratio of the D and G band intensities is not constant as the position is varied (Fig. 5.8c-d). For lateral displacements (Fig. 5.8c), there are ratios of 11 and 32 between the minimal and maximal intensities determined numerically for the D and G bands respectively. For vertical displacements (Fig. 5.8d), the maximum and minimum values of the average intensity differ by factors of around four and five times for the D and G bands respectively.

For the lateral displacement of the flake, the ratios of the intensities of the GO D and G bands were extracted from experimental spectra when a flake was next to the wall and when moved further towards the centre of the channel. These ratios were then used as a multiplier on the numerically determined intensity for the flake next to the wall (position 2 in Fig. 5.8a) to determine an approximate displacement. Positions approximated using experimental data in tandem with the numerically determined results are closely matched to the values observed using optical microscopy techniques, falling within the experimental error.

The positions of the individual GO flakes within the liquid crystal host can be accurately predicted from the Raman spectra, specifically by looking at the G and D band intensities relative to a reference position. Table 5.1 summarises the predicted positions shown in Fig. 5.8c. For each of the six experimental positions determined, there was a strong agreement between the predictions made using the D and G band intensities respectively, with the greatest disparity being just 2 *%* of the optofluidic waveguide width. For each experimental flake position, there are two predicted values given for the D and G peaks respectively. This is due to centrosymmetric nature of the cavity in the *x* direction. This centro-symmetry is also responsible for the smooth nature of the numerically determined curves. By breaking this symmetry- for example by using an off-centre laser spot or by having walls of different permittivity- the numerical analysis would no longer return a centrosymmetric intensity profile which may lead to a single position being determinable.

Table 5.1*: Summary of positions predicted for various flake alignments by comparing to reference data (*) normalised relative to numerically determined values.*

Flake designation	Normalised D band intensity (a.u.)	Position corresponding to D band intensity (% of cavity width)	Normalised G band intensity (a.u.)	Position corresponding to G band intensity (% of cavity width)	Difference between D and G positions (% of cavity width)
Ref*	0.05*	0.000 1.000	0.18*	0.000 1.000	0.0000
A	0.09597	0.045 0.955	0.33937	0.034 0.966	1.1000
B	0.14839	0.071 0.929	0.47437	0.060 0.940	1.1000
C	0.15806	0.081 0.920	0.56063	0.075 0.925	0.5500
D	0.32177	0.173 0.827	1.05563	0.153 0.847	2.0000
E	0.5	0.258 0.742	1.35	0.238 0.762	1.9230
F	1.55	0.489 0.511	2.06	0.496 0.504	0.7000

For flake position A, optical microscopy determined that the flake was aligned precisely next to the wall of the optofluidic waveguide. The position as determined from the Raman spectrum suggested the flake was displaced by around 4.5 *%* if looking at the D band or 3.4 *%* if looking at the G band. Similarly, for flake position E, optical microscopy determined that the flake was positioned 21 *%* of the way across the channel. The position as determined from the Raman spectrum suggested the flake was displaced by around 25.8 *%* if looking at the D band or 23.8 *%* if looking at the G band. For flake position F, optical microscopy determined that the flake was positioned 45 *%* of the way across the channel. The position as determined from the Raman spectrum suggested the flake was displaced by around 48.9 *%* if looking at the D band or 49.6 *%* if looking at the G band. In all cases, the position predicted from both the D and G bands individually was within a few *%* of the optical microscopy measurement. It was estimated that the optical microscopy measurements had an error of approximately ±5 *%* due to the difficulty in accurately observing the flake edges and hence the centre of the flake. The lateral position can therefore be determined with similar precision to optical microscopy (approx. ±5%) currently, but with scope for the error to be reduced significantly by improving the signal-to-noise ratio.

For the vertical displacement of the flake, again the ratios of the intensities of the GO D and G bands were extracted, this time from data with the flake at the bottom of the channel and further towards the surface. The ratios were then used to multiply the numerically determined intensity with the flake at the bottom of the channel to determine an approximate displacement. The numerical analysis covering the effect of vertical flake position shows close agreement with the experimental data. The vertical position of the flake cannot be determined from optical microscopy but the close agreement of the positions determined separately from the D and G bands confirms that the method is accurate. Therefore, the predictions made from the Raman spectra are the most accurate method of determining the vertical position currently available. While this technique is proposed as a method for monitoring self-assembly of 3D metastructures comprised of 2D materials, this approach may also find applications in a wide range of other areas such as controlling flake alignment for liquid phase deposition of 2D materials[10,66] or for spatial monitoring of nanoparticle distributions[207].

In two dimensions.

Let us then look to extend this methodology to two dimensions. In this case the aim shall be to track molybdenum disulfide particles dispersed in a liquid crystal host. The microfluidic structures used were carefully designed to enhance the intensity of the Raman spectroscopy signal from the molybdenum disulfide particles. To achieve this enhancement, the desirable microfluidic geometry was determined from numerical analysis of the Raman light generated under laser excitation at 532 nm, at normal incidence. The backscattered Raman signal intensity was again numerically determined for wavelengths corresponding to the scattering from the Raman active bands using the scattering matrix method. The molybdenum disulfide flakes within the nanocomposite were modelled as a system of chaotically-oriented oscillating electrical dipoles within the microfluidic channel, with the dipole emission as the origin of the Raman signal. They were assumed to have widths of 1 µm while being negligibly thick. The previously proposed and demonstrated silicon-on-insulator (SOI) based optofluidic waveguide channel design for in-situ micro-Raman were used for the detection and monitoring of the integrated nanocomposite, where enhancement is achieved due to tuning of the Fabry-Pérot type resonances within the geometry of the microfluidic structure. The channels are bounded by: air above, two silicon walls, and a silicon dioxide buffer layer below. Below the buffer oxide layer is the silicon substrate. The optofluidic waveguide design was optimised to significantly enhance the back-scattered Raman signal from the incorporated molybdenum disulfide nanoplatelets. Channels were designed to be 15 µm deep and 3.7 µm across, and the buffer oxide layer to be 2 µm thick (Figure 5.9).

Having utilised careful design of the geometry to enhance the Raman signal of a particle, a method to accurately track the position of the liquid dispersed particles in two dimensions simultaneously is desired. A method combining numerical determination of the dependence of the Raman signal intensity on a particle's position with experimental spectral analysis has been developed.

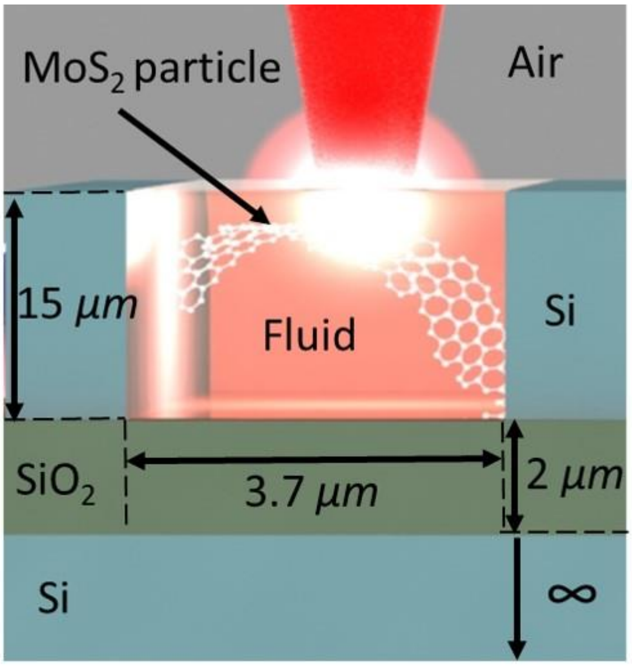

Figure 5.9. *Schematic of the cavity design showing dimensions.*

Again, using a scattering matrix method, let us first establish the effect of a particle's position on the intensity, here for the two characteristic bands of molybdenum disulfide at wavenumbers of 386 cm^{-1} and 404 cm^{-1} respectively in the case of a monolayer[178,208]. The effect of the flake position on the Raman signal intensity was modelled by varying the position of the oscillating dipoles within the optofluidic waveguide channel both laterally (*x*) and vertically (*y*), with the third dimension (*z*) invariant in this case and therefore displacement in the *z*-direction has no effect on the Raman signal. However, the only barrier to modelling with a variant *z* is the increasing computational time required.

Two methods for analysing the effect of the particle position in two dimensions simultaneously were considered. First, the individual contributions of moving the particle in one dimension while keeping the other fixed at its central point was considered. By then convolving the two individual contributions one gets an estimation of the full effect of moving the particle in two dimensions. This method would be ideal, as it requires considerably less computational power due to the greatly reduced number of points which should be analysed. However, to test the accuracy the analysis was performed over the full 2D grid as well. Although the general pattern is fairly similar between the two methods, there are significant differences between the relative intensities between points. As such, it should be considered necessary to use the more time-intensive second method and to simulate for each point within the 2D grid in order to have an accurate estimate.

Very little difference is immediately observable owing to the very small difference in wavelength between the Raman photons scattered after interaction of the laser light with the two Raman bands of monolayer molybdenum disulfide respectively (Figure 5.10a-b). The scattered radiation is expected to have energies corresponding to wavelengths of 543.15 *nm* and 543.69 *nm* respectively. However, one can then analyse the difference in the predicted intensities, alongside the ratio between them, at which point a stronger inter-band variance is observable (Figure 5.10c-d).

As test samples to demonstrate the applicability of this technique, liquid crystalline nanocomposite materials consisting of molybdenum disulfide flakes dispersed in a nematic liquid

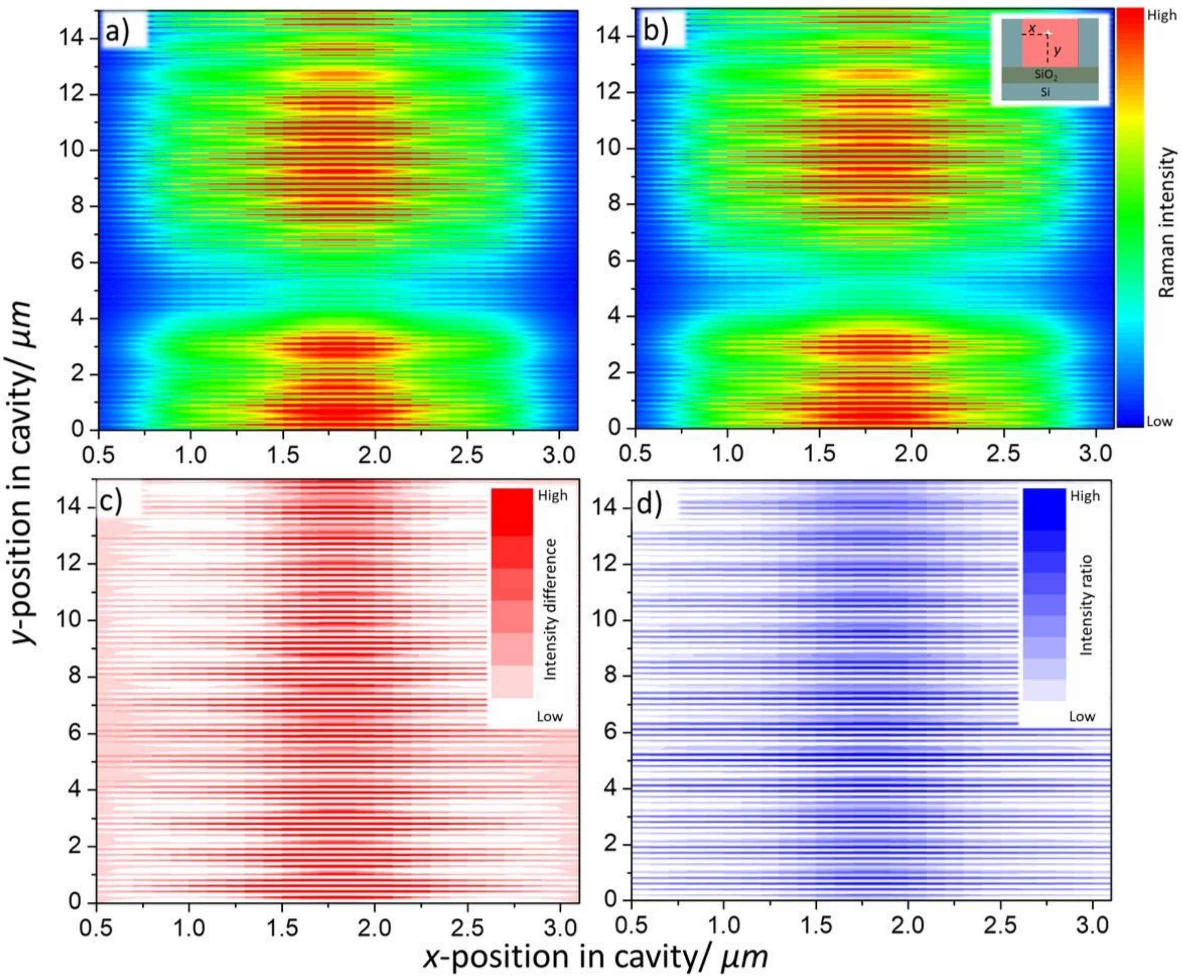

***Figure 5.10**: **a-b)** The predicted intensity for the Raman bands of monolayer MoS$_2$ with emission corresponding to wavelengths of 543.15 nm and 543.69 nm respectively under excitation by a 532 nm laser. Inset: schematic of the cavity showing nanoparticle at position (x,y) in the cavity. **c)** The difference between the Raman intensity for the two bands and **d)** the ratio between the intensities of the bands. By comparing experimental spectra to these numerical results, one can determine the nanoparticle position accurately.*

crystal were synthesised via the following procedure. Molybdenum disulfide was exfoliated to few-layer thicknesses from the bulk solid by use of a liquid phase exfoliation method, wherein ultrasonication of molybdenum disulfide dispersed in a suitably chosen organic solvent induces cleavage of the interlayer van der Waals bonding, with significantly less disruption of the intralayer bonding. This produces a solution containing a range of particle sizes, with platelet shapes typically being observed. Resulting dispersions of few-layer molybdenum disulfide were then centrifuged to remove any residual bulk, or otherwise large, molybdenum disulfide particles. The centrifuged dispersions were then mixed with commercial nematic liquid crystal formulations and subsequently ultrasonicated to ensure homogeneous mixing. The organic solvent was then removed from the mixture under vacuum using a Schlenk line to leave homogeneously dispersed molybdenum disulfide particles suspended in the liquid crystal host. The resultant liquid crystalline nanocomposite was then integrated into microfluidic structures on silicon-on-insulator chips. Dispersions of other 2D materials can also be produced by the same method, and further integrated in the same way as well. Using scanning electron microscopy, and polarised light microscopy, the integration of molybdenum disulfide nanoparticles into microfluidic channels can be clearly observed.

One can then take the experimental Raman spectrum measured for a particle at an unknown position within the microfluidic channel and extract the peak intensities for each of the Raman bands. One advantage of this methodology is that the Raman spectra can be gathered at very high speed, owing to the fact that measurements are only required at a small number of wavelengths and thus there is no need to spend time measuring over a greater range of wavelengths– in essence, the repetition rate of scanning and hence also of positional determination is limited only by the mechanical properties of the Raman spectrometer itself. It should be noted that the procedure below is significantly easier to apply for two or more dimensions simultaneously, than that for a single tracking dimension[5].

The peak intensities are then normalised against the spectrum for a particle of the same size and shape taken in a microfluidic reservoir where there is negligible influence of the microfluidic geometry on the signal intensity. Normalisation is used to account for the fact that the intensities of different Raman bands are not expected to be identical under standard conditions -a fact that the scattering matrix method used doesn’t consider. The normalisation process also removes any enhancement observed due to the substrate rather than the microfluidic structure. There are two requirements for the spectrum used for normalisation: firstly, the aforementioned lack of microfluidic geometry influence on the signal, and secondly, that the liquid depth is equivalent to that in the channels where particle tracking is taking place.

From the normalised data, the ratios of the peaks for the two Raman bands of molybdenum disulfide are calculated. The absolute difference in intensity is also calculated. Let us then compare the normalised peak intensity differences and ratios to those established from the numerical calculations (Figure 5.11). Initially, a broad range either side of the exact peak difference or ratio is used to establish the possible positions of the particle (Figure 5.11 insets). A range of values either side of the precise experimental values is used in order to account for experimental errors in the spectral acquisitions. By narrowing down the range, a decreasing number of possibilities are observed. By comparing the possibilities for the position using each of the peak difference and peak ratios separately, a single point of coalescence can be found corresponding to the particle's precise position within the channel (Figure 5.11). By taking multiple spectra at fixed time intervals, particles can be tracked spatially within the cavity, as their positions change with time. Temporal resolution is limited by the available sampling rate of the Raman spectrometer used.

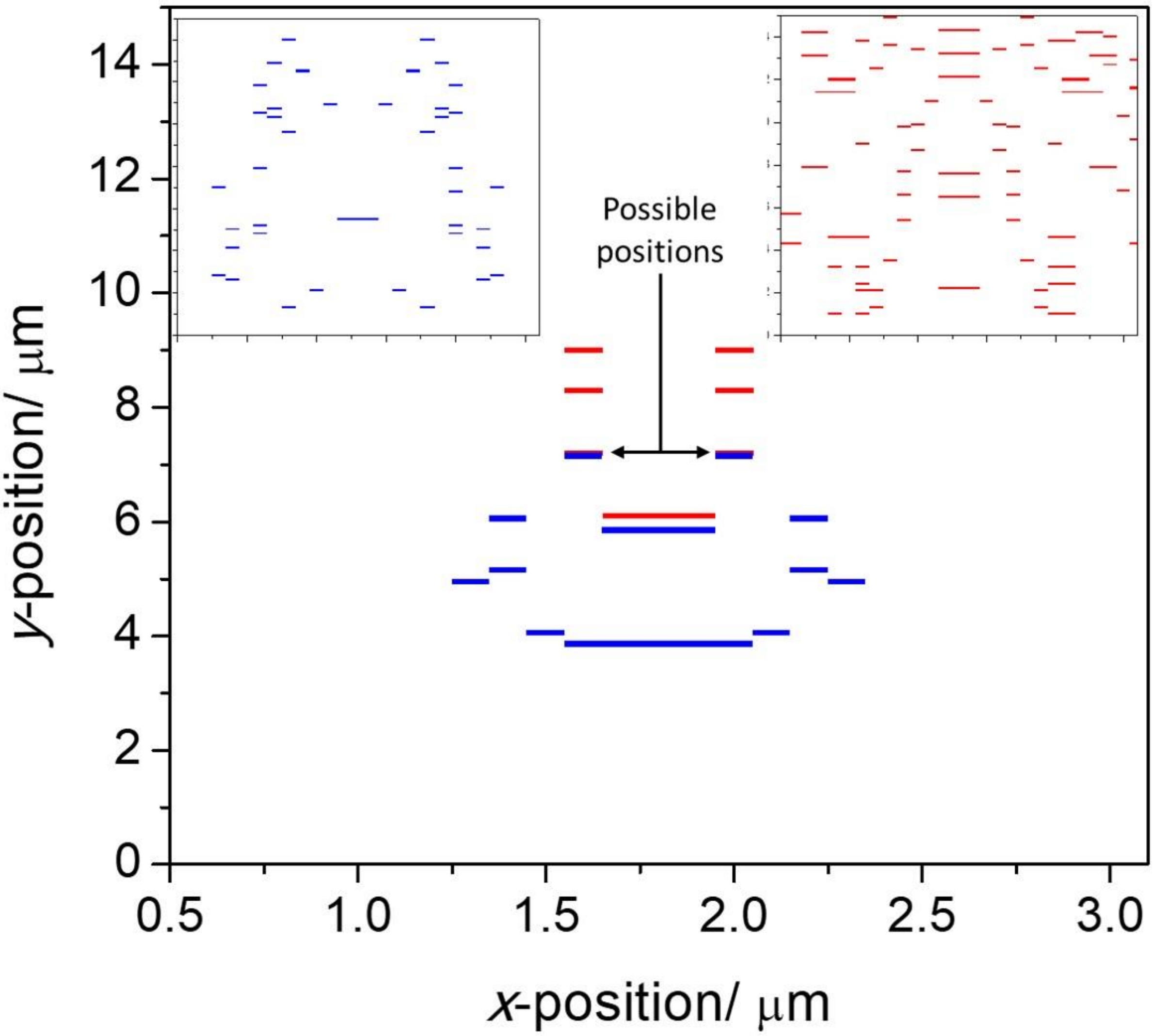

Figure 5.11: *Determination of particle positions by combining numerical analysis and experimental data for differences (blue) and ratios (red) of the two Raman bands of molybdenum disulfide. The differences have been slightly offset so that the overlapping region is clear. Insets: The possible positions using a wider range round the precise experimental values.*

It should be noted that the cavities used were symmetric in the x-direction, hence two possible positions are determined with no way to distinguish them. This would easily be rectified by the use of an asymmetric cavity, or by an off-centre alignment of the exciting Raman laser. There are two potential limiting factors to the accuracy of the positional determination achieved. Firstly, the resolution of the numerically determined data set. However, this can readily be mitigated given greater preparatory computational time. Secondly, the accuracy of the experimental spectra. This can also be improved by a number of different means. Further optimisation of the cavities used to give greater signal enhancement would reduce the percentage errors involved. Alternatively, spectra could be acquired for longer, sacrificing potential temporal resolution in exchange for spatial accuracy.

In three dimensions.

In the cases considered previously, tracking in three dimensions would be impossible as the third (z) direction is considered to be both invariant and infinite to simplify the computation. Though it would be of considerable benefit to understand the effect of complex 3D geometries on the Raman signal - and hence be able to track particles within them – such work is beyond the scope of this thesis. Breaking the invariance in the third dimension would occur for example when considering a tapered microfluidic device, but the analysis of such a system using the scattering matrix method would be extremely computationally expensive.

5.3 Further considerations.

Particle rotation and angle.

So far, only particles aligned parallel to the bottom of the microfluidic channel have been considered. One can also numerically analyse the effect of rotating a particle in the x-y plane. In order to do so, it becomes necessary to model the particle as a series of oscillating dipoles, rather than as the single oscillating dipole considered previously. With the particle parallel to the bottom of the channel, a symmetric particle can be reduced to a single oscillating dipole as the symmetry causes the contributions of the dipoles on either side to cancel each other. By rotating the particle, that symmetry is broken and hence a greater number of dipoles should be considered.

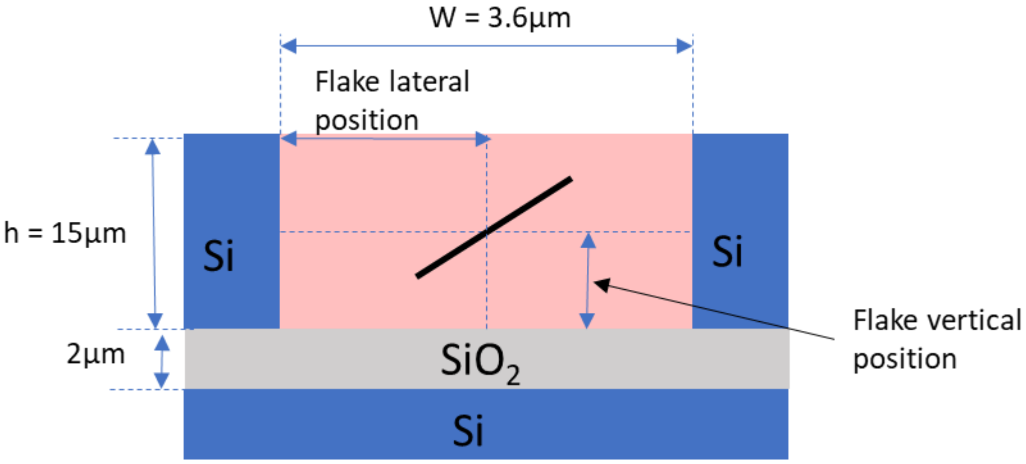

Figure 5.12: *Schematic of the geometry of the structure used in particle rotation simulations.*

Here, a 2D graphene oxide particle is considered. One can model the particle as an ensemble of 99 oscillating dipoles evenly distributed in a linear arrangement. Using the scattering matrix method as before, let us analyse the effect of rota ting the particle from a position parallel (0°) to the bottom of the microfluidic channel incrementally to a position perpendicular to the bottom of the channel

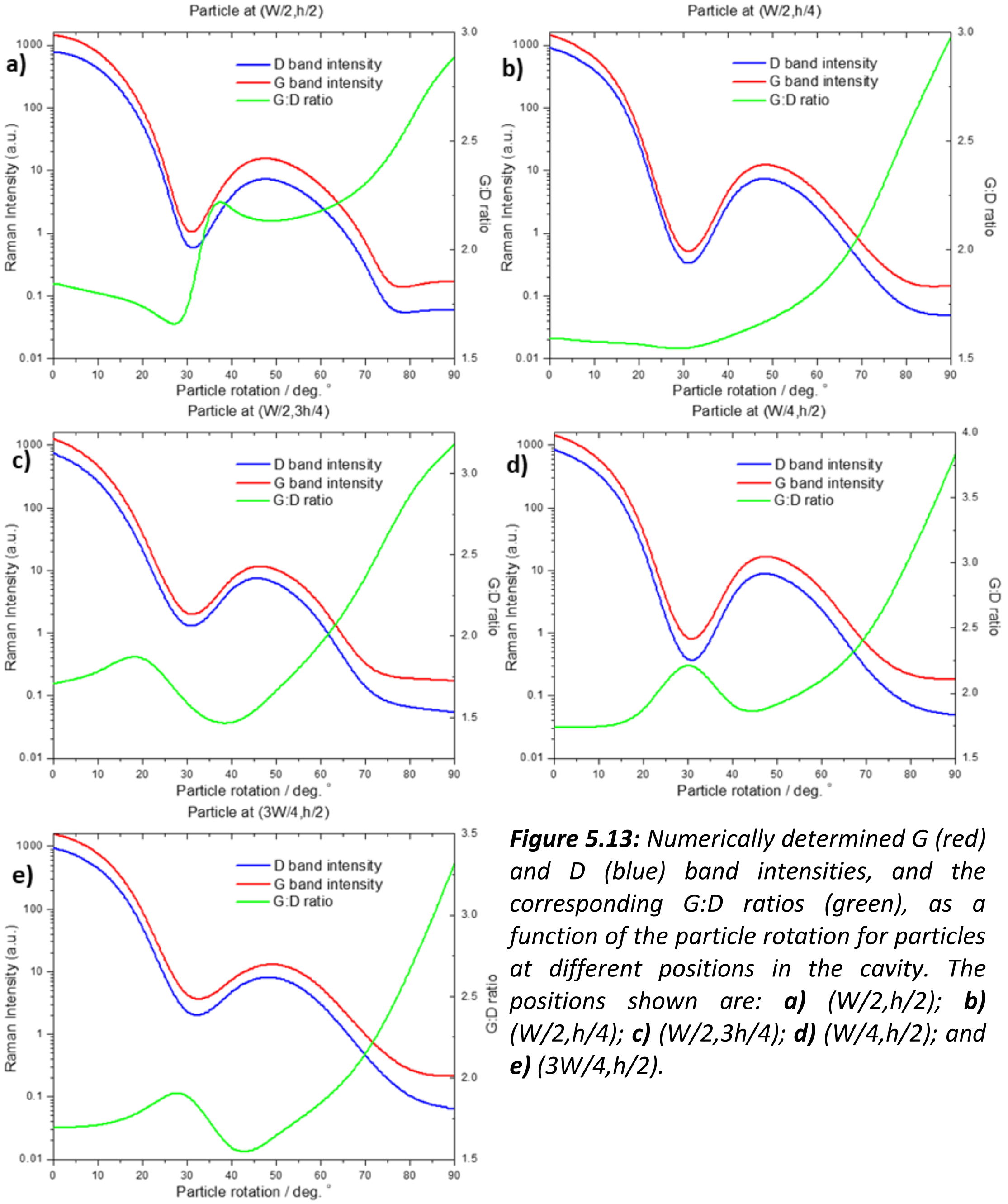

Figure 5.13: *Numerically determined G (red) and D (blue) band intensities, and the corresponding G:D ratios (green), as a function of the particle rotation for particles at different positions in the cavity. The positions shown are:* ***a)*** *(W/2,h/2);* ***b)*** *(W/2,h/4);* ***c)*** *(W/2,3h/4);* ***d)*** *(W/4,h/2); and* ***e)*** *(3W/4,h/2).*

(90°). A schematic of the geometry used in the simulations is given in Figure 5.12. The analysis is repeated with the particle assumed to be centred at different points within the channel (Fig. 5.13). At all points the general form of the dependence of the G and D band intensities is the same. In particular, a clear minimum of the intensity is always observed with the particle rotated through 30°. When considering the ratios of the G and D bands, a more complex relationship is observable. Comparing the ratios if the G and D bands at different positions, a strong positional dependence is evident (Fig. 5.14).

Hence it is clear that the particle rotation and position are coupled and cannot be considered independently. Note also that the symmetry of the microfluidic cavity in the x direction is broken by the presence of the rotated flake such that the intensities are different depending on the direction of displacement along the x direction.

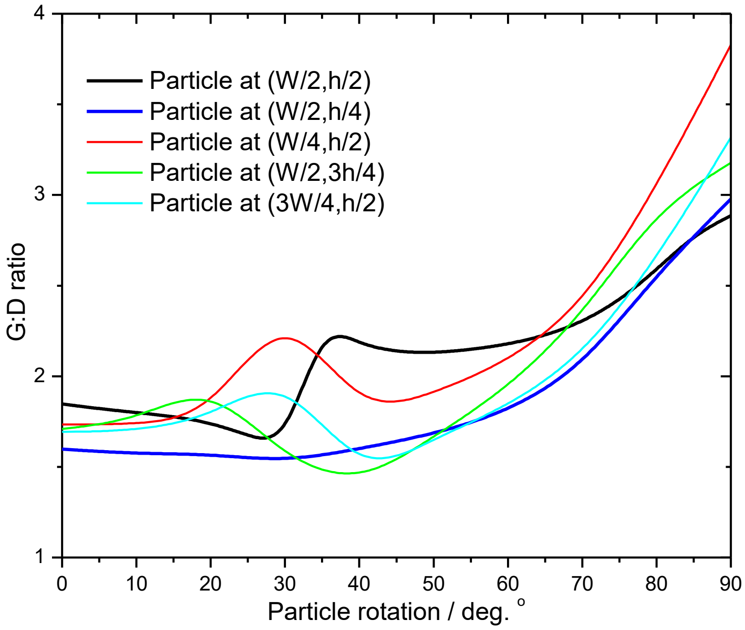

Figure 5.14: *G:D ratio as a function of the particle rotation, plotted for different particle positions within the cavity.*

Multiple particles.

As yet, only a single particle has been considered. Often in real systems multiple particles will be detected at the same time, or will be present in the same area. There is particular interest in behaviour of structured arrays of particles with clearly defined spacings, as these are representative of the ensemble of mesogens in a liquid crystal (or of particles dispersed in an aligned liquid crystal) where the minimisation of energy for the system requires a well-defined and consistent separation between particles.

Again, let us look at the scattering matrix method analysis for the Raman intensity of the G and D bands of graphene oxide. First, let us consider the effect of increasing the number of particles

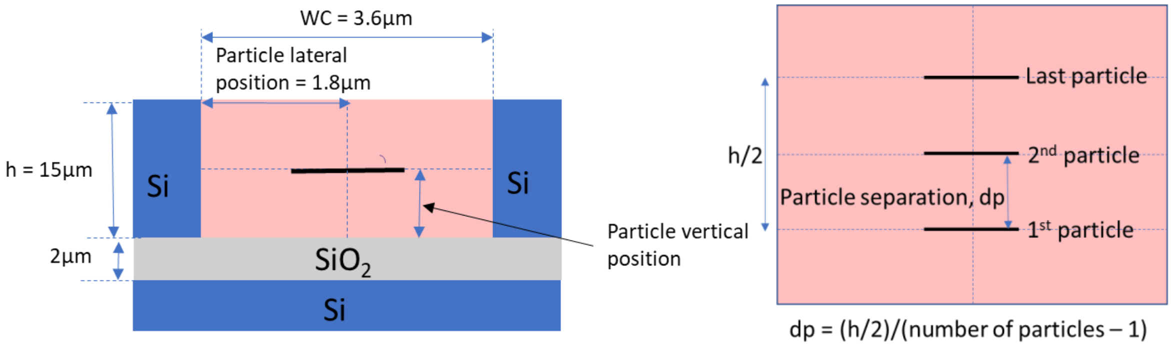

Figure 5.15: *Schematic representation of the geometry and parameters used when numerically analysing the Raman signal from an array of particles evenly spaced over a fixed distance.*

in an array, with the array covering the central two quarters, vertically, of the microfluidic cavity (Fig. 5.15). The particles are spaced equally, with the spacing therefore decreasing as the number of particles is increased. The particles are all modelled as a system of 99 oscillating dipoles evenly distributed in a linear arrangement. Initially, the particles are considered to all be aligned parallel to the bottom of the microfluidic cavity. The Raman intensity is normalised to the number of dipoles present in the array, representing the average intensity per dipole in the system. Naturally with more particles present one would expect a greater signal, but the particular interest here is in any changes due to the interactions between the fields generated by the ensemble of oscillating dipoles rather than an absolute intensity. Let us also consider the effect of rotating all the particles in the array through 45° (Fig. 5.16). The observed dependence of the Raman intensity is non-trivial (Fig. 5.17). Interestingly, this is seen to suppress the Raman signal substantially for all cases of the number of flakes in the array.

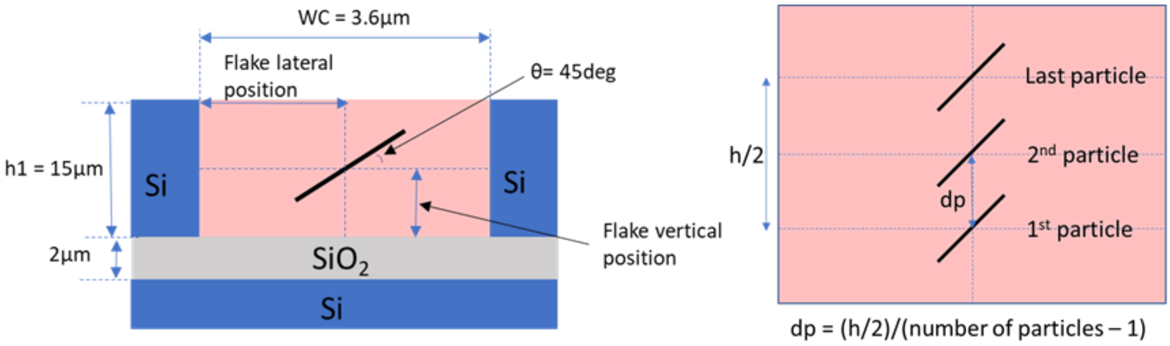

Figure 5.16: *Schematic representation of the geometry and parameters used when numerically analysing the Raman signal from an array of particles evenly spaced over a fixed distance and rotated by 45° relative to the bottom of the cavity.*

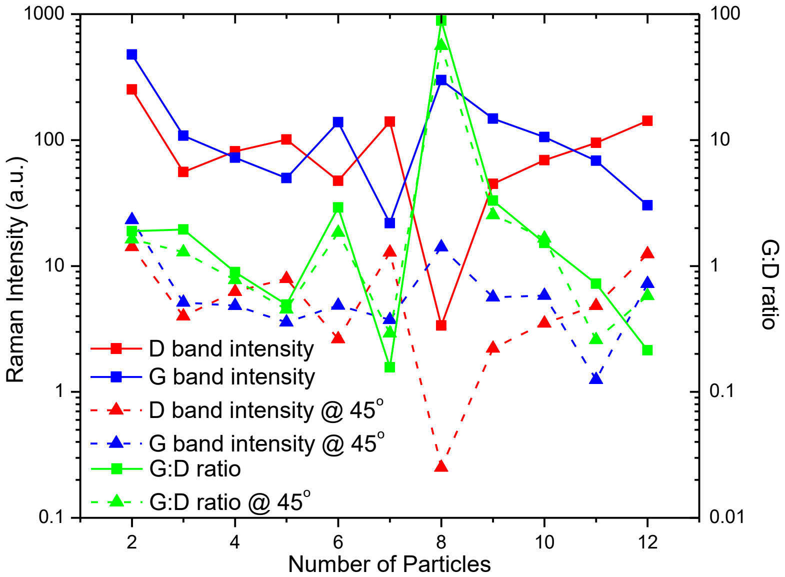

Figure 5.17: *G (blue) and D (red) band intensity dependence on the number of particles in an array, and the corresponding G:D ratio (green), for particles aligned parallel (solid lines, squares) to the bottom of the cavity and at 45° (dashed lines, triangles).*

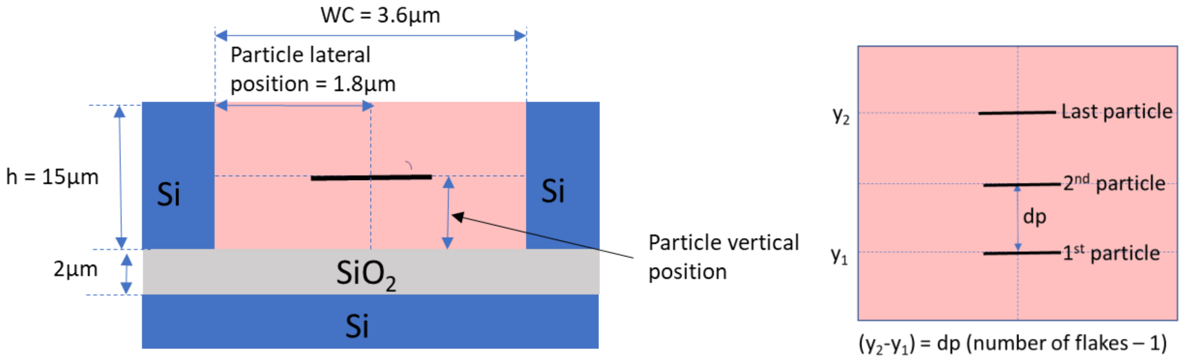

Figure 5.18: *Schematic representation of the geometry and parameters used when numerically analysing the Raman signal from an array of particles evenly spaced over a variable distance* y_2*-*y_1*.*

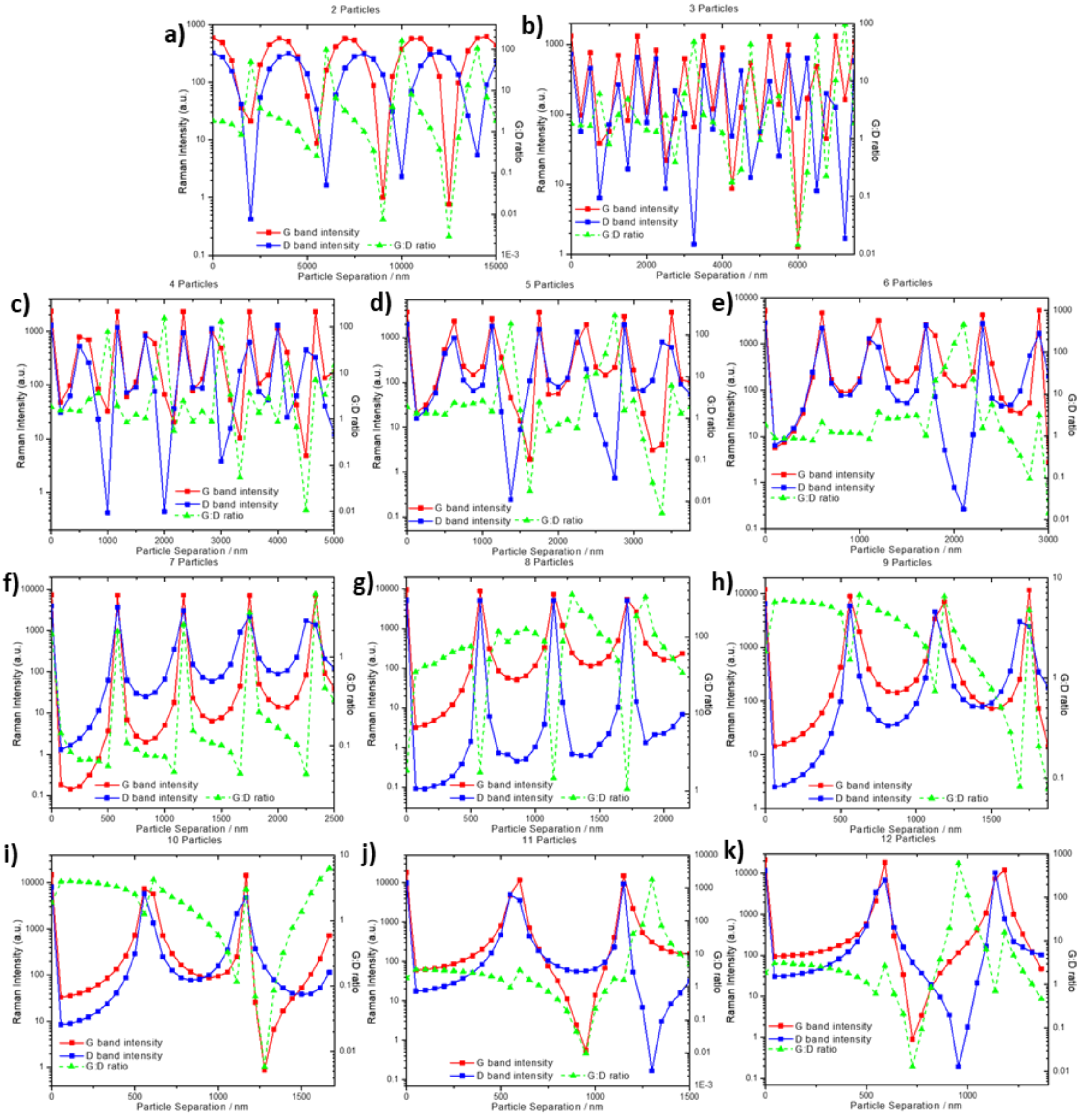

Figure 5.19: *G (blue) and D (red) band intensity dependence on the spacing of particles in an array, and the corresponding G:D ratio (green), for arrays of:* ***a)*** *two particle;* ***b)*** *three particles;* ***c)*** *four particles;* ***d)*** *five particles;* ***e)*** *six particles;* ***f)*** *seven particles;* ***g)*** *eight particles;* ***h)*** *nine particles;* ***i)*** *ten particles;* ***j)*** *eleven particles; and* ***k)*** *twelve particles respectively.*

So far, the array size has been considered to be constant, and adjusted the particle separation to fit that size. Further investigation was undertaken of the effect of different particle separations, while keeping the same number of particles. Let us consider an array of particles aligned parallel to the bottom of the cavity, with the array centred at the centre of the cavity (Fig. 5.18). The limit on the particle spacing is determined by the height of the cavity (in this case, 15µm). For all numbers of particles, it can be clearly seen that the Raman intensity is dramatically increased for specific particle spacings, while being effectively zero at spacings in between (Fig. 5.19). As the number of particles increases, the gap between the 'islands' of strong intensity increases also, and less 'islands' are observed. The origin of such strong spacing dependence is likely to come from the coupling of the individual resonances of the particles. This would imply a strong wavelength dependence, hence the difference in the intensities between the G and D bands.

Consideration of laser focus.

So far, no attention has been paid to the focus of the laser. It has always been considered that the laser is perfectly focused at the top of the cavity. This assumption is unlikely to be realistic as there would be no clear way to ensure that the focus was correctly achieved. Let us consider the opposite extreme, where the laser is perfectly focused on the particle under investigation. This will allow one to gauge the potential effect of the laser focus, in order to determine how necessary accurate focussing is in order to enable particle tracking for example.

Therefore, a second code was developed to analyse the same system. In the first code, an excitation field emitted from a point at the top surface of the cavity, approximating a Gaussian laser

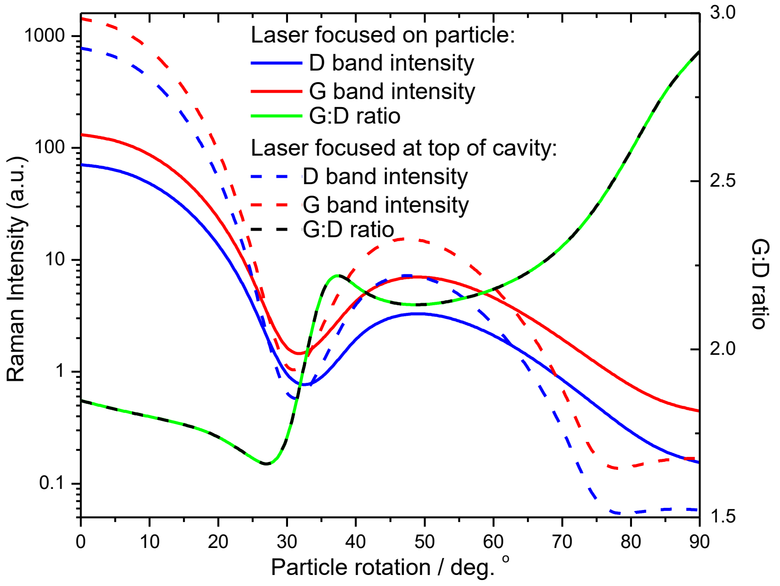

Figure 5.20: *Comparison of the effect of the laser focus position (focused on the particle – solid lines, squares; focused on the top of the cavity – dashed lines, triangles) on the Raman intensity of the G (blue) and D (red) bands, and the corresponding G:D ratio (green), for a particle being rotated.*

beam incident at the central point of the width of the cavity was considered. In the second code, it is assumed that the excitation field is 'emitted', as if scattered, directly at the same points as the dipoles representing the particle(s) under investigation. In this case, a Gaussian beam is again approximated, but this time directly incident on the particle and undergoing no scattering or attenuation until it reaches the position of the particle.

One can then compare the previous results for particle rotation with those gained from the new code (Fig. 5.20). Little difference is seen in the shape of the curve between the two analyses – the only difference is the absolute intensity at each point. Importantly though, the G:D ratio is identical for both cases.

One can also compare the previous results for multiple particles with those found from the new code (Fig. 5.21). Here, a huge difference is seen in the predicted intensities depending on the laser focus. By shifting the laser focus, one shifts the resonance of the excitation field which then greatly impacts the overall expected Raman intensity. However, again the ratio of the intensities of the G and D bands remains constant – it is independent of the focus of the laser.

From the comparisons of the laser focus, it is clear that the laser focus is an experimental parameter that should be tightly controlled so as not to introduce errors when comparing experimental data to the numerically determined data, for example when attempting to track particles.

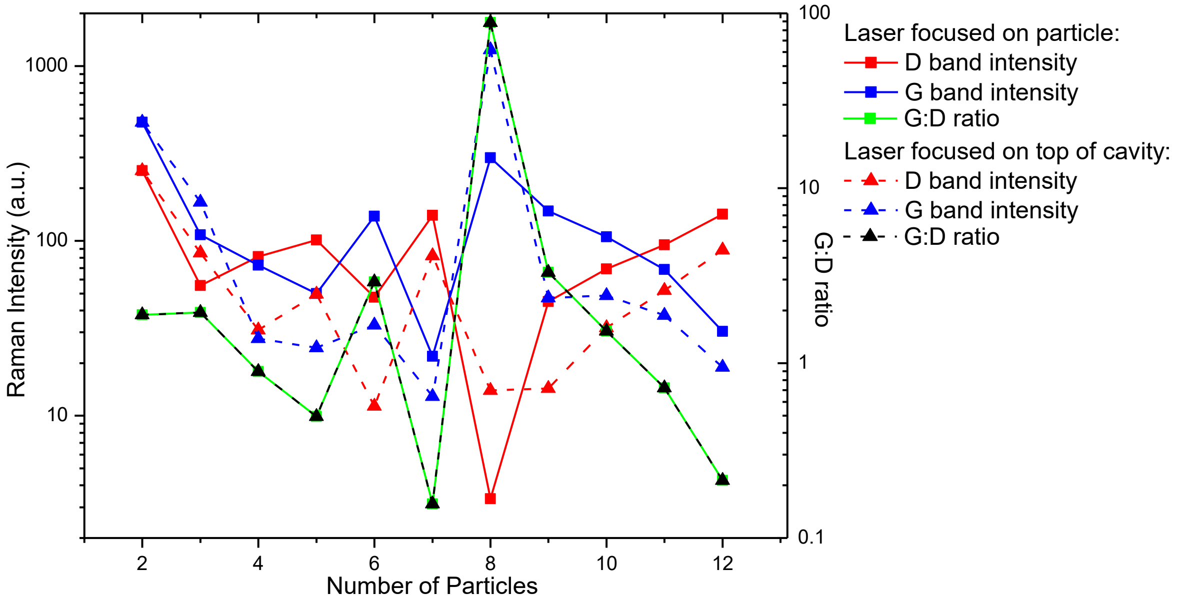

Figure 5.21: *Comparison of the effect of the laser focus position (focused on the particle – solid lines, squares; focused on the top of the cavity – dashed lines, triangles) on the Raman intensity of the G (blue) and D (red) bands, and the corresponding G:D ratio (green), for arrays containing different numbers of particles.*

Other materials.

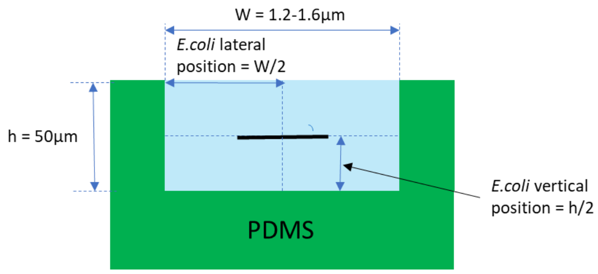

Figure 5.22: *Schematic representation of the geometry and parameters used when numerically analysing the Raman signal from e.coli bacteria as a function of the channel width W.*

2D materials, and specifically graphene oxide particles, have been predominantly considered so far. However, the techniques proposed are not limited to any particular particle – the only limitation is that the particle should possess Raman active vibrations. Further investigation has been undertaken of how the signal for *e.coli* bacteria can be enhanced by a similar method. In this case, let us consider a polydimethylsiloxane microfluidic structure (Fig. 5.22) typically used for studies of bacteria, and look at how different microfluidic channel widths embedded with the structure could affect attempts to characterise the bacteria using Raman spectroscopy. In this case, let us consider the host fluid in the channel to be water. *E.coli* has a large number of Raman active bands of interest. Hence, let us consider the effect of the channel width on the Raman intensity across a broad range of wavenumbers (Fig. 5.23). Again one can see that there is a clear possibility to tune the parameters of the microfluidic structure to maximise the Raman signal intensity. The same Raman bands are observed in each spectrum, but with strong differences in the relative intensities. Also, some bands appear to shift for different channel widths, this can be explained as an effect of the enhancement/ suppression of the Raman signal at different wavenumbers, rather than as a shift in the vibrational resonance.

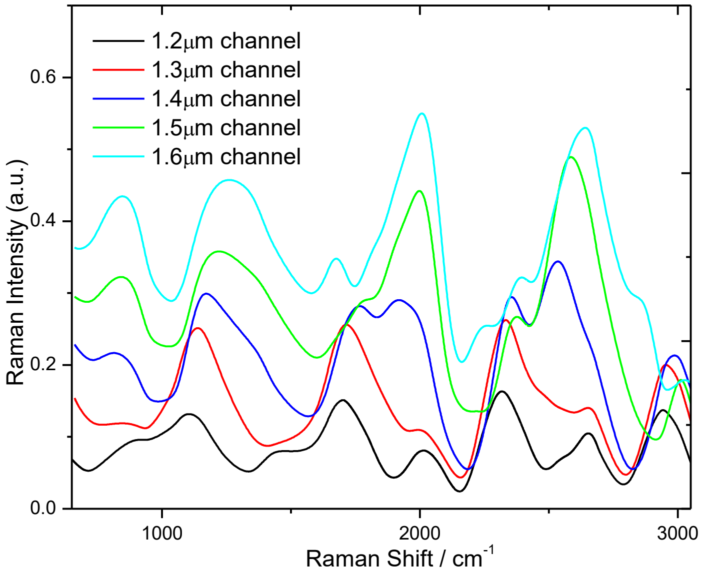

Figure 5.23: *Variation of the Raman signal intensity over the range of Raman shifts where the Raman bands of the bacteria* e. coli *are located. The effect of changing the microfluidic channel width is considered.*

5.4 Determination of nanoparticle shapes.

In the previous sections, a 2D particle with the long axis aligned along the (invariant) z axis has been considered. However, one can also consider other particle shapes and orientations by similar methods. When considering tracking particles in two dimensions simultaneously, the Raman intensity for dipoles oscillating at a grid of positions within a microfluidic cavity has effectively been considered.

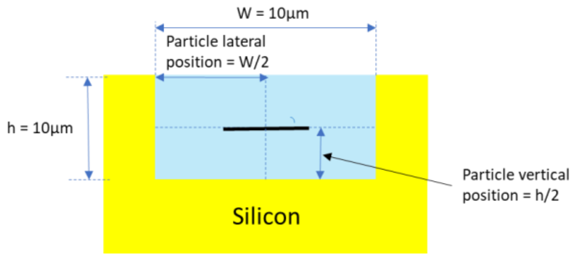

Figure 5.24: *Schematic representation of the geometry and parameters used when numerically analysing the Raman signal for different particle shapes.*

Here, let us consider a simplified cavity with silicon walls and a host fluid of water (Fig. 5.24). The width and depth are both set to 10µm. A scattering matrix method is used as before to predict the Raman intensity for dipoles placed at different points on a fine grid within the channel. To then consider flakes of different shapes, one can select the specific dipoles from this grid to give an overall intensity. One can also consider particles of different sizes using the same methodology. To do so, one can automate the procedure of selecting points from the grid. First a centre point for the particle is set. Then let us fix the number of sides of the particle shape, and the rotation of the shape. Here, the difference in the intensity for different polygon geometries (triangle, square, diamond, pentagon, hexagon, decagon, hectogon [100 sides], circle) containing approximately equivalent numbers of dipoles (same area) is shown. One can observe that there are clear differences depending on the particle shape (Table 5.1), suggesting that particle shapes could be accurately ascertained from Raman spectroscopy data. In the case of a circular particle, the particle geometry is modelled as a many-sided polygon. As the number of sides is increased, the polygon becomes increasingly circular in shape. It is shown that increasing the number of sides of the polygon converges on the solution of a circle (Fig. 5.25) beyond a certain threshold number of sides (between 100 and 1000 in this case, but

Table 5.2: *Raman intensities for particles of different shapes with approximately the same area.*

Shape	Raman Intensity (a.u.)
Triangle	80527
Square	55230
Kite	53486
Pentagon	65200
Hexagon	72139
Decagon	82120
Hectogon	87900
Circle	87953

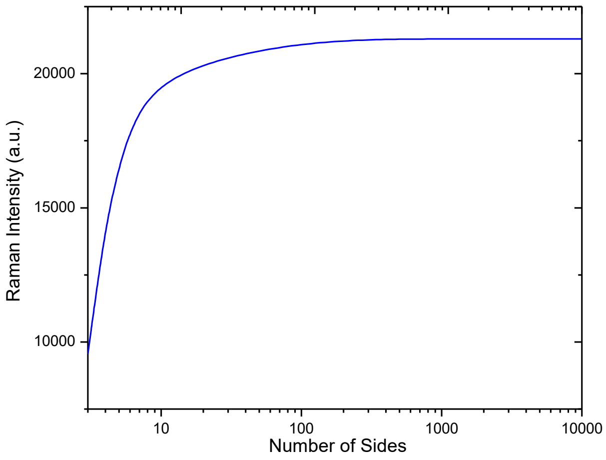

Figure 5.25: *Raman intensity dependence on the number of sides of the polygon, showing the convergence towards the solution for a circle.*

the value would depend on the spacing between points in the grid of determined intensities, as well as on the cavity dimensions), the polygon will contain the same number of dipoles in any case and hence beyond that threshold the polygon can be considered as fully representative of a circle. One can also observe a strong size dependence on the Raman intensity. By considering a range of particle sizes, while fixing the shape, one can observe a general increase in the intensity as the size increases for all shapes (Fig. 5.26). The size adjustment scales the length of each side of the polygon by a scaling factor, increasing the area of the particle, and hence the number of dipoles contained within it.

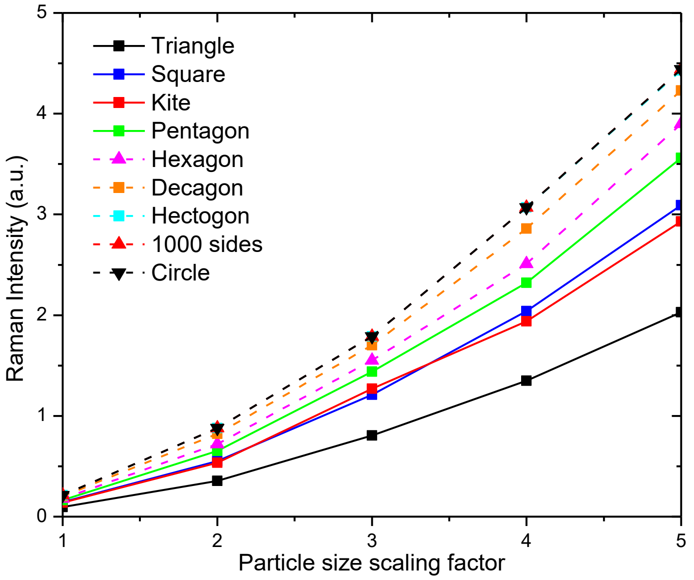

Figure 5.26: *Variation of the Raman intensity for particles of different shapes as the side length is increased by a scaling factor.*

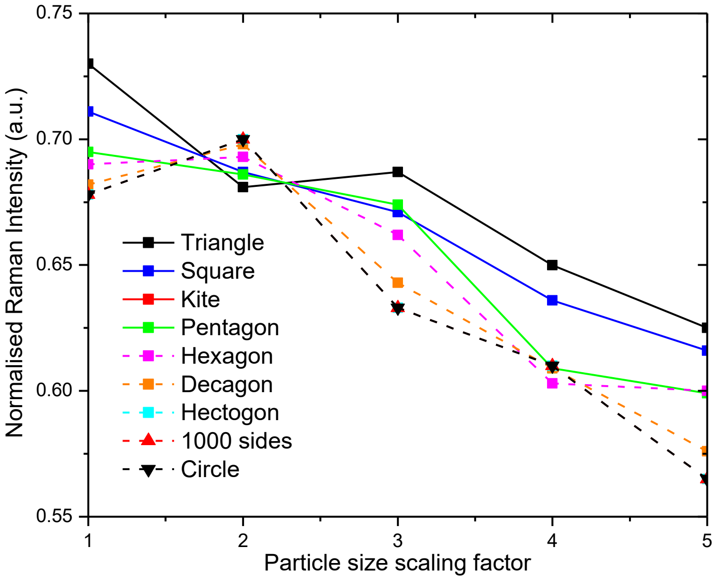

Figure 5.27: *Variation of the normalised Raman intensity for particles of different shapes as the side length is increased by a scaling factor.*

This increase is however non-linear, and non-trivial, as can be observed by normalising the intensities to the number of dipoles within the shape (Fig. 5.27). Hence the particle size should always be considered as a key characteristic when predicting the Raman intensity.

5.5 Determination of nanoparticle concentrations.

Looking at a broader area of a microfluidic cavity containing many particles, it would be interesting to be able to extract the particle concentration from the Raman data. In order to do so, one must first assume that the particles are uniform in size and shape (as already shown, size and shape have a significant effect on the Raman signal for a particle depending on its position within a microfluidic cavity). One must also assume a homogeneous distribution of the particles in the cavity such that the average position can be approximated to the centre of the cavity (as it has already been shown that the position of the particles, particularly any displacement from the centre of the cavity, has a strong effect on the predicted Raman intensity). One can then judge the relative concentrations at different points in the cavity by comparing the experimental Raman intensities of the bands relating to the particles. As a test case, let us look at dispersions of graphene oxide in water at different concentrations. The dispersions are contained within polystyrene cuvettes. Raman spectra are taken with the cuvette on its side, and the laser focused on the side of the cuvette. The laser spot size was around 100µm. The cuvette path length, i.e. the depth of the water containing dispersed graphene oxide, was 1cm. As the Raman spectra contains features related to the host fluid (water) and the cuvette material (polystyrene) in addition to the GO of interest, the Raman spectra are complex (Fig. 5.28). Nevertheless, one can extract the intensities at the positions of the G and D bands for GO and

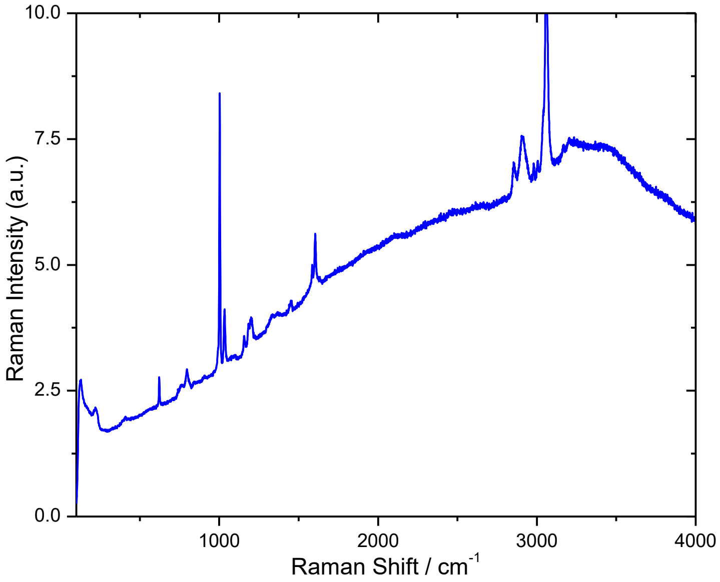

Figure 5.28: *Typical Raman spectrum obtained for a graphene oxide dispersion in water, contained within a polystyrene cuvette. Peaks relating to each of the three materials are present.*

Table 5.3: *Raman intensities and calculated values of the relative concentration from the D and G bands of graphene oxide dispersed in water and measured in a polystyrene cuvette. The order of the values for the determined relative concentrations is also given.*

Sample	Spectrum	Normalised Raman Intensity		Relative Concentration from:				Concentration rank (low to high)
		G band	D band	G band	D band	Average of G and D bands	Using average of two spectra	
1	1	1.000	0.930	1.000	1.000	1.000	1.266	6
	2	1.532	1.424	1.532	1.532	1.532		
2	1	-0.263	-0.214	-0.263	-0.230	-0.246	-0.122	1
	2	-0.018	0.021	-0.018	0.022	0.002		
3	1	1.456	1.448	1.456	1.558	1.507	1.259	5
	2	0.978	0.970	0.978	1.043	1.011		
4	1	0.706	0.585	0.706	0.629	0.668	0.585	3
	2	0.538	0.432	0.538	0.465	0.502		
5	1	1.183	0.961	1.183	1.034	1.109	1.020	4
	2	0.997	0.806	0.997	0.867	0.932		
6	1	1.483	1.210	1.483	1.301	1.392	1.341	7
	2	1.361	1.133	1.361	1.219	1.290		
7	1	0.455	0.543	0.455	0.584	0.519	0.356	2
	2	0.134	0.232	0.134	0.250	0.192		

use them to estimate the relative concentrations of different samples (Table 5.2). However, one sees little consistency even between different spectra for the same sample. In some cases, one can also extract negative relative concentrations, which are clearly unphysical. While the exact concentrations in the cuvettes were unknown (due to surface interactions and precipitation effects), the general order of increasing concentration for the different samples was expected to follow 2<7<1<3<4<5<6 as this was the order of extraction from an orginal solution with a concentration of around 500mg.mL^{-1}. Each sample was extracted from the top fraction, which should always contain the lowest concentration due to the effect of gravity causing sedimentation, and also due to aggregation. From this data, the ranking 2<7<4<5<3<1<6 is obtained. It is clear therefore that looking directly at the Raman intensity for the bands of the material is insufficient to ascertain the concentration effectively. It should be stressed that only the relative concentration, rather than an absolute concentration, can be extracted in this manner at best. Ideally, one would be able to extract an absolute concentration, but this would only be possible where data for a known concentration was already available.

To overcome this issue, let us consider the Raman bands of the host fluid. The host fluid spectrum can easily be taken without any particles present, and this can be used as a guiding baseline. One can then take spectra for different concentrations of particles and compare to that baseline. One can note that the intensity of the Raman bands of the host fluid can be directly related to the scattering volume of the fluid. As the concentration of the particles is increased, the scattering volume of the host fluid must correspondingly decrease, and hence a decrease in the Raman intensity is expected.

Table 5.4: *Raman intensities and calculated values of the change relative to a pure water baseline (B), from the water O-H stretching band at 3057 cm^{-1} in the spectra graphene oxide dispersed in water and measured in a polystyrene cuvette. The order of the values for the determined relative concentrations of graphene oxide as determined from the change in the Raman intensity is also given.*

Sample	Spectrum	Raman Intensity	Average of two spectra	Normalised relative to Sample B	Change in Raman Intensity (%)	Concentration rank (low to high)
B	1	2.029	2.126	1.000	0.000	-
	2	2.224				
1	1	1.644	1.601	0.753	24.690	3
	2	1.558				
2	1	2.247	2.102	0.989	1.115	1
	2	1.958				
3	1	1.528	1.575	0.741	25.924	4
	2	1.622				
4	1	1.483	1.514	0.712	28.802	5
	2	1.545				
5	1	1.407	1.439	0.677	32.300	6
	2	1.472				
6	1	1.417	1.422	0.669	33.126	7
	2	1.427				
7	1	1.691	1.768	0.832	16.835	2
	2	1.845				

This decrease can be directly related to the concentration of the particles, and therefore one can extract the particle concentration without considering the Raman bands of the particle. From the spectrum, one can look at the Raman band at 3057cm^{-1} which relates to an O-H stretching mode in the water molecule[209]. By analysing the different spectra at this wavenumber, one obtains the values in Table 5.3. Here the concentrations in the order 2<7<1<3<4<5<6 are obtained as expected. At this point, one has the relative concentrations of the samples. The percentage change in the Raman intensity of the water peak tells one the percentage change in the scattering volume of water, and

Table 5.5: *Calculated concentration values using the change in the Raman intensities, relative to a pure water baseline (B), from the water O-H stretching band at 3057 cm^{-1} in the spectra of graphene oxide dispersed in water and measured in a polystyrene cuvette. Relative and approximate absolute values for the concentration are given.*

Sample	Change in Raman Intensity (%)	Relative Concentration	Approximate Absolute Concentration / g.mL^{-1}
2	1.115	1.000	0.020
7	16.835	15.104	0.303
1	24.690	22.151	0.444
3	25.924	23.258	0.467
4	28.802	25.840	0.518
5	32.300	28.978	0.581
6	33.126	29.719	0.596

5.6 Conclusions.

In this Section, a new characterisation technique, based on Raman spectroscopy is developed, in order to ascertain information about the positions and alignment of 2D material particles dispersed in fluids. In Section 5.1, microfluidic structures were designed to enhance the Raman signal from the 2D materials by up to an order of magnitude, and the enhancement was experimentally confirmed. It is also experimentally shown that integrated 2D material fluid composites can be dynamically controlled using either applied electric fields, or by laser excitation. Section 5.2 demonstrated how the enhanced Raman signal is utilised to enable the tracking of particle positions in one and two dimensions respectively. By numerical analysis of the expected Raman signal, it was observed that there is a strong positional dependence of the Raman signal intensity. Combining that numerical analysis with experimental Raman spectra allowed accurate positional determination for particles dispersed in a fluid. It was also discussed how the technique would be further applied to three-dimensional particle tracking. In Section 5.3, it was analysed how other geometric properties of the particle, or experimental considerations, can influence the Raman signal intensity. Specifically, consideration was given to how particle rotation and angle, the presence of arrays of multiple particles, the focus of the laser, or changing the material under investigation can modify (or otherwise not) the Raman spectrum of the sample. Particle rotation was found to strongly affect the Raman signal. The maximum signal was obtained with the particle parallel to the bottom of the cavity, with a minimum occurring with the particle rotated through around 30°. The shape of the rotational dependence is independent of the particle position, but importantly the ratios of different peaks depend on both the position and the rotation. In Section 5.4, it was shown that the shape of the particle strongly influences the Raman signal, demonstrating potential for shape analysis *via* Raman spectroscopy. It was also shown that the particle size affects the Raman intensity, but in a non-linear manner. In Section 5.5, a method was presented to extract the concentration of dispersed particles from the Raman spectra by only looking at the Raman bands of the host fluid. Whilst looking at the Raman bands of the dispersed 2D material proved challenging and gave inaccurate results, looking at the bands for the host fluid proved to give results that agreed with the expected relative concentrations and absolute values of the order expected.

6. Applications of 2D Material Liquid Crystals.

2D material liquid crystals have many existing and potential applications, as discussed in sections 2 and 3. Consideration is given to how liquid crystalline dispersions enable the fabrication of highly uniform thin films, and how these films can then be applied. Preliminary applications of the thin films are considered. The terahertz properties of the thin films are considered. Their potential for use in laser cavities as saturable absorbers is also considered. Finally, the integration of 2D materials with photonic devices, and how that integration could be used to enable better device operation are considered.

6.1 Thin film fabrication.

To demonstrate one area where the liquid crystalline dispersions could find application, dispersions were filtered from a dispersion of WS_2 in IPA at 5 mg.mL^{-1}, to produce homogeneous thin films from stacked layers of few-layer WS_2. Such films have been widely explored for different two-dimensional materials, and liquid crystalline dispersions of graphene oxide and molybdenum disulfide have been shown to produce higher quality films than non-LC dispersions[66,130,131]. These thin films were then readily transferred to substrates (Fig. 6.1a-c).

Transfer or deposition of thin films produced from filtering of the liquid crystalline dispersion was achieved in accordance with the method described by Shin et al[210], marking a facile and scalable method towards large scale integration of the two-dimensional material. The general steps of the method followed were:

1. Rapid filtering from the LC crystal state to remove the solvent. For this purpose, polytetrafluoroethylene (PTFE) filter substrates were used with pore sizes of 0.02µm.
2. Transfer to the desired substrate through an IPA and heat-assisted lift-off process, as described in the literature.

This process is compatible with many different substrates. Thin films produced in this manner were successfully transferred to: silicon for Raman mapping; Kapton for terahertz measurements; polyethylene terephthalate (PET); and silver mirrors for laser cavity applications.

Films transferred from the LC state show far greater homogeneity than those from non-LC (see Section 4.2) dispersions (Fig. 6.1c). By using liquid crystalline dispersions for filtering, as opposed to non-liquid crystalline dispersions, a significant increase in the homogeneity of the deposited films is observed. Importantly, individual flakes of WS_2 exfoliated by liquid phase exfoliation can be photoluminescent when deposited from the liquid crystal state (Fig. 6.1d), as is also observed for flakes produced by other methods. After transfer to a substrate, Raman spectroscopy mapping (Fig.

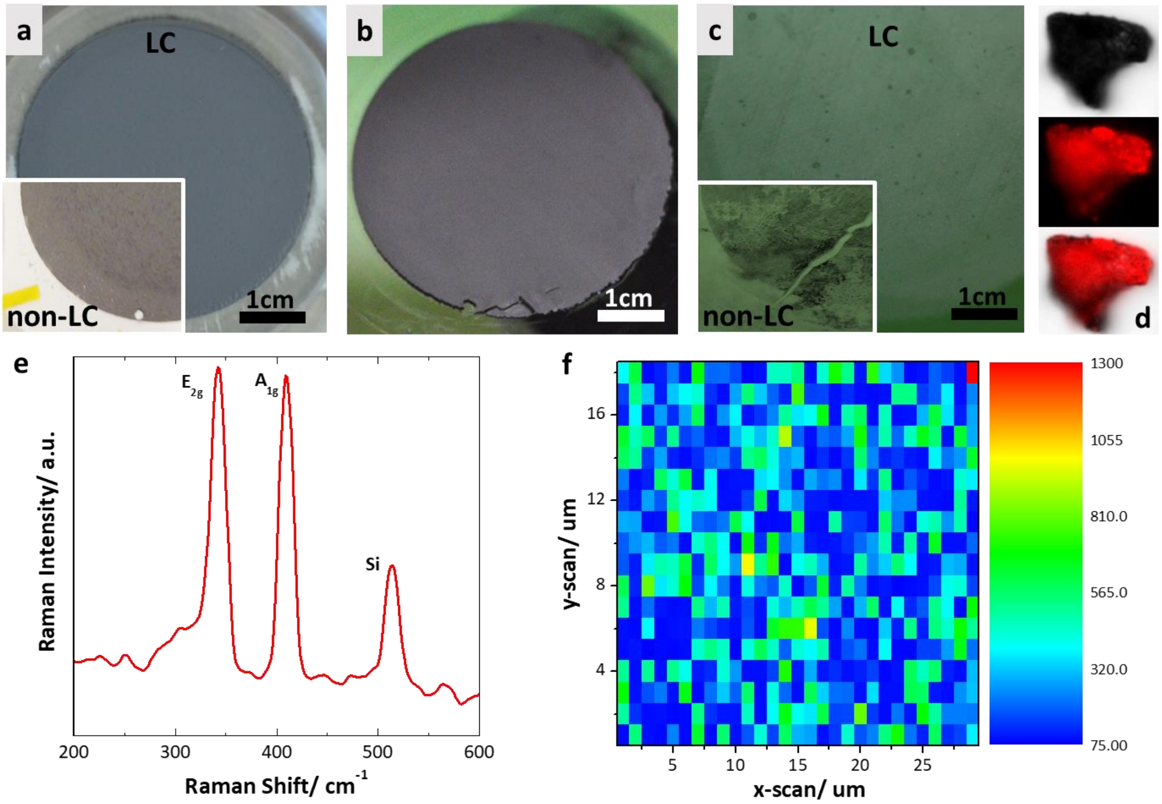

Figure 6.1: a-c) *Progression of a dried film produced from a liquid crystalline dispersion of tungsten disulphide:* ***a)*** *deposition onto filter from an LC dispersion, inset- a deposition onto the filter from a non-LC dispersion,* ***b)*** *the resultant film;* ***c)*** *a considerably thinner film produced by the same method from the liquid crystalline phase, inset- the film produced from the non-LC filtrate.* ***d)*** *Photoluminescence of a single representative flake from the liquid crystalline phase.* ***e)*** *Raman spectrum of few-layer WS_2 showing the two expected peaks in addition to a silicon peak.* ***f)*** *Raman map of the E_{2g} peak of WS_2 showing coverage across the whole surface for an area of 29 µm x 18 µm.*

6.1e-f, Fig. 6.2) of the surface shows complete coverage across large areas- evidenced by the presence of both the A_{1g} and E_{2g} peaks expected for WS_2-, with the variation in signal owing to differing numbers of layers present and surface roughness causing changes in focus.

Raman maps were produced to show the coverage over large areas on silicon, deposited from the liquid crystalline dispersions. Coverage across a wide area is seen by looking at the A_{1g} peak of tungsten disulfide (Fig. 6.2a), which is found to always be present in the spectra. The coverage is non-uniform in terms of layer thicknesses of the individual flakes as well as the overall film thickness, hence the variable intensity. The film thickness (and possibly density) inhomogeneity is also evident from the variable intensity of the silicon substrate peak in the Raman spectra (Fig. 6.2b). The optical image corresponding to the mapped area of the film is shown in Figure 6.2c. The approximate points at which individual Raman spectra were taken are shown by the green grid on the image, although there is some misalignment between the internal optics used for imaging mapped areas, and the optics used for Raman scanning.

The ability to cover large areas with few- or monolayer WS_2 opens up great possibilities in photovoltaic devices, owing to the photoluminescence of WS_2 in the visible range.

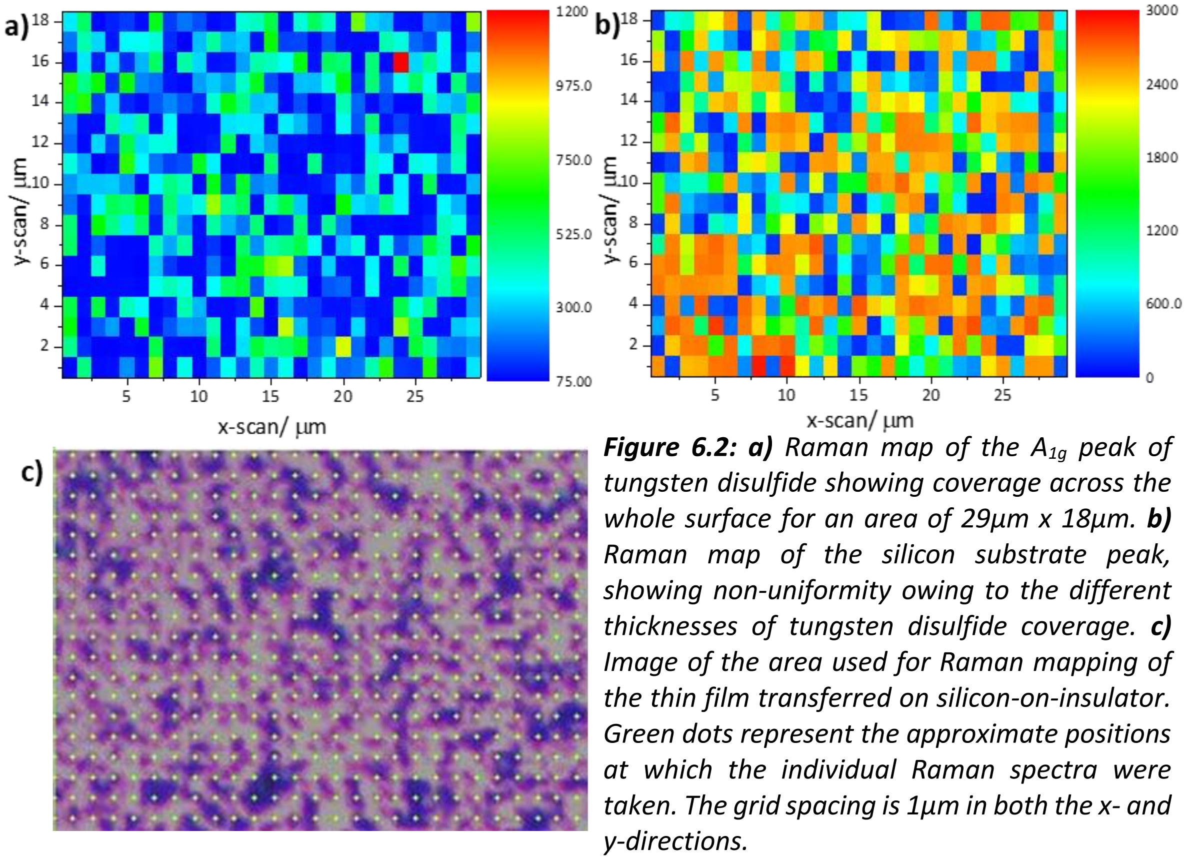

Figure 6.2: a) *Raman map of the* A_{1g} *peak of tungsten disulfide showing coverage across the whole surface for an area of 29µm x 18µm.* ***b)*** *Raman map of the silicon substrate peak, showing non-uniformity owing to the different thicknesses of tungsten disulfide coverage.* ***c)*** *Image of the area used for Raman mapping of the thin film transferred on silicon-on-insulator. Green dots represent the approximate positions at which the individual Raman spectra were taken. The grid spacing is 1µm in both the x- and y-directions.*

6.2 Terahertz applications.

Using the method described in the previous section, WS_2 thin films were transferred to Kapton substrates for measurements in the terahertz (THz) regime. WS_2 is a promising material for applications including laser-induced generation, detection, and conversion of terahertz radiation[211], as this field is currently experiencing both rapid growth, while also suffering from a lack of suitable materials. In particular, materials for use in THz generation, detection and conversion suffer from expensive or difficult device integration, or from poor efficiency of processes. Hence, a key requirement is to improve the integration process from a standpoint of cost, scalability and ease. The terahertz frequency range has noteworthy applications for use in non-invasive medicine control, safety and ultrafast information transfer systems. The transmission of samples in a broadband THz range (0.1–0.8 THz) by use of a laboratory terahertz time-domain spectrometer[212] was studied. The experimental set-up scheme is presented in Figure 6.3. A femtosecond laser (fs laser - the active medium – Yb:KYW; λ = 1055 nm, pulse duration 10 0 fs, repetition rate 70 MHz, output power 3.8 W) radiation beam was divided by a beam splitter (BS) into pump and probe beams. The pump beam was

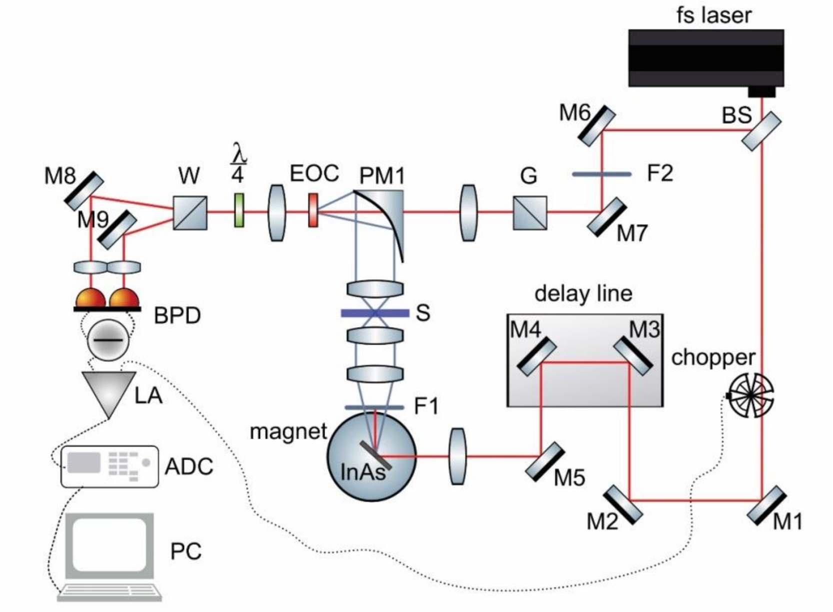

Figure 6.3: *THz time-domain spectrometer scheme. M1-9 – mirrors; BS – beam splitter; F1-F2 - IR filters; S – sample; PM1 – parabolic mirror; EOC – electro-optical crystal; W - Wollaston prism; BPD – balanced photodetector; LA – lock-in amplifier; ADC – analogue-digital converter; PC – personal computer.*

modulated by an optical chopper (OC), passed through a delay line and focused into a THz generator (based on the photo-Dember effect and electron shifting) that consists of a bulk InAs semiconductor placed in a strong magnet field of 2.4 T. Generated radiation passed through a polytetrafluoroethylene filter (F1) to cut off the pump beam, followed by lenses and the sample (S), with some absorption and refraction. To detect THz generation, an electro-optic method was used, with the transmitted THz pulse is collimated by an electro-optical crystal ([100] CdTe crystal (EOC)) for electro-optic detection by an off-axis parabolic mirror (PM). The polarization of the probe beam was fixed by a Glan prism (G) to 45° relative to the THz radiation polarization. The probe beam is also focused onto the same spot of the CdTe crystal. The birefringence in the CdTe crystal induced by the electric field of the THz pulse changes the polarization of the probe beam. The induced change in polarization was measured by a system consisting of a quarter-wave plate (λ/4), Wollaston prism (W), mirrors M_8, M_9, and a balanced photodetector (BPD). An amplified signal was transmitted to a computer (PC) via an analogue-to-digital converter (ADC). The THz-TDS measurements were performed several times at different points of the samples and the averaged values were taken. The beam spot size in this setup is around 3 mm. The integral transmittance of the sample surface was measured. The obtained time dependencies of the THz pulse electric field (wave forms) in the absence of a sample, when passed though substrates, and when passed through films on the substrates were used to calculate THz frequency-domain spectra by means of Fourier analysis.

Using this set-up, the transmission of a thin WS_2 film transferred to a Kapton substrate was measured. The parameters of THz radiation were: spectral range from 0.01 to 1.5 THz with maximum

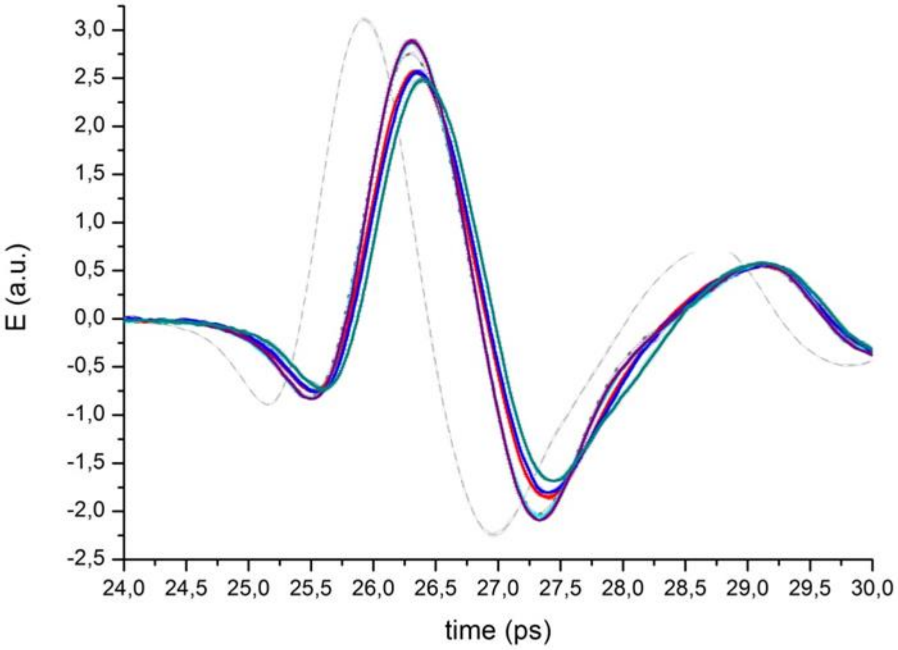

Figure 6.4. *Time dependences of the electric field E(t) of the terahertz pulses through: an air reference (grey dashed), a Kapton substrate (blue dashed) and* WS_2 *on Kapton samples (solid lines).*

at 0.595 THz, average power 30 µW, FWHM 0.45 ps. The time dependence of the electric field $E_{ref}(t)$ of the THz pulse (Fig. 6.4) is obtained, so one can then calculate the complex reference spectrum of the THz pulse $G_{ref}(\omega)$, by calculating the Fourier transform of the corresponding time sequence. By placing the required object in the path of THz radiation, it is possible to measure the change in the temporal form of the THz pulse and the complex spectrum of radiation transmitted through it – $E_{obj}(\omega)$ and $G_{obj}(\omega)$. The transmission spectra (Fig. 6.5) of samples were calculated using the following relationship:

$$T_{layer+Kapton}(\omega) = \frac{\left|G_{layer+Kapton}(\omega)\right|}{\left|G_{air}(\omega)\right|} \tag{19}$$

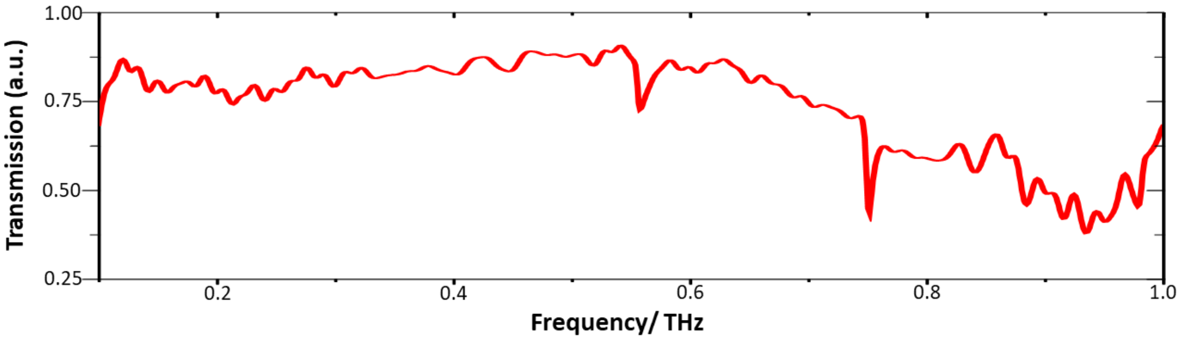

Figure 6.5. *Transmission in the terahertz regime, through a thin film of* WS_2 *transferred onto a Kapton substrate. Measurement is relative to an air reference.*

The Kapton substrate was chosen due to its low absorption in the terahertz region from 0.1 to 2.5 THz. It can be observed that the WS_2 film is transparent in the broadband region from 0.1 to 1.0 THz. Transparency in the THz range is very useful for generation, detection and modulation applications in THz devices. Drawing on the example of another common transparent 2D material, graphene, the use of such thin layers has been shown to increase the efficiency of the optic-THz conversion[213], allow control of the polarization and modulate THz radiation[214]. WS_2 material is also interesting to consider in terms of another effect; the influence of magnetic part of electromagnetic field in the THz range is more perceptible than in visible range, so theoretically the influence of the terahertz magnetic field in such magnetically sensitive materials (WS_2) can be determined. If chirality exists in the visible range, it also can be present in the THz region. One can assume that with the help of WS_2 it will be possible to control the magnetic field of a THz pulse, as shown in the concept of spin-current driven THz oscillator devices[215].

The films give comparable results to those produced previously by other methods such as chemical vapour deposition as reported in the literature[211,216–218], but also have significant further benefits such as: greater scalability; reduced cost; high homogeneity; and a fine control of the film thickness spanning multiple orders of magnitude. Such films could therefore find applications in Terahertz modulation devices.

Further THz measurements were performed on other WS_2 films fabricated from liquid crystalline tungsten disulfide dispersions.

To obtain a LC phase dispersion, an initial 500 mL solution was prepared in a sealed beaker. IPA was used as the solvent and bulk WS_2 particles (Sigma-Aldrich 243639), with dimensions around a few microns on average as the solute at a concentration of 5 $mg.mL^{-1}$.To break down the material a process of ultrasonication in an ultrasonic bath (James Products 120W High Power 2790ml Ultrasonic Cleaner) filled with deionised water was used. Five, hour-long, periods, separated by 30 minutes each to prevent excessive heating of the solvent, were used to ensure sufficient exfoliation of the sample. The resultant dispersions were then put through a process of centrifugation for 10 minutes at 2000 rpm to remove residual bulk material and narrow the distribution of particle sizes present in the solution. After centrifugation, the solution was fractioned, with only the supernatant extracted, to ensure only suitably sized particles remained. The resultant solution was then dried under vacuum (~0.1 atm) in a Schlenk line to fully remove the solvent, before being re-dispersed in IPA again at concentration of 1, 5 and 100 $mg.mL^{-1}$. After re-dispersion, the solutions were again ultrasonicated (for a few minutes) to prevent any aggregated exfoliated particles remaining in the solutions. As the concentration is changed significantly following the centrifugation step, it is necessary to re-establish the concentration following that step. Re-dispersing allows for accurate knowledge of the concentrations of the solutions without affecting the properties of the dispersed 2D material particles. The tungsten disulfide dispersions of all concentrations showed a separation of phases as the volume fraction of the liquid crystal phase was less than 100%.

For the first sample (denoted WS_2_S), 50 µL of solution from the upper, lower concentration, non-LC phase fraction was drop cast directly onto the Kapton substrate and allowed to dry. For the second sample (WS_2_L), 50 µL of solution from the lower down, higher concentration, LC phase fraction was used. Drop cast samples were dried on a hot plate at 70°C for 5 minutes. In both cases, individual particle sizes were measured by atomic force microscopy and scanning electron microscopy, with average sizes determined as 2.5 µm^2 laterally and thickness of 3.9 nm. The difference was the significantly greater overall film thickness for the L sample versus the S sample, owing to the greater concentration of tungsten disulfide in the liquid crystal phase fraction. For transfer to PET, a thin film transfer method was used. First 20 mL of the liquid crystalline solution was filtered using a Büchner flask- under vacuum- onto a nano-porous polytetrafluoroethylene membrane. The film on the membrane was then transferred to the substrate using a heat and IPA assisted method. The substrate was wetted slightly with IPA while heating to 70°C on a hot plate. The membrane was quickly transferred onto the substrate, and as the IPA evaporated through the membrane, the thin film of tungsten disulfide was released from the membrane and hence transferred to the substrate after removal of the membrane. Two samples were produced- one from the 1 mg.mL^{-1} dispersion (WS_2_LC) and the other from the 5 mg.mL^{-1} dispersion (WS_2_HC). Again, average individual tungsten disulfide particle sizes were determined as 2.5 µm^2 laterally and thickness of 3.9 nm. The overall film thicknesses were determined to be approximately 1 and 10 µm respectively. Figure 6.6 shows SEM

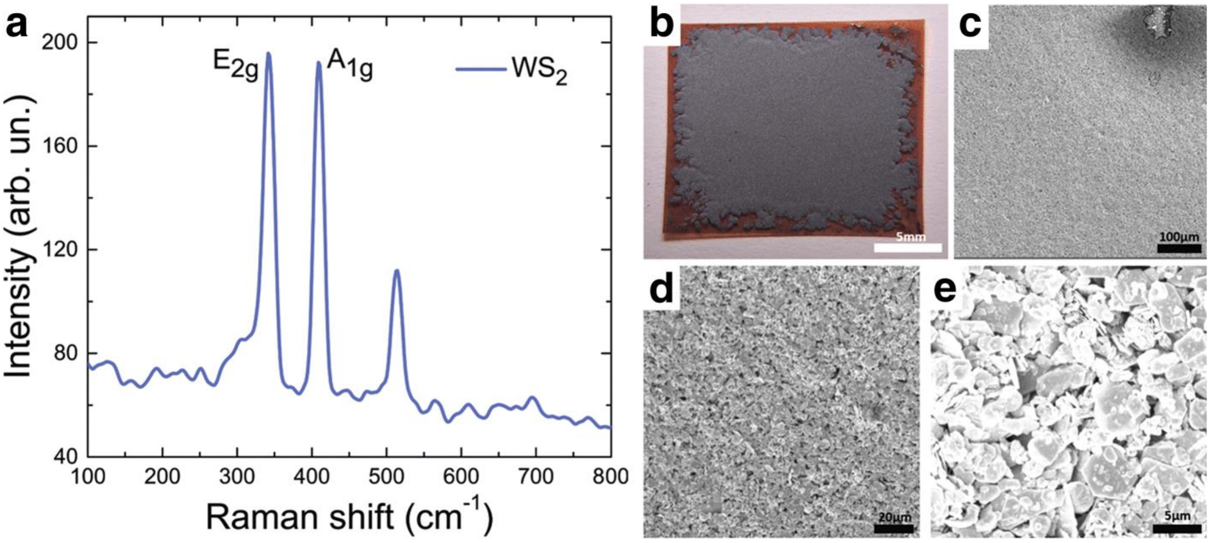

***Figure 6.6.** Raman spectra, photograph and SEM images of WS_2 sample under study. **a)** Raman spectrum of a few-layer WS_2 film on silicon. **b)** Photo of the drop cast film of WS_2 on Kapton. (**c–e)** SEM images of the drop cast film of WS_2 on Kapton at magnifications of **(c)** ×2000, **(d)** ×8000 and **(e)** ×40000.*

and optical images of the WS_2 samples. The Raman spectrum of the film is also presented. In both cases, the uniformity of the coverage is noticeable. From SEM analysis, it can be seen that the majority of the particles are well aligned with the substrate, although some (typically smaller) particles are aligned perpendicular to the substrate. This general alignment is expected when depositing thin films from LC dispersions[17,66,130,219].

The transmission spectra in the visible - near infrared range of WS_2 samples are shown in Fig. 6.7. The experimental data represents the integral transmittance of the samples. Hence, the scattering losses caused by the surface roughness are not separately evaluated; only the overall contribution of the sample to the transmitted radiation is taken into consideration.

Varying the structure dimensions, specifically the film thickness, from 1 to 10 µm for WS_2 LC-based thin films on polyethylene terephthalate (PET) causes a change of the transmission in the range from 400-1100 nm of up to 35%. This is expected due to the greater overall optical density of the thicker film produced from the higher concentration solution.

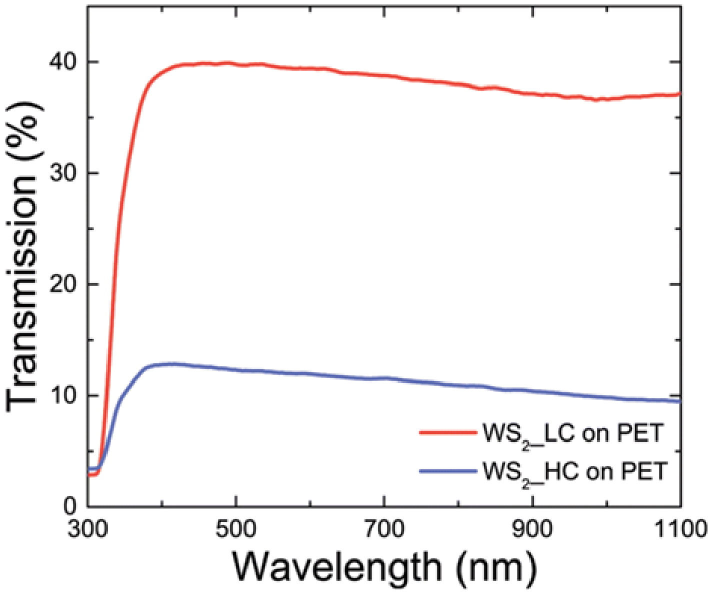

Figure 6.7. *Transmission in the visible and near-IR ranges of* WS_2 *film fabricated from LC phase solutions of different concentrations.* WS_2*_LC sample was produced from a 1 mg* mL^{-1} *solution and* WS_2*_HC from a 5 mg.*mL^{-1} *solution.*

WS_2 on Kapton substrate, shown for different film thicknesses as described in the experimental methods, is fairly transparent in the THz range (Fig. 6.8). The transmission can be easily varied by choosing an appropriate concentration of the LC solution which is then transferred to substrate, and hence controlling the thickness of the drop-cast film. Transparency in the THz range is very useful for generation, detection and modulation applications for THz devices.

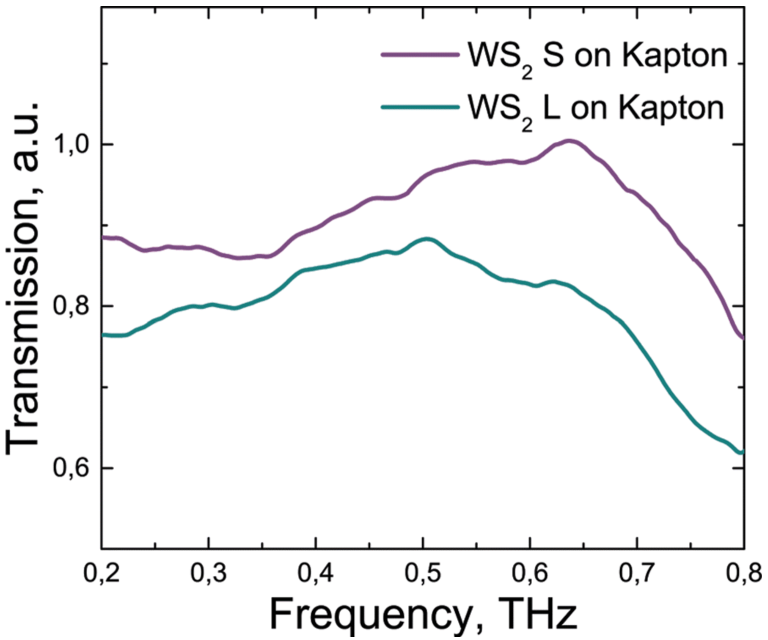

Figure 6.8. *Transmission of WS$_2$ samples in the THz frequency range. Spectra of WS$_2$ films on Kapton substrates, produced from a non-LC, low concentration fraction (WS$_2$ S) and from a LC phase, high concentration fraction (WS$_2$ L).*

6.3 Laser cavity applications.

Q-switching is a technique used to produce a pulsed output beam from a laser. This technique allows the generation of laser pulses with much higher peak powers, but with the same average power that would be achieved with continuous wave operation.

Q-switching is achieved by having a variable attenuator inside the laser cavity. When the attenuator is 'on', light which leaves the gain medium is not reflected back within the cavity, and therefore lasing cannot begin. This attenuation inside the laser cavity gives a corresponding decrease in the quality factor (Q) of the optical resonator. The variable attenuator is known as the 'Q-switch'. Initially the laser medium is pumped while the Q-switch is 'on' to prevent light returning into the gain medium. This produces a population inversion, but laser operation cannot yet occur. Since the rate of stimulated emission is dependent on the amount of light entering the medium, the amount of energy stored in the gain medium increases as the medium is pumped. Due to losses from various processes, after a specific time the energy stored will reach a maximum; the gain medium is then said to be saturated. The Q-switch is then rapidly changed from a low to high Q, allowing light to be returned to the gain medium and optical amplification by stimulated emission (lasing) to begin. As there is already considerable energy stored in the gain medium, the amount of light in the cavity builds very rapidly, with a corresponding rapid decrease in the energy stored. The net result is a short pulse of laser light. There are two main types of Q-switching:

1. Active Q-switching

Here, the Q-switch is an externally controlled variable attenuator such as a mechanical device (shutter, chopper etc.) or an electro-optic device (Pockels cell etc.). As it is externally controlled, the pulse repetition rate can be controlled.

2. Passive Q-switching

In this case, the Q-switch is a saturable absorber, a material for which the transmission increases when the intensity of light exceeds a threshold value. As the laser power increases, the absorber saturates, and the losses are rapidly reduced due to the increased transmission. The pulse rate in this case can only be indirectly controlled (e.g. by changing the pump power) and hence the rate is largely dependent on the properties of the absorber itself. As such, different absorber geometries or structures could result in different pulse repetition rates.

Figure 6.9. *Photograph showing the non-uniform coverage and poor adhesion of the* WS_2*films on the silver mirrors.*

Thin films were also transferred to five highly reflective silver mirror substrates. These mirrors were then tested as saturable absorbers for use in laser cavities. The laser cavities consisted of a gain medium (Erbium-doped crystal) sandwiched between two mirrors. The first mirror was one of those coated with the WS_2 thin film as a saturable absorber. The second mirror was a less reflective output coupler allowing transmission of the laser light. These initial test samples suffered from several difficulties relating to the transfer of the material. That is, the coverage was largely non-uniform and the adhesion of the films to the mirror surface was poor (Fig. 6.9). However, initial tests showed that Q-switching could still be achieved (Fig. 6.10), although was generally unstable and inconsistent

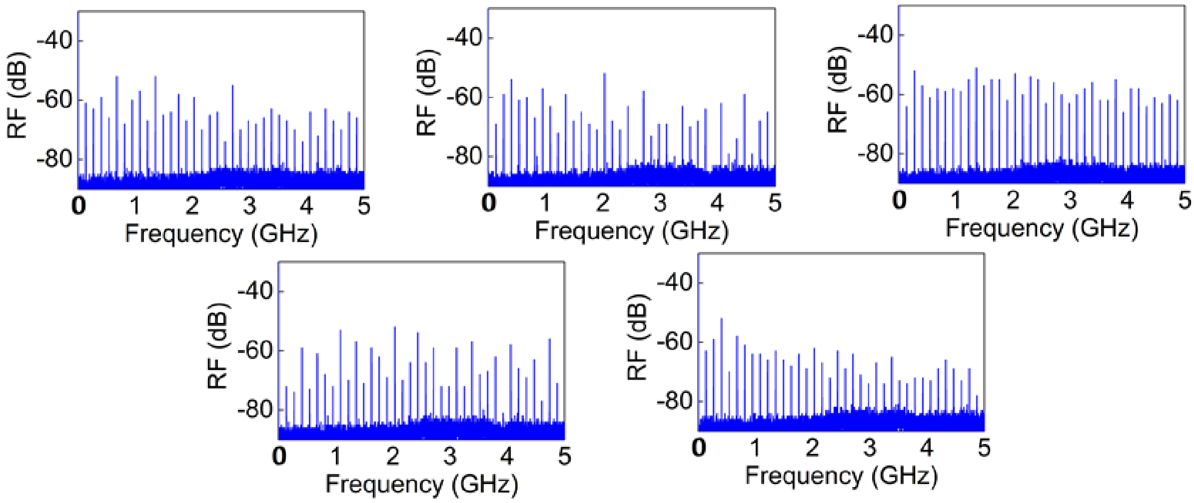

Figure 6.10. *Lasing operation of the five thin films of* WS_2 *on silver mirrors as a function of frequency illustrated by the radiofrequency (RF) output spectra.*

between samples. The radiofrequency (RF) output spectra are measured across a broad frequency range. A regular spacing of the peaks, corresponding to the pulse repetition rate, is observed for all samples. However, the magnitude (and signal-to-noise ratio) of the peaks is inconsistent, suggesting that the Q-switching is unstable for all of the samples. In this case, Q-switching would be achieved passively. For these samples, mode-locked operation has not been achieved. Mode-locking is a technique by which a laser can be made to produce a train of even-intensity pulses, equally spaced in the frequency domain. Mode-locking requires a fixed-phase relationship between the modes of the cavity between the longitudinal modes in the laser cavity such that constructive interference occurs. The failure to achieve mode-locked operation is likely due to the high fluence threshold due to the films being thicker than would be typically desired.

6.4 Integration with photonic devices.

To integrate with photonic devices, thin films were transferred to silicon nitride substrates (Si_3N_4). Si_3N_4 is chosen due to its negligible absorption at the wavelengths typically used for optical communications using silicon photonics (typically $\lambda = 1550\, nm$). As an initial test case, simple straight waveguides were considered. The waveguides should support the propagation of light, with an absorption defined by the imaginary part of the effective refractive index. By positioning a 2D material on top of the waveguide, one can modify the effective refractive index and hence the

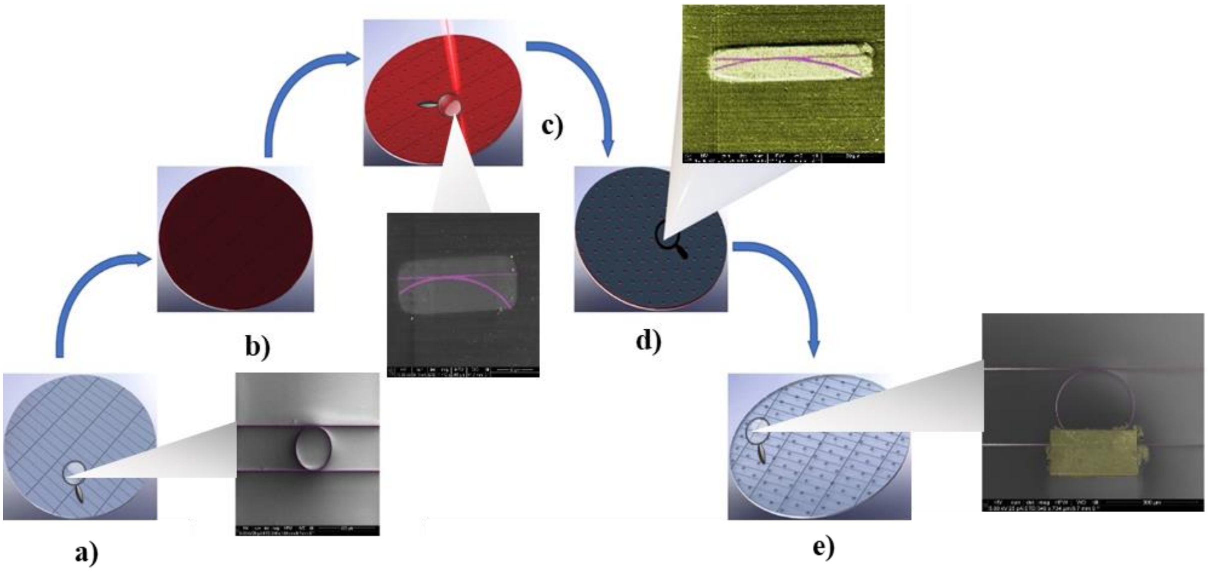

Figure 6.11. *Back-end CMOS fabrication process flow for the integration of 2D materials with photonic devices.* ***a)*** *SOI wafer with pre-existing photonic structures.* ***b)*** *Photoresist deposition onto the photonics wafer.* ***c)*** *Development of micro-trenches and other structures within the photoresist layer, down to the photonic waveguide layer, as a template for 2D material deposition.* ***d)*** *Wafer-scale transfer of 2D material thin film.* ***e)*** *SOI photonic wafer with 2D materials controllably integrated onto the photonic structures and devices after photoresist removal.*

absorption of the waveguide. As a further test case, microring resonators were considered. The purpose of a microring resonator is to preferentially transmit a particular wavelength corresponding to the resonance of the ring. The resonance of the ring is dependent upon its effective refractive index, and by integrating 2D materials with the ring structure, one can modify that effective refractive index. Firstly, the photonic structures (Fig. 6.11a) were produced. E-beam lithography followed by inductively coupled plasma reactive ion etching (JLS RIE) was used to fabricate waveguide and micro-ring devices from a 150nm-thick Si_3N_4 layer, supported on a SiO_2 isolating layer of 2 µm on top of a base layer of thick silicon. A TI PRIME adhesion promoter and MaN 2403 (polymethylmethacrylate [PMMA]) e-beam resist were used to allow patterns to be designed using an NBL e-beam system, followed by post exposure bake for 90 seconds at 90°C to reflow the resist surface and reduce sidewall roughness. The etching was performed with a CHF_3/O_2 reactive gas mixture.

Thin films of 2D materials were deposited using back-end processes. The first step here required a photoresist mask to be created to define the areas where the material should be deposited. Above the Si_3N_4 photonic layer, a 1 µm thick photoresist was produced via spin-coating. This was followed by pattering using a laser writing method with a precision of 0.6 µm and using n-methyl pyrrolidone to remove the exposed areas. This gave defined trenches within the photoresist layer, reaching down to the photonic layer (Fig. 6.11b-c). With the photoresist removed from the required areas, thin films were transferred onto the top of the wafer (Fig. 6.11d) by the methods previously described. After removal of the photoresist mask, final individual devices with specific, micron-size structures of 2D materials- as desired and designed - were achieved (Figs. 6.11e and 6.12).

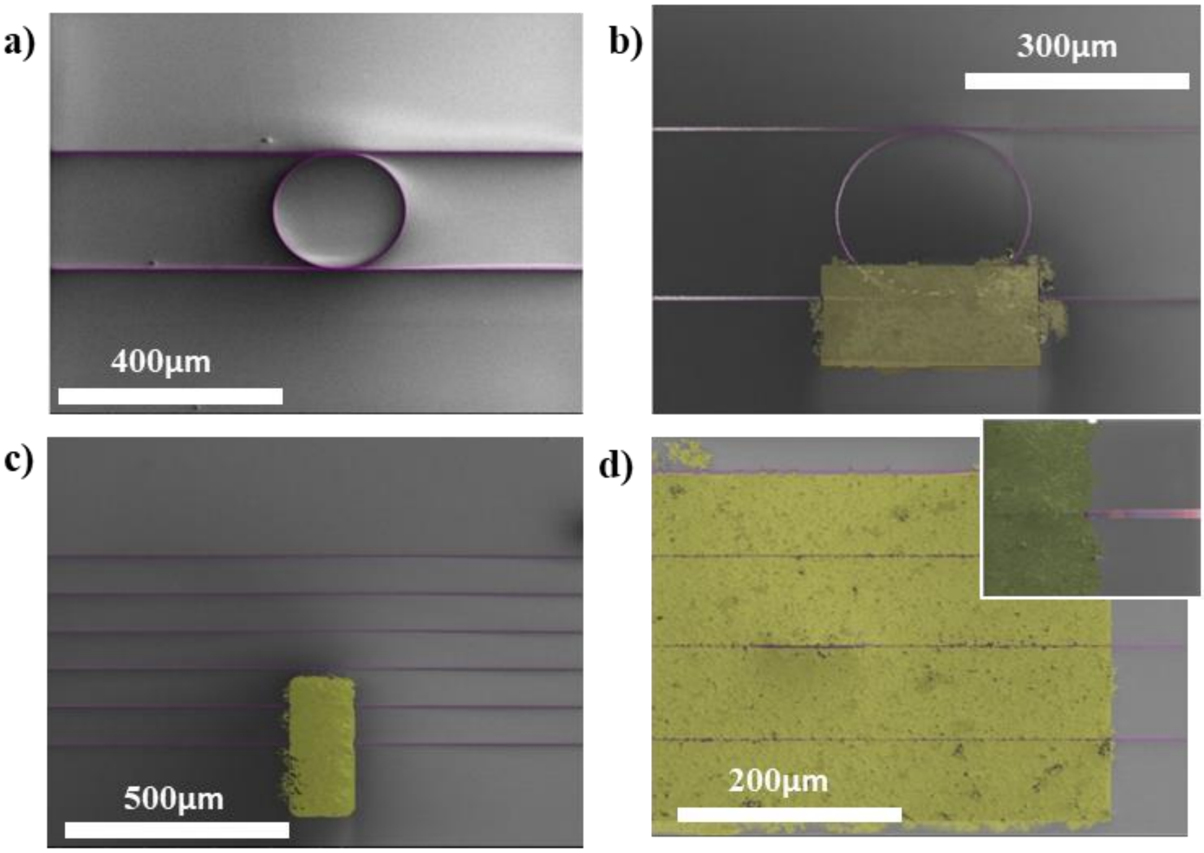

Figure 6.12. *False colour SEM images of:* ***a)*** *a Si_3N_4 micro-ring resonator (purple) add drop filter structure, with a 100µm radius and 1.2µm width;* ***b)*** *a 300 x 200µm rectangular liquid-exfoliated graphene patch (yellow) on the top of the add-drop filter structure;* ***c)*** *bare waveguides at the top and a 100 x 400µm graphene patch across the bottom waveguide structures; and* ***d)*** *large-area liquid-exfoliated graphene covering multiple waveguide structures (Inset: zoomed view on the graphene coverage over the waveguide).*

The thickness of the different 2D materials deposited on top of the different Si_3N_4 structures can be controlled. A complete analytical study of how the width and the thickness of different 2D materials can affect the TE mode as it propagates along a standard silicon nitride waveguide is therefore required. Herein, let us consider the case of a Si_3N_4 waveguide with dimensions (Fig. 6.13) of: width W_{wg} =1.2 μm and thickness h_{wg} = 0.3 μm. This will give rise to the possibility for the development of different 2D material-based modulators and filters. The effect of three different 2D materials, all of which are known to form a liquid crystal phase under suitable conditions, and are therefore ideal candidates for the production of highly uniform thin films for use in photonic devices is considered. To analyse the expected effect of the addition of the 2D materials to the structures, analysis of the light propagation through photonic structures was undertaken using a transfer matrix method combined with Comsol Multiphysics software. The subsequent subsections detail the results of the theoretical modelling

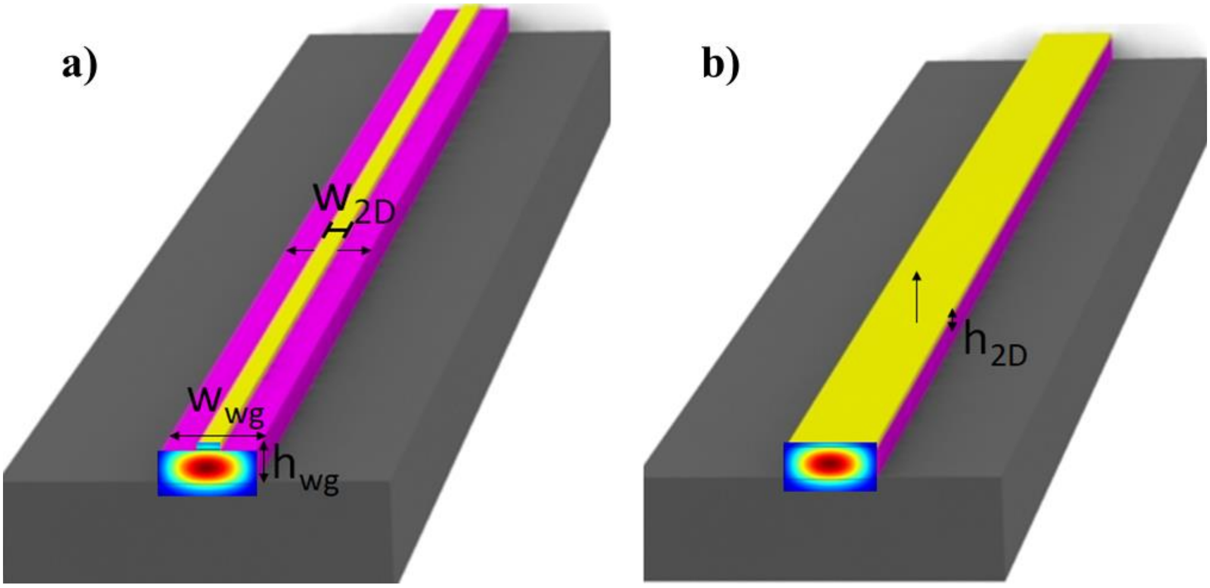

Figure 6.13. *Schematic of the different dimensions that can be controlled when depositing 2D materials onto the waveguide. One can look specifically at using different width* ***(a)*** *and thickness* ***(b)*** *of the 2D materials on top of a standard* Si_3N_4 *waveguide of* $W_{wg} = 1.2\ \mu m$ *width and* $h_{wg} = 0.3\ \mu m$ *thick.*

Graphene.

In single-layer graphene, the conduction and valence bands meet each other at the Dirac points, resulting in a gapless, semi-metallic band structure with no absorption peaks in the ultra-broad range from far infrared (FIR) to ultraviolet (UV). The linear structure of the dispersion leads to the universal optical conductance of the interband transition[220], which has been experimentally confirmed[221]. Single-layer graphene absorbs 2.3% of perpendicularly incident light within the infrared-to-visible spectral range. The absorption coefficient is precisely defined by $e^2/\hbar c$, the fine-structure constant. The special behaviour of graphene is due to its 2D structure that confines electrons in one atomic layer, and also due to the low density of states (DOS) near the Dirac points, which causes the Fermi energy to shift significantly with variation of the carrier density[222]. For example, a Fermi level shift of up to 0.9 eV has been experimentally demonstrated using the electrostatic field gating technique[223]. The tuneable bandgap of graphene offers great opportunities and flexibility for infrared and visible light manipulation.

A parametric sweep in thickness and width has been studied. By changing the dimensions of the flakes deposited on top of the waveguides, a change in the effective refractive index is observed, and consequently a modulation of the signal. In Figure 6.14a-b the alteration of the effective refractive index in the visible range is plotted. As can be seen, graphene shows a continuous change in the effective refractive index as a function of both parameters. The absorption coefficient of the graphene

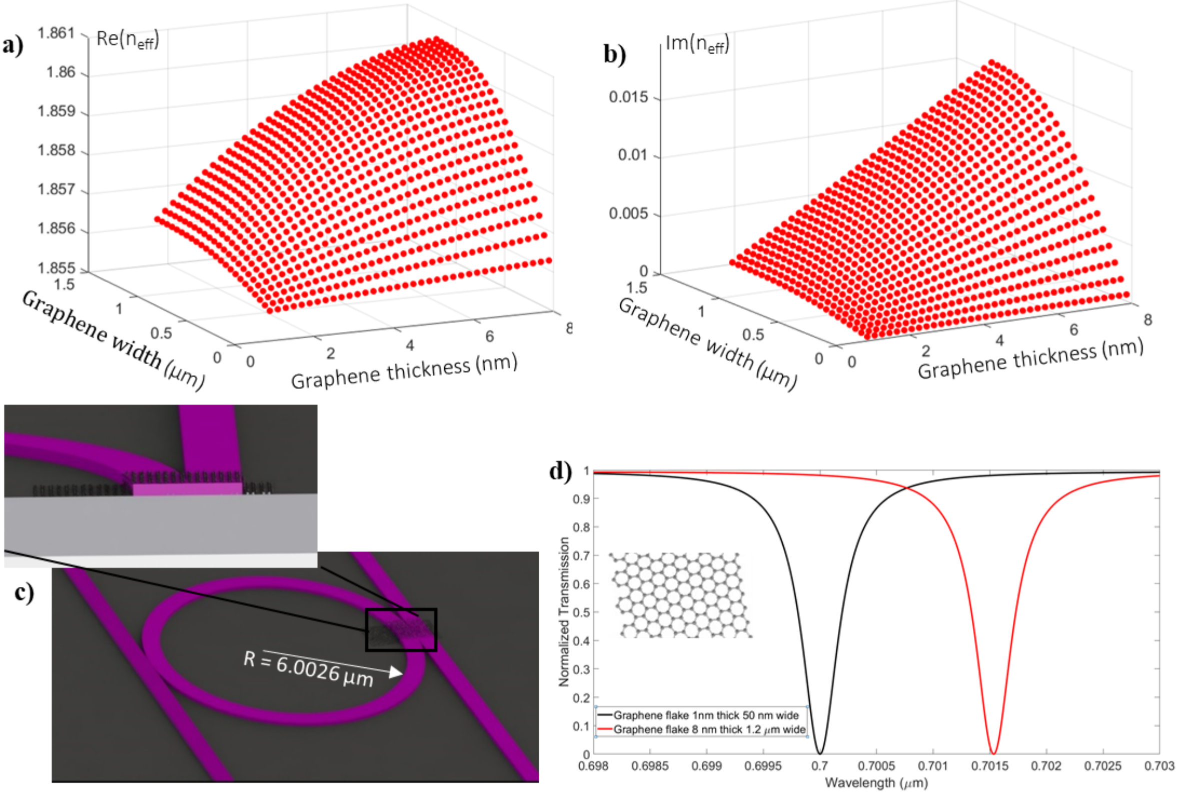

Figure 6.14. a) *The real part of the effective refractive index for different widths and thicknesses of graphene.* ***b)*** *The imaginary part of the effective refractive index for different widths and thicknesses of graphene.* ***c)*** *Schematic of an add-drop filter with integrated graphene flakes.* ***d)*** *The drop-port transmission spectra of a micro-ring-resonator-based add–drop filter with a radius R = 6.0026 μm, α = 2 cm^{-1}, and coupling coefficient $\kappa = 0.4$ for a graphene flake of 1 nm thick and 50 nm wide (black line) and for a graphene flake of 1.2 μm wide (covering all the waveguide) and 8 nm thick (red line).*

goes from being a transparent material with no absorption up to 0.016, and the real part of the refractive index changes by 4x10^{-3}. The proposed designs are based on coupled micro-resonator structures (Fig. 6.14c). Using the Transfer Matrix Method developed by Yariv [224] the drop-port transmission spectra of a micro-ring resonator-based add–drop filter was calculated. For a radius R = 6 μm, α = 2 cm^{-1}, and coupling coefficient $\kappa = 0.4$, when the thickness of the graphene is equal to 1 nm and the width to 50 nm, the effective refractive index is $n_{eff} = 1.856 + 1.2 \cdot 10^{-4}i$. This gives a corresponding resonant wavelength of 700 nm (Fig. 6.14d). Increasing the thickness up to 8nm and the width up to 1.2μm of the graphene flake, an effective refractive index of 1.86 + 0.016i is determined. Here, the resonant wavelength corresponds to 701.6 nm (Fig. 6.14d). Hence, modifying the thickness and width of the graphene flakes deposited on the top of waveguides, a 0.23% shift in the resonance of the micro-ring resonator structure is achieved.

To provide a complete overview of tuneable devices using graphene at optical communications wavelengths, the optical properties of graphene should be considered. One of the most important properties of graphene is its gate-variable optical conductivity[225]; that is, the conductivity of graphene can be tuned by applying voltages which will change the carrier density in the graphene and, consequently, the Fermi level. The dependence of graphene's optical conductivity on inter- and intra-band transitions has been analytically derived at 0K and at 300K[226]. The complex optical conductivity $\sigma\ (\omega, \mu, \Gamma, T)$ depends on the angular frequency ω, chemical potential μ, charged particle scattering rate τ, the relaxation time $\Gamma = \tau^{-1}$, and finally the temperature T [1]. The dynamic optical conductance of graphene can be derived from the Kubo formula:

$$\sigma_{total}(w,\ \mu, \Gamma, T) = \sigma_{intra} + \sigma'_{inter} + \mathrm{i}\sigma''_{inter}\,. \tag{20}$$

The intra-band conductivity σ_{intra} has the Drude form:

$$\sigma_{intra} = \frac{\sigma_0 4\mu}{\pi} \cdot \frac{1}{\hbar\tau_1^{-1} - i\hbar\omega} \tag{21}$$

where $\sigma_0 = \frac{\pi e^2}{2h} = 60.8\ \mu s$ is the universal optical conductance and τ_1^{-1} is the relaxation rate specifically associated with intra-band transitions. The inter-band contributions then have the forms:

$$\sigma'_{inter} = \sigma_0 \left(1 + \frac{1}{\pi}\arctan\frac{\hbar w - 2\mu}{\hbar\tau_2^{-1}} - \frac{1}{\pi} arctan \frac{\hbar w + 2\mu}{\hbar\tau_2^{-1}}\right)\ ; \tag{22}$$

and

$$\sigma''_{inter} = \ -\frac{\sigma_0}{2\pi}\ln\frac{(2\mu + \hbar\omega)^2 + \hbar^2\tau_2^{-2}}{(2\mu - \hbar\omega)^2 + \hbar^2\tau_2^{-2}}; \tag{23}$$

where τ_2^{-1} is the relaxation rate specifically associated with inter-band transitions. The complex dielectric function $\varepsilon\ (\mu)$ can be obtained from the complex optical conductivity of graphene as given by:

$$\varepsilon(\mu) = 1 + \frac{i\sigma(\mu)}{\omega\varepsilon_0\delta}\ ; \tag{24}$$

where δ is the graphene thickness layer and ε_0 is the permittivity of vacuum. For further calculations, $\lambda = 1550\ nm$, T=296K, $\tau_1 = 10\ fs$ and τ_2= 1.2 ps were chosen. One can then select graphene layer thicknesses of 0.4 nm and 0.7 nm respectively to roughly correspond to mono- and bi-layer graphene films. In (Fig. 6.15) the dielectric dependence with the change in the Fermi level has been plotted, a parametric sweep of the Fermi level from 0 eV up to 1eV has been studied for different graphene flake thicknesses.

When the chemical potential is varied between 0.4 eV and 0.6 eV, the dielectric constant undergoes a significant change. In the case of 0.4 nm thick graphene, a change from $\varepsilon(0.4eV) = 14.21 + 14.65i$ to $\varepsilon(0.6eV) = -5.168 + 1.111i$ is observed. Using Comsol Multiphysics, the effective refractive index associated each of those Fermi level values respectively has been calculated as $n_{eff}(0.4eV) = 1.5355 - 1.735\ 10^{-3}i$ and $n_{eff}(0.6eV) = 1.5332 - 1.\ 289 \cdot 10^{-4}i$. In the case of a 0.7 nm thick flake, the change in the dielectric constant goes from $\varepsilon(0.40eV) = 9.097 + 8.334i$

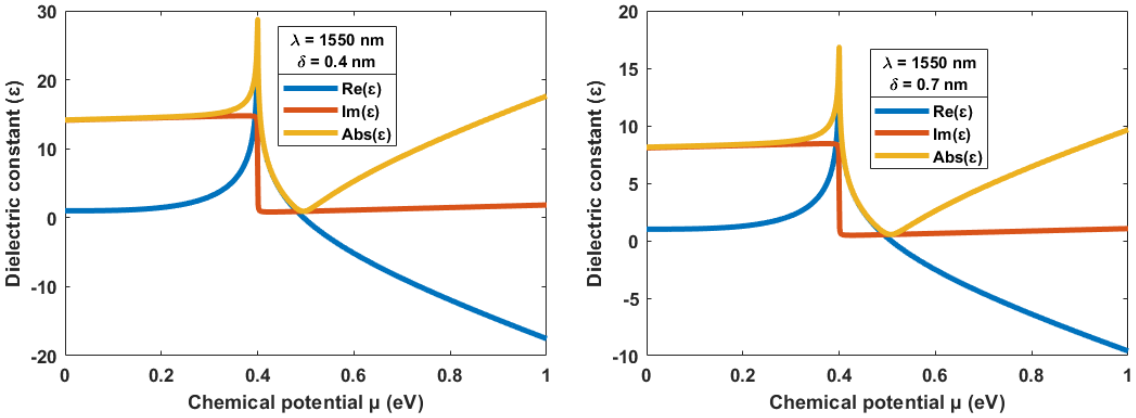

__Figure 6.15. a)__ Calculated dielectric constant for a 0.4 nm thick flake of graphene (real part, imaginary part and magnitude) as a function of the chemical potential μ*, at a wavelength* $\lambda = 1550\,nm$*. __b)__ Calculated dielectric constant for a 0.7 nm thick flake of graphene (real part, imaginary part and magnitude) as a function of the chemical potential* μ*, at a wavelength* $\lambda = 1550\,nm$*.*

to $\varepsilon(0.60eV) = -2.492 + 0.6322i$, and consequently the effective refractive index goes from $n_{eff}(0.4eV) = 1.5356 - 1.\ 7277 \cdot 10^{-3}i$ and $n_{eff}(0.6eV) = 1.5333 - 1.\ 2943 \cdot 10^{-4}i$. Using these values, a 0.148% shift in the resonance of the add-drop filter for a 0.4 nm thick graphene flake is achieved, and again 0.148% in the case of a 0.7nm thick flake (Fig. 6.16). Note that the optimal radii in each case for the ring are slightly different as the flake thickness is changed.

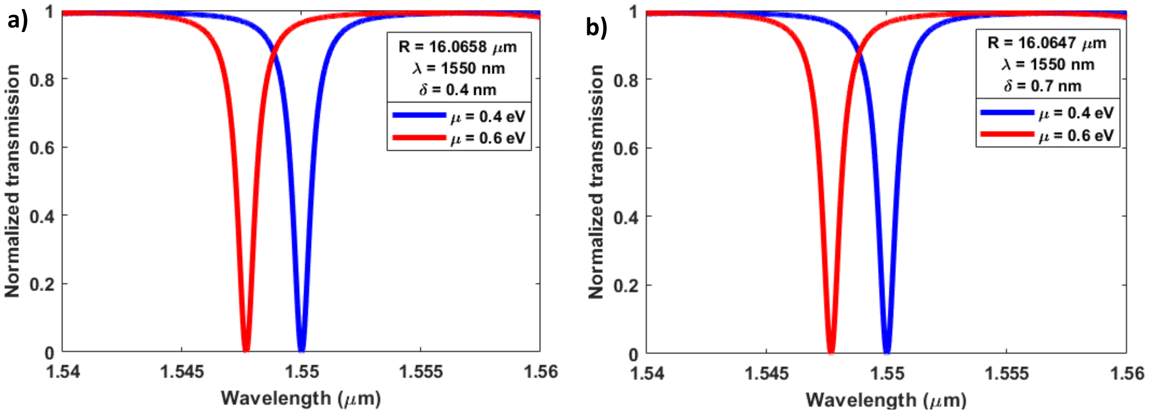

***Figure 6.16.** Drop-port transmission spectra of a micro-ring resonator-based add–drop filter with **(a)** radius R = 16.0658 μm and a 0.4 nm thick graphene flake, and **(b)** radius R = 16.0647 μm and a 0.7 nm thick graphene flake. In both cases, α = 2 cm*$^{-1}$*, and the coupling coefficient* $\kappa = 0.4$ *at a wavelength* $\lambda = 1550\,nm$*.*

Tungsten disulfide.

In the case of WS_2, the effective refractive index for a 1nm thick and 50 nm wide flake is $n_{eff} = 1.855 + 2.255 \cdot 10^{-5}i$ corresponding to a resonant wavelength of 700 m, for a fixed radius of 6.0058 µm. Increasing the thickness and the width of the flake up to 8nm and 1.2 μm respectively, the change in the real part of the effective refractive determined for the studied range is 0.023 (Fig. 6.17a). The imaginary part increases to $3\ x\ 10^{-3}$ (Fig. 6.17b), and a resonant wavelength of 698 nm is found corresponding to a -0.29% shift in the resonance of the add-drop filter. (Fig. 6.17c). Using micro-ring resonators (Fig. 6.17d) with radii R = 6 μm, quality factors (Q) of the order of $10^2 - 10^3$ are achieved. By increasing the radius of the micro-ring, a reduction in the scattering losses is obtained, and an increase of at least two orders of magnitude in the quality factor, up to $10^5 - 10^6$ for radii on the order of 50 µm is achievable.

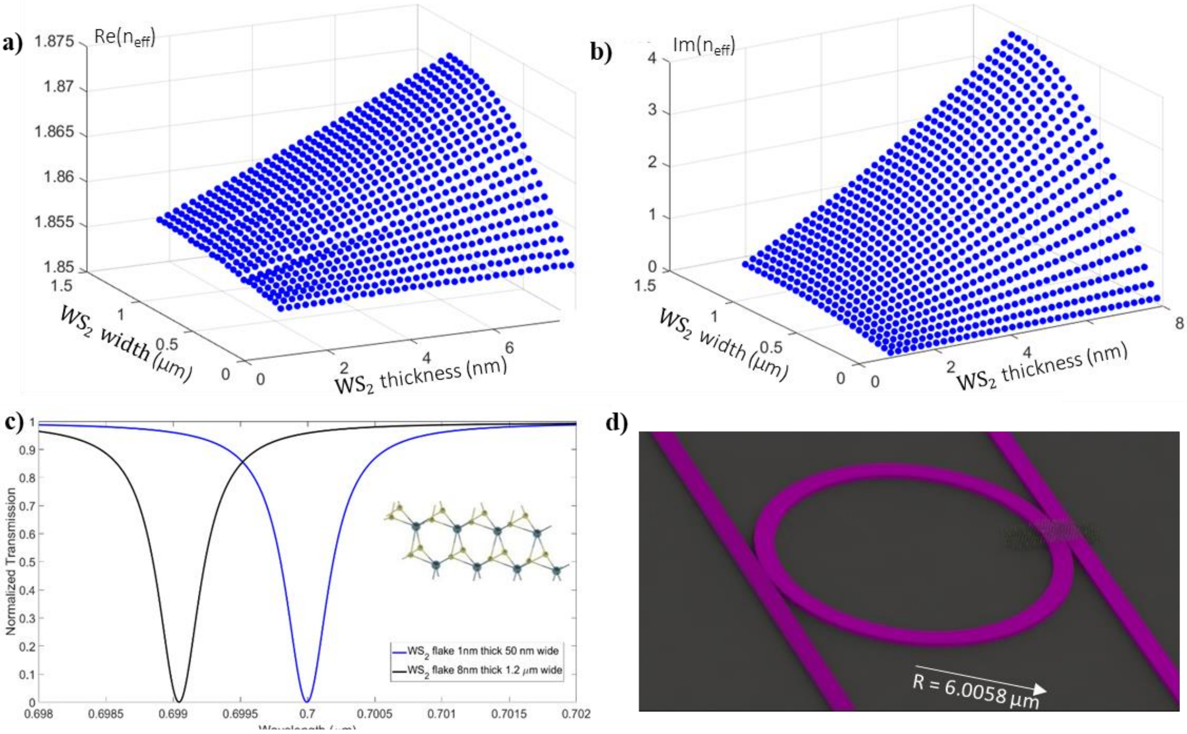

Figure 6.17. a) *The real part of the effective refractive index for different widths and thicknesses of tungsten disulfide.* ***b)*** *The imaginary part of the effective refractive index for different widths and thicknesses of tungsten disulfide.* ***c)*** *Schematic of an add-drop filter with integrated tungsten disulfide flakes.* ***c)*** *The drop-port transmission spectra of a micro-ring-resonator-based add–drop filter with a radius R = 6.0058 µm, α = 2 cm^{-1}, and coupling coefficient $\kappa = 0.4$ for a tungsten disulfide flake of 1 nm thick and 50 nm wide (black line) and for a tungsten disulfide flake of 1.2 µm wide (covering all the waveguide) and 8 nm thick (red line).*

Molybdenum disulfide.

In the case of using MoS$_2$, the effective refractive index for a 1 nm thick and 50 nm wide flake is $n_{eff} = 1.851 + 5.4 \cdot 10^{-5}i$ corresponding to a resonant wavelength of 700 m, for a fixed radius of 6.0188 µm. Increasing the thickness and the width of the flake up to 3.8 nm and 1.2 μm respectively, the change in the real part of the effective refractive for the studied range is 0.041 (Fig. 6.18a). The

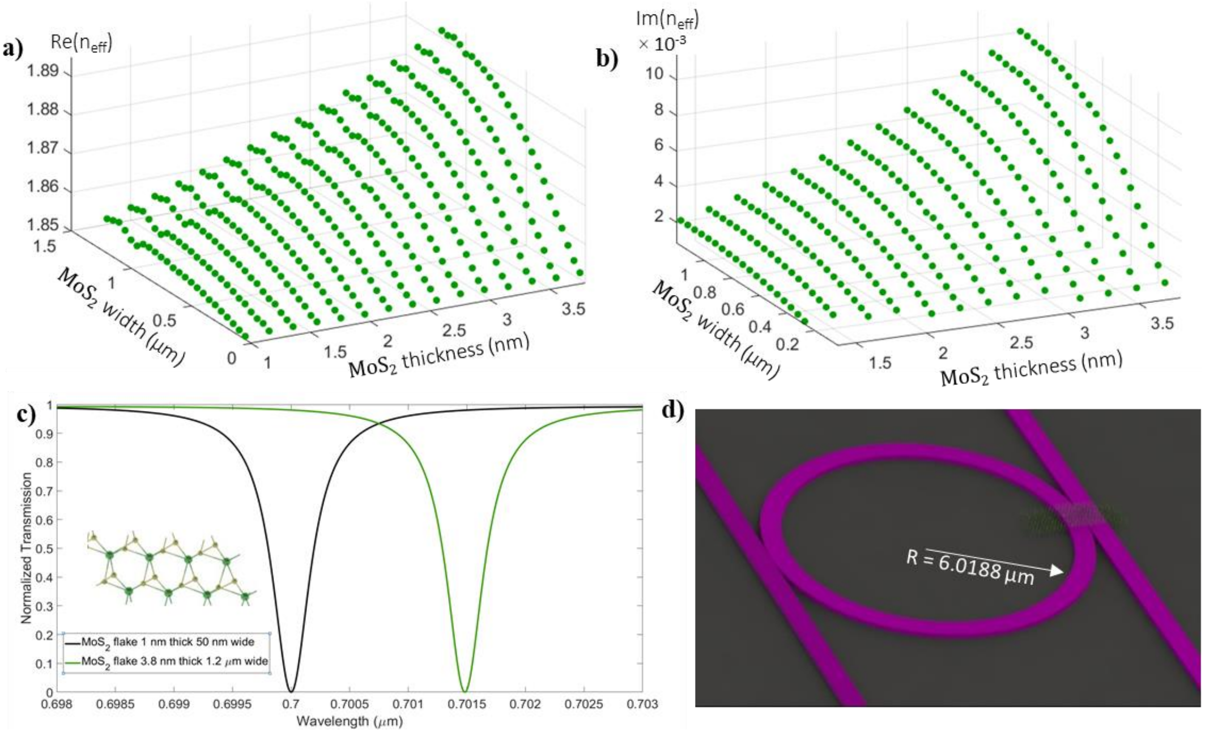

Figure 6.18. a) *The real part of the effective refractive index for different widths and thicknesses of molybdenum disulfide.* ***b)*** *The imaginary part of the effective refractive index for different widths and thicknesses of molybdenum disulfide.* ***c)*** *Schematic of an add-drop filter with integrated molybdenum disulfide flakes.* ***c)*** *The drop-port transmission spectra of a micro-ring-resonator-based add–drop filter with a radius R = 6.0188 μm, α = 2 cm^{-1}, and coupling coefficient $\kappa = 0.4$ for a molybdenum disulfide flake of 1 nm thick and 50 nm wide (black line) and for a molybdenum disulfide flake of 1.2 μm wide (covering all the waveguide) and 8 nm thick (red line).*

imaginary part increases to $1\, x\, 10^{-2}$ (Fig.6.18 b), giving a resonant wavelength of 701.5 nm corresponding to a 0.21% shift in the resonance of the add-drop filter (Fig. 6.18c-d).

6.5 Conclusions.

In this section, the first applications of the developed 2D material fluid composites were considered. In Section 6.1, the production of thin films of tungsten disulfide using the liquid crystal phase dispersions was detailed. The developed thin films show remarkable uniformity when compared to those produced from non-liquid crystalline dispersions. In Section 6.2, the terahertz transmission properties of the developed thin films were investigated, which show strong potential for future applications in terahertz generation and detection. In Section 6.3 laser cavity applications of the thin films were considered. It was shown that unstable Q-switched lasing can be achieved using the tungsten disulfide thin films as saturable absorbers coated on the mirrors forming the laser cavity. In Section 6.4 a study of the prospective integration of 2D materials with photonic structures such as waveguides and microring resonators was presented. The route to integration of the thin films (*via* lithography and film transfer techniques), and the expected properties obtained for the photonic structures after integration were discussed. It was shown that the integration of the 2D materials can modify the effective refractive index of the photonic structures, and that the resonance of the structures can therefore be tuned.

7. Final Conclusions and Future Prospects.

In section 4.1, the synthesis and investigation of the properties of nematic liquid crystals doped with dispersed particles of different 2D materials were detailed. The 2D materials were successfully dispersed in the liquid crystal, and the liquid crystal can equally be used to dynamically control the positions and orientations of the dispersed 2D materials particles. However, the analysis of the switching properties of the composite materials was less promising. From the results gained, it is clear that the inclusion of 2D materials in a conventional nematic liquid crystal host either negatively or negligibly impacts the performance of the liquid crystal. Switching times are found to be slower, threshold voltages more or less unchanged, nematic-isotropic transition temperatures to be lower, and the linear and circular dichroism to be inconclusively impacted. This limits the potential applications of the materials. Significant further work would be needed to mitigate the negative impacts of the inclusion of the 2D materials. Particularly damaging is the slower switching time – modern technology increasingly demands faster operation of devices. Hence, consideration was given to another type of 2D material liquid crystal that could overcome some of these issues.

In Section 4.2, the possibility of liquid crystal phases forming spontaneously for dispersions of tungsten disulfide in organic solvents was examined. While different solvents can affect the rate, efficiency and quality of particles obtained by liquid phase exfoliation, due to the fact that controlling the concentration generally relies on drying and redispersion the solvent choice for obtaining a liquid crystalline state can be independent of that for exfoliation. Particle sizes obtained by liquid phase exfoliation have been analysed by several techniques. The most interesting results were obtained by dynamic light scattering which matched the results of other techniques, despite not being applicable in theory to high aspect ratio particles. Liquid crystalline states were obtained in different organic solvents, and their properties investigated. Linear and circular dichroism were shown for the different liquid crystalline dispersions, but the positions of peaks are shifted or entirely different depending on the solvent. The different properties achievable with different solvents show that there is no single definable 'best' solvent for use. Rather, the choice of solvent should be application driven. For example, to achieve reconfigurable circular dichroism at 750 nm, IPA would be the best choice, whereas at 230nm chloroform is preferable. The single condition is that WS_2 should be soluble enough to allow dispersion at the necessary concentrations, which is broadly true for all organic solvents. This work demonstrates that using only standard liquid phase exfoliation processes (ultrasonication, centrifugation and control of concentration) a liquid crystalline state of WS_2 particles can be achieved in a range of solvents.

The discovery that WS_2 LC dispersions can simultaneously demonstrate reconfigurability under applied magnetic field and circular dichroism, while also combining the intrinsic optical and electrical properties of the 2D WS_2 flakes is of significant interest, opening the way towards countless applications in opto-electronics and photonics such as switchable filtering devices. Future optimisation and tuning of the synthesis holds great potential for the generation of a new class of true reconfigurable '*wonder materials*', with applications encompassing: thin film and membrane depositions; display devices; inks; terahertz modulators; and others. The discovery of this novel reconfigurable phase could lead to a marked expansion in the uptake of WS_2 for device-based applications, due to the increased scope for scalable integration with reduced drawbacks such as time, cost and quality as well as the significant boost in the range of potential uses with the observation of reconfigurable circular dichroism. There is also the potential to develop liquid crystals based on a wide variety of other materials. In fact, any 2D material (of which a few thousand are currently known) can form a liquid crystalline dispersion in theory. The challenge is largely about the effective exfoliation and maintaining dispersion within the solvent.

In Section 5, a new characterisation technique, based on Raman spectroscopy, was developed in order to ascertain information about the positions and alignment of 2D material particles dispersed in fluids. In Section 5.1, microfluidic structures were designed to enhance the Raman signal from the 2D materials by up to an order of magnitude, and the enhancement was subsequently experimentally confirmed. It was also shown experimentally that integrated 2D material fluid composites can be dynamically controlled using either applied electric fields, or by laser excitation. In Section 5.2, it was demonstrated that the enhanced Raman signal can be utilised to enable the tracking of particle positions in one and two dimensions respectively. From numerical analysis of the expected Raman signal, one observes a strong positional dependence of the Raman signal intensity. Combining that numerical analysis with experimental Raman spectra allowed accurate positional determination for particles dispersed in a fluid. It was also discussed how the technique would be further applied to three-dimensional particle tracking. In Section 5.3, an analysis of how other geometric properties of the particle, or experimental considerations, can influence the Raman signal intensity was presented. Specifically, consideration was given to the particle rotation and angle, the presence of arrays of multiple particles, the focus of the laser, or changing the material under investigation can modify (or otherwise not) the Raman spectrum of the sample. Particle rotation was found to strongly affect the Raman signal. The maximum signal was obtained with the particle parallel to the bottom of the cavity, with a minimum occurring with the particle rotated through around 30°. The shape of the rotational dependence is independent of the particle position, but importantly the ratios of different peaks depend on both the position and the rotation. In Section 5.4, it was shown that the shape of the particle strongly influences the Raman signal, demonstrating potential for shape analysis *via* Raman spectroscopy. It was also shown that the particle size affects the Raman intensity, but in a non-linear manner. In Section 5.5, a method was presented to extract the concentration of dispersed particles from the Raman spectra by only looking at the Raman bands of the host fluid. Whilst looking at the Raman bands of the dispersed 2D material proved challenging and gave inaccurate results, looking at the bands for the host fluid proved to give results that agreed with the expected relative concentrations and absolute values of the order expected.

In Section 6, the first applications of the developed 2D material fluid composites were considered. In Section 6.1, the production of thin films of tungsten disulfide using the liquid crystal phase dispersions was detailed. The developed thin films show remarkable uniformity when compared to those produced from non-liquid crystalline dispersions. In Section 6.2, the terahertz transmission properties of the developed thin films were investigated, and found to show strong potential for future applications in terahertz generation and detection. In Section 6.3, consideration was given to potential laser cavity applications of the thin films. It was shown that unstable Q-switched lasing can be achieved using the tungsten disulfide thin films as saturable absorbers coated on the mirrors forming the laser cavity. In Section 6.4 a study of the prospective integration of 2D materials with photonic structures such as waveguides and microring resonators was presented. Therein, the route to integration of the thin films (*via* lithography and film transfer techniques), and the expected properties obtained for the photonic structures after integration were discussed. It was shown that the integration of the 2D materials can modify the effective refractive index of the photonic structures, and that the resonance of the structures can therefore be tuned.

In terms of future work, there are several strands that require further exploration or improvement. Firstly, it is still desirable to develop new materials. The most immediately accessible possibility is to develop liquid crystals based on other 2D materials. With the addition of the work presented in this thesis, there have now been liquid crystal phases shown for just four 2D materials (graphene, graphene oxide, molybdenum disulfide and tungsten disulfide). However, there are over 2000 known 2D materials. The theory predicting the existence of the liquid crystal phase demands only a high aspect ratio, and hence there should be no limit on which 2D materials can form a liquid crystal phase. Therefore, there are potentially over 2000 remaining 2D material liquid crystals to be synthesised for the first time. There is also scope to improve the properties of those that are already known. For example, tuning the particle sizes could be used to shift the concentration required to achieve a liquid crystalline state, while dispersing in other solvents could increase the lifetime of the liquid crystal phase before aggregation occurs.

When considering the use of Raman spectra for tracking, the greatest current need is for greater experimental confirmation of the numerical analysis. For example, the Raman spectral intensities for particles of different shapes and sizes are yet to be corroborated against the predicted data. Beyond that, the next step will be to package all of the potential variables together in order to accurately predict the Raman intensities for arbitrary particles. The ultimate goal would then be to combine this in real-time with the experimental data to achieve high-speed *in-situ* particle tracking.

Finally, there is an extremely promising future for the application of 2D material fluid composites. While preliminary results are shown and described using the thin films produced, there is still scope to improve the quality of the thin films. The thin films produced are more uniform than those produced from non-liquid crystalline solutions, but they do not show perfect uniformity still. Optimisation is still required at two steps of the process – firstly in the filtering onto membranes, and secondly in the transfer from the membrane to the substrate. This optimisation should also be undertaken in the context of the desired application, rather than as a catch-all method as has been used here. It still remains also to effectively integrate the developed films with other substrates, for other applications. The first key goal there would be to achieve integration of thin films with controllable dimensions into photonic devices in order to experimentally validate the predicted tuning possibilities. Also requiring further consideration is the integration of the developed materials with devices in the liquid state. While this is easily achieved for the nematic liquid crystals doped with dispersed 2D materials, it has not yet been achieved for the dispersions of 2D materials in organic solvents. There are two key problems that must be overcome for that integration to be successful. First, the evaporation of the organic solvents when confined in small volumes should be considered, possibly by using higher boiling point solvents instead (although the greater viscosity of higher boiling point would limit the switching performance). Second, the aggregation of the 2D materials when confined in small volumes should be mitigated. This could be achieved for example by adding surfactant molecules, or other stabilisers, to the dispersion. Alternatively, changing the solvents used to obtain dispersions of greater stability is a possibility. Once the 2D material fluid composites based on 2D material dispersions in organic solvents can be successfully integrated in the liquid phase, then their switching properties can be effectively analysed. The expectation is that such materials will show substantially better (faster times, lower voltages) switching properties than conventional nematic liquid crystals.

References.

1. Bao, Q. & Loh, K. P. Graphene Photonics, Plasmonics, and Broadband Optoelectronic Devices. *ACS Nano* **6**, 3677–3694 (2012).
2. Spearing, S. M. Materials issues in microelectromechanical systems (MEMS). *Acta Mater.* **48**, 179–196 (2000).
3. Gaponenko, S. V. *Introduction to Nanophotonics*. (2010).
4. Huang, Y. & Mason, A. J. Lab-on-CMOS integration of microfluidics and electrochemical sensors. *Lab Chip* **13**, 3929 (2013).
5. Hogan, B. T. *et al.* Dynamic in-situ sensing of fluid-dispersed 2D materials integrated on microfluidic Si chip. *Sci. Rep.* **7**, 42120 (2017).
6. Behabtu, N. *et al.* Spontaneous high-concentration dispersions and liquid crystals of graphene. *Nat. Nanotechnol.* **5**, 406–411 (2010).
7. Xia, F., Wang, H., Xiao, D., Dubey, M. & Ramasubramaniam, A. Two-dimensional material nanophotonics. *Nat. Photonics* **8**, 899–907 (2014).
8. Ferrari, A. C. *et al.* Raman Spectrum of Graphene and Graphene Layers. *Phys. Rev. Lett.* **97**, 187401 (2006).
9. Ferrari, A. C. *et al.* Science and technology roadmap for graphene, related two-dimensional crystals, and hybrid systems. *Nanoscale* **7**, 4598–4810 (2015).
10. Jalili, R. *et al.* Organic Solvent-Based Graphene Oxide Liquid Crystals: A Facile Route toward the Next Generation of Self-Assembled Layer-by-Layer Multifunctional 3D Architectures. *ACS Nano* **7**, 3981–3990 (2013).
11. He, L. *et al.* Graphene oxide liquid crystals for reflective displays without polarizing optics. *Nanoscale* **7**, 1616–1622 (2015).
12. Tie, W. *et al.* Dynamic electro-optic response of graphene/graphitic flakes in nematic liquid crystals. *Opt. Express* **21**, 19867 (2013).
13. Li, Q. *Nanoscience with Liquid Crystals*. (Springer International Publishing, 2014). doi:10.1007/978-3-319-04867-3
14. Coles, H. & Morris, S. Liquid-crystal lasers. *Nat. Photonics* **4**, 676–685 (2010).
15. Caputo, R. *et al.* POLICRYPS: a liquid crystal composed nano/microstructure with a wide range of optical and electro-optical applications. *J. Opt. A Pure Appl. Opt.* **11**, 024017 (2009).
16. Ni, X., Emani, N. K., Kildishev, A. V, Boltasseva, A. & Shalaev, V. M. Broadband Light Bending with Plasmonic Nanoantennas. *Science (80-.).* **335**, 427–427 (2012).
17. Hogan, B. T., Kovalska, E., Craciun, M. F. & Baldycheva, A. 2D material liquid crystals for optoelectronics and photonics. *J. Mater. Chem. C* **5**, 11185–11195 (2017).

18. Hogan, B. T. *et al.* 2D WS 2 liquid crystals: tunable functionality enabling diverse applications. *Nanoscale* **11**, 16886–16895 (2019).
19. Zhukova, M. O. *et al.* Transmission Properties of FeCl3-Intercalated Graphene and WS2 Thin Films for Terahertz Time-Domain Spectroscopy Applications. *Nanoscale Res. Lett.* **14**, 225 (2019).
20. Faneca, J., Torres Alonso, E., Craciun, M., Baldycheva, A. & Hogan, B. T. 2D materials integrated in Si3N4 photonics platform. in *Silicon Photonics XIII* (eds. Reed, G. T. & Knights, A. P.) **10537**, 8 (SPIE, 2018).
21. Zheludev, N. I. & Kivshar, Y. S. From metamaterials to metadevices. *Nat. Mater.* **11**, 917–924 (2012).
22. Zheludev, N. All change, please. *Nat. Photonics* **1**, 551–553 (2007).
23. *Phase Change Materials*. (Springer US, 2009). doi:10.1007/978-0-387-84874-7
24. Tao, H. *et al.* Reconfigurable Terahertz Metamaterials. *Phys. Rev. Lett.* **103**, 147401 (2009).
25. Fu, Y. H. *et al.* A Micromachined Reconfigurable Metamaterial via Reconfiguration of Asymmetric Split-Ring Resonators. *Adv. Funct. Mater.* **21**, 3589–3594 (2011).
26. Ou, J.-Y., Plum, E., Zhang, J. & Zheludev, N. I. An electromechanically reconfigurable plasmonic metamaterial operating in the near-infrared. *Nat. Nanotechnol.* **8**, 252–255 (2013).
27. Aksu, S. *et al.* Flexible Plasmonics on Unconventional and Nonplanar Substrates. *Adv. Mater.* **23**, 4422–4430 (2011).
28. Won, R. Integrating silicon photonics. *Nat. Photonics* **4**, 498–499 (2010).
29. Lipson, M. Guiding, modulating, and emitting light on Silicon-challenges and opportunities. *J. Light. Technol.* **23**, 4222–4238 (2005).
30. Reed, G. T. & Knights, A. P. *Silicon photonics : an introduction*. (John Wiley, 2004).
31. Dekker, R., Usechak, N., Först, M. & Driessen, A. Ultrafast nonlinear all-optical processes in silicon-on-insulator waveguides. *J. Phys. D. Appl. Phys.* **40**, R249–R271 (2007).
32. Baldycheva, A., Tolmachev, V. A., Berwick, K. & Perova, T. S. Multi-channel Si-liquid crystal filter with fine tuning capability of individual channels for compensation of fabrication tolerances. *Nanoscale Res. Lett.* **7**, 387 (2012).
33. Novoselov, K. S. Electric Field Effect in Atomically Thin Carbon Films. *Science (80-.).* **306**, 666–669 (2004).
34. Li, X. *et al.* Graphene Films with Large Domain Size by a Two-Step Chemical Vapor Deposition Process. *Nano Lett.* **10**, 4328–4334 (2010).
35. Reina, A. *et al.* Large Area, Few-Layer Graphene Films on Arbitrary Substrates by Chemical Vapor Deposition. *Nano Lett.* **9**, 30–35 (2009).

36. Sun, Z. *et al.* Growth of graphene from solid carbon sources. *Nature* **468**, 549–552 (2010).

37. Wei, D. *et al.* Synthesis of N-Doped Graphene by Chemical Vapor Deposition and Its Electrical Properties. *Nano Lett.* **9**, 1752–1758 (2009).

38. Hernandez, Y. *et al.* High-yield production of graphene by liquid-phase exfoliation of graphite. *Nat. Nanotechnol.* **3**, 563–568 (2008).

39. Lotya, M., King, P. J., Khan, U., De, S. & Coleman, J. N. High-Concentration, Surfactant-Stabilized Graphene Dispersions. *ACS Nano* **4**, 3155–3162 (2010).

40. O'Neill, A., Khan, U., Nirmalraj, P. N., Boland, J. & Coleman, J. N. Graphene Dispersion and Exfoliation in Low Boiling Point Solvents. *J. Phys. Chem. C* **115**, 5422–5428 (2011).

41. Ogino, I., Yokoyama, Y., Iwamura, S. & Mukai, S. R. Exfoliation of Graphite Oxide in Water without Sonication: Bridging Length Scales from Nanosheets to Macroscopic Materials. *Chem. Mater.* **26**, 3334–3339 (2014).

42. Paredes, J. I., Villar-Rodil, S., Martínez-Alonso, A. & Tascón, J. M. D. Graphene Oxide Dispersions in Organic Solvents. *Langmuir* **24**, 10560–10564 (2008).

43. Qi, X. *et al.* Size-specified graphene oxide sheets: ultrasonication assisted preparation and characterization. *J. Mater. Sci.* **49**, 1785–1793 (2014).

44. Zhang, L. *et al.* Size-controlled synthesis of graphene oxide sheets on a large scale using chemical exfoliation. *Carbon N. Y.* **47**, 3365–3368 (2009).

45. Backes, C. *et al.* Guidelines for Exfoliation, Characterization and Processing of Layered Materials Produced by Liquid Exfoliation. *Chem. Mater.* **29**, 243–255 (2017).

46. Kim, J. *et al.* Direct exfoliation and dispersion of two-dimensional materials in pure water via temperature control. *Nat. Commun.* **6**, (2015).

47. Chen, J. H., Jang, C., Xiao, S., Ishigami, M. & Fuhrer, M. S. Intrinsic and extrinsic performance limits of graphene devices on SiO 2. *Nat. Nanotechnol.* **3**, 206–209 (2008).

48. Peng, L. *et al.* An iron-based green approach to 1-h production of single-layer graphene oxide. *Nat. Commun.* **6**, 5716 (2015).

49. Kim, D. W., Kim, D., Min, B. H., Lee, H. & Jung, H.-T. Sonication-free dispersion of large-area graphene oxide sheets using internal pressure from release of intercalated carbon dioxide. *Carbon N. Y.* **88**, 126–132 (2015).

50. Sun, X., Luo, D., Liu, J. & Evans, D. G. Monodisperse Chemically Modified Graphene Obtained by Density Gradient Ultracentrifugal Rate Separation. *ACS Nano* **4**, 3381–3389 (2010).

51. Shen, T.-Z., Hong, S.-H. & Song, J.-K. Effect of centrifugal cleaning on the electro-optic response in the preparation of aqueous graphene-oxide dispersions. *Carbon N. Y.* **80**, 560–564 (2014).

52. Zhang, W. *et al.* Size fractionation of graphene oxide sheets by the polar solvent-selective

natural deposition method. *RSC Adv.* **5**, 146–152 (2015).

53. Wang, X., Bai, H. & Shi, G. Size Fractionation of Graphene Oxide Sheets by pH-Assisted Selective Sedimentation. *J. Am. Chem. Soc.* **133**, 6338–6342 (2011).
54. Zhu, Y. *et al.* Graphene and Graphene Oxide: Synthesis, Properties, and Applications. *Adv. Mater.* **22**, 3906–3924 (2010).
55. Novoselov, K. S. *et al.* Two-dimensional gas of massless Dirac fermions in graphene. *Nature* **438**, 197–200 (2005).
56. Geim, A. K. Graphene: Status and Prospects. *Science (80-.).* **324**, 1530–1534 (2009).
57. Marcano, D. C. *et al.* Improved Synthesis of Graphene Oxide. *ACS Nano* **4**, 4806–4814 (2010).
58. Hummers, W. S. & Offeman, R. E. Preparation of Graphitic Oxide. *J. Am. Chem. Soc.* **80**, 1339–1339 (1958).
59. Dreyer, D. R., Park, S., Bielawski, C. W. & Ruoff, R. S. The chemistry of graphene oxide. *Chem. Soc. Rev.* **39**, 228–240 (2010).
60. Liu, Z. *et al.* Nonlinear optical properties of graphene oxide in nanosecond and picosecond regimes. *Appl. Phys. Lett.* **94**, 021902 (2009).
61. Zheng, X., Jia, B., Chen, X. & Gu, M. In Situ Third-Order Non-linear Responses During Laser Reduction of Graphene Oxide Thin Films Towards On-Chip Non-linear Photonic Devices. *Adv. Mater.* **26**, 2699–2703 (2014).
62. Loh, K. P., Bao, Q., Eda, G. & Chhowalla, M. Graphene oxide as a chemically tunable platform for optical applications. *Nat. Chem.* **2**, 1015–1024 (2010).
63. Fakhri, P., Vaziri, M. R. R., Jaleh, B. & Shabestari, N. P. Nonlocal nonlinear optical response of graphene oxide-Au nanoparticles dispersed in different solvents. *J. Opt.* **18**, 015502 (2016).
64. Ganatra, R. & Zhang, Q. Few-Layer MoS 2 : A Promising Layered Semiconductor. *ACS Nano* **8**, 4074–4099 (2014).
65. Xu, M., Liang, T., Shi, M. & Chen, H. Graphene-Like Two-Dimensional Materials. *Chem. Rev.* **113**, 3766–3798 (2013).
66. Jalili, R. *et al.* Processable 2D materials beyond graphene: MoS 2 liquid crystals and fibres. *Nanoscale* **8**, 16862–16867 (2016).
67. Kobayashi, K. & Yamauchi, J. Electronic structure and scanning-tunneling-microscopy image of molybdenum dichalcogenide surfaces. *Phys. Rev. B* **51**, 17085–17095 (1995).
68. Li, H., Wu, J., Yin, Z. & Zhang, H. Preparation and Applications of Mechanically Exfoliated Single-Layer and Multilayer MoS 2 and WSe 2 Nanosheets. *Acc. Chem. Res.* **47**, 1067–1075 (2014).
69. Wilson, R. L., Kemball, C. & Galwey, A. K. Catalytic exchange of hydrogen sulphide and of hydrogen with deuterium on disulphides of molybdenum and tungsten. *Trans. Faraday Soc.*

58, 583 (1962).

70. KIERAN, P. Some catalytic reactions of thiophene on disulfides of tungsten and molybdenum. *J. Catal.* **4**, 394–402 (1965).
71. Tenne, R., Margulis, L., Genut, M. & Hodes, G. Polyhedral and cylindrical structures of tungsten disulphide. *Nature* **360**, 444–446 (1992).
72. Grayfer, E. D., Kozlova, M. N. & Fedorov, V. E. Colloidal 2D nanosheets of MoS 2 and other transition metal dichalcogenides through liquid-phase exfoliation. *Adv. Colloid Interface Sci.* **245**, 40–61 (2017).
73. Upadhyayula, L. C., Loferski, J. J., Wold, A., Giriat, W. & Kershaw, R. Semiconducting Properties of Single Crystals of n - and p -Type Tungsten Diselenide (WSe 2). *J. Appl. Phys.* **39**, 4736–4740 (1968).
74. Ruppert, C., Aslan, O. B. & Heinz, T. F. Optical Properties and Band Gap of Single- and Few-Layer MoTe 2 Crystals. *Nano Lett.* **14**, 6231–6236 (2014).
75. Kubota, Y., Watanabe, K., Tsuda, O. & Taniguchi, T. Deep Ultraviolet Light-Emitting Hexagonal Boron Nitride Synthesized at Atmospheric Pressure. *Science (80-.).* **317**, 932–934 (2007).
76. Nicolosi, V., Chhowalla, M., Kanatzidis, M. G., Strano, M. S. & Coleman, J. N. Liquid Exfoliation of Layered Materials. *Science (80-.).* **340**, 1226419–1226419 (2013).
77. Hu, S. *et al.* Proton transport through one-atom-thick crystals. *Nature* **516**, 227–230 (2014).
78. Kirby, B. J. (Brian J. *Micro- and nanoscale fluid mechanics : transport in microfluidic devices*. (Cambridge University Press, 2010).
79. Tabeling, P. *Introduction to microfluidics*. (Oxford University Press, 2010).
80. Whitesides, G. M. The origins and the future of microfluidics. *Nature* **442**, 368–373 (2006).
81. Kasirga, T. S., Ertas, Y. N. & Bayindir, M. Microfluidics for reconfigurable electromagnetic metamaterials. *Appl. Phys. Lett.* **95**, 214102 (2009).
82. Li, W. & Valentine, J. Metamaterial Perfect Absorber Based Hot Electron Photodetection. *Nano Lett.* **14**, 3510–3514 (2014).
83. Joannopoulos, J. D., Johnson, S. G., Winn, J. N. & Meade, R. D. *Photonic Crystals : Molding the Flow of Light (Second Edition).* (Princeton University Press, 2008).
84. Chandrasekhar, S. *Liquid Crystals*. (Cambridge University Press, 1992). doi:10.1017/CBO9780511622496
85. de Gennes, P. G. & Prost, J. *The Physics of Liquid Crystals*. (Oxford University Press, 1995). doi:0-19-852024-7
86. Reinitzer, F. Contributions to the knowledge of cholesterol. *Liq. Cryst.* **5**, 7–18 (1989).
87. Reinitzer, F. Beiträge zur Kenntniss des Cholesterins. *Monatshefte für Chemie - Chem. Mon.* **9**,

421–441 (1888).

88. Planer. Notiz über das Cholestearin. *Ann. der Chemie und Pharm.* **118**, 25–27 (1861).

89. Trokhymchuk, A. On Julius Planer's 1861 paper 'Notiz über das Cholestearin' in Annalen der Chemie und Pharmacie. *Condens. Matter Phys.* **13**, 1–4 (2010).

90. Sluckin, T. J., Dunmur, D. A. & Stegemeyer, H. *Crystals that flow : classic papers from the history of liquid crystals*. (Taylor & Francis, 2004).

91. Castellano, J. A. *Liquid Gold*. (WORLD SCIENTIFIC, 2005). doi:10.1142/5622

92. Chen, R. H. *Liquid crystal displays : fundamental physics and technology*. (Wiley, 2011).

93. Kwok, H.-S., Naemura, S. & Ong, H. L. *Progress in Liquid Crystal Science and Technology*. (WORLD SCIENTIFIC, 2013). doi:10.1142/8571

94. Vetrov, S. Y., Pyatnov, M. V. & Timofeev, I. V. Photonic defect modes in a cholesteric liquid crystal with a resonant nanocomposite layer and a twist defect. *Phys. Rev. E* **90**, 032505 (2014).

95. Zografopoulos, D. C., Asquini, R., Kriezis, E. E., D'Alessandro, A. & Beccherelli, R. Guided-wave liquid-crystal photonics. *Lab Chip* **12**, 3598 (2012).

96. Li, P. *et al.* Tunable Lyotropic Photonic Liquid Crystal Based on Graphene Oxide. *ACS Photonics* **1**, 79–86 (2014).

97. Tolmachev, V. a. *et al.* Electro-tuning of the photonic band gap in SOI-based structures infiltrated with liquid crystal. in *Proceedings of SPIE* (eds. Righini, G. C., Honkanen, S. K., Pavesi, L. & Vivien, L.) **6996**, 69961Z (2008).

98. Xu, Z. & Gao, C. Graphene chiral liquid crystals and macroscopic assembled fibres. *Nat. Commun.* **2**, 571 (2011).

99. Li, J., Wen, C.-H., Gauza, S., Lu, R. & Wu, S.-T. Refractive Indices of Liquid Crystals for Display Applications. *J. Disp. Technol.* **1**, 51–61 (2005).

100. Kang, S.-W., Sprunt, S. & Chien, L.-C. Ordered Polymer Microstructures Obtained Using Pattern Forming States of a Cholesteric Liquid Crystal as Templates. *Adv. Mater.* **13**, 1179–1182 (2001).

101. Dierking, I. & Al-Zangana, S. Lyotropic Liquid Crystal Phases from Anisotropic Nanomaterials. *Nanomaterials* **7**, 305 (2017).

102. Donisi, D. *et al.* A Switchable Liquid-Crystal Optical Channel Waveguide on Silicon. *IEEE J. Quantum Electron.* **46**, 762–768 (2010).

103. D'Alessandro, a. & Asquini, R. Liquid Crystal Devices for Photonic Switching Applications: State of the Art and Future Developments. *Mol. Cryst. Liq. Cryst.* **398**, 207–221 (2003).

104. Campoli, F. *et al.* Use of Ptfe Alignment Layers in Passive Addressed SSFLC Displays. *Mol. Cryst. Liq. Cryst. Sci. Technol. Sect. A. Mol. Cryst. Liq. Cryst.* **304**, 357–362 (1997).

105. Bitar, R., Agez, G. & Mitov, M. Cholesteric liquid crystal self-organization of gold nanoparticles.

Soft Matter **7**, 8198 (2011).

106. Blanc, C., Coursault, D. & Lacaze, E. Ordering nano- and microparticles assemblies with liquid crystals. *Liq. Cryst. Rev.* **1**, 83–109 (2013).

107. Jose, R., Skačej, G., Sastry, V. S. S. & Žumer, S. Colloidal nanoparticles trapped by liquid-crystal defect lines: A lattice Monte Carlo simulation. *Phys. Rev. E* **90**, 032503 (2014).

108. Wang, X., Miller, D. S., Bukusoglu, E., de Pablo, J. J. & Abbott, N. L. Topological defects in liquid crystals as templates for molecular self-assembly. *Nat. Mater.* **15**, 106–112 (2016).

109. Higashiguchi, K., Yasui, K., Ozawa, M., Odoi, K. & Kikuchi, H. Spatial distribution control of polymer nanoparticles by liquid crystal disclinations. *Polym. J.* **44**, 632–638 (2012).

110. Pires, D., Fleury, J.-B. & Galerne, Y. Colloid Particles in the Interaction Field of a Disclination Line in a Nematic Phase. *Phys. Rev. Lett.* **98**, 247801 (2007).

111. Coursault, D. *et al.* Linear Self-Assembly of Nanoparticles Within Liquid Crystal Defect Arrays. *Adv. Mater.* **24**, 1461–1465 (2012).

112. Li, Y. *et al.* Periodic assembly of nanoparticle arrays in disclinations of cholesteric liquid crystals. *Proc. Natl. Acad. Sci.* **114**, 2137–2142 (2017).

113. Yu, L., Cheng, Z., Dong, Z., Zhang, Y. & Yu, H. Photomechanical response of polymer-dispersed liquid crystals/graphene oxide nanocomposites. *J. Mater. Chem. C* **2**, 8501–8506 (2014).

114. Xu, Z. & Gao, C. Aqueous Liquid Crystals of Graphene Oxide. *ACS Nano* **5**, 2908–2915 (2011).

115. Aboutalebi, S. H., Gudarzi, M. M., Zheng, Q. Bin & Kim, J.-K. Spontaneous Formation of Liquid Crystals in Ultralarge Graphene Oxide Dispersions. *Adv. Funct. Mater.* **21**, 2978–2988 (2011).

116. Kim, J. E. *et al.* Graphene Oxide Liquid Crystals. *Angew. Chemie Int. Ed.* **50**, 3043–3047 (2011).

117. Bates, M. A. & Frenkel, D. Nematic–isotropic transition in polydisperse systems of infinitely thin hard platelets. *J. Chem. Phys.* **110**, 6553–6559 (1999).

118. Konkena, B. & Vasudevan, S. Glass, Gel, and Liquid Crystals: Arrested States of Graphene Oxide Aqueous Dispersions. *J. Phys. Chem. C* **118**, 21706–21713 (2014).

119. Jalili, R. *et al.* Formation and processability of liquid crystalline dispersions of graphene oxide. *Mater. Horiz.* **1**, 87–91 (2014).

120. Hong, S.-H., Shen, T.-Z. & Song, J.-K. Electro-optical Characteristics of Aqueous Graphene Oxide Dispersion Depending on Ion Concentration. *J. Phys. Chem. C* **118**, 26304–26312 (2014).

121. Lin, F., Tong, X., Wang, Y., Bao, J. & Wang, Z. M. Graphene oxide liquid crystals: synthesis, phase transition, rheological property, and applications in optoelectronics and display. *Nanoscale Res. Lett.* **10**, 435 (2015).

122. Senyuk, B. *et al.* Nonlinear Photoluminescence Imaging of Isotropic and Liquid Crystalline Dispersions of Graphene Oxide. *ACS Nano* **6**, 8060–8066 (2012).

123. Zakri, C. *et al.* Liquid crystals of carbon nanotubes and graphene. *Philos. Trans. R. Soc. A Math. Phys. Eng. Sci.* **371**, 20120499–20120499 (2013).

124. Bao, C. *et al.* On the dispersion systems of graphene-like two-dimensional materials: From fundamental laws to engineering guidelines. *Carbon N. Y.* **107**, 774–782 (2016).

125. Stankovich, S. *et al.* Stable aqueous dispersions of graphitic nanoplatelets via the reduction of exfoliated graphite oxide in the presence of poly(sodium 4-styrenesulfonate). *J. Mater. Chem.* **16**, 155–158 (2006).

126. Jones, R. R., Hooper, D. C., Zhang, L., Wolverson, D. & Valev, V. K. Raman Techniques: Fundamentals and Frontiers. *Nanoscale Res. Lett.* **14**, 231 (2019).

127. Supur, M., Ohkubo, K. & Fukuzumi, S. Photoinduced charge separation in ordered self-assemblies of perylenediimide–graphene oxide hybrid layers. *Chem. Commun.* **50**, 13359–13361 (2014).

128. Nasab, M. G. & Kalaee, M. Epoxy/graphene oxide/liquid polysulfide ternary nano-composites: rheological, thermal and mechanical, characterization. *RSC Adv.* **6**, 45357–45368 (2016).

129. Jalili, R. *et al.* Scalable One-Step Wet-Spinning of Graphene Fibers and Yarns from Liquid Crystalline Dispersions of Graphene Oxide: Towards Multifunctional Textiles. *Adv. Funct. Mater.* **23**, 5345–5354 (2013).

130. Akbari, A. *et al.* Large-area graphene-based nanofiltration membranes by shear alignment of discotic nematic liquid crystals of graphene oxide. *Nat. Commun.* **7**, 10891 (2016).

131. Fu, K. *et al.* Graphene Oxide-Based Electrode Inks for 3D-Printed Lithium-Ion Batteries. *Adv. Mater.* **28**, 2587–2594 (2016).

132. Liu, Y., Xu, Z., Gao, W., Cheng, Z. & Gao, C. Graphene and Other 2D Colloids: Liquid Crystals and Macroscopic Fibers. *Adv. Mater.* **29**, 1606794 (2017).

133. Narayan, R., Kim, J. E., Kim, J. Y., Lee, K. E. & Kim, S. O. Graphene Oxide Liquid Crystals: Discovery, Evolution and Applications. *Adv. Mater.* **28**, 3045–3068 (2016).

134. Meng, F. *et al.* Graphene-Based Fibers: A Review. *Adv. Mater.* **27**, 5113–5131 (2015).

135. Xu, Z. & Gao, C. Graphene fiber: a new trend in carbon fibers. *Mater. Today* **18**, 480–492 (2015).

136. Naficy, S. *et al.* Graphene oxide dispersions: tuning rheology to enable fabrication. *Mater. Horiz.* **1**, 326–331 (2014).

137. Kim, M. J., Park, J. H., Yamamoto, J., Kim, Y. S. & Scalia, G. Electro-optic switching with liquid crystal graphene. *Phys. status solidi - Rapid Res. Lett.* **10**, 397–403 (2016).

138. Zhu, Z. *et al.* Tough and Thermosensitive Poly(N -isopropylacrylamide)/Graphene Oxide Hydrogels with Macroscopically Oriented Liquid Crystalline Structures. *ACS Appl. Mater. Interfaces* **8**, 15637–15644 (2016).

139. Kim, M. *et al.* Reduced graphene oxide (RGO) enriched polymer network for highly-enhanced electro-optic performance of a liquid crystalline blue phase. *RSC Adv.* **7**, 16650–16654 (2017).

140. Shen, T.-Z., Hong, S.-H. & Song, J.-K. Electro-optical switching of graphene oxide liquid crystals with an extremely large Kerr coefficient. *Nat. Mater.* **13**, 394–399 (2014).

141. Kim, J. Y. & Kim, S. O. Electric fields line up graphene oxide. *Nat. Mater.* **13**, 325–326 (2014).

142. Ahmad, R. T. M., Hong, S.-H., Shen, T.-Z. & Song, J.-K. Optimization of particle size for high birefringence and fast switching time in electro-optical switching of graphene oxide dispersions. *Opt. Express* **23**, 4435 (2015).

143. Lee, K. E. *et al.* Liquid Crystal Size Selection of Large-Size Graphene Oxide for Size-Dependent N-Doping and Oxygen Reduction Catalysis. *ACS Nano* **8**, 9073–9080 (2014).

144. Brettschneider, T., Dorrer, C., Bründel, M., Zengerle, R. & Daub, M. Wafer-level packaging and laser bonding as an approach for silicon-into-lab-on-chip integration. *J. Micromechanics Microengineering* **23**, 055005 (2013).

145. Dan, B. *et al.* Liquid crystals of aqueous, giant graphene oxide flakes. *Soft Matter* **7**, 11154 (2011).

146. Gudarzi, M. M., Moghadam, M. H. M. & Sharif, F. Spontaneous exfoliation of graphite oxide in polar aprotic solvents as the route to produce graphene oxide – organic solvents liquid crystals. *Carbon N. Y.* **64**, 403–415 (2013).

147. Zheltikov, A. M. Coherent anti-Stokes Raman scattering as a local probe for nanocomposite materials: theoretical introduction into nanoCARS. *J. Opt. Soc. Am. B* **22**, 605 (2005).

148. Xu, J., Wang, K., Zu, S.-Z., Han, B.-H. & Wei, Z. Hierarchical Nanocomposites of Polyaniline Nanowire Arrays on Graphene Oxide Sheets with Synergistic Effect for Energy Storage. *ACS Nano* **4**, 5019–5026 (2010).

149. Maragò, O. M., Jones, P. H., Gucciardi, P. G., Volpe, G. & Ferrari, A. C. Optical trapping and manipulation of nanostructures. *Nat. Nanotechnol.* **8**, 807–819 (2013).

150. Moynihan, S., Lovera, P., O'Carroll, D., Iacopino, D. & Redmond, G. Alignment and Dynamic Manipulation of Conjugated Polymer Nanowires in Nematic Liquid Crystal Hosts. *Adv. Mater.* **20**, 2497–2502 (2008).

151. Dierking, I., Scalia, G., Morales, P. & LeClere, D. Aligning and Reorienting Carbon Nanotubes with Nematic Liquid Crystals. *Adv. Mater.* **16**, 865–869 (2004).

152. Thomas, M. R. *et al.* Nematic Director-Induced Switching of Assemblies of Hexagonally Packed Gold Nanorods. *Adv. Mater.* **24**, 4424–4429 (2012).

153. Alam, T. M. & Pearce, C. J. Impact of graphene incorporation on the orientational order of graphene/liquid crystal composites. *Chem. Phys. Lett.* **592**, 7–13 (2014).

154. Rumpf, R. C. IMPROVED FORMULATION OF SCATTERING MATRICES FOR SEMI-ANALYTICAL METHODS THAT IS CONSISTENT WITH CONVENTION. *Prog. Electromagn. Res. B* **35**, 241–261 (2011).

155. Ko, D. Y. K. & Inkson, J. C. Matrix method for tunneling in heterostructures: Resonant tunneling in multilayer systems. *Phys. Rev. B* **38**, 9945–9951 (1988).

156. Dyakov, S. A. *et al.* Optical properties of grooved silicon microstructures: Theory and experiment. *J. Exp. Theor. Phys.* **113**, 80–85 (2011).

157. Kravets, V. G. *et al.* Engineering optical properties of a graphene oxide metamaterial assembled in microfluidic channels. *Opt. Express* **23**, 1265 (2015).

158. Xu, Z. & Gao, C. Graphene in Macroscopic Order: Liquid Crystals and Wet-Spun Fibers. *Acc. Chem. Res.* **47**, 1267–1276 (2014).

159. Onsager, L. THE EFFECTS OF SHAPE ON THE INTERACTION OF COLLOIDAL PARTICLES. *Ann. N. Y. Acad. Sci.* **51**, 627–659 (1949).

160. van der Kooij, F. M., Kassapidou, K. & Lekkerkerker, H. N. W. Liquid crystal phase transitions in suspensions of polydisperse plate-like particles. *Nature* **406**, 868–871 (2000).

161. Mounet, N. *et al.* Two-dimensional materials from high-throughput computational exfoliation of experimentally known compounds. *Nat. Nanotechnol.* **13**, 246–252 (2018).

162. Zannotti, A., Diebel, F., Boguslawski, M. & Denz, C. Chiral Light in Helically Twisted Photonic Lattices. *Adv. Opt. Mater.* **5**, 1600629 (2017).

163. Passaseo, A., Esposito, M., Cuscunà, M. & Tasco, V. Materials and 3D Designs of Helix Nanostructures for Chirality at Optical Frequencies. *Adv. Opt. Mater.* **5**, 1601079 (2017).

164. Ge, J., He, L., Goebl, J. & Yin, Y. Assembly of Magnetically Tunable Photonic Crystals in Nonpolar Solvents. *J. Am. Chem. Soc.* **131**, 3484–3486 (2009).

165. Chen, C.-Y., Hsieh, C.-F., Lin, Y.-F., Pan, R.-P. & Pan, C.-L. Magnetically tunable room-temperature 2 pi liquid crystal terahertz phase shifter. *Opt. Express* **12**, 2625 (2004).

166. Yu, Y., Fong, P. W. K., Wang, S. & Surya, C. Fabrication of WS2/GaN p-n Junction by Wafer-Scale WS2 Thin Film Transfer. *Sci. Rep.* **6**, 37833 (2016).

167. Song, J.-G. *et al.* Layer-Controlled, Wafer-Scale, and Conformal Synthesis of Tungsten Disulfide Nanosheets Using Atomic Layer Deposition. *ACS Nano* **7**, 11333–11340 (2013).

168. Georgiou, T. *et al.* Vertical field-effect transistor based on graphene–WS2 heterostructures for flexible and transparent electronics. *Nat. Nanotechnol.* **8**, 100–103 (2013).

169. Ratha, S. & Rout, C. S. Supercapacitor Electrodes Based on Layered Tungsten Disulfide-Reduced Graphene Oxide Hybrids Synthesized by a Facile Hydrothermal Method. *ACS Appl. Mater. Interfaces* **5**, 11427–11433 (2013).

170. Merki, D. & Hu, X. Recent developments of molybdenum and tungsten sulfides as hydrogen evolution catalysts. *Energy Environ. Sci.* **4**, 3878 (2011).

171. Yan, P. *et al.* Microfiber-based WS_2-film saturable absorber for ultra-fast photonics. *Opt. Mater. Express* **5**, 479 (2015).

172. Bhandavat, R., David, L. & Singh, G. Synthesis of Surface-Functionalized WS 2 Nanosheets and Performance as Li-Ion Battery Anodes. *J. Phys. Chem. Lett.* **3**, 1523–1530 (2012).

173. Notley, S. M. High yield production of photoluminescent tungsten disulphide nanoparticles. *J. Colloid Interface Sci.* **396**, 160–164 (2013).

174. Posudievsky, O. Y. *et al.* Liquid exfoliation of mechanochemically nanostructured tungsten disulfide to a graphene-like state. *Nanotechnology* **29**, 085704 (2018).

175. Coleman, J. N. *et al.* Two-Dimensional Nanosheets Produced by Liquid Exfoliation of Layered Materials. *Science (80-.).* **331**, 568–571 (2011).

176. Molas, M. R., Nogajewski, K., Potemski, M. & Babiński, A. Raman scattering excitation spectroscopy of monolayer WS2. *Sci. Rep.* **7**, 5036 (2017).

177. Li, Y. *et al.* Accurate identification of layer number for few-layer WS 2 and WSe 2 via spectroscopic study. *Nanotechnology* **29**, 124001 (2018).

178. Liang, L. & Meunier, V. First-principles Raman spectra of MoS2, WS2 and their heterostructures. *Nanoscale* **6**, 5394 (2014).

179. Lin, L.-S., Bin-Tay, W., Aslam, Z., Westwood, A. V. K. & Brydson, R. Determination of the lateral size and thickness of solution-processed graphene flakes. *J. Phys. Conf. Ser.* **902**, 012026 (2017).

180. Green, M. J., Parra-Vasquez, A. N. G., Behabtu, N. & Pasquali, M. Modeling the phase behavior of polydisperse rigid rods with attractive interactions with applications to single-walled carbon nanotubes in superacids. *J. Chem. Phys.* **131**, 084901 (2009).

181. Wensink, H. H. & Vroege, G. J. Isotropic–nematic phase behavior of length-polydisperse hard rods. *J. Chem. Phys.* **119**, 6868–6882 (2003).

182. van der Beek, D. & Lekkerkerker, H. N. W. Liquid Crystal Phases of Charged Colloidal Platelets. *Langmuir* **20**, 8582–8586 (2004).

183. Padmajan Sasikala, S. *et al.* Graphene oxide liquid crystals: a frontier 2D soft material for graphene-based functional materials. *Chem. Soc. Rev.* **47**, 6013–6045 (2018).

184. Kumar, P., Maiti, U. N., Lee, K. E. & Kim, S. O. Rheological properties of graphene oxide liquid crystal. *Carbon N. Y.* **80**, 453–461 (2014).

185. Lee, K. E. & Kim, S. O. Graphene Oxide Liquid Crystals Special Issue, Editorial. *Part. Part. Syst. Charact.* **34**, 1700261 (2017).

186. Khan, A. A. *et al.* Graphene and chiral nematic liquid crystals: a focus on lasing. *RSC Adv.* **5**,

57437–57443 (2015).

187. Shivanandareddy, A. B., Krishnamurthy, S., Lakshminarayanan, V. & Kumar, S. Mutually ordered self-assembly of discotic liquid crystal–graphene nanocomposites. *Chem. Commun.* **50**, 710–712 (2014).

188. Li, S. *et al.* Enhanced Photorefractive and Third-Order Nonlinear Optical Properties of 5CB-Based Polymer-Dispersed Liquid Crystals by Graphene Doping. *J. Phys. Chem. C* **118**, 18015–18020 (2014).

189. Engel, M. *et al.* Light–matter interaction in a microcavity-controlled graphene transistor. *Nat. Commun.* **3**, 906 (2012).

190. Islam, M. M. *et al.* Liquid Crystalline Graphene Oxide/PEDOT:PSS Self-Assembled 3D Architecture for Binder-Free Supercapacitor Electrodes. *Front. Energy Res.* **2**, (2014).

191. Soltani, M., Inman, J. T., Lipson, M. & Wang, M. D. Electro-optofluidics: achieving dynamic control on-chip. *Opt. Express* **20**, 22314 (2012).

192. Fan, Y., Wei, Z., Li, H., Chen, H. & Soukoulis, C. M. Photonic band gap of a graphene-embedded quarter-wave stack. *Phys. Rev. B* **88**, 241403 (2013).

193. Castriota, M. *et al.* In situ polarized micro-Raman investigation of periodic structures realized in liquid-crystalline composite materials. *Opt. Express* **19**, 10494 (2011).

194. Guddala, S., Dwivedi, V. K., Vijaya Prakash, G. & Narayana Rao, D. Raman scattering enhancement in photon-plasmon resonance mediated metal-dielectric microcavity. *J. Appl. Phys.* **114**, 224309 (2013).

195. Zheltikov, A. M. Nano-optical dimension of coherent anti-Stokes Raman scattering. *Laser Phys. Lett.* **1**, 468–472 (2004).

196. Kuzik, L. A., Yakovlev, V. A. & Mattei, G. Raman scattering enhancement in porous silicon microcavity. *Appl. Phys. Lett.* **75**, 1830–1832 (1999).

197. Mamichev, D. A. *et al.* Enhanced Raman scattering in multilayer structures of porous silicon. *J. Raman Spectrosc.* **42**, 1392–1395 (2011).

198. Mamichev, D. A. *et al.* Enhanced Raman scattering in grooved silicon matrix. *Phys. status solidi* **246**, 173–176 (2009).

199. Hui Chen, Z., Long Tan, Q., Lao, J., Liang, Y. & Guang Huang, X. Reconfigurable and tunable flat graphene photonic crystal circuits. *Nanoscale* **7**, 10912–10917 (2015).

200. Dyakov, S. A. *et al.* Surface states in the optical spectra of two-dimensional photonic crystals with various surface terminations. *Phys. Rev. B* **86**, 115126 (2012).

201. Christ, A., Tikhodeev, S. G., Gippius, N. A., Kuhl, J. & Giessen, H. Waveguide-Plasmon Polaritons: Strong Coupling of Photonic and Electronic Resonances in a Metallic Photonic Crystal Slab.

Phys. Rev. Lett. **91**, 183901 (2003).

202. Tikhodeev, S. G., Yablonskii, A. L., Muljarov, E. A., Gippius, N. A. & Ishihara, T. Quasiguided modes and optical properties of photonic crystal slabs. *Phys. Rev. B* **66**, 045102 (2002).
203. Dyakov, S. A. *et al.* Influence of the buffer layer properties on the intensity of Raman scattering of graphene. *J. Raman Spectrosc.* **44**, 803–809 (2013).
204. Sengupta, A., Herminghaus, S. & Bahr, C. Liquid crystal microfluidics: surface, elastic and viscous interactions at microscales. *Liq. Cryst. Rev.* **2**, 73–110 (2014).
205. Hogan, B. T. *et al.* Videos of the effect of applied electric fields and laser excitation on the orientation and position of 2D materials dispersed in nematic liquid crystals. (2017). doi:10.24378/exe.1643
206. Twombly, C. W., Evans, J. S. & Smalyukh, I. I. Optical manipulation of self-aligned graphene flakes in liquid crystals. *Opt. Express* **21**, 1324 (2013).
207. Mezzenga, R. & Ruokolainen, J. Nanoparticles in the right place. *Nat. Mater.* **8**, 926–928 (2009).
208. Ramakrishna Matte, H. S. S. *et al.* MoS2 and WS2 Analogues of Graphene. *Angew. Chemie Int. Ed.* **49**, 4059–4062 (2010).
209. Carey, D. M. & Korenowski, G. M. Measurement of the Raman spectrum of liquid water. *J. Chem. Phys.* **108**, 2669–2675 (1998).
210. Shin, D.-W. *et al.* A New Facile Route to Flexible and Semi-Transparent Electrodes Based on Water Exfoliated Graphene and their Single-Electrode Triboelectric Nanogenerator. *Adv. Mater.* **30**, 1802953 (2018).
211. Yang, D.-S., Jiang, T. & Cheng, X.-A. Optically controlled terahertz modulator by liquid-exfoliated multilayer WS_2 nanosheets. *Opt. Express* **25**, 16364 (2017).
212. Osipova, M. O., Grachev, Y. V. & Bespalov, V. G. Performance enhancement of terahertz time-domain spectrometry. in *Asia Communications and Photonics Conference 2014* AF4A.5 (OSA, 2014). doi:10.1364/ACPC.2014.AF4A.5
213. Tong, J., Muthee, M., Chen, S.-Y., Yngvesson, S. K. & Yan, J. Antenna Enhanced Graphene THz Emitter and Detector. *Nano Lett.* **15**, 5295–5301 (2015).
214. Kuzhir, P. P. *et al.* Main principles of passive devices based on graphene and carbon films in microwave—THz frequency range. *J. Nanophotonics* **11**, 032504 (2017).
215. Walowski, J. & Münzenberg, M. Perspective: Ultrafast magnetism and THz spintronics. *J. Appl. Phys.* **120**, 140901 (2016).
216. Docherty, C. J. *et al.* Ultrafast Transient Terahertz Conductivity of Monolayer MoS 2 and WSe 2 Grown by Chemical Vapor Deposition. *ACS Nano* **8**, 11147–11153 (2014).
217. Zhang, L. *et al.* Terahertz surface emission of d-band electrons from a layered tungsten disulfide

crystal by the surface field. *Phys. Rev. B* **96**, 155202 (2017).

218. Fan, Z. *et al.* Optical Controlled Terahertz Modulator Based on Tungsten Disulfide Nanosheet. *Sci. Rep.* **7**, 14828 (2017).

219. Hogan, B. T. *et al.* Magnetically Tunable Chirality in 2D Liquid Crystalline WS2 Nanocomposites. *arXiv Prepr. arXiv1804.04745* (2018).

220. Kuzmenko, A. B., van Heumen, E., Carbone, F. & van der Marel, D. Universal Optical Conductance of Graphite. *Phys. Rev. Lett.* **100**, 117401 (2008).

221. Nair, R. R. *et al.* Fine Structure Constant Defines Visual Transparency of Graphene. *Science (80-.).* **320**, 1308–1308 (2008).

222. Wang, F. *et al.* Gate-Variable Optical Transitions in Graphene. *Science (80-.).* **320**, 206–209 (2008).

223. Chen, C.-F. *et al.* Controlling inelastic light scattering quantum pathways in graphene. *Nature* **471**, 617–620 (2011).

224. Poon, J. *et al.* Matrix analysis of microring coupled-resonator optical waveguides. *Opt. Express* **12**, 90 (2004).

225. Hu, X. & Wang, J. High Figure of Merit Graphene Modulator Based on Long-Range Hybrid Plasmonic Slot Waveguide. *IEEE J. Quantum Electron.* **53**, 1–8 (2017).

226. Chang, Y., Liu, C., Zhong, Z. & Norris, T. B. Extracting the complex optical conductivity of true two- dimensional layers by ellipsometry. in *CLEO: 2014* **261909**, 3–4 (2014).

227. Mitov, M. Liquid-Crystal Science from 1888 to 1922: Building a Revolution. *ChemPhysChem* **15**, 1245–1250 (2014).